DISS. ETH NO. 22035

Numerical investigations of rotating MHD in a spherical shell.

A dissertation submitted to

ETH ZÜRICH

for the degree of

Doctor of Sciences

presented by

ANDREY SHEYKO

MSc. in applied Physics and Mathematics
Moscow Institute of Physics and Technology (Russian Federation)

born on December 06, 1984

citizen of Russian Federation

accepted on the recommendation of

Prof. Dr. Andrew Jackson, examiner
Dr. Chris Finlay, co-examiner
Prof. Dr. Rainer Hollerbach, co-examiner
Dr. Johannes Wicht, co-examiner

2014

"Главное – делайте всё с увлечением: это страшно украшает жизнь."

Лев Давидович Ландау

"It is important to do everything with enthusiasm, it embellishes life enormously."

Lev Landau

Abstract

Motions of liquid metal inside the Earth's outer core are responsible for generating the geo-magnetic field in a dynamo process. We use a pseudo-spectral magnetohydrodynamic code to investigate dynamos maintained by various mechanisms. Boundary conditions (BC) and governing parameters are varied with the purpose of modelling the Earth's core. An accurate means to benchmark codes with so-called pseudo-vacuum magnetic BCs is proposed and an alternative way to drive a laboratory dynamo, by fluid injection is investigated.

Many prominent features in the observed core surface magnetic field are not yet explained due to the intrinsic complexity of the system and the difficulty in solving the model equations with the Earth's core parameters. It is however possible to gradually advance the models towards a geophysically relevant parameter regime as greater computing resources become available. We present dynamo simulations at rapid rotation rates ($E = \nu/(2\Omega d^2) = 3 \cdot 10^{-7}$ and 10^{-6}) that are at the cutting edge of geodynamo research today. We vary the convection strength by a factor of 30 and ratio of magnetic to viscous diffusivities by a factor of 20 ($0.05 \leq Pr_m \leq 1$) using a heat flux outer BC. This regime has been little explored due to significant computing resources required: several tens of millions cpu-hours were consumed to obtain the presented results. We report energy spectra of steady solutions, a comparison of volume-integrated characteristics of fields with the proposed rotating convection and dynamo scaling laws, time- and longitude- averages of force and energy balances, and the structure of the dynamos deep in the shell and on the CMB in relation to the selection of control parameters.

Insulating magnetic boundary conditions (used for the mentioned above big runs) are not easy to implement in non-spectral codes. A more convenient pseudo-vacuum boundary condition (setting to zero tangential magnetic field) may be used instead for practical reasons. We present essential properties of two dynamo solutions with regular deterministic characteristics operating with pseudo-vacuum BCs. One of them has been used in the community benchmark paper (Jackson et al., 2014). We also present analytical solutions for the decay rates of magnetic field decay modes in a sphere and in a spherical shell.

We investigate in addition the capability of a laboratory dynamo to be driven by the fluid injection (from one boundary and draining off from another boundary). A linear calculation is used to delineate the curve defining the onset of non-axisymmetric velocity modes: these modes are only possible in a limited range of injection strengths and rotation rates. We also conduct a set of experiments with the magnetic induction equation included and identified dynamos in several cases.

Kurzfassung

Die Bewegungen des flüssigen Metalls im äusseren Erdkern sind für die Generierung des Geomagnetfeldes in einem Dynamoprozess zuständig. Wir verwenden einen pseudo-spektralen magnetohydrodynamischen Code um Dynamos zu untersuchen, die durch verschiedenen Mechanismen aufrechterhalten werden. Die Randbedingungen (RB) und die dominierenden Parameter werden mit dem Ziel variiert den Erdkern zu modellieren. Es wird ein genaues Hilfsmittel vorgeschlagen um Codes mit sogenannten pseudo-vakuum magnetischen RBen zu benchmarken und es wird ein alternativer Weg untersucht, durch Fluidinjektionen, einen Labordynamo anzutreiben.

Aufgrund der Komplexität des Systems und Schwierigkeiten bei der Lösung der Modellgleichung mit den Erdkern Parametern konnten viele typischen Merkmale des auf der Kernoberfläche beobachteten Magnetfeldes noch nicht erklärt werden. Da mittlerweile grössere Rechenressourcen verfügbar geworden sind ist es jedoch möglich die Modelle schrittweise an das Regime der geophysikalisch relevanten Parameter heranzuführen. Wir präsentieren Dynamosimulationen bei grossen Drehzahlen ($E = \nu/(2\Omega d^2) = 3 \cdot 10^{-7}$ und 10^{-6}), welche an der Spitze der heutigen Geodynamoforschung stehen. Wir variieren die Konvektionsstärke um einen Faktor von 30 und das Verhältnis der magnetischen zu den viskosen Diffusionen um einen Faktor von 20 ($0.05 \leq Pr_m \leq 1$) unter Verwendung einer äusseren Wärmefluss RB. Das Regime wurde bislang wenig erforscht, da es erhebliche Rechenressourcen erfordert: es wurden mehrere zehn Millionen CPU-Stunden verbraucht, um die vorgestellten Ergebnisse zu erhalten. Wir zeigen Energiespektren der stetigen Lösungen, einen Vergleich von der volumenintegrierten Eigenschaften der Felder mit der vorgeschlagenen Drehkonvektion und Dynamo Skalierungsgesetze, über Zeit und Länge gemittelte Kräftegleichgewichte und Energiebilanzen und die Struktur von Dynamos tief in der Schale und an der CMB in Bezug auf die Auswahl der dominierenden Parameter.

Isolierende magnetische Randbedingungen (die für die oben genannten grossen Simulationen verwendet wurden), sind nicht einfach in nicht-spektrale Codes zu implementieren. Stattdessen kann aus den praktischen Gründen eine günstigere pseudo-vakuum Bedingung (tangentiales Magnetfeld auf Null gesetzt) angewendet werden. Wir zeigen wesentliche Eigenschaften von zwei Dynamo Lösungen mit regulären deterministischen Merkmalen die mit den pseudo-vakuum RBen bestimmt wurden. Eine dieser wurde im Gemeinschafts-Benchmarkartikel (Jackson et al., 2014) verwendet. Wir präsentieren auch analytische Lösungen für die Zerfallsrate der Magnetfeld-Zerfallsmoden in einer Sphäre und in einer sphäri-

schen Schale.

Ausserdem untersuchen wir die Fähigkeit eines Labordynamos von der Fluidinjektion (von einem Rand und dem Ausfluss am anderen Rand) angetrieben zu werden. Es wird eine lineare Berechnung zum Skizzieren der Kurve für die Bestimmung des Ausbruchs von nicht-axialsymmetrischen Geschwindigkeitsmoden angewandt: diese Moden können nur in einem begrenzten Bereich von Injektionsstärke und Drehzahl auftreten. Wir führen auch eine Reihe von Experimenten unter Einbeziehung der Gleichung der magnetischen Induktion durch und identifizierten in mehreren Fällen Dynamos.

Contents

Acknowledgments

I would like to acknowledge those who have helped me complete this PhD. Primarily, I would like to express my profound gratitude to both my supervisors Chris Finlay and Andrew Jackson. On my very first visit to Zürich I was captivated by Andy's charisma and love for science and decided to apply for a PhD in his group. From the start I have received tremendous and continuous support from Chris. His self-discipline and almost encyclopedic knowledge of the subject still impresses me. I hope that I was able to acquire the attitude to research demonstrated by Chris and Andy. I feel very lucky to have had these scientific advisers.

I would like to thank Philippe Marti for introducing me to his spherical MHD code, to many technical aspects of code development, to HPC basics and for his patience in answering all my questions.

I thank Prof. Rainer Hollerbach for his readiness and enthusiasm to discuss anything related to fluid dynamos and his ability to express complicated ideas in a lucid and precise way. I would like to thank him also for providing and explaining his spherical MHD code and also for helping to benchmark my modification to the Philippe's code.

I thank Dr. Jean Favre from Swiss National Supercomputing Centre (CSCS) for his extensive support in visualization, his visits to the EPM where he presented software advancements related to scientific visualization.

I am very grateful to Dr. Ataru Sakuraba for sharing details of his spectacular MHD calculations and for helpful discussions at different conferences. It was pleasure to speak some Russian with him and learn a couple of Japanese words.

Zacharias Stelzer gave me access to scaling laws he developed, with permition to use them before publication, for which I am very grateful. I am also very grateful to Zacharias for taking me to a hospital after a ski accident in the Davos forest at the EPM ski trip. (I sincerely thank Dr. Andreas Gehring for taking me out of there.)

There were many useful meetings, seminars and conferences where I participated during this PhD and I am grateful to all those who were involved. In particular I thank Dr. Nicolas Gillet for sharing his experience in MHD simulations, Dr. Peter Davidson for the informative conversation about energy spectra during the Ascona meeting 2013, Dr. Eric King and Dr. Jonathan Aurnou for the helpful discussion related to scaling laws and large MHD calculations at SEDI 2012.

I would like to thank Dr. Jonathan Aurnou for inviting me to his session at the AGU 2013 and CSCS for supporting my attendance there.

Lugano May 2014   Andrey A. Sheyko

Chapter 1

Introduction

Andrey Sheyko. July 16, 2014.

1.1   Motivation

Earth's liquid core is hidden away from the surface by 3000 kilometres of silicate mantle. Information about the fluid motions inside it comes primarily in an indirect manner from geomagnetic observations. Furthermore at the Earth's surface only the poloidal component of the magnetic field can be measured. All other information including the toroidal component of the magnetic field is practically invisible for the surface observer. This lack of information leads to the greatly ill-posed problem of recovering the detailed state of the outer core, in particular its velocity and magnetic fields. One approach to understanding what happens inside the core is to attempt to explain and reproduce dynamical features of the *core-mantle boundary* (CMB) magnetic field using numerical simulations of core magnetohydrodynamics.

The field on the CMB can be inferred by the downward continuation of surface measurements assuming the mantle may be approximated as an insulator on the long time scales of interest. Jackson (2003) examined high resolution images of the field at the core surface in 1980 and 2000, constructed using high-quality satellite data and utilizing a maximum entropy regularization technique. He found intense low latitude wave-like features. These features move essentially east-west, and Finlay and Jackson (2003) found clear westward motion of these features over the past four hundred years. The drift of the equatorial spots may represent material flow or could represent wave motion, and discrimination of these two effects could provide new information on the strength of the hidden toroidal field of the Earth.

Detailed analyses of suitable numerical simulations have an important role to play in testing the correspondence between observations and current theory. Recently constructing 3-D models of the magnetic field in the core has become possible. A Spherical Dynamo Code (Willis et al., 2007) coupled with 3-D visualization software (ParaView, VisIt) gives us the opportunity to trace dynamical features, that is to say to 'look inside' a putative outer core and

to study the crucial processes in greater detail than was previously possible.

This document includes following topics: basic theory (chapter 1 and Appendix A), numerical implementation (chapter 2), a search of dynamos in systems with flow driven through porous boundaries (chapter 4), tests concerning dynamos with pseudo-vacuum boundaries (chapter 3), and rapidly rotating, convection-driven dynamos (chapter 5). Chapters 4 and 3 describe the influence of two unusual boundary conditions on the behaviour of conducting fluid with the magnetic field. Chapter 5 describes in detail how dynamos requiring unusually high computational resources can give a more detailed picture of the Earth's core. A focus in these demanding simulations is to examine the types of convective motions and waves that might exist in the core, in the presence of a magnetic field. These waves and/or convective motions might account for the presence of equatorial flux spots seen in the equatorial region of the core (Jackson, 2003).

1.2   A brief history of MHD theories of the geodynamo

The first definite finding about the origin of the magnetic field on the Earth's surface was made by Karl Friedrich Gauss. The harmonic analysis of the field data available at that time prompted the conclusion that the source of the magnetic field is inside the Earth (Gauss, 1839).

By the start of the 20th century physics already reached the level sufficient to foresee the feasibility of creating the magnetic field by the convection of an electrically conducting fluid in the core of the Earth. The crucial advance was to realize that magnetism and hydrodynamics can inter-play forming in certain conditions a coupled system, and to realize that such a system can exist within the Earth. Parallels between the magnetic fields of the Earth and the Sun were drawn quite early. It is possible to observe the convective region in the Sun with relatively simple instruments, and it is much easier to make sustainable conclusions about the involving processes. In 1919 British[1] physicist Sir Joseph Larmor stated (Larmor, 1919) that "it is possible for the internal cyclic motion to act after the manner of the cycle of a self-exciting dynamo, and maintain a permanent magnetic field from insignificant beginnings, at the expense of some of the energy of the internal circulation". Although his short report was dedicated to the origin of solar magnetic field, J. Larmor also speculated that the fluidity of the Earth's interior could be responsible for its magnetic field.

At that time it was not definitely known whether or not the Earth had a liquid core. In 1906 Richard Dixon Oldham (Oldham, 1906) found a discontinuity at the depth of 3884km by the analysis of seismic waves. Revision by Beno Gutenberg (Gutenberg, 1913) gave another value for the discontinuity: 2900km, which is very close to the contemporary value for the depth of the outer core (PREM[2] gives 2891km). But it was still assumed that the material below

---

[1]Actually Sir Joseph Larmor was from Northern Ireland and all Ireland was part of the UK when he did his crucial work on the dynamo.

[2]Preliminary Reference Earth Model, Dziewonski and Anderson (1981).

this depth was solid, or, in other words, allows shear seismic waves. The first explicit and influential statement that the core is liquid was made by Sir Harold Jeffreys in 1926 [3](Jeffreys, 1926). The solid inner core in the center of the Earth was discovered later by the Danish seismologist Inge Lehmann (1936). PREM estimates the inner core depth as 5149.5km. It is worth to mention PREM's value for the Earth's radius. The distance between ocean surface and planet's center has a mean spherical reference value of 6371km.

Thomas Cowling being good in showing that theories of others are wrong[4], demonstrated that an axisymmetric magnetic fields cannot be maintained by a fluid motion disproving the Larmor's Sun spots theory. His elegant proof, which can be found in Cowling (1933) with helpful illustrations in Cowling (1975), uses special points in an axisymmetric magnetic field, where the magnetic field $\mathbf{B} = 0$ but current density $\mathbf{j} \neq 0$. Such points with non-zero currents ($\mathbf{j} = \nabla \times \mathbf{B}/\mu$, where μ is magnetic permeability) should exist by geometrical considerations, but can not be maintained by either an electrostatic field (currents are closed in loops), nor by fluid motions ($\mathbf{u} \times \mathbf{B} = 0$ because $\mathbf{B} = 0$). This brings the conclusion: maintenance of such an axisymmetric field is impossible. In his article in 1933 Cowling extrapolated the conclusion saying that "the general magnetic fields of the Sun and the Earth cannot be self-maintained, as was suggested by Larmor". Fortunately, several subsequent discoveries in dynamo theory showed ways around Cowling's objection, and this was not the end of the story.

Bullard and Gellman (1954) and Takeuchi and Shimazu (1953) used truncated numerical series expansions in attempts to demonstrate the ability of a fluid flow to reproduce the magnetic field. The work of English geophysicist Sir Edward Bullard and Harvey Gellman, his PhD student and later a famous Canadian consultant in computer technologies, is particularly interesting. They implemented spherical harmonic decomposition (see chapter 2) and numerical integration techniques in many ways similar to those used today. The computations were made using 240 hours on the British National Computer ACE (Automatic Computing Engine, which was initially designed by the English mathematician and computer scientist Alan Turing, 1946). Gibson and Roberts (1967) however showed that the flows used by Bullard are not in fact dynamos. The problem was in too low truncation degree. But in fifties those results were an important stimulus for further progress in dynamo theory.

Backus (1958) and Herzenberg (1958) developed rigorous proofs of the existence of dynamos for certain prescribed velocity fields. George Backus, an American geophysicist, used periodic time-dependence of the velocity field to create a dynamo. In his dynamo a toroidal shear symmetric about the rotation axis proceeds long enough to produce from the lowest axisymmetric poloidal mode and a very large toroidal mode (the lowest free-decay toroidal mode, see definitions of the poloidal and toroidal field components in sec.B.3). Then the velocity field is turned off, and during period of stasis everything else almost dies out, leaving

---

[3]According to (Brush, 1980) the first published suggestion that observed seismic velocities imply a fluid core was by the Russian Leonid Leybenzon in 1911.

[4]As a student of Edward Milne, Thomas Cowling has disproved the conclusion by Sydney Chapman that the magnetic field of the Sun could not extend out very far (Cowling, 1985).
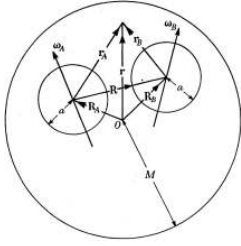
Figure 1.1*: Herzenberg's dynamo. Two conducting rigid spheres rotate inside a non-moving conductor and feed one another with magnetic field.*

only the toroidal field. Then almost any velocity which has a radial component, and non-axisymmetric, can produce the necessary poloidal field. Herzenberg's dynamo is shown in fig.1.1. Two conducting rigid spheres rotate inside a non-moving conductor and feed one another with magnetic field. Although the configurations seems to be very artificial, dynamos in stellar binary systems may operate in a similar way (Dolginov and Urpin, 1979).

The following sections will address the outstanding issues of current dynamo research: choice of driving mechanisms and thermal *BC (boundary conditions)*, scaling laws, waves, field morphology compared to the Earth.

1.3   Energy sources and driving mechanisms for the geodynamo

Even if all mechanical arrangements inside the Earth are suitable for the dynamo action (the planet is large, rapidly rotating and contains conductive fluid layer) a source of energy sufficient to drive the necessary motions is required. The following sources of energy are accessible in the Earth's core: latent heat from the freezing inner core, heat flux from the inner core, radioactive reactions, ohmic heat, gravitational energy carried by light elements. The convection can be driven thermally or by the light elements which are released when heavy components freeze out to form the inner core. This mechanism was proposed by the soviet scientist Stanislav Braginsky (Braginsky, 1963). With some simplifications it is possible to include both heat and light elements in a single transport equation.

The magnetic Prandtl number which measures the ratio of the viscous to the ohmic dissipation is of the order 10^{-7} for Earth's outer core and most liquid metals (Gans, 1972). This small number shows that energies are mostly dissipated via ohmic heat[5] unlike in the mantle, where only viscous dissipation is important. At the first sight it seems inconsistent to find that the ohmic heating is not included in the heat flux balance for most geodynamo models. If we put aside the usual desire to simplify the model, the reason is low efficiency of the dynamo, i.e. the small ratio of magnetic energy production to the available heat fluxes. Roberts et al. (2003)

---

[5]Here we refer to transformation into thermal energy as dissipation. Thermal energy is in turn transported resulting in heat fluxes through boundaries.

estimated upper limit for the ohmic dissipation rate of 1TW which is much smaller than the power available for convection (compare e.g. to the total heat 44TW coming out of the Earth's surface). New values for the thermal conductivity of iron (Pozzo et al., 2012) suggest the heat conducted down the adiabat is ~ 15TW, much larger than that dissipated. Although some of the numerical models include ohmic heat (e.g. Anufriev et al., 2005).

Light elements bring additional complications into the system. It is possible that they are gathered in a thin stable layer on the top of the core. Such a layer would be stable because buoyancy would be negative there (heavy hot elements penetrating the layer find themselves amongst lighter elements and sink backwards). This "inverse ocean" was proposed by S. Braginsky as well (Braginsky, 1999).

Most existing simulations of the Earth's dynamo assume uniform internal heating (or absence of it) and uniform boundary conditions (constant temperature or heat flux). Seismic observations and the modeling of the mantle convection suggest that the heat flux at the core-mantle boundary is non-uniform. Earth-like non-uniform boundary conditions may, for example, be the source of some departures from equatorial symmetry in the time averaged field structure (e.g. Olson and Christensen, 2002; Gubbins et al., 2007; Aubert et al., 2007).

In Backus (1975) obtained an important and fundamental bound on the ratio of the rate of production of mechanical or magnetic energy to the heat leaving the core through the mantle. The idealized thermally driven dynamo is constructed from a Carnot engine and a simple mechanical dynamo (see fig.1.2). The upper estimate on the rate of mechanical energy W obtained from the available heat flux Q_h is given by $\frac{W}{Q_h} \leq \frac{\theta_h}{\theta_c} - 1 \approx 0.34$ using estimates of the Earth's core maximum ($\theta_h \approx 5000$, Gubbins, 2007) and CMB ($\theta_c \approx 3739$) temperatures. Mechanical energy in the core is dissipated mostly via ohmic heat, so the same number gives an estimate for the maximum ratio 0.34 of magnetic energy dissipation to heat flow. This also gives a rough estimation on the upper bound of magnetic field in the core (600mT by Backus, 1975). This thermodynamic view on thermal driven dynamos will be useful in the context of scaling laws based on the heat transport discussed in the chapter 5.
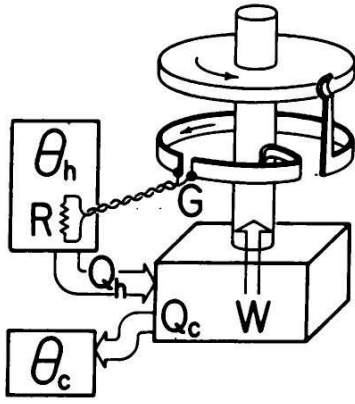
Figure 1.2*: Disc dynamo driven by a Carnot engine operating out of a hot reservoir which includes both radioactive heat and the ohmic heat from the dynamo current. The Carnot engine operates between hot reservoir at temperature θ_h and cold reservoir at temperature θ_c and extracts heat from the reservoir at a rate Q_h. The rate at which the engine deposits the heat in the cold reservoir is Q_c. All the resistance in the dynamo circuit is contained in the resistor R. $W = Q_c(\theta_h/\theta_c - 1)$ is the supply of the mechanical power and at steady state it equals to the ohmic heat RI^2 if I is the current in the dynamo circuit.*

1.4   Influence of the thermal boundary condition in modelling the geodynamo

The Earth's mantle and the core convect on drastically different time scales. Typical velocities in the mantle are 20 mm/year (Lallemand and Funicello, 2009), whereas the low viscosity core fluid is inferred to move much more rapidly at 0.5 mm/sec (e.g. Holme, 2007). The core convects a million times faster than the mantle. No wonder that the core mantle boundary is seen differently from the inner and outer sides. For the mantle the core's surface to a good approximation maintains a constant temperature. The quickly convecting core adapts to any change in the structure of mantle virtually instantly, making lateral variations of temperature negligible. From the other side, convection in the mantle acts as a very slow modulation of the fast evolving core. At core's time scales the radial distribution of temperature is persistent in mantle, this keeps the value of the heat flux coming out of the core-mantle boundary almost constant, for example on the time scales of secular variation[6]. The preferable boundary condition for the core is therefore a heat flux boundary condition.

Sakuraba and Roberts (2009) have compared dynamo simulations at extremely low Ekman number ($E = \dfrac{\nu}{2\Omega d^2} \approx 10^{-6}$, where ν is kinematic viscosity of the convecting fluid, Ω is angular velocity and d is a typical length scale of the rotating container) investigating the differences between cases with the heat flux and the constant temperature boundary conditions. The heat flux boundary condition was found to produce much larger structures both in convection and magnetic field patterns (fig. 1.3). Moreover, the simulation with heat flux boundary

---

[6]The geomagnetic *secular variation* describes changes of the Earth's magnetic field on time scales of the order of one year and larger. See, e.g., Jackson et al. (2000).

(a) Constant Temperature

(b) Constant heat flux
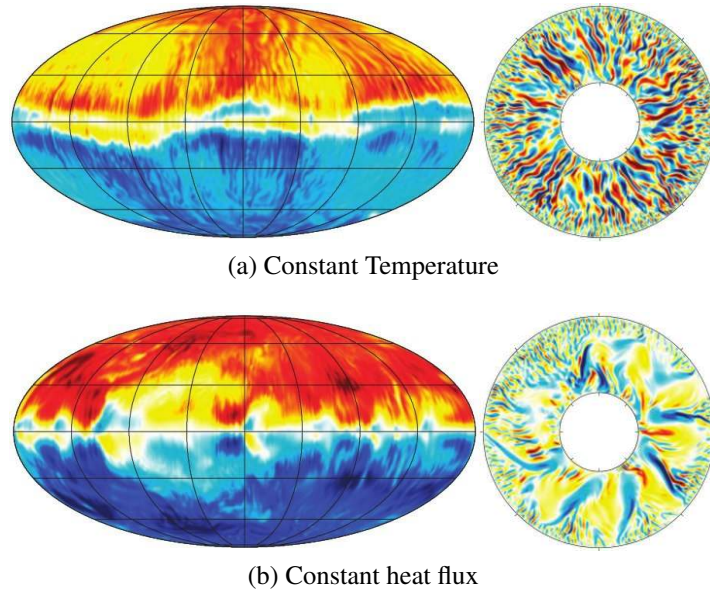
Figure 1.3*: The radial component of the magnetic field at the outer boundary (left) and of the velocity in the equatorial plane (right). Both panels (a) and (b) have the same scale. A field which is directed outwards is depicted by red color, opposite one is blue, Sakuraba and Roberts (2009). Simulation has parameters $E = 1.1834 \cdot 10^{-6}$, $Ro = 1.1834 \cdot 10^{-6}$, $Ra = 219.7$, $q = 0.2$ which are defined in chapter 5.*

conditions generated a much larger and much more dipolar (i.e. Earth-like) magnetic field.

In Hori et al. (2010, 2012) the difference in scale between cases with fixed flux and fixed temperature were observed already at a much larger Ekman number of $E = 10^{-4}$. A difference is that multipolar fields were found when fixed temperature condition was used. Beyond that, it was shown that the presence of magnetic field generally increases the flow scale irrespective of the temperature boundary condition via the Lorentz force.

The reason for large length scale convection in dynamos with heat flux boundary conditions is not yet understood. In chapter 5 we will study a suite of dynamos with heat flux boundary conditions to clarify the mechanisms involved.

1.5 Waves in Earth's core and in dynamo simulations

Waves are often the leading order (linear) response of a dynamical system to an external perturbation. They are easily tackled analytically by linearising the governing equations. Not surprisingly, wave solutions were identified quite early in the history of the MHD.

Alfvén (1942) predicted the existence of electromagnetic-hydromagnetic waves later called after him. Every motion of the conducting liquid in a magnetic field gives rise to an electromotive force which produces an electric current. The magnetic field acting on the current with mechanical forces changes the state of motion of the fluid. And this mutual interaction between fluid and magnetic field produces wave with the velocity $V_A = B_0 / \sqrt{\rho \mu}$ (where B_0 is the strength of magnetic field and ρ is the density of fluid) in the direction of the magnetic field. In an ideal medium without viscous and ohmic dissipation the dispersion relation of
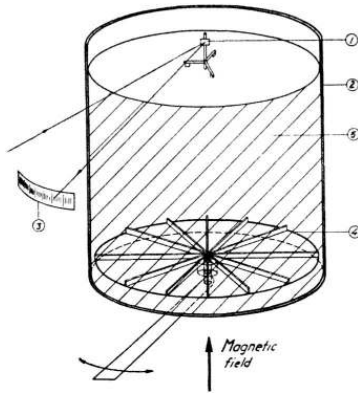
Figure 1.4*: Arrangement of the experiment on Alfvén waves by Lundquist (1949): (1) floating mirror, (2) stainless steel cylinder, (3) scale, (4) vibrating disk, (5) mercury.*

these waves is $\omega = \pm V_A (\mathbf{k} \cdot \mathbf{B}_0)$ with the wave-vector $\mathbf{k}$. Alfvén waves are both non-dispersive and non-isotropic. Alfvén's explanation of the sun spots required these waves to carry disturbances from the inner part of the Sun to its surface. Experimental confirmation of existence of these waves was found later by Lundquist (1949).

His setup (fig.1.4) visually illustrates the physical conditions required for the existence of Alfvén waves. A strong magnetic field of 1.3T was required to obtain waves travelling fast enough that several cycles could be measured before their decay due to Ohmic dissipation. Motions of the disk (4) produced waves seen by the movement of the floating mirror (1). Assuming a magnetic field of strength 0.5mT and outer core density $10^4 \, kg/m^3$ Alfvén waves would have a speed of $140 \, km/yr$ (Gubbins, 2007) so they would travel across the core in 16 years.

But due to the rapid rotation of Earth's core, Coriolis forces (which do not enter into Alfvén's classical theory) should also be considered. Based on his estimation of the relative importance of the Coriolis force in the Sun (14 times stronger than the magnetic force), Lehnert (1954) was the first to consider the influence of the Coriolis force in an MHD system. He found that the presence of rotation significantly modifies properties of the waves when $\Omega L / V_A \gg 1$, where L is the wavelength of the disturbance and Ω is the angular velocity. If the direction of the wave vector, the rotation and magnetic field are all aligned $V = \pm V_A ((1 + \chi^2)^2 \pm \chi)$ with $\chi = \Omega L / (2\pi V_A)$. This means both a slow and a fast solution become possible. Apart from the derivation of these new waves, called now Magneto-Coriolis (*MC-waves*), he introduced a ratio which is known now as the Lehnert number[7] $Le = \dfrac{B}{2L\Omega(\rho\mu)^{1/2}}$ describing the relative importance of the Lorentz force and the Coriolis force. In this non-dimensional number the Alfvén speed is used as the estimation of velocity on which rotation acts to create Coriolis force. A special type of Alfvén waves are *torsional oscillations*. These are rotations of fluid cylinders concentric with the Earth's rotational axis, about that axis. Torsional oscillations are responsible for the decadal variations of a few milliseconds in the length

---

[7]Lehnert (1954) actually defined the inverse of this ratio.

of the day as a result of exchange of the angular momentum between the Earth fluid outer core and solid mantle. The analysis of these waves in numerical simulations can be found in Wicht and Christensen (2010).

By adding details concerning the driving mechanisms and the geometry of the system, a large number of waves are in principle possible in the Earth's core. A classification of these waves from the point of view of involved timescales can be found in Hollerbach (2003).

Certain observable features of the geomagnetic field may perhaps be explained by the MHD waves. For example Braginsky (1967) suggested *MAC-waves*[8] as the cause of the westward drift[9]. In the next section 1.8 we will discuss wave-like features of the observable geomagnetic field that may be explained either by some intrinsic MHD waves or by the corresponding convection structures. Our dynamo simulations in the chapter 5 are aimed to reproduce such features and to understand their internal structure.

1.6   The lowest Ekman number simulations

Geodynamo simulations – how realistic are they? The question was posed by Glatzmaier (2002) and remains an important and controversial issue. Powers of the Ekman number E define the finest length scales in a dynamo simulation and it serves as a simple measure of complexity in a fluid dynamo. The Earth's Ekman number is estimated to be 10^{-15}, some eight orders of magnitude lower than the nowadays achievable in numerical simulations i.e. $E = 10^{-7}$. The Earth's core with $E = 10^{-7}$ would contain a sticky liquid like a peanut butter fluid instead of very liquid molten metal. Even such highly viscous computations require enormous resources and long integration times (months on the biggest supercomputers).

Is it possible to calculate the MHD of the Earth's core with truly appropriate parameters? Then we would need to resolve tiny structures compared with respect to the planet's size. The Ekman boundary layer is $E^{1/2}r_o \approx 20cm$, and the Earth's core radius $r_o = 3480km$. The tremendous three-dimensional grid will therefore need to have $N = (E^{-1/2})^3 \approx 10^{22}$ elements. The number of operations to inverse a matrix scales like[10] N^3, so 10^{66} operations are needed just for a single inversion. High performance computers will soon be able to perform 10^{18} floating point operations per second. Such a computer would need 10^{41} years to perform one inversion. Furthermore, the timestep is proportional to the size of the grid element Δr. The amount of time steps needed to model a sensible amount of time therefore palpably increases when the grid is refined. That is to say, the brute-force calculation of the MHD equations with Earth's core parameters seems to be hopeless with the present-day technologies. But perhaps

---

[8]As the name implies, MAC-waves are influenced by Magnetic (Lorentz), Archimedean (buoyancy), and Coriolis forces, which the dominant forces in the Navier-Stokes equation.

[9]The non-dipolar component of the Earth's magnetic field is subjected to the so-called *westward drift* during at least few recent centuries. See, for example, Dumberry and Finlay (2007).

[10]For the numerical method called LU decomposition the cost to inverse a matrix with the size N is approximately $\frac{2}{3}N^3$, see Trefethen and Bau III (1997).

there is a hope in reaching an asymptotic regime, where the influence of the viscosity on large structures disappears.

The era of contemporary geodynamo simulations started with the work of Glatzmaier and Roberts (1995). They developed "the first three-dimensional (3D), time-dependent, self-consistent numerical solution of the magneto-hydrodynamic (MHD) equations that describes thermal convection and magnetic field generation in a rapidly rotating spherical fluid shell with a solid conducting inner core". They demonstrated a dynamo with an Ekman number $E = 10^{-6}$. The way they succeeded in obtaining such a low Ekman number with comparatively modest resolution (49 Chebyshev radial, 32 latitudinal, 64 in longitudinal levels) was through the use of the hyperdiffusivity, i.e. the viscosity has been dependent on the harmonic degree l, $\nu(l) = \nu_o(1 + 0.075 l^3)$. This treatment of the viscosity filters out fine structures, but can lead to an essentially different behavior of a dynamo (e.g. Zhang and Jones, 1997; Grote et al., 2000).

Miyagoshi et al. (2011) performed dynamo calculations with $E = 0.54 \cdot 10^{-6}$, and unity values of *Prandtl Pr* and *magnetic Prandtl Pr_m numbers* ($Pr = \nu/\kappa$ is the ratio of the viscous and the thermal diffusivities, $Pr_m = \nu/\eta$ is the ratio of the viscous and the magnetic diffusivities). Constant temperatures were kept on both boundaries ($T(r_i)/T(r_o) = 2$). No-slip condition has been invoked for the velocity field. Pseudo vacuum boundary conditions were used for the magnetic field (see definition in chapter 3). Discretisation was done with the finite-difference method with so-called "Yin-Yang" overset grid to avoid problems at the poles. They have obtained a convective structure composed of narrow sheet plumes. The magnetic field that is parallel to the plumes was localized in the sheets. Magnetic energy was an order of magnitude larger than the kinetic. To give some idea about the complexity of the solution, it is worth mentioning that authors used a virtual reality system for the visualisation.

Takahashi and Shimizu (2012) have performed dynamo calculations with $Pr_m = 2$ and $Pr = 1$ keeping $E = 10^{-5}$. Constant heat flux was kept on both boundaries (top flux is 2.8 times bigger than the bottom flux). Both boundaries were electrically insulating. The Boussinesq approximation and a pseudo-spectral method were employed. They have obtained large magnetic field (55 times stronger magnetic than kinetic energy) . The convection was organised in localised thin sheet-like plumes with large scale retrograde azimuthal flows. The energy budget was magnetostrophic, i.e. Lorentz, Coriolis and buoyancy forces were dominant.

Wicht and Christensen (2010) investigated oscillations of co-axial cylinders (so-called torsional oscillations) varying Ekman numbers down to $E = 1.5 \cdot 10^{-6}$ (although with four-fold azimuthal symmetry to save computational time) with Prandtl number $Pr = 1$ and magnetic Prandtl number $Pr_m = 0.5$. They employed pseudo-spectral method. Even though *Alfvén Mach number* (ratio of the flow and wave velocities) was relatively large in the model with the lowest Ekman number, they clearly identified propagation of the torsional oscillations after integrating the model for several dipole decay times.

Sakuraba and Roberts (2009) also used a pseudo-spectral method for the low Ekman num-

ber calculation: $E \approx 1.2 \cdot 10^{-6}$, magnetic Prandtl number $Pr_m = 0.2$ and Prandtl number $Pr = 1$. They have shown the importance of the heat flux boundary condition to obtain large scale magnetic field. Besides that the westward drift of the Earth-like equatorial features was found in their model.

1.7 Scaling laws and parametric studies

Recently a huge amount of data from diverse sources (observational, experimental and numerical modeling) and for different dynamo regimes has started to be available for statistical analysis and extraction of intrinsic relationships. The dependency between the model parameters (primary physical properties such as geometry, viscosity, density, driving power) and the observable variables can be described by generally empirical relationships which is known as a scaling law. These laws are best formulated in non-dimensional form because this reduces the number of variables involved (as expressed by the Buckingham's π-theorem).

Aurnou (2007) discusses an asymptotic behaviour of scaling laws. Let us for example consider a function $f(x)$ which has an asymptotic behaviour in a particular subspace of parameters x. For intermediate values of x the function varies strongly with x and if experiments are done with these values of x, it may be hard to predict the behaviour in other regions of x. On the contrary, if experiments are done in the asymptotic regime, the extrapolated function may well describe more extreme conditions, for example those of the Earth's core. However the question whether experiments reach the asymptotic regime is challenging. Aurnou (2007) investigates several scaling laws checking them against numerical and laboratory experiments.

Aubert et al. (2009) have used the buoyancy power p (defined as the volume integral of the scalar product of the velocity and the buoyancy force) for the power law αp^{β} giving estimations of the rms velocity and magnetic field (where α and β are empirical constants). In the parameter range for the Ekman number $3 \cdot 10^{-5} \ll E \ll 3 \cdot 10^{-4}$, magnetic Prandtl number $1 \ll Pr_m \ll 10$ and Prandtl number $Pr = 1$ a good agreement with the numerical experiments was obtained for the chosen α's and β's.

Christensen and Aubert (2006) suggest scalings based on the convective heat transfer and modified definitions of control parameters. The control parameters are made free of thermal or viscous diffusivities (as e.g. Kraichnan, 1962, proposes that strong turbulence would destroy boundary layers diminishing influence of diffusivity coefficients on the state of the convecting fluid). Stelzer and Jackson (2013) re-investigates the subject using a large database of data from numerical experiments. They conclude that the available data inclines scaling laws towards having diffusion coefficients.

Another example of a scaling law may be the ratio of the Lorentz and Coriolis forces

which is traditionally measured by the *Elsasser number*

$$\Lambda = \frac{B^2}{2\rho\mu_o\eta\Omega},\tag{1.1}$$

where B is the magnetic field strength, ρ is the fluid density, μ_0 is the magnetic constant, η is the magnetic diffusivity and Ω is the core's rotation rate.

Here, the Coriolis and Lorentz forces (per volume) have order of magnitude $2\rho\Omega U$ and JB respectively. We use the current density $J = UB/(\mu_0\eta)$ from Ohm's law, $\mathbf{J} = \sigma(\mathbf{E} + \mathbf{u} \times \mathbf{B})$ taking into account only the induction part $\sigma(\mathbf{u} \times \mathbf{B})$ and ignoring the angle between $\mathbf{u}$ and $\mathbf{B}$ ($\mathbf{u}$ and U denote fluid velocity and its magnitude correspondingly).

Soderlund et al. (2012) argued that the magnetic field is not important for the formation of the flow pattern in dynamo simulations and also suggested to redefine the Elsasser number. They instead obtained an expression for the current density for the eq.(1.1) from Ampere's law $\mathbf{J} = \frac{1}{\mu_0}\boldsymbol{\nabla} \times \mathbf{B}$. Scaling J as $\frac{B}{\mu_0 l_B}$ (the magnetic field varies on the length scale l_B) leads to a "dynamic Elsasser number":

$$\Lambda_d = \frac{B^2}{2\rho\mu_o\Omega U l_B} = \frac{\Lambda}{R_m}\frac{D}{l_B}.\tag{1.2}$$

Soderlund et al. (2012) claim that the new Elsasser number Λ_d better characterizes influence

(a) Magnetic   (b)   (c) Non-magnetic
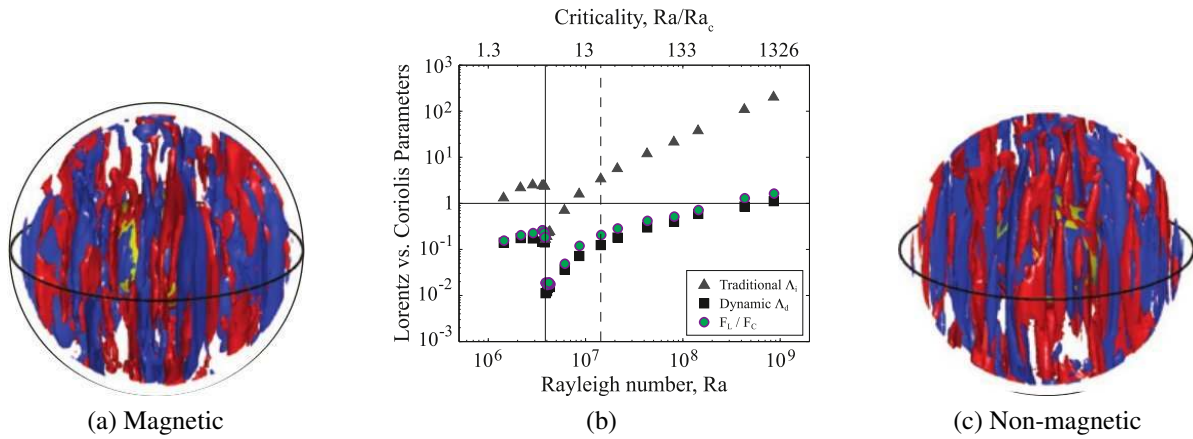
Figure 1.5*: Comparison of the dynamo and non-magnetic simulations. (a,c) Isosurfaces of instantaneous axial vorticity. (b) Comparison of the calculated Lorentz to Coriolis force integral ratios against the traditional and dynamic Elsasser numbers as the function of the Rayleigh number. $Ra = 4.9Ra_c$, $E = 10^{-4}$. From Soderlund et al. (2012).*

of the Lorentz force. Fig.(1.5) shows that the flow patterns in dynamo simulation (with magnetic field) and hydrodynamic simulation (no magnetic field) are quite similar, although the traditional Elsasser number is larger than one. The dynamic Elsasser number matches the volume integrated ratio of the Lorentz and Coriolis forces in the simulations very well. Conclusions about the negligible influence of the Lorenz force in Soderlund et al. (2012) were

made for a relatively high Ekman number $E = 10^{-4}$. Consideration of faster rotating dynamos with lower viscosity (i.e. lower E) may change the conclusion about the importance of the Lorentz force. The difficulty of using this definition of Elsasser number is that l_B is not an observable in the Earth's core quantity and it is not easy to evaluate it.

In chapter 5 we will check some of existing scaling laws against data from our numerical experiments with comparatively low Ekman numbers.

1.8   Low latitude field structures in geodynamo simulations

Geomagnetic observations provide evidence for the existence of strong equatorial magnetic flux spots at the core surface, at the outer edge of the geodynamo (fig.1.6). These concentrations are found to occur as distinctive series north and south of the geomagnetic equator below the Atlantic hemisphere. They are seen in both the equatorially symmetric and equatorially antisymmetric parts of the field, but are characterized by the fact they are not reversed flux patches. Rather they are concentrations of field with the same polarity as the dominant polarity in the hemisphere in which occur. This feature has been difficult for high Ekman number, low *magnetic Reynolds number* ($R_m = \dfrac{Ud}{\eta}$, where U is a typical fluid velocity, d is a length scale and η is magnetic diffusion rate) dynamo simulations to reproduce (see discussion below).

Jackson (2003) suggested that these low latitude intense flux spots could be the result of equatorially trapped waves (e.g. Zhang, 1993) modified by the strong underlying toroidal magnetic field, assuming that magnetic diffusion can be neglected. The equatorial "waveguide" owes its existence to the spherical geometry of the core and special properties of the Coriolis force in this region (Finlay, 2005). In this case, magnetic diffusion is neglected and flux concentrations are produced by convergence of horizontal flow close to the CMB. Although some properties of Zhang's waves help in explaining the geomagnetic observations, it is not clear whether this simple model is directly relevant for the Earth's core where vigorous convection is expected.
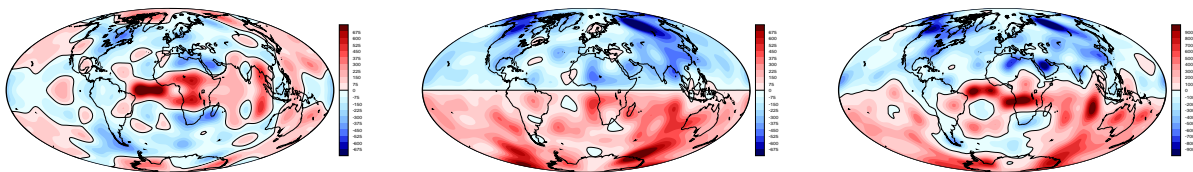
Figure 1.6: *Radial component of the magnetic field on the CMB. Left to right: equatorially symmetric, equatorially antisymmetric , both components. Finlay et al. (2012), see discussion in Jackson (2003).*

Another mechanism that has been invoked as an explanation of the low latitude flux spots is known as "flux expulsion". It was previously investigated by Bloxham (1986) in an attempt (Aubert et al., 2008) to explain inverse flux features in the southern hemisphere under

Africa and southern Atlantic. Bloxham's toy numerical model (see fig.1.7a) consists of two counter-rotating convection cells producing an upwelling. The magnetic field which was initially parallel to the upper surface, is expelled outside from the eddies and eventually diffused through the boundary. In the context of the low latitude spots, the toroidal field is forced to meander by the action of flow upwellings, convected to the outer boundary and diffused through the surface of the core in a violation of the frozen flux approximation. This mechanism produces flux spots of opposite signs that should be added to the background field at the CMB, and appears to be compatible with the maps in fig.(1.6). Christensen et al. (1998) have described how such a mechanism can operate in convection-driven dynamos, to create equatorial flux spots with reversed polarity at low latitudes (often seen in high Ekman number, low magnetic Reynolds number simulations) bundles of toroidal field (fig.1.7b). Downwellings close to the CMB require converging flow patterns which modulate toroidal field bundles and produce magnetic field concentrations seen at the CMB as bipolar flux spots.

(a)   (b)   (c)
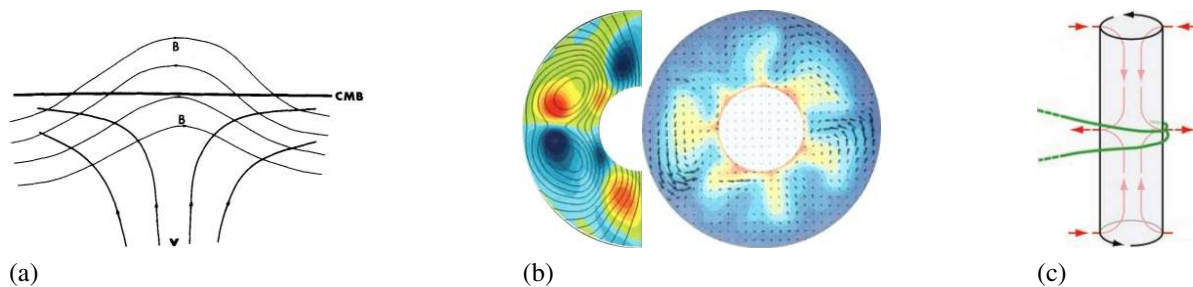
Figure 1.7: *(a) Schematic illustration of expulsion of toroidal field by an upwelling motion, Bloxham (1986). (b) Left: Axisymmetric part of the toroidal field (blue: westward, red: eastward). Solid lines show the axisymmetric poloidal field. Right: Colours indicate the temperature in the equatorial plane, Christensen et al. (1998). (c) Cyclone (black), Secondary circulation (red), Magnetic bundle (green), Aubert et al. (2008).*

Further details of this mechanism were elucidated by Aubert et al. (2008), who have shown in detail how equatorial flux patches (usually with reversed polarity) are created by the cyclones outside of the tangent cylinder (fig.1.7c). Secondary circulation[11] (due to the Ekman pumping, necessary to keep a steady state rotation rate in a vortex) in this vortex concentrates field lines at the equator and push them towards outer boundary.

In another context, Brown et al. (2011) suggest that the magnetic field in the convective region of rapidly rotating suns can be organized into large banded, wreath-like structures positioned near the equator (fig.1.8). Persistent wreaths of magnetic field lines survive despite being embedded in vigorous convective upflows and downflows. The toroidal field in these wreaths is produced by the shear flow (Ω-effect). Convective flows create again the distinctive waviness visible in the structure of wreaths. It seems possible that similar toroidal structures could exist in the Earth's core through the interaction of the toroidal field with convection close to the CMB and that these may be responsible for the wave-like structures that have been

---

[11]The appearance of a secondary flow in a vortex is pictorially described in Einstein (1926) in his solution of the "tea leaves paradox" (why do tea leaves at the bottom of a cup move towards the center of the cup after the water is stirred).

imaged at the CMB. Such distinctive magnetic characteristics of the equatorial region may be a common feature of low Ekman number dynamos driven by rapidly rotating convection in a shell.

Parameters (low Ekman number E and magnetic Prandtl number Pr_m, large driving parameter Ra, where ν is a viscous diffusion rate) in the simulations described in chapter 5 are chosen in a view to increase magnetic Reynolds number R_m and to obtain at low latitudes not only reversed field patches, but also more geomagnetically relevant patches of the same sign as the dominant field in the northern/southern hemisphere. We will analyse the influence of individual terms in equations, energy production components and time-behaviour of the magnetic field with the aim to understand the origin of these field structures.
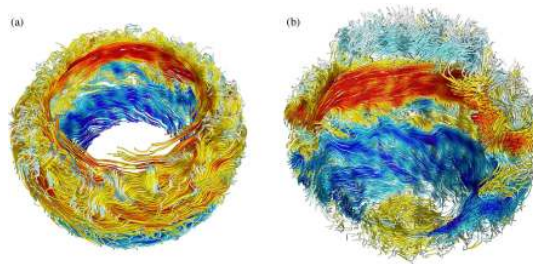
Figure 1.8*: Wreaths of magnetic field which appear in numerical simulations of rapidly rotating stars. Lines trace the magnetic field, colours denote the amplitude and polarity of the azimuthal field, Brown et al. (2011).*

Chapter 2

Numerical implementation

2.1 Summary of governing equations for convection-driven rotating MHD

The equations representing Boussinesq convention in a rotating MHD spherical shell may be written in the form:

$$
\begin{cases}
\left(Ro\, \dfrac{\partial}{\partial t} - E\boldsymbol{\nabla}^2 \right) \mathbf{u} &=& \mathbf{N}_u - \boldsymbol{\nabla}\hat{P}, \\[2ex]
\left(\dfrac{\partial}{\partial t} - \boldsymbol{\nabla}^2 \right) \mathbf{B} &=& \mathbf{N}_B, \\[2ex]
\left(\dfrac{\partial}{\partial t} - q\boldsymbol{\nabla}^2 \right) \Theta &=& N_T,
\end{cases}
\tag{2.1}
$$

where non-linear terms $\mathbf{N}$ appear in the form:

$$
\begin{aligned}
\mathbf{N}_u &= Ro\,\mathbf{u} \times (\boldsymbol{\nabla} \times \mathbf{u}) + (\boldsymbol{\nabla} \times \mathbf{B}) \times \mathbf{B} + q\,Ra\,\Theta\,\mathbf{r} - \hat{\mathbf{z}} \times \mathbf{u}, \\
\mathbf{N}_B &= \boldsymbol{\nabla} \times (\mathbf{u} \times \mathbf{B}), \\
N_T &= \varepsilon - \mathbf{u} \cdot \boldsymbol{\nabla}\Theta,
\end{aligned}
\tag{2.2}
$$

Parameters in equations 2.1 have following definitions:

$$
\begin{aligned}
\text{Magnetic Rossby number} \quad & Ro = \frac{\eta}{2\Omega d^2}, \\[1.5ex]
\text{Ekman number} \quad & E = \frac{\nu}{2\Omega d^2}, \\[1.5ex]
\text{Modified Rayleigh number} \quad & Ra = \frac{g\,\alpha\,\Delta T\,d}{2\Omega\kappa}, \\[1.5ex]
\text{Roberts number} \quad & q = \kappa/\eta.
\end{aligned}
\tag{2.3}
$$

Further details of the approximations made in deriving these equations and the links to other non-dimensionalizations can be found in the Appendix A. In this chapter, the numerical solution of these equations is described.

2.1.1 Boundary conditions

2.1.1.1 On the velocity

The MHD equations will be solved in a rotating spherical shell (in the space between two concentrical spheres). Boundary conditions are applied on the inner and outer spherical surfaces: r_i and r_o. In the Earth's interior these correspond to the boundaries of the inner and outer cores.

Two kinds of boundary conditions on the velocity are possible: *no-slip* and *stress-free*. Viscous coupling between two media resulting in continuity of stress tangential to the interface velocity is called *no-slip*. When tangential stresses do not act in the boundary region it is the *stress-free* case. This condition is in the application to the Earth's core regarded as a computational simplification based on the assumption, that the viscous boundary layer is thin (Kuang and Bloxham, 1999).

For both possible boundary conditions the boundaries are also considered to be impermeable ($u_r = 0$).

No-slip

In this case all the components of the velocity should be zero at the boundary. Making (r, θ, φ)[1] components of vector spherical harmonics (eq. B.26) zero on the boundaries gives:

$$
\begin{aligned}
{[\mathbf{T}_\alpha]}_r + {[\mathbf{P}_\alpha]}_r &= l_\alpha(l_\alpha + 1)\frac{p_\alpha}{r} Y_\alpha && = 0, \\
{[\mathbf{T}_\alpha]}_\theta + {[\mathbf{P}_\alpha]}_\theta &= \frac{\tau_\alpha}{\sin\theta}\frac{\partial Y_\alpha}{\partial\varphi} + \left(\frac{p_\alpha}{r} + \frac{\mathrm{d}p_\alpha}{\mathrm{d}r}\right)\frac{\partial Y_\alpha}{\partial\theta} && = 0, \\
{[\mathbf{T}_\alpha]}_\varphi + {[\mathbf{P}_\alpha]}_\varphi &= -\tau_\alpha(r)\frac{\partial Y_\alpha}{\partial\theta} + \frac{1}{\sin\theta}\left(\frac{p_\alpha}{r} + \frac{\mathrm{d}p_\alpha}{\mathrm{d}r}\right)\frac{\partial Y_\alpha}{\partial\varphi} && = 0
\end{aligned}
\tag{2.4}
$$

(where l_α is a spherical harmonic degree, p_α and τ_α are spherical harmonic coefficients defined in B.23a, B.23b, Y_α is a spherical harmonic defined in B.14, $\mathbf{T}_\alpha$ and $\mathbf{P}_\alpha$ are vector spherical harmonics defined in B.20b, B.20c). Consequently the boundary conditions are satisfied provided,

$$
\tau_\alpha = 0, \quad p_\alpha = 0, \quad \frac{\mathrm{d}p_\alpha}{\mathrm{d}r} = 0.
\tag{2.5}
$$

Stress-free

Tangential to the boundary, components of the stress should be zero. Correspondingly tangential to the boundary components of the rate-of-strain tensor (indices $_{r\theta}$ and $_{r\varphi}$) should be

---

[1]*Spherical coordinates* (r, θ, φ) we define in such a way that $\theta = 0$ at the north pole, φ grows anti-clockwise if looking from the north pole, $\hat{\theta} \times \hat{\varphi} = \hat{\mathbf{r}}$.

zero. Taking these components from Acheson (1990) (p. 355),

$$2e_{\varphi r} = \frac{1}{r\sin\theta}\frac{\partial u_r}{\partial\varphi} + r\frac{\partial}{\partial r}\left(\frac{u_\varphi}{r}\right) = 0,$$
$$2e_{r\theta} = r\frac{\partial}{\partial r}\left(\frac{u_\theta}{r}\right) + \frac{1}{r}\frac{\partial u_r}{\partial\theta} = 0.$$

(2.6)

Due to the condition of non-penetration $u_r = 0$, one only needs to make the following expressions zero:

$$\frac{\partial}{\partial r}\left(\frac{u_\theta}{r}\right) = \frac{\partial}{\partial r}\left(\frac{u_\varphi}{r}\right) = 0$$

(2.7)

And again from the equation (B.26), and using the fact that $u_r = 0$ together with eq.(2.7):

$$
\begin{aligned}
[\mathbf{T}_\alpha]_r + [\mathbf{P}_\alpha]_r &= l_\alpha(l_\alpha + 1)\frac{p_\alpha}{r}Y_\alpha &&= 0, \\
\frac{\partial}{\partial r}\frac{1}{r}[\mathbf{T}_\alpha + \mathbf{P}_\alpha]_\theta &= \frac{\partial}{\partial r}\frac{1}{r}\left(\frac{\tau_\alpha}{\sin\theta}\frac{\partial Y_\alpha}{\partial\varphi} + \left(\frac{p_\alpha}{r} + \frac{\mathrm{d}p_\alpha}{\mathrm{d}r}\right)\frac{\partial Y_\alpha}{\partial\theta}\right) &&= 0, \\
\frac{\partial}{\partial r}\frac{1}{r}[\mathbf{T}_\alpha + \mathbf{P}_\alpha]_\varphi &= \frac{\partial}{\partial r}\frac{1}{r}\left(-\tau_\alpha(r)\frac{\partial Y_\alpha}{\partial\theta} + \frac{1}{\sin\theta}\left(\frac{p_\alpha}{r} + \frac{\mathrm{d}p_\alpha}{\mathrm{d}r}\right)\frac{\partial Y_\alpha}{\partial\varphi}\right) &&= 0.
\end{aligned}
$$

(2.8)

Then, from eq.(2.8)a, $p_\alpha = 0$ and using the following:

$$\frac{\partial}{\partial r}\frac{1}{r}\left(\frac{p_\alpha}{r} + \frac{\mathrm{d}p_\alpha}{\mathrm{d}r}\right) = \frac{\partial^2 p_\alpha}{\partial r^2} - \frac{\cancel{p_\alpha}}{\cancel{r^3}} = \frac{\partial^2 p_\alpha}{\partial r^2} = 0,$$

(2.9)

$$\frac{\partial}{\partial r}\frac{1}{r}(\tau_\alpha) = \frac{1}{r}\left(\frac{\partial}{\partial r} - \frac{1}{r}\right)\tau_\alpha = 0.$$

(2.10)

We eventually find that the necessary conditions are:

$$\left(\frac{\partial}{\partial r} - \frac{1}{r}\right)\tau_\alpha = 0, \quad p_\alpha = 0, \quad \frac{\partial^2 p_\alpha}{\partial r^2} = 0.$$

(2.11)

2.1.1.2   On the magnetic field

Recall the notation (Appendix B) for the poloidal and toroidal scalars which is again used here,

$$\mathbf{B} = \mathbf{\nabla}\times(T\mathbf{r}) + \mathbf{\nabla}\times\mathbf{\nabla}\times(P\mathbf{r}).$$

(2.12)

In an insulating medium, Maxwell's equations require the field to satisfy

$$\mathbf{\nabla}\times\mathbf{B} = 0$$

(2.13)

which allows the representation

$$\mathbf{B} = -\mathbf{\nabla}U;$$

(2.14)

the solenoidal nature of **B** then requires

$$\boldsymbol{\nabla}^2 U = 0,$$
$$U(r, \theta, \varphi) = \sum_\alpha A_\alpha r_\alpha^l Y_\alpha(\theta, \varphi) + B_\alpha r_\alpha^{-(l+1)} Y_\alpha(\theta, \varphi). \tag{2.15}$$

Insulating boundaries

a) External

If the field is entirely internally produced,

$$\mathbf{B} = O\left(\frac{1}{r^3}\right), \quad r \to \infty \tag{2.16}$$

which leads to

$$A_\alpha = 0 \tag{2.17}$$

in the eq.(2.15). We can obtain matching conditions at the boundary by equating the components of **B** given by (2.14) and by (B.26). Continuity of B_r requires

$$B_\alpha = l_\alpha r^{l_\alpha+1} P_\alpha, \quad r = r_o; \tag{2.18}$$

continuity of B_θ and B_φ requires

$$T_\alpha = 0, \quad B_\alpha = -r^{l+1}\frac{\partial}{\partial r}(P_\alpha r), \quad r = r_o. \tag{2.19}$$

Equating the two requirements on B_α, the boundary conditions for each harmonic are obtained as

$$T = 0, \quad \left(\frac{\partial}{\partial r} + \frac{l+1}{r}\right)P = 0 \quad \text{on } r_o. \tag{2.20}$$

b) Internal

The field in the core must respect regularity at the origin,

$$T_\alpha = O(r^{l_\alpha+1}), \quad P_\alpha = O(r^{l_\alpha+1}), \quad r \to 0, \tag{2.21}$$

requiring

$$B_\alpha = 0. \tag{2.22}$$

Continuity of B_r with (B.26) gives

$$A_\alpha = -(l_\alpha + 1)P_\alpha/r^{l_\alpha-1}, \quad r = r_i; \tag{2.23}$$

continuity of B_θ, B_φ with (B.26) gives

$$T_\alpha = 0, \quad A_\alpha = -(P_\alpha r)'/r^l, \quad r = r_i. \tag{2.24}$$

Equating the two requirements on A_α, the boundary conditions for each harmonic are obtained as

$$T = 0, \quad \left(\frac{\partial}{\partial r} - \frac{l}{r}\right)P = 0 \quad \text{on } r_i. \tag{2.25}$$

Conducting boundaries

Following Marti and Willis (2009) at the interface of a conducting inner core we denote the jump across the interface as $[\cdot]$ and write:

$$[T] = 0, \quad [P] = 0, \quad \left[\frac{\partial}{\partial r}P\right] = 0, \quad \boldsymbol{\nabla}_1^2\left[\frac{\partial}{\partial r}T\right] = \frac{1}{r}\hat{\mathbf{r}}\cdot\boldsymbol{\nabla}\times(B_r[\mathbf{u}]) \quad \text{on } r_i.[2] \tag{2.26}$$

Magnetic diffusivities in the inner and outer cores are assumed the same. The last condition simplifies with no-slip boundaries to $[\partial T/\partial r] = 0$.

2.1.1.3 On the Co-density

The following decomposition is employed for the co-density:

$$T = \sum_\alpha T_\alpha(r)Y_\alpha(\theta,\varphi). \tag{2.27}$$

Two possible boundary conditions on the co-density are:

Constant co-density

$$\sum_\alpha T_\alpha = \zeta(\theta,\varphi), \tag{2.28}$$

Constant co-density flux

$$\sum_\alpha \frac{\partial}{\partial r}T_\alpha = q(\theta,\varphi). \tag{2.29}$$

2.1.2 Solution of the governing equations

In this section we give a rough picture of how the solution of the governing equations (2.1) is obtained numerically.

2.1.2.1 Spectral decomposition of the governing equations

The equations of convection-driven rotating MHD eq. (2.1) can be written in scalar form by substitution of the poloidal-toroidal decomposition (see eq. B.20b, B.20c). By this method, the equations are split into two parts for the poloidal and toroidal scalar components respectively. The derivation in the next two sections follows the development by Kuang and Bloxham (1999), Willis et al. (2007) and Marti and Willis (2009).

---

[2]$\boldsymbol{\nabla}_1^2 = -\frac{l(l+1)}{r^2}$ or $\boldsymbol{\nabla}_1^2 f = \frac{1}{r^2\sin\theta}\frac{\partial}{\partial\theta}\left(\sin\theta\frac{\partial f}{\partial\theta}\right) + \frac{1}{r^2\sin^2\theta}\frac{\partial^2 f}{\partial\varphi^2}$, $\hat{\mathbf{r}}$ is a unit vector in radial direction.

2.1.2.1.1 Scalar form of the induction equation

The magnetic field in the induction equation,

$$\left(\frac{\partial}{\partial t} - \nabla^2\right)\mathbf{B} = \mathbf{N}_B,\tag{2.30}$$

(eq.2.1b) can be decomposed by substituting the poloidal-toroidal expansion for the magnetic field

$$\mathbf{B} = \nabla \times T\,\mathbf{r} + \nabla \times \nabla \times P\,\mathbf{r}.\tag{2.31}$$

Taking $\hat{r} \cdot \nabla\times$ of eq.(2.30) leaves only the toroidal component T. Together with the decomposition of the equation by the spherical harmonics (eq.B.18) and using the fact that $\nabla^2 Y_\alpha = -\dfrac{l_\alpha(l_\alpha + 1)}{r^2} Y_\alpha$ from eq.(B.17) and expressions for projections of vector spherical harmonics (eq.B.26) we obtain:

$$\left(\frac{\partial}{\partial t} - \nabla^2\right)T^\alpha = \frac{r}{l(l+1)}f_1^\alpha(r).\tag{2.32}$$

Similarly, taking $\hat{r}\cdot$ of the induction equation (2.30), we obtain an equation for the poloidal scalar P:

$$\left(\frac{\partial}{\partial t} - \nabla^2\right)P^\alpha = \frac{r}{l(l+1)}f_2^\alpha(r),\tag{2.33}$$

where f_1^α, f_2^α, P^α and T^α are defined by:

$$\begin{aligned} T &= \sum_\alpha T^\alpha(r)\,Y_\alpha(\theta,\varphi) & \hat{r}\cdot(\nabla\times\mathbf{N}_B) &= \sum_\alpha f_1^\alpha(r)\,Y_\alpha(\theta,\varphi) \\ P &= \sum_\alpha P^\alpha(r)\,Y_\alpha(\theta,\varphi) & \hat{r}\cdot(\mathbf{N}_B) &= \sum_\alpha f_2^\alpha(r)\,Y_\alpha(\theta,\varphi) \end{aligned}\tag{2.34}$$

The non-linear term $\mathbf{N}_B$ is computed in physical coordinates. Therefore a transform between physical and spectral coordinates is required on each timestep. Such a method is called *pseudo-spectral*.

2.1.2.1.2 Scalar form of the Navier-Stokes equation

Analogous transforms to those in the previous section can also be applied for the Navier-Stokes equation (2.1a),

$$\left(Ro\,\frac{\partial}{\partial t} - E\nabla^2\right)\mathbf{u} = \mathbf{N}_u - \nabla\hat{P},\tag{2.35}$$

the only difference being that we have to take one more curl each time to get rid of pressure term $\nabla\hat{P}$. From the poloidal-toroidal decomposition

$$\mathbf{u} = \nabla \times \tau\,\mathbf{r} + \nabla \times \nabla \times p\,\mathbf{r}\tag{2.36}$$

we obtain the following equations:

$$\left(Ro\,\frac{\partial}{\partial t} - E\boldsymbol{\nabla}^2\right)\tau^\alpha = \frac{r}{l(l+1)}f_3^\alpha \tag{2.37}$$

and for p

$$\begin{cases} \left(Ro\,\dfrac{\partial}{\partial t} - E\boldsymbol{\nabla}^2\right)p^\alpha &=\ g^\alpha, \\[2mm] -\boldsymbol{\nabla}^2 g^\alpha &=\ \dfrac{r}{l(l+1)}f_4^\alpha, \end{cases} \tag{2.38}$$

where

$$\begin{aligned} \tau &= \sum_\alpha T_b^\alpha(r)\,Y_\alpha(\theta,\varphi) \\ p &= \sum_\alpha P_b^\alpha(r)\,Y_\alpha(\theta,\varphi) \end{aligned}\ ;\quad \begin{aligned} \hat{r}\cdot(\boldsymbol{\nabla}\times\mathbf{N}_u) &= \sum_\alpha f_3^\alpha(r)\,Y_\alpha(\theta,\varphi) \\ \hat{r}\cdot(\boldsymbol{\nabla}\times\boldsymbol{\nabla}\times\mathbf{N}_u) &= \sum_\alpha f_4^\alpha(r)\,Y_\alpha(\theta,\varphi) \end{aligned}\ . \tag{2.39}$$

2.1.2.1.3 Expansion of the heat equation

The heat equation is itself a scalar. So it can be directly expanded in a spherical harmonic series as shown in eq.(B.18).

2.1.2.2 Solution at a particular time

In this section we follow Willis et al. (2007) and describe how equations 2.38 are treated using a Green's function (influence matrix, see e.g. Daube, 1992) approach. A linear combination of these elementary solutions is then sought with the purpose of satisfying conditions which are not taken into account in the elementary problems but needed to be met to obtain a solution to the initial problem. In the influence matrix technique the principle of superposition of solutions to elementary problems is used. This technique may be seen as an application of numerical Green's functions.

2.1.2.2.1 Green's functions

A Green's function $G(x, z)$ for the Hermitian operator $\mathcal{L}$ along with specified boundary conditions is defined (see, for example, Riley et al., 2002) as the function which satisfies

$$\mathcal{L}\,G(x,z) = \delta(x - z) \tag{2.40}$$

and the boundary conditions. If we are looking for the solution of the inhomogeneous differential equation

$$\mathcal{L}y(x) = f(x), \tag{2.41}$$

the solution of this equation can be found by:[3]

$$y(x) = \int_c^d G(x, z) f(z) dz.$$

(2.42)

2.1.2.2.2   Solution by means of Green's functions

The system (2.38) is of the form

$$\begin{cases} X\, P = g \\ Q\, g = f \end{cases},$$

(2.43)

where Q and X are differential operators and f is a time-dependent nonlinear term. The solution can therefore be expressed as the linear combinations

$$P = \bar{P} + aP_G + bP'_G,$$

(2.44)

$$g = \bar{g} + ag_G + bg'_G$$

(2.45)

of the solutions to three independent systems:

$$\begin{cases} X\bar{P} = \bar{g} \\ Q\bar{g} = f \end{cases},$$

$$\begin{cases} XP_G = g_G \\ Qg_G = 0 \end{cases}, \quad \begin{cases} XP'_G = g'_G \\ Qg'_G = 0 \end{cases}$$

(2.46)

with the boundary conditions

	g_G	g'_G	$\dfrac{\partial}{\partial r}P_G$	$\dfrac{\partial}{\partial r}P'_G$	$\bar{g}$
on r_i	1	0	0	0	0
on r_o	0	1	0	0	0

(2.47)

where operators X and Q in this case of eq.(2.38) are:

$$\begin{aligned} X &= Ro\,\frac{\partial}{\partial t} - E\nabla^2, \\ Q &= -\nabla^2, \end{aligned}$$

(2.48)

and the nonlinear time-dependent term f is,

$$\sum_\alpha \frac{l(l+1)}{r} Y_\alpha\, f = \hat{r} \cdot (\nabla \times \nabla \times \mathbf{N}_u).$$

(2.49)

---

[3]It can be easily proved. We apply operator $\mathcal{L}$ to the eq.(2.42) and obtain $f(x) = \int_c^d \mathcal{L}G(x,z)f(z)dz = \int_c^d \delta(x-z)f(z)dz \equiv f(x)$.

The two lower equations' systems in (2.46) are independent of time and the Greens functions P_G and P'_G can be precomputed.

The coefficients a, b are determined by the no-penetration condition, $P = \bar{P} + aP_G + bP'_G = 0$ on r_i, r_o, solving the influence matrix

$$
\begin{bmatrix} P_G(r_i) & P'_G(r_i) \\ P_G(r_o) & P'_G(r_o) \end{bmatrix} \begin{bmatrix} a \\ b \end{bmatrix} = - \begin{bmatrix} \bar{P}(r_i) \\ \bar{P}(r_o) \end{bmatrix}. \tag{2.50}
$$

2.1.2.3 Time evolution (predictor-corrector) algorithm

The model equation for each harmonic mode can be written in the form

$$
(a\frac{\partial}{\partial t} - b\boldsymbol{\nabla}^2)f = N, \tag{2.51}
$$

Coefficients a, b depend on the particular equation being solved and the nonlinear terms have been evaluated on each radial point by the spherical transform method, and are solved as described in section (B.4). The predictor at time t_q, with Euler nonlinear terms and implicitness c is defined as

$$
a\frac{f_1^{q+1} - f^q}{\Delta t} - b\left(c\boldsymbol{\nabla}^2 f_1^{q+1} + (1-c)\boldsymbol{\nabla}^2 f^q\right) = N^q, \tag{2.52}
$$

where the coefficient c is called "implicitness". Regrouping terms gives the predictor step

$$
\left(a\frac{1}{\Delta t} - bc\boldsymbol{\nabla}^2\right)f_1^{q+1} = \left(a\frac{1}{\Delta t} + b(1-c)\boldsymbol{\nabla}^2\right)f^q + N^q. \tag{2.53}
$$

Multiple corrector iterations are then implemented as

$$
\left(a\frac{1}{\Delta t} - bc\boldsymbol{\nabla}^2\right)f_{j+1}^{q+1} = \left(a\frac{1}{\Delta t} + b(1-c)\boldsymbol{\nabla}^2\right)f^q + c\,N_j^{q+1} + (1-c)\,N^q, \tag{2.54}
$$

or equivalently, the correction $f_{j+1}^{q+1} = f_j^{q+1} + f_{corr}$

$$
\left(a\frac{1}{\Delta t} - bc\boldsymbol{\nabla}^2\right)f_{corr} = c\,N_j^{q+1} - c\,N_{j-1}^{q+1}, \tag{2.55}
$$

where $j = 1, 2, \ldots$ and $N_0^{q+1} = N^q$. The size of the correction $\|f_{corr}\|$ must reduce at each iteration for time-stepping scheme to be stable. For $c = \frac{1}{2}$ the scheme is second order such that $\|f_{corr}\| \sim \Delta t^2$. For the runs presented in this thesis we have used $c = 0.5$.

For more information on time-stepping schemes in general see for example Boyd (2000), Canuto et al. (2010) or "Numerical recipes" (Press, 2007). This predictor-corrector method was originally implemented by Willis et al. (2007) to calculate the evolution of the modes in the system.

2.1.2.4 Timestep control

The size of the timestep is set by the minimum of global and local criteria, respectively,

$$\Delta t = C \min(Ro, \sqrt{E}) \qquad \Delta t = C \min(d / |\hat{\mathbf{u}}|), \qquad 0 < C < 1, \qquad (2.56)$$

where C is the Courant number[4]. The length d is either Δr or Δh, where $\Delta h = r / \sqrt{l(l+1)}$ and the velocity $\hat{\mathbf{u}}$ is either the radial or angular part of the sum of the fluid velocity $\mathbf{u}$ and the 'reduced' Alfvén velocity $\mathbf{u}_R$ (Walker et al., 1998),

$$\mathbf{u}_R = \mathbf{u}_A^2 / \sqrt{\mathbf{u}_A^2 + \mathbf{u}_I^2}, \quad \mathbf{u}_A = \mathbf{B} / \sqrt{Ro}, \quad |\mathbf{u}_I| = (E + Ro)/(2\, d\, Ro), \qquad (2.57)$$

where $\mathbf{u}_A$ is the usual Alfvén velocity and the alteration by $\mathbf{u}_I$ accounts for damping effects (see Chandrasekhar, 1961, §39*b*).

The timestep should also be small enough such that the corrector norm $\|f_{corr}\|$ is satisfactorily small. This may be particularly important for integrating initial transients. In the runs presented in this thesis the value of the Courant number C = 0.8 was used.

2.1.2.5 Adaptive timestep control

In the previous section 'physical' conditions on the timestep are summarised. Apart from this, the timestep is controlled by the value of the corrector f_{corr} (see sec.2.1.2.3). If the implicitness is $c = \frac{1}{2}$, then the corrector term is proportional to the square of the timestep, i.e. $\|f_{corr}\| \sim \Delta t^2$. Denoting by indexes "$n$" and "$o$" variables at the new and the old timesteps correspondingly,

$$\begin{cases} f_{corr}^n = \xi \cdot (\Delta t_n)^2 \\ f_{corr}^o = \xi \cdot (\Delta t_o)^2 \end{cases} \Rightarrow \Delta t_n = \Delta t_o \cdot \sqrt{\frac{f_{corr}^n}{f_{corr}^o}} \qquad (2.58)$$

where ξ is a constant.

For the implementation in the code the new timestep is renamed as "corr_dt" and the old one as "dt", then

$$\text{corr\_dt} = \text{dt} \cdot \sqrt{\frac{\text{par\_dterr}}{\text{corr\_err}}} \qquad (2.59)$$

---

[4]Courant number is usually defined as $\frac{u\,\Delta t}{d}$.

where "corr_err" is the relative error and is calculated as below:

$$f_{corr} = \begin{pmatrix} \cdot & \cdot & & \cdot & \cdot \\ \cdot & \cdot & & \cdot & \cdot \\ \cdot & f_{corr}^{max} & & \cdot & \cdot \\ \cdot & \cdot & & \cdot & \cdot \end{pmatrix} \tag{2.60}$$

corr_err= $\dfrac{f_{corr}^{max}}{f+1}$, f - is the value of the spectral coefficient for which the corrector step error is maximal.

The variable "par_dterr" is an adjustable parameter specifying the desired relative error at the corrector step. The parameter can be tuned depending on specific calculation. In many of calculations presented in this thesis the value 10^{-3} was used.

For more details on the choice of the time-integration scheme see Marti (2012).

2.2 Parallelisation

The parallelisation is done in radius. The spherical domain is decomposed in spherical shells. In physical space, each CPU receives several spherical shells. In spectral space a certain amount of spherical harmonics are on a single CPU.

Data is split over the spherical harmonics for the linear parts of the code. Curls, gradients and matrix inversions for the timestepping do not couple modes. All radial points for a particular harmonic mode are located on the same processor. Separate harmonics may locate on separate cores. Data is split radially when calculating spherical transforms and when evaluating products in real space. More details on the parallelisation algorithm see in Marti and Willis (2009); Marti (2012).

2.3 Benchmarking

The term benchmark originates from land surveyors who were using marks in stone structures ensuring reference points (a 'bench' for a leveling rod) for future measurements. A numerical benchmark is a reference problem, which solution is a well known. It is important to be sure that different numerical codes give the same (within errors) solutions for the benchmark. The reference problem should be chosen in such a way that it involves execution of all central parts of the code but on the other hand the benchmark shall be as simple as possible to be able to be tackled within limited resources. Another requirement for the benchmark is an easy way to get numerical diagnostics. In this section we present results of two benchmark exercises for our code: non-magnetic and magnetic.

The parameter regime chosen for the non-magnetic results is analysed in Jones et al. (2000). In this paper asymptotic and numerical results are obtained for the onset of convec-

Ta	R_J	ω	Pr	M
10^9	$4.761 \cdot 10^6$	$4.428 \cdot 10^2$	1	9

Table 2.1: *Parameters, predicted rotational rate ω and first excited harmonic M in the non-magnetic benchmark simulation. Non-dimensionalisation is as in Jones et al. (2000).*

E_J	$R_J E_J^{4/3}$	$\omega E_J^{2/3}$	Pr	Pr_m	M	Λ	ω
10^{-5}	5.3491	0.41664	1	1	11	$10^{-5/3}$	897.6

Table 2.2: *Parameters, predicted rotational rate ω and first excited harmonic M in the magnetic benchmark simulation. Non-dimensionalisation is as in Jones et al. (2003).*

tion in a rapidly rotating sphere. Parameters and the predicted rotational rate for the chosen non-magnetic run are defined in tab.(2.1) (non-dimensionalisation as in Jones et al., 2000).

For the magnetic benchmark the magnetoconvection problem from Jones et al. (2003) was selected. The onset of convection is significantly influenced by a strong imposed magnetic field. The parameters and the predicted rotational rate for the chosen non-magnetic run are defined in tab.(2.2) (non-dimensionalisation as in Jones et al., 2003).

Non-dimensional parameters in Jones et al. (2000, 2003) are different only by the choice whether Taylor number $Ta = 4\Omega^2 r_o^4/\nu^2$ or Ekman number $E_J = \nu/(2\Omega r_o^2)$ are used. The conversion rule between these two non-dimensional numbers is $Ta = E_J^{-2}$. The transform between non-dimensionalisations used in this thesis and Jones et al. (2003) is presented in section (C.3). Rather than Jones et al. (2000, 2003) who modeled a full sphere, our code is limited to the spherical shell geometry, but we make the inner core negligibly small by setting $r_i/r_o = 0.01$.

The transformation of parameters of the non-magnetic benchmark (tab.2.1) to Willis et al. (2007) non-dimensionalisation, defined in eq.(2.3), is shown in figure (2.1). Although there is no magnetic field in the simulation, equations (2.1) are non-dimensionalised in such a way that the arbitrary chosen Pr_m has to be defined to make them consistent, e.g. $Pr_m = 1$. In eq.(2.62) we convert parameters of the magnetic benchmark (tab.2.2) into our non-dimensionalisation. In table (2.3) parameters for both benchmarks are presented in the same way as they appear in our code.

Both magnetic and non-magnetic benchmark have the solution in the form $W(s,z)e^{i(M\varphi - \omega t)}$, where ω is a phase speed, M is a harmonic order and s and z are cylindrical coordinates. We will compute the values of the phase speed ω to compare them with the results from Jones et al. (2000, 2003).

$$\begin{cases} E = (Ta)^{-1/2} \cdot \left(\frac{r_o}{d}\right)^2 = 10^{-4.5} \cdot (1/0.99)^2 \approx 32.2648 \cdot 10^{-6} \\ Ra = R \cdot E \cdot \left(\frac{d}{r_o}\right)^4 = 4.761 \cdot 10^6 \cdot 10^{-4.5} \cdot (0.99)^4 \approx 144.624 \\ q = Pr_m/Pr = 1 \\ Ro = E/Pr_m = E \\ \Omega = 442.8 \end{cases} \quad (2.61)$$

$$\begin{cases} E = E_J \cdot \left(\frac{r_0}{d}\right)^2 = (1/0.99)^2 \cdot 10^{-5} = 1.0203 \cdot 10^{-5} \\ Ra = \begin{aligned} & R_J \cdot E_J \left(\frac{d}{r_0}\right)^4 = R_J E_J^{4/3}/E_J^{1/3} \cdot \left(\frac{d}{r_0}\right)^4 = \\ & = 5.3491/10^{-5/3} \cdot (0.99)^4 = 238.4999 \end{aligned} \\ q = Pr_m/Pr = 1 \\ Ro = E/Pr_m = E \\ \Omega = 897.6 \end{cases} \quad (2.62)$$

Figure 2.1: *Conversion of the parameters for the non-magnetic (eq.2.61) and magnetic (eq.2.62) benchmark into our non-dimensionalisation. $_J$ denotes non-dimensionalisation of Jones et al. (2003) or Jones et al. (2000).*

Ro = 32.2648d-6	N = 132	rotation = .false.	
Ra = 146d0	Nic = 1	velocity = .true.	velocity = 'SF_SF'
E = 32.2648d-6	L = 48	codensity = .true.	codensity = 'CNST_CNST'
q = 1d0	M = 48	magnetic = .false.	
rratio = 0.01d0	Mp = 1	mag_impose = .false.	
Ro = 1.0203d-5	N = 132	rotation = .false.	
Ra = 239.0d0	Nic = 1	velocity = .true.	velocity = 'SF_SF'
E = 1.0203d-5	L = 90	codensity = .true.	codensity = 'CNST_CNST'
q = 1.0d0	M = 90	magnetic = .true.	
rratio = 0.01d0	Mp = 1	mag_impose = .true.	

Table 2.3: *Parameters of the non-magnetic (top) and magnetic (bottom) benchmarks as they appear in the code (see Marti and Willis, 2009, for the notation).*

2.3.1 Boundary and initial conditions, imposed magnetic field

Non-magnetic boundary and initial conditions are the same for both magnetic and non-magnetic benchmarks.

Temperature

The stationary temperature profile with an uniform internal heating ε is a solution of $q\boldsymbol{\nabla}^2 T + \varepsilon = 0$. Defining $\varepsilon = 3q$, the general solution is $T = 1/2(-r^2 + K/r + L)$. Choosing $K = 0$, $L = r_o^2$ we obtain the temperature boundary conditions:

$$T \text{ at outer boundary}: \quad 0.0,$$

$$T \text{ at inner boundary}: \quad \tfrac{1}{2}(r_o^2 - r_i^2).$$

The initial temperature profile is $T = 1/2(r_o^2 - r^2)$.

Velocity

Stress-free condition is on both boundaries. As for the initial condition, poloidal harmonics were randomly excited with the amplitude of the resulting velocity field 10^{-7}.

Magnetic

In the magnetic case boundaries are electrically insulating. The initial magnetic field is composed of randomly excited components in the same manner as for the velocity field.

Imposed magnetic field

The background field is $\mathbf{B}_0$: $\quad \hat{\varphi} \cdot \mathbf{B}_0 = \Lambda^{1/2} r \sin(\theta) = 0.14678 r \sin(\theta)$. The meridional section of the imposed magnetic field is shown in fig.(2.2).
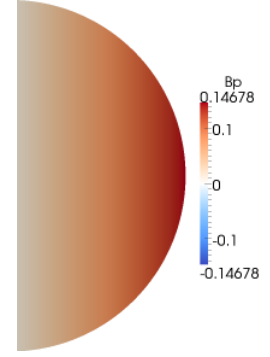
Figure 2.2: *The meridional cut of φ-component (other are zero) of the imposed magnetic field of the magnetic benchmark run with parameters defined in eq.(2.62).*

2.3.2   Results

First, we define the collected diagnostics. The kinetic energy is $E_{kin} = 1/2 \int \mathbf{u}^2 dV$, the non-dimensional kinetic energy dissipation is calculated as $D_{kin} = E/Ro \int (\nabla \times \mathbf{u})^2 dV$ [5]. In the similar way magnetic energy $E_{mag} = 1/(2Ro) \int \mathbf{B}^2 dV$ and its dissipation $D_{mag} = 1/Ro \int (\nabla \times \mathbf{B})^2 dV$ are defined. These definitions are also collected in table (5.4) in chapter (5).

The time evolution of these diagnostics is presented in fig.(2.3) and (2.6). Beyond that time dependencies of individual harmonics are presented in fig.(2.4) and (2.5). We are not interested in the amplitude of the saturated state, since only the onset of convection is considered.

Snapshots from the simulations are shown in fig.(2.7) for the non-magnetic run and in fig.(2.8) for the magnetic run.

The phase speed computed in the non-magnetic experiment is $\omega = 435.2 \pm 0.1$ and in the magnetic experiment it is $\omega = 880.0 \pm 1.7$. The difference between the theoretical and numerical values in both cases is less than 2% (compare with values in tab.2.1). This relatively large error is likely due to the presence of the small inner core in our numerical model and

---

[5]The dissipation is calculated as the power $-\dfrac{E}{Ro} \int u \nabla^2 u dV$ of the viscous force. Using vector identities $u\nabla^2 u = -u \cdot (\nabla \times \nabla \times u) = -u \cdot (\nabla \times \xi) = -(\nabla \cdot (\xi \times u) + \xi \cdot (\nabla \times u))$. As a result $-\int u\nabla^2 u dV = \int (\nabla \times u) \times u dS + \int (\nabla \times u)^2 dV$. With no-slip boundaries the first surface integral is zero. With stress-free boundary conditions this is not generally true. Nevertheless the definition $\int (\nabla \times u)^2 dV$ for the dissipation is used in this chapter even in the stress-free case.
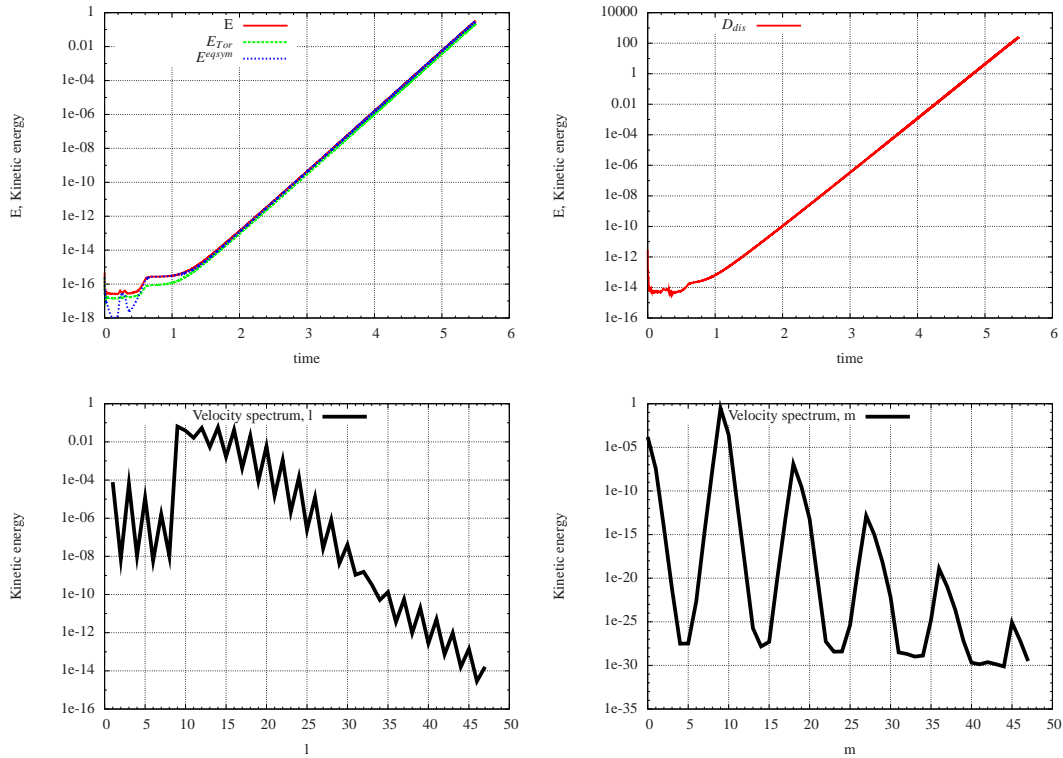
Figure 2.3: *Top row: Kinetic energy E (left) and its dissipation D_{dis} vs. time (right). Bottom row: Kinetic energy spectrum in the end of the simulation vs. harmonic degree l (left) and vs. harmonic order m (right).*

high sensitivity of the phase speed on the geometry of the system. A few other benchmarks with more proper for our code geometries (e.g. from Christensen et al., 2001, see chapter 3) were conducted with almost exact correspondence with reference values.

In the following chapter we present another benchmark exercise with magnetic boundary conditions which are convenient for use in non-spectral codes.
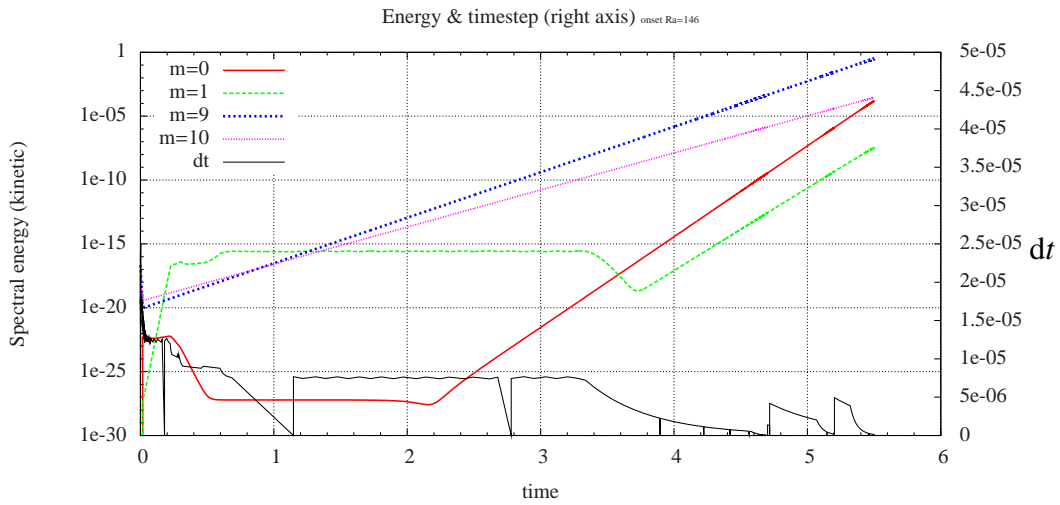
Figure 2.4: *Time behaviour of the energy spectral components in the non-magnetic benchmark simulation with parameters defined in eq.(2.61). "dt" is the timestep, the right axis is labeled with values in units of time.*
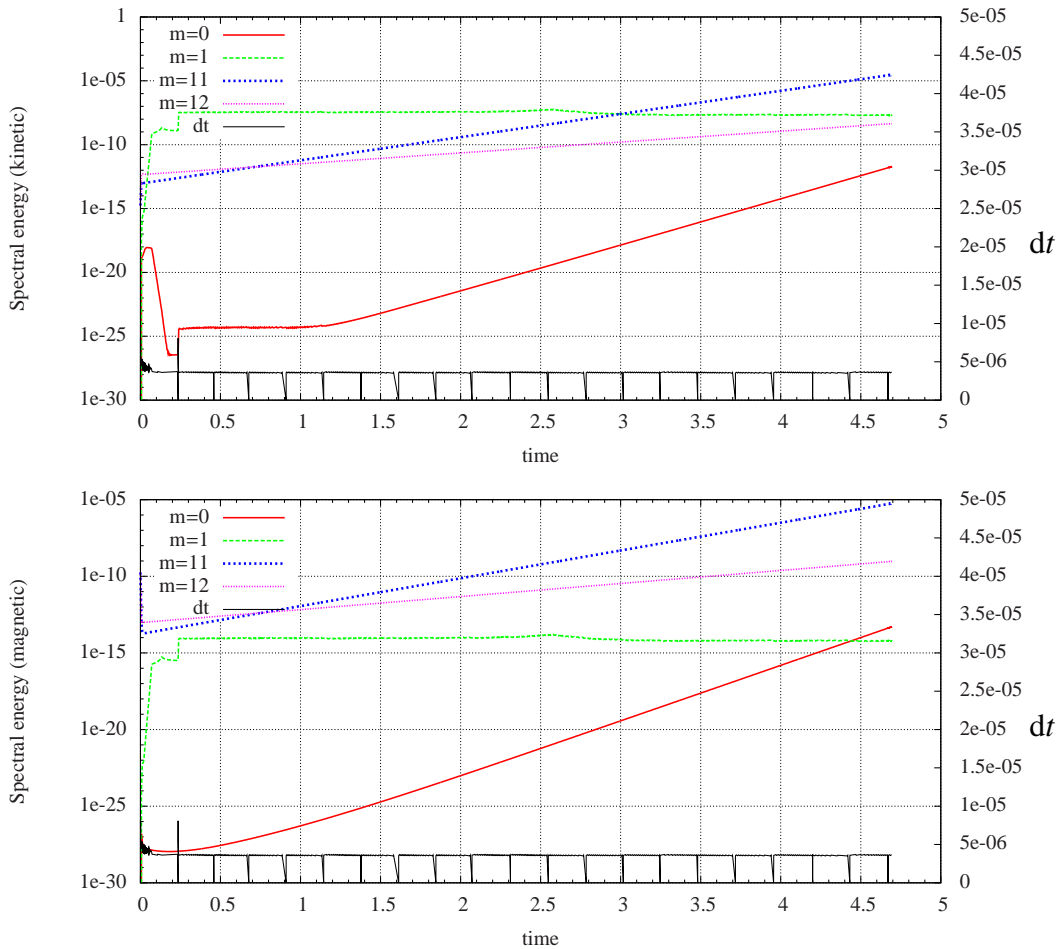
Figure 2.5: *Time behaviour of the energy spectral components in the magnetic benchmark simulation defined in eq.(2.62). "dt" is the timestep, the right axis is labeled with values in units of time.*
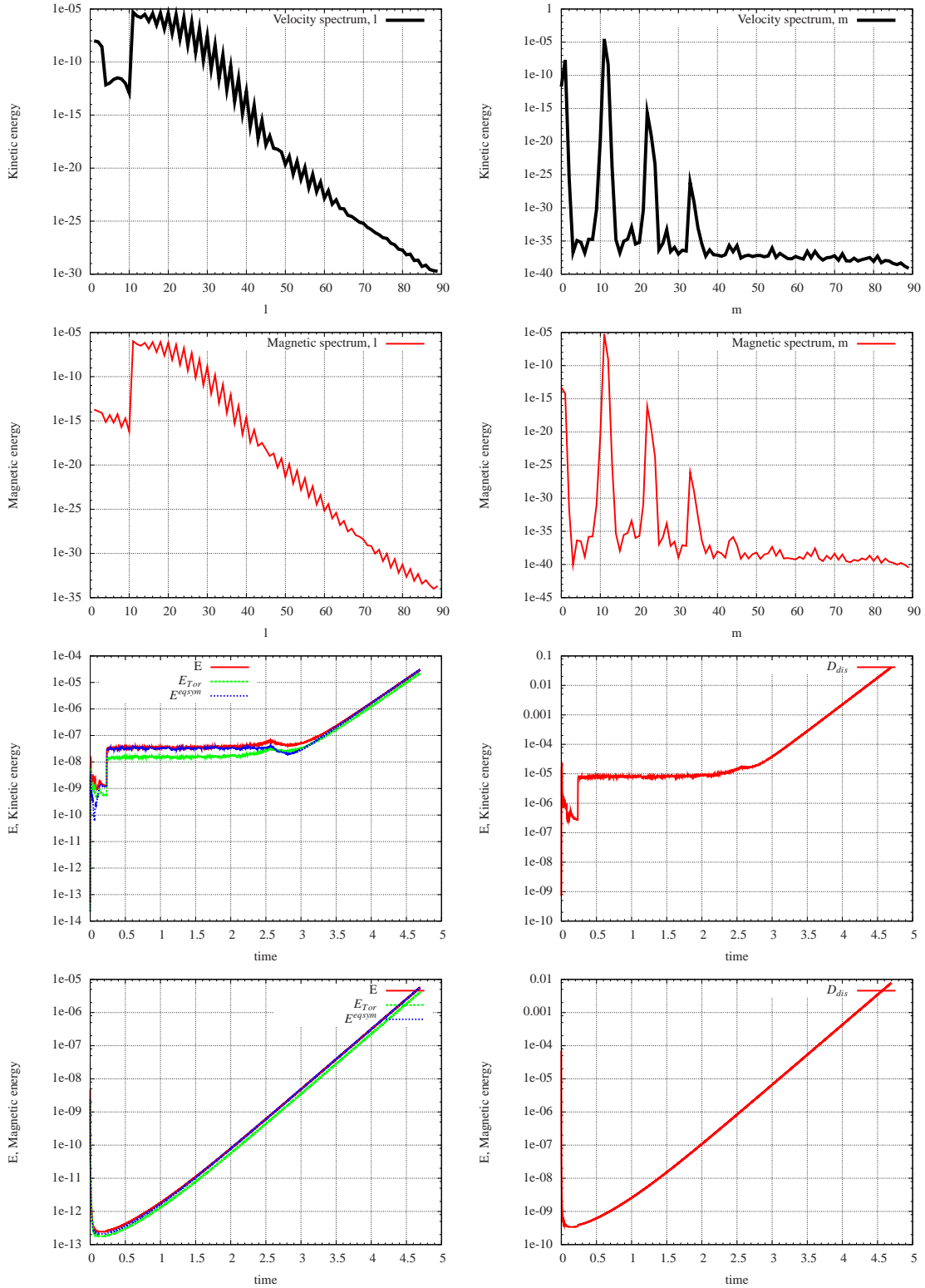
Figure 2.6*: Diagnostics for the magnetic benchmark simulation defined in in eq.(2.62). The top two rows are kinetic and magnetic energy spectra vs. harmonic degree l (left) and vs. harmonic order m in the end of the run. The bottom two rows are the kinetic and magnetic energies vs. time.*

(a) Equatorial cut   (b) Meridional cut
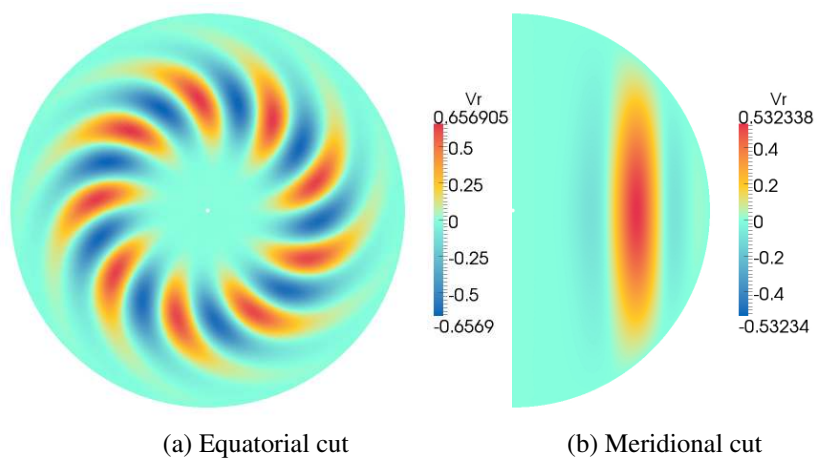
Figure 2.7: *Radial velocity field at time t = 5.49883 in the non-magnetic benchmark simulation with parameters defined in eq.(2.61).*

(a) Equatorial cut   (b) Meridional cut

(c) Equatorial cut   (d) Meridional cut
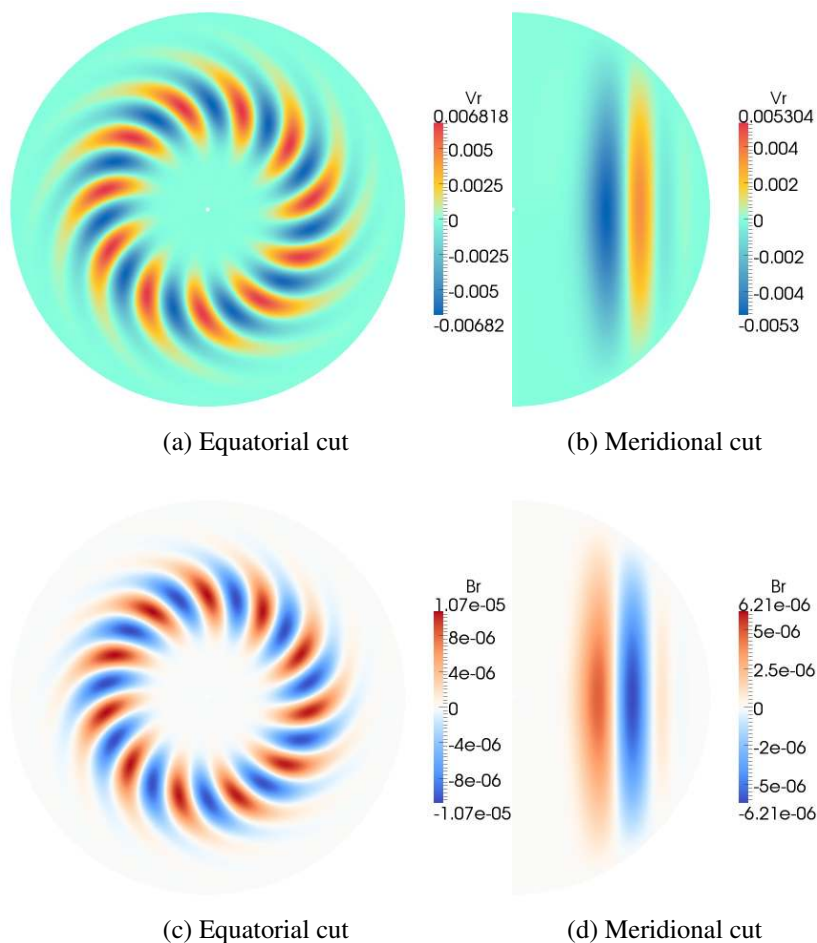
Figure 2.8: *Radial velocity (first row) and magnetic (second row) fields at time 4.69518 in the magnetic benchmark simulation with parameters defined in eq.(2.62).*

Chapter 3

Formulation of the benchmark problem for MHD-systems with pseudo-vacuum magnetic boundaries

Introduction

Candidates for a benchmark study for the convection-driven magnetohydrodynamic dynamo problem in a rotating spherical shell with the "pseudo-vacuum" magnetic boundary condition are presented in this report. One of these candidates has been used for a community comparison, the results of which are reported in Jackson et al. (2014). The form of the magnetic boundary condition is:

$$B_\theta = B_\varphi = 0\big|_{r_i, r_o},$$
(3.1)

r_i and r_o denote inner and outer radii of the spherical shell. This represents equating the component of the magnetic field tangential to the spherical boundary to zero. A physically relevant example can be constructed with the material with infinite magnetic permeability. Imagine two media with magnetic permeabilities $\mu_{solid} = \infty$ and μ_{liquid} in contact. Continuity of the magnetic field requires that $H_\parallel$ ($=B_\parallel/\mu$) and $B_\perp$ are continuous. If $\mu_{solid} = \infty$ this gives $B_\parallel^{liquid}/\mu_{liquid} = B_\parallel^{solid}/\infty = 0$, i.e. $B_\parallel^{liquid} = 0$. Here signs $\parallel$ and $\perp$ denote vector components parallel to the surface and normal to it correspondingly. When the pseudo-vacuum condition is satisfied, then the radial component of the current on boundaries is zero ($(\nabla \times \mathbf{B})_r|_{r_i, r_o} = 0$). The locality of this condition is an advantage in finite difference numerical schemes.

The condition on B_r can be extracted from the differential form of the Gauss's law for magnetism:

$$\nabla \cdot \mathbf{B} = 0.$$
(3.2)

If tangential components of the field are zero (eq.3.1), this law in spherical coordinates con-

tains only radial component of the field:

$$\frac{\partial}{\partial r}(r^2 B_r) = 0|_{r_i, r_o},\tag{3.3}$$

or simply:

$$\left(2 + r\frac{\partial}{\partial r}\right)B_r = 0|_{r_i, r_o}.\tag{3.4}$$

3.1   MHD equations

The chosen form of the non-dimensionalised magnetohydrodynamic equations is:

$$\begin{cases} \left(Ro\,\frac{\partial}{\partial t} - E\boldsymbol{\nabla}^2\right)\mathbf{u} &= Ro\,\mathbf{u}\times(\boldsymbol{\nabla}\times\mathbf{u}) + (\boldsymbol{\nabla}\times\mathbf{B})\times\mathbf{B} + q\,Ra\,T\,\mathbf{r} - \hat{\mathbf{z}}\times\mathbf{u} - \boldsymbol{\nabla}\hat{P}, \\[2mm] \left(\frac{\partial}{\partial t} - \boldsymbol{\nabla}^2\right)\mathbf{B} &= \boldsymbol{\nabla}\times(\mathbf{u}\times\mathbf{B}), \\[2mm] \left(\frac{\partial}{\partial t} - q\boldsymbol{\nabla}^2\right)T &= -\mathbf{u}\cdot\boldsymbol{\nabla}T, \end{cases}\tag{3.5}$$

$$\boldsymbol{\nabla}\cdot\mathbf{B} = 0,\ \boldsymbol{\nabla}\cdot\mathbf{u} = 0.\tag{3.6}$$

Here we have used the non-dimensionalisation

$$\begin{array}{ll} \text{Length } r \rightarrow (d = r_o - r_i)\,r, & \text{Time } t \rightarrow d^2/\eta\,t, \\[2mm] \text{Magnetic } B \rightarrow (2\Omega\rho_0\mu_0\eta)^{\frac{1}{2}}\,B, & \text{Temperature } T \rightarrow \Delta T\,T \end{array}\tag{3.7}$$

with dimensionless parameters:

$$\begin{array}{lll} \text{Magnetic Rossby number} & Ro = \eta/(2\Omega d^2), \\[2mm] \text{Ekman number} & E = \nu/(2\Omega d^2), \\[2mm] \text{Modified Rayleigh number} & Ra = \dfrac{g\,\alpha\,\Delta T\,d}{2\Omega\kappa}, \\[3mm] \text{Roberts number} & q = \kappa/\eta. \end{array}\tag{3.8}$$

The ratio $r_i/r_o = 0.35$ is used for simulations in this chapter. Together with the definition of the unit of length d it gives $r_i = 7/13$, $r_o = 20/13$.

3.1.1   Magnetic boundary condition in spectral form

Magnetic vector **B** can be written in terms of the toroidal and poloidal scalar fields, T and P:

$$\mathbf{B} = \boldsymbol{\nabla}\times(T\mathbf{r}) + \boldsymbol{\nabla}\times\boldsymbol{\nabla}\times(P\mathbf{r}).\tag{3.9}$$

Projections of the magnetic field on the axes of the spherical coordinate system can be obtained directly from the scalar fields P and T:

$$\begin{cases} B_r = -r\boldsymbol{\nabla}_1^2 P, \\ B_\theta = \dfrac{1}{\sin\theta}\dfrac{\partial T}{\partial\varphi} + \dfrac{1}{r}\dfrac{\partial}{\partial r}\left(r\dfrac{\partial P}{\partial\theta}\right), \\ B_\varphi = -\dfrac{\partial T}{\partial\theta} + \dfrac{1}{r\sin\theta}\dfrac{\partial}{\partial r}\left(r\dfrac{\partial P}{\partial\varphi}\right), \end{cases} \tag{3.10}$$

where

$$\boldsymbol{\nabla}_1^2 f = \frac{1}{r^2\sin\theta}\frac{\partial}{\partial\theta}\left(\sin\theta\frac{\partial f}{\partial\theta}\right) + \frac{1}{r^2\sin^2\theta}\frac{\partial^2 f}{\partial\varphi^2} = -\frac{l(l+1)}{r^2}. \tag{3.11}$$

Here we used the fact that the toroidal and poloidal scalars can be decomposed in spherical harmonics of the form:

$$\hat{Y}_l^m(\theta,\varphi) = P_l^m(\cos\theta)e^{im\varphi}. \tag{3.12}$$

The boundary condition (3.1) with the use of equations (3.10) can be satisfied by keeping the toroidal scalar $T = 0$ on the boundaries and:

$$\frac{\partial(Pr)}{\partial r} = 0\bigg|_{r=r_i,r_o}. \tag{3.13}$$

The same equation, but expanded, is:

$$\left(\frac{\partial}{\partial r} + \frac{1}{r}\right)P = 0\bigg|_{r=r_i,r_o}. \tag{3.14}$$

3.1.2   Numerical method

A spherical harmonic expansion on spherical surfaces (L degrees and M orders), finite differences in the radial direction (N-points on Chebyshev grid), and an adaptive predictor-corrector semi-implicit time-stepping algorithm are used.

3.2   Decay modes

For the equation

$$\left(\frac{\partial}{\partial t} - \boldsymbol{\nabla}^2\right)\mathbf{B} = 0 \tag{3.15}$$

to be true, the coefficients of the spectral decomposition of the poloidal scalar should comply with the equation:

$$\frac{\partial P}{\partial t} = \frac{1}{r^2}\frac{\partial}{\partial r}r^2\frac{\partial P}{\partial r} - \frac{l(l+1)}{r^2}P. \tag{3.16}$$

Substitution of

$$P(r,t) = f(r)e^{-pt} \tag{3.17}$$

gives an equation, whose particular solutions are spherical Bessel functions of the first and second kind ($\sqrt{2\pi/z}J_{l+\frac{1}{2}}(z)$ and $\sqrt{2\pi/z}Y_{l+\frac{1}{2}}(z)$, [1] where z= $\sqrt{p}r$, see Abramowitz and Stegun, 1970). We search for the solution in the form:

$$f(r) \sim \left(\alpha\, J_{l+\frac{1}{2}}(kr) + Y_{l+\frac{1}{2}}(kr)\right)/\sqrt{r}, \tag{3.20}$$

where $k = \sqrt{p}$. Equation (3.20) should satisfy magnetic boundary condition (3.14):

$$\left(\frac{\partial}{\partial r} + \frac{1}{r}\right)f = 0\bigg|_{r=r_i,r_o}. \tag{3.21}$$

Our code with the boundary condition (3.1) is tested against decay modes in the next two subsections.

3.2.1   Decay modes in a sphere

Bessel functions of the second kind are singular in the origin, and are not suitable for the full sphere. We are looking for the slowest decaying mode among *J*'s:

$$f(r) \sim J_{l+\frac{1}{2}}(kr)/\sqrt{r}, \tag{3.22}$$

In this case only one boundary exists (r_o), where we apply the condition (3.14):

$$\left(\sqrt{r}J_{l+\frac{1}{2}}(kr)\right)'\bigg|_{r_o} = 0, \tag{3.23}$$

or:

$$J_{l+\frac{1}{2}}(kr_o) + 2r_okJ'_{l+\frac{1}{2}}(kr_o) = 0. \tag{3.24}$$

---

[1]Bessel functions of the order 3/2, which will be used in the next subsections, can be presented by the elementary functions:

$$J_{\frac{3}{2}}(x) = \sqrt{\frac{2\,x}{\pi}}\left(\frac{\sin x}{x^2} - \frac{\cos x}{x}\right), \tag{3.18}$$

$$Y_{\frac{3}{2}}(x) = \sqrt{\frac{2\,x}{\pi}}\left(-\frac{\cos x}{x^2} - \frac{\sin x}{x}\right). \tag{3.19}$$

The recurrence relation

$$x\, J'_\nu(x) + \nu\, J_\nu(x) = x J_{\nu-1}(x) \tag{3.25}$$

and substitution of $x = kr_o$ give:

$$x\, J_{l-\frac{1}{2}}(x) - l\, J_{l+\frac{1}{2}}(x) = 0. \tag{3.26}$$

The smallest zero is $x_0 = 2.743707$, $l = 1$. It corresponds to the decay rate $p = k^2 = (x_0/r_o)^2 = 7.527930/r_o^2$. Numerically we have there decay rate $p = 7.527926/r_o^2$.

Figure (3.1) presents the decay rate of the magnetic field calculated in our numerical code (the size of the inner core is set to a small value, initial condition can be chosen arbitrary because only the slowest decay mode survives at the end of the simulation) versus theoretical value.
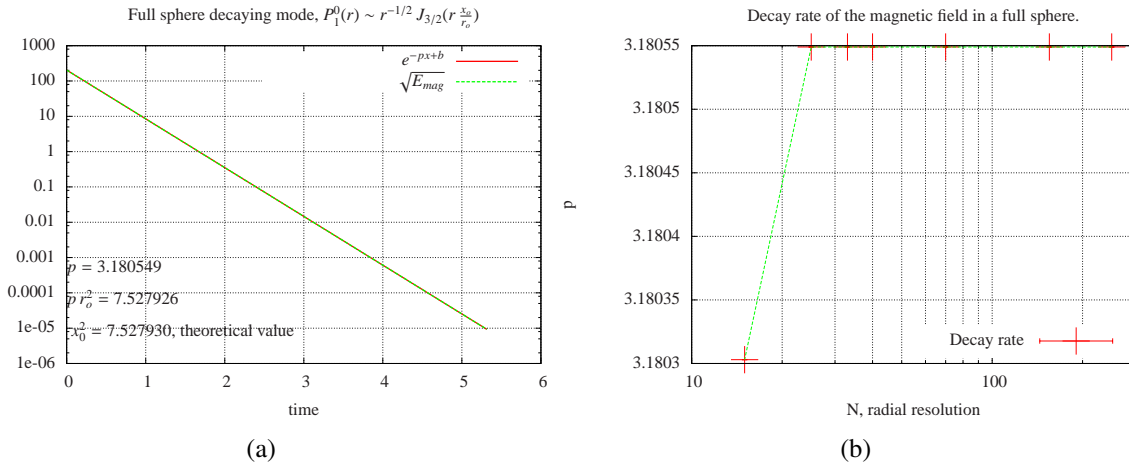
Figure 3.1: *(a)Plotted on a log-linear scale, the decay is linear in time. (b) Convergence of the decay rate with radial resolution.*

3.2.2   Decay modes in a spherical shell

Radially dependent part of a poloidal scalar of a particular solution of the eq.(3.15) in a spherical shell has to be a linear combination of J's and Y's to satisfy the boundary conditions on two sides: r_i and r_o. For the radial function:

$$f(r) = \left(\alpha\, J_{l+\frac{1}{2}}(kr) + Y_{l+\frac{1}{2}}(kr) \right) / \sqrt{r}, \tag{3.27}$$

the boundary conditions are:

$$\alpha \left(kr\, J_{l-\frac{1}{2}}(k\,r) - l\, J_{l+\frac{1}{2}}(k\,r) \right) + kr\, Y_{l-\frac{1}{2}}(k\,r) - l\, Y_{l+\frac{1}{2}}(k\,r) = 0 \Big|_{r=r_i,r_o}. \tag{3.28}$$

Denoting $a(x) = x J_{l-\frac{1}{2}}(x) - l J_{l+\frac{1}{2}}(x)$ and $b(x) = x Y_{l-\frac{1}{2}}(x) - l Y_{l+\frac{1}{2}}(x)$, we get:

$$\begin{cases} \alpha\, a(k\, r_i) + b(k\, r_i) = 0, \\ \alpha\, a(k\, r_o) + b(k\, r_o) = 0. \end{cases} \tag{3.29}$$

Hence, equation for k is:

$$a(kr_i)\, b(kr_o) = a(kr_o)\, b(kr_i). \tag{3.30}$$

And the smallest $k = 1.492617$, when $l = 1$, $\alpha = -2.721321$. $ri = 7/13$, $ro = 20/13$. This value of k corresponds to the decay rate $p = k^2 = 2.227904$. Numerically we find a decay rate of $p = 2.227903$.

Figure (3.2) presents the decay rate of the magnetic field calculated in our numerical code
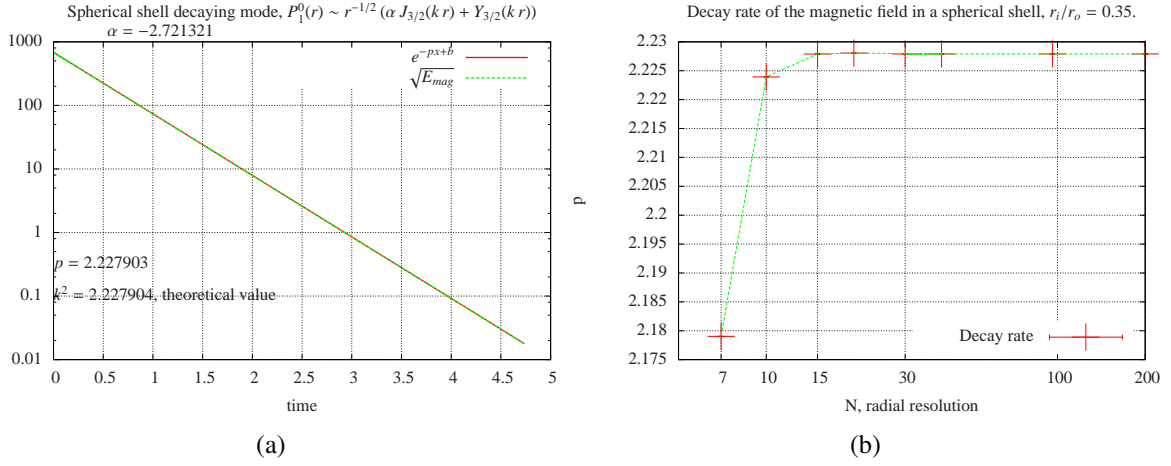
Figure 3.2: *(a) Plotted on a log-linear scale, the decay is linear in time. (b) Convergence of the decay rate with radial resolution.*

and its dependence on the resolution.

3.3 Stable dynamos

In this section we describe stable dynamos (where the magnetic energy is constant in time) which can be suitable for a benchmark study. The parameters are suggested by Harder and Hansen (2005). Two parameter regimes are presented, which differ by the value of the Roberts number: $q = 5$ and $q = 8$. The ratio of the viscous and thermal diffusivities (called Prandtl number, $\nu/\kappa = E/(q\, Ro)$) is the same and equal to one in both cases, causing the Rossby numbers to be different.

The Roberts number describes the ratio of the thermal and magnetic diffusivities, that is to say the fluid of the case $q = 8$ conducts heat faster than in the other case (in magnetic time units

d^2/η).

Stable dynamos are obtained in both parameter regimes. The solutions have fourfold symmetry in longitude and are symmetric about equator. In some calculations fourfold symmetry was used to restrict the spherical harmonic expansion and accordingly the computer time (runs with resolution 96/60/53 and 50/32/29, see tables 3.2 and 3.1).

In order to compare results obtained at different resolutions and control convergence, resolution is defined following Christensen et al. (2001) as the third root of the number of degrees of freedom for each scalar variable:

$$R = N^{1/3} \left(L\,(2M+1) - M^2 + M + 1 \right)^{1/3}. \tag{3.31}$$

3.3.1   Initial magnetic field

We have created an initial condition that satisfies the boundary condition. The spectral form
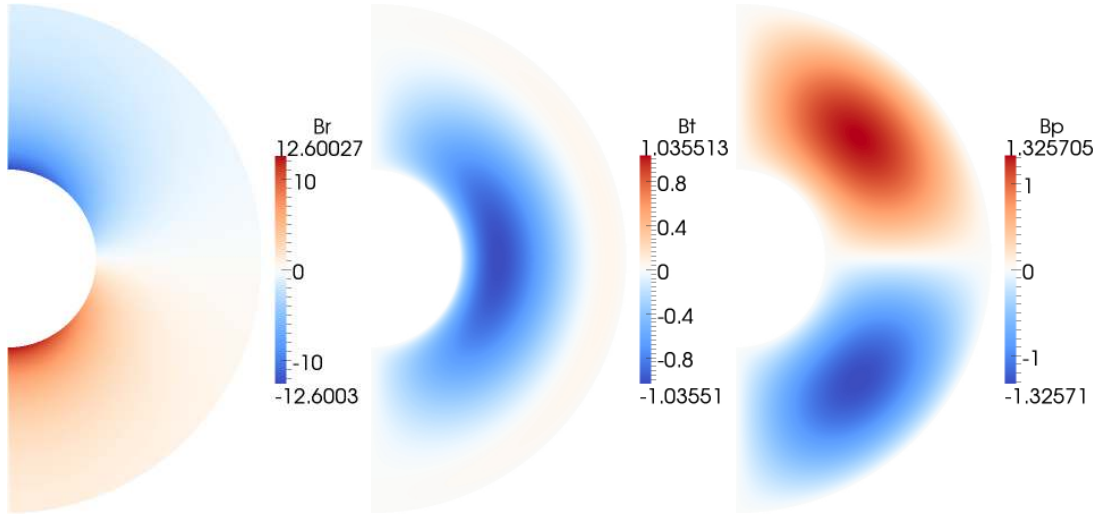
Figure 3.3: Initial magnetic field for the pseudo-vacuum benchmark, meridional slices.

of the initial magnetic field is:

$$
\begin{cases}
\qquad\qquad T_2^0 = \dfrac{1}{\sqrt{2}}\dfrac{5}{4}\,\sin\pi\,(r - r_i), \\[2ex]
P_1^0 = \dfrac{1}{\sqrt{2}}\dfrac{5}{16}\left(-48\,r_i\,r_o + (4\,r_o + r_i\,(4 + 3\,r_o))\,6r - 4(4 + 3\,(r_i + r_o))\,r^2 + 9\,r^3\right).
\end{cases}
\tag{3.32}
$$

The same field in physical coordinates is:

$$
\begin{aligned}
B_r &= \frac{1}{\sqrt{2}}\frac{5}{8}\frac{-48\,r_i\,r_o + (4\,r_o + r_i\,(4 + 3\,r_o))\,6r - 4(4 + 3\,(r_i + r_o))\,r^2 + 9\,r^3}{r}\cos\theta, \\
B_\theta &= -\frac{1}{\sqrt{2}}\frac{15}{4}\frac{(r - r_i)\,(r - r_o)\,(3\,r - 4)}{r}\sin\theta, \\
B_\varphi &= \frac{1}{\sqrt{2}}\frac{15}{8}\sin\pi(r - r_i)\sin 2\theta.
\end{aligned}
\tag{3.33}
$$

It is easy to see that $B_\theta = B_\varphi = 0$ at r_i and r_o, and the condition $\frac{\partial}{\partial r}(r^2 B_r) = 0|_{r_i,r_o}$ is satisfied as well (see eq.3.3). This initial magnetic field is shown in fig.(3.3).

3.3.2   Initial temperature field and boundary conditions

The initial temperature is the same as in Christensen et al. (2001)

$$
T = \frac{r_o r_i}{r} - r_i + \frac{21}{\sqrt{17920\pi}}(1 - 3x^2 + 3x^4 - x^6)\sin^4\theta\cos 4\varphi,
\tag{3.34}
$$

where $x = 2r - r_i - r_o$. This describes a conductive state with a perturbation of harmonic degree and order four super-imposed. The temperature is fixed on the boundaries: $T(r_i) = 1$, $T(r_o) = 0$. The defined here initial temperature field is shown in fig.(3.4).
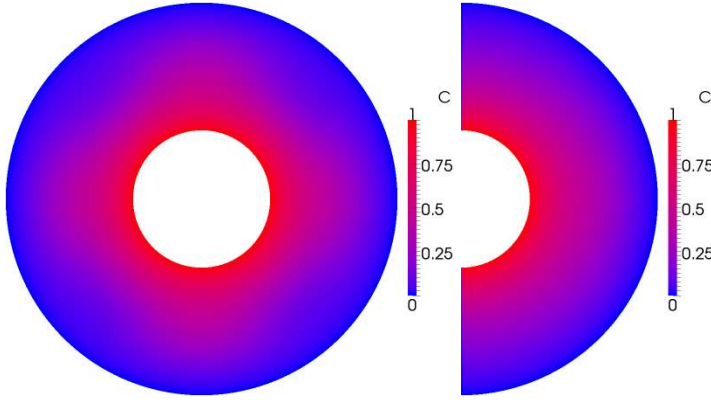
Figure 3.4: *Initial temperature for the pseudo-vacuum benchmark, equatorial and meridional slices.*

3.3.3   Initial velocity field and boundary conditions

Initial velocity is zero. No-slip and non-penetrating boundary conditions are imposed.

3.3.4   Diagnostic quantities

From participants in the benchmark study Jackson et al. (2014) we requested the data described below.

Global data

The solution is steady in a drifting frame and is given in the form $(\mathbf{u}, \mathbf{B}, T) = f(r, \theta, \varphi - \omega t)$. Angular speed ω, magnetic and kinetic energies, which are defined as:

$$E_{mag} = \frac{1}{2 \, Ro} \int B^2 \, dV,$$
(3.35)

$$E_{kin} = \frac{1}{2} \int u^2 \, dV$$
(3.36)

are requested.

Local data

A point where local data are to be taken is fixed in the drifting reference frame. We take a point at a mid depth ($r = (r_i + r_o)/2$) in the equatorial plane ($\theta = \pi/2$) whose φ-coordinate is given by the conditions $u_r = 0$ and $\dfrac{\partial u_r}{\partial \varphi} > 0$. For this point u_φ, B_θ and T are requested.

3.3.5   Case q=5

Parameters are the same as in the Christensen et al. (2001) benchmark Case 1 (see table C.5 for the conversion), in our non-dimensionalisation:

E	Ra	q	Ro
$0.5 \cdot 10^{-3}$	32.50	5	10^{-4}

Results of the integration are in figure (3.5). Requested data of the simulation are in the table (3.1). They are plotted in the figure (3.6). The run was integrated for nine magnetic dif-

N	L	M	V_φ	B_θ	T	E_{mag}	E_{kin}	ω	dt
50	32	29	-58.0792	0.9860	0.4261	79849.4	14892.8	3.7656	1.6272e-05
80	42	42	-58.1670	0.9931	0.4259	80076.3	14847.3	3.7510	1.5903e-05
96	48	48	-58.1705	0.9935	0.4259	80076.2	14846.9	3.7489	1.6108e-05
96	60	53	-58.1796	0.9929	0.4260	80074.7	14847.2	3.7490	1.5779e-05
128	64	64	-58.1786	0.9930	0.4259	80072.7	14846.9	3.7489	1.5795e-05
200	100	100	-58.1786	0.9930	0.4259	80072.7	14846.5	3.7488	1.5741e-05

Table 3.1: *Case q = 5 with pseudo-vacuum boundaries, output data.*

fusion times before data were gathered. Field structure of the case $q = 5$ is shown in fig.(3.7) and fig.(3.8). The snapshot is taken in the region where the dynamo is steady.
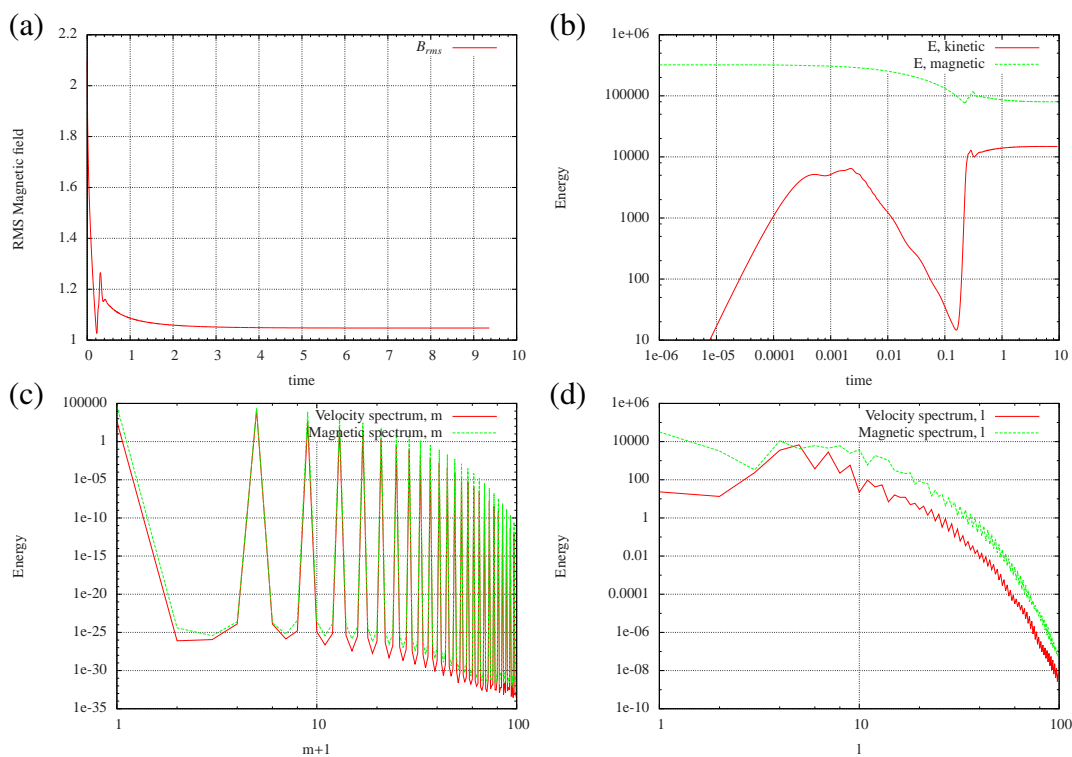
Figure 3.5: *Behaviour of the case $q = 5$. (a) B_{rms} vs. time (b) E_{mag} and E_{kin} vs. time on the log-log scale (c,d) Kinetic and magnetic energy spectral components vs. spherical harmonic degree l and harmonic order m.*

(a) u_φ

(b) B_θ

(c) E_{kin}

(d) E_{mag}

(e) T

(f) ω
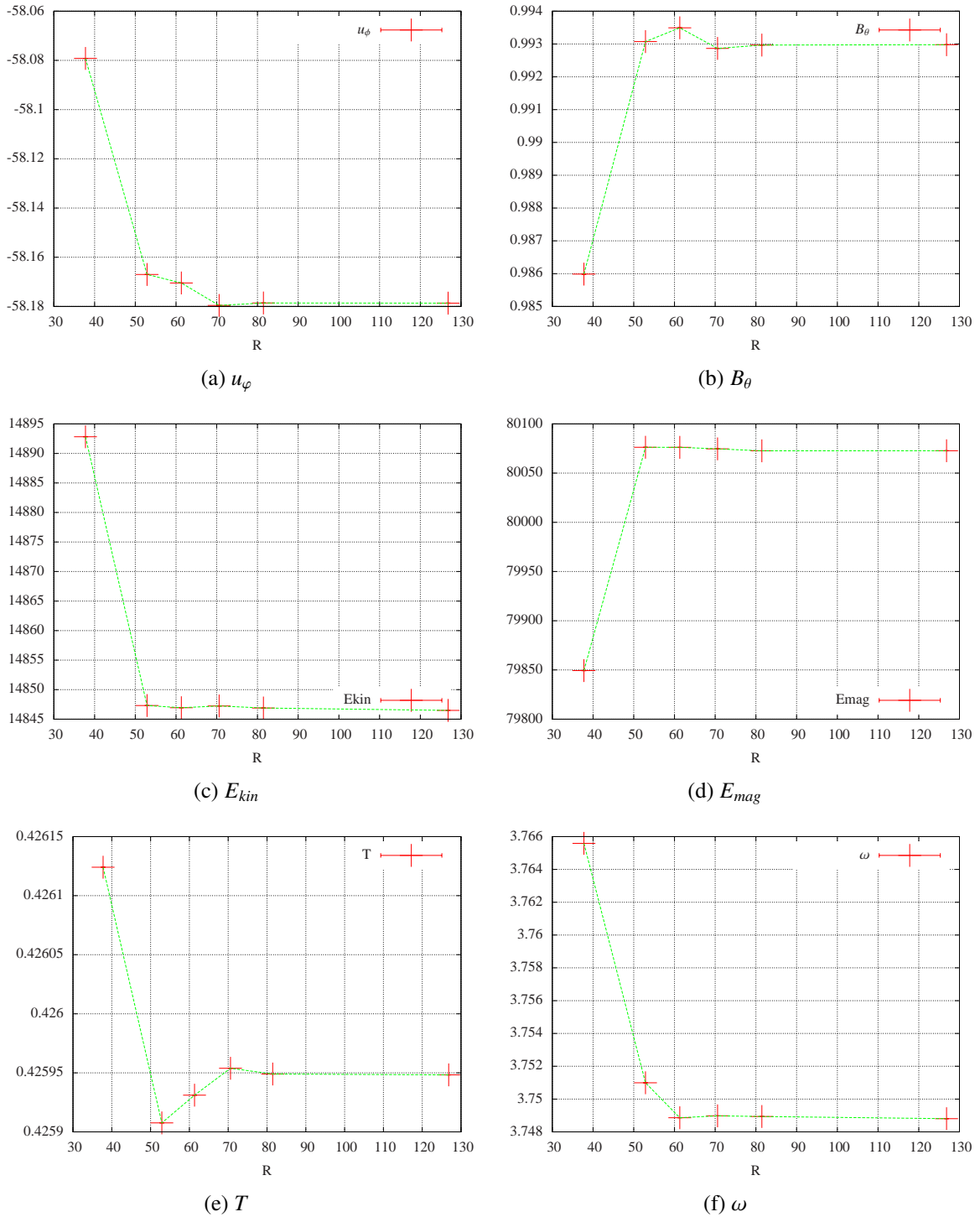
Figure 3.6*: Resolution tests, the pseudo-vacuum benchmark case q=5.*

(a) B_r (b) B_θ (c) B_φ

(d) u_r (e) u_θ (f) u_φ (g) T
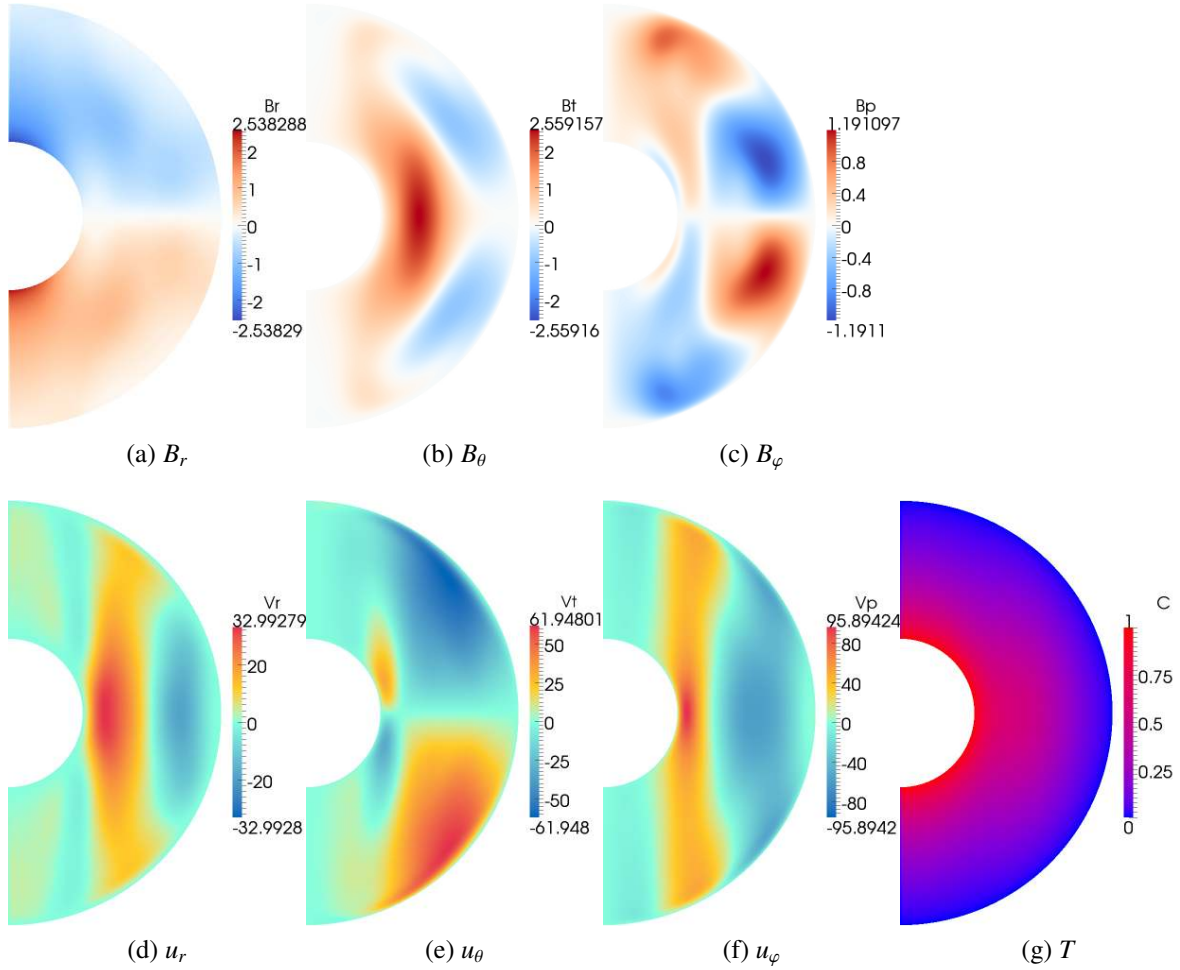
Figure 3.7: *The pseudo-vacuum benchmark case q = 5. Meridional sections of the solution. The plane chosen for the sections includes the benchmark point (defined in seq.3.3.4).*

(a) B_r (b) B_θ (c) B_φ

(d) u_r (e) u_θ (f) u_φ (g) T
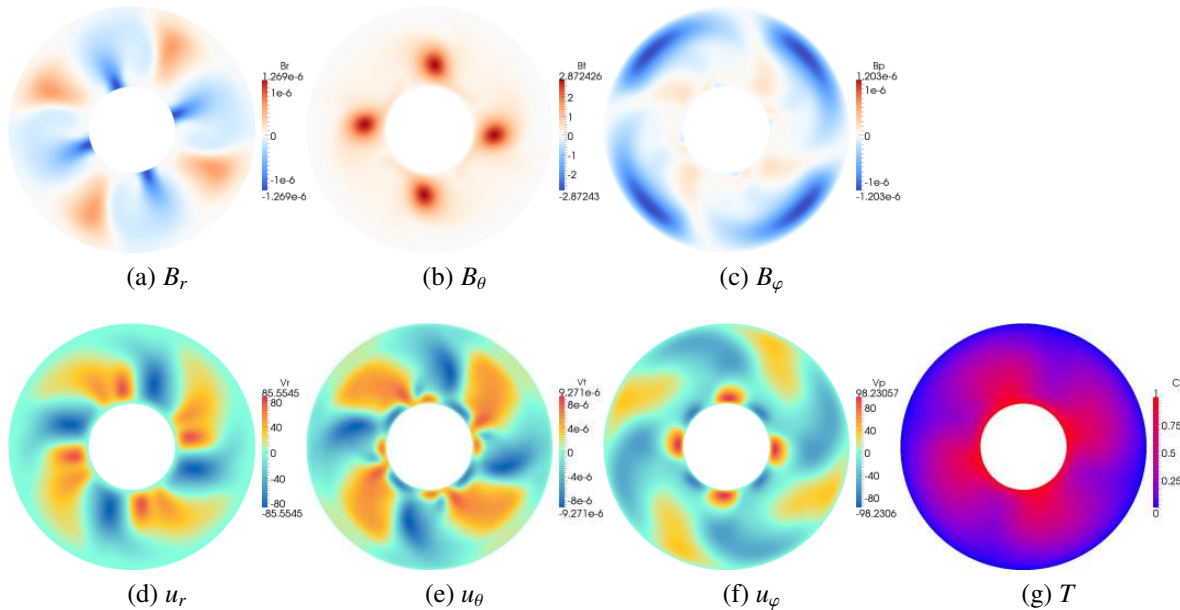
Figure 3.8: *The pseudo-vacuum benchmark case q = 5. Equatorial sections of the solution. The plane chosen for the sections includes the benchmark point (defined in seq.3.3.4).*

3.3.6   Case q=8

The Ekman and Rayleigh numbers are the same as in the subsection (3.3.5), Rossby number is changed to keep $Pr = 1$. In our non-dimensionalisation parameters are:

E	Ra	q	Ro
$0.5 \cdot 10^{-3}$	32.50	8	$0.625 \cdot 10^{-4}$

Fig. (3.9) shows results of the calculation. Requested data from the simulation are in the
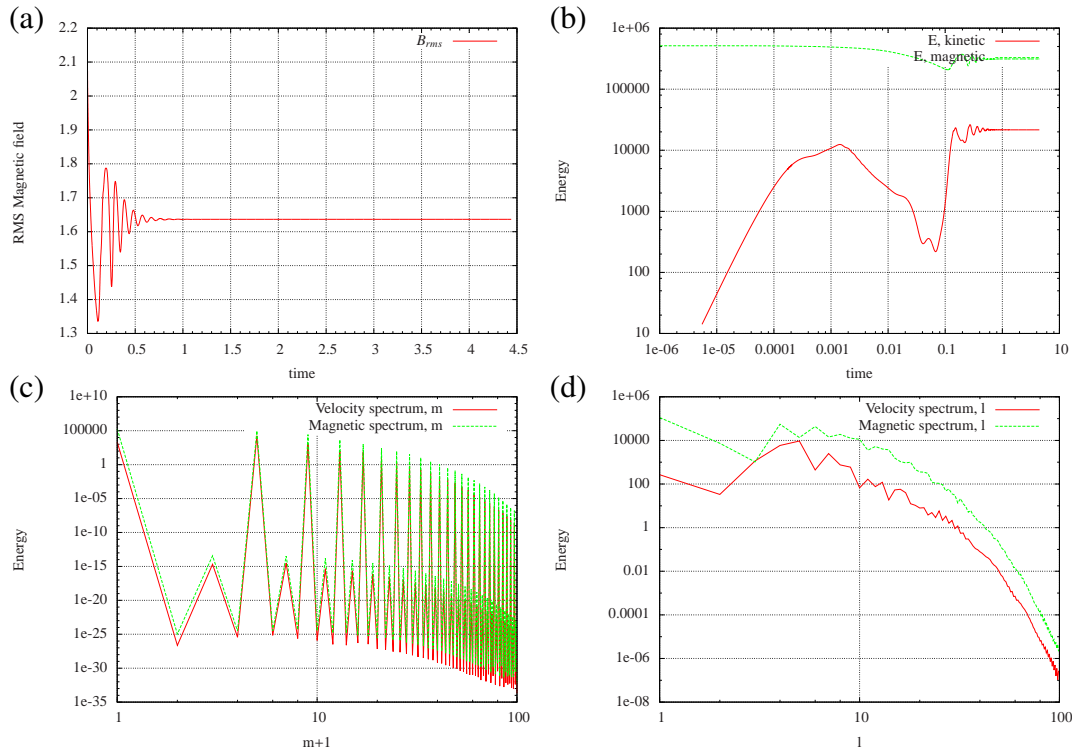
Figure 3.9: *Behaviour of the case $q = 8$. (a) B_{rms} vs. time (b) E_{mag} and E_{kin} vs. time on the log-log scale (c,d) Kinetic and magnetic energy spectral components vs. spherical harmonic degree l and harmonic order m.*

table (3.2). They are plotted on the figure (3.10). Field structure of the case $q = 5$ is shown in

N	L	M	V_φ	B_θ	T	E_{mag}	E_{kin}	ω	dt
50	32	29	-81.2134	2.1734	0.3936	313177.6	21721.3	5.4749	9.4191e-06
80	42	42	-80.8965	2.1840	0.3929	312801.5	21641.7	5.5857	9.1640e-06
96	48	48	-80.8549	2.1825	0.3930	312749.0	21628.1	5.5959	9.2062e-06
96	60	53	-80.9374	2.1820	0.3932	312771.9	21635.2	5.5886	9.1855e-06
128	64	64	-80.9292	2.1826	0.3932	312760.8	21635.1	5.5884	9.1591e-06
200	100	100	-80.9318	2.1823	0.3932	312754.7	21634.9	5.5882	9.1498e-06

Table 3.2: *Case $q = 8$ with pseudo-vacuum boundaries, output data.*

fig.(3.7) and fig.(3.8). The snapshot is taken in the steady region of the dynamo.

(a) u_φ

(b) B_θ

(c) E_{kin}

(d) E_{mag}

(e) T

(f) ω
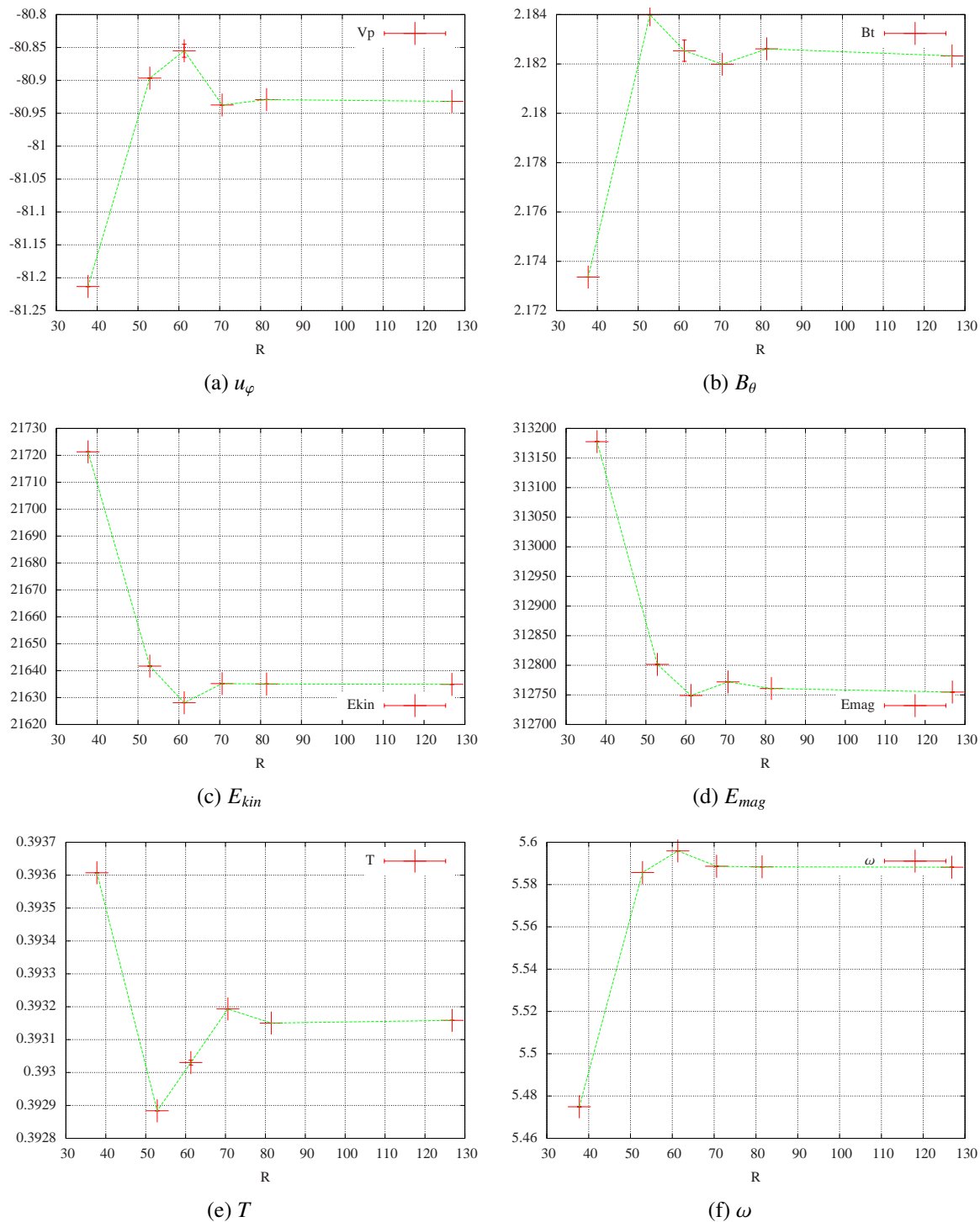
Figure 3.10: *Resolution tests, the pseudo-vacuum benchmark case q=8*

(a) B_r (b) B_θ (c) B_φ

(d) u_r (e) u_θ (f) u_φ (g) T
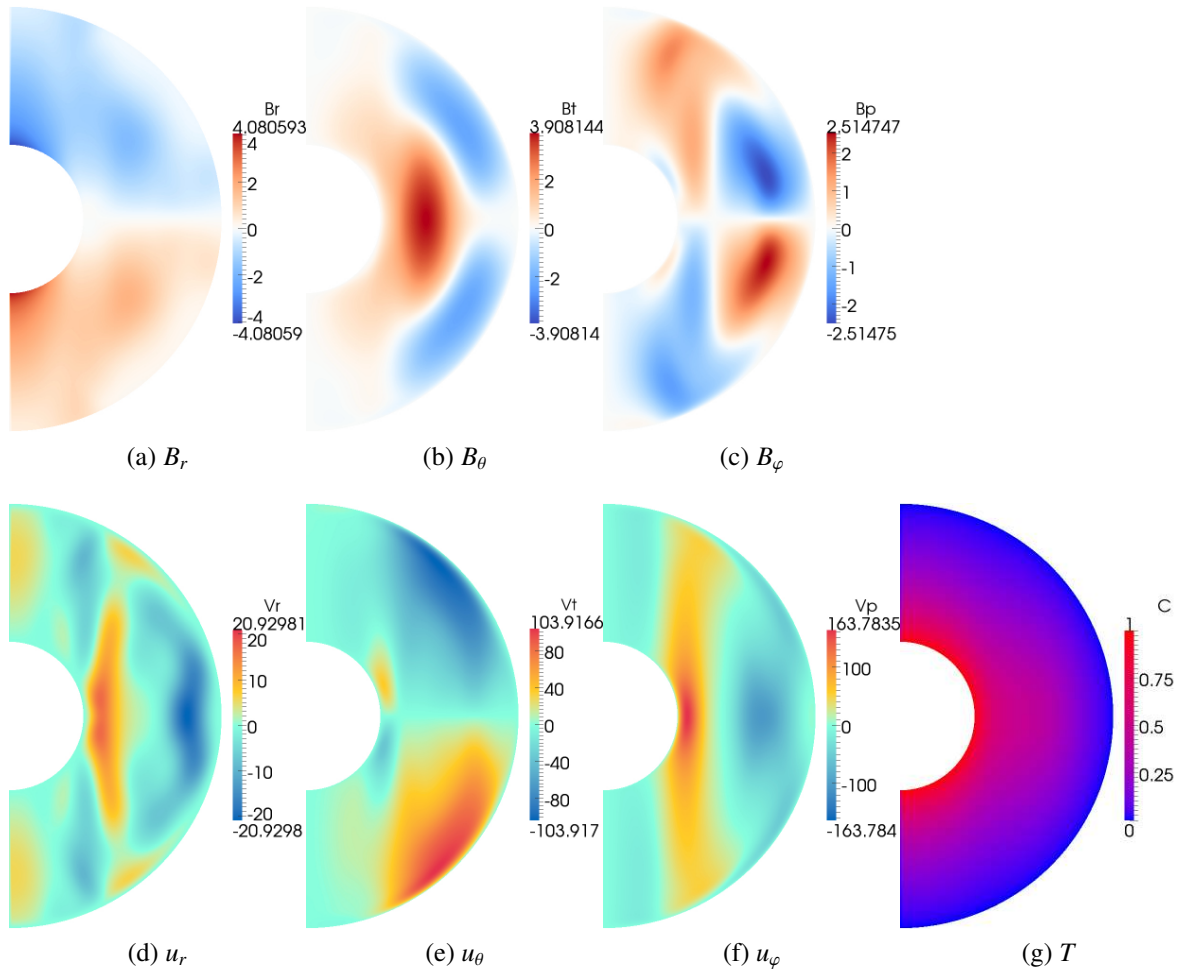
Figure 3.11: *The pseudo-vacuum benchmark case $q = 8$. Meridional sections of the solution. The plane chosen for the sections includes the benchmark point (defined in seq.3.3.4).*

(a) B_r (b) B_θ (c) B_φ

(d) u_r (e) u_θ (f) u_φ (g) T
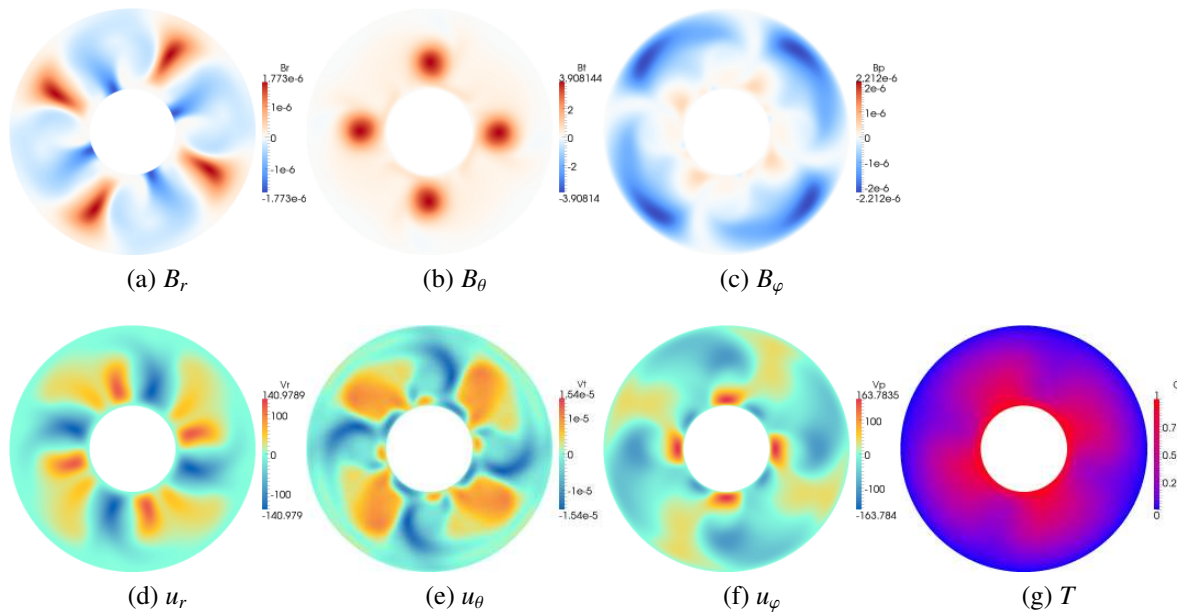
Figure 3.12: *The pseudo-vacuum benchmark case $q = 8$. Equatorial sections of the solution. The plane chosen for the sections includes the benchmark point (defined in seq.3.3.4).*

3.3.7 Timestep

The timestep is adaptive and in principle can change, but at the steady state it is almost constant. Dependence of the timestep on the resolution is in figure (3.13).
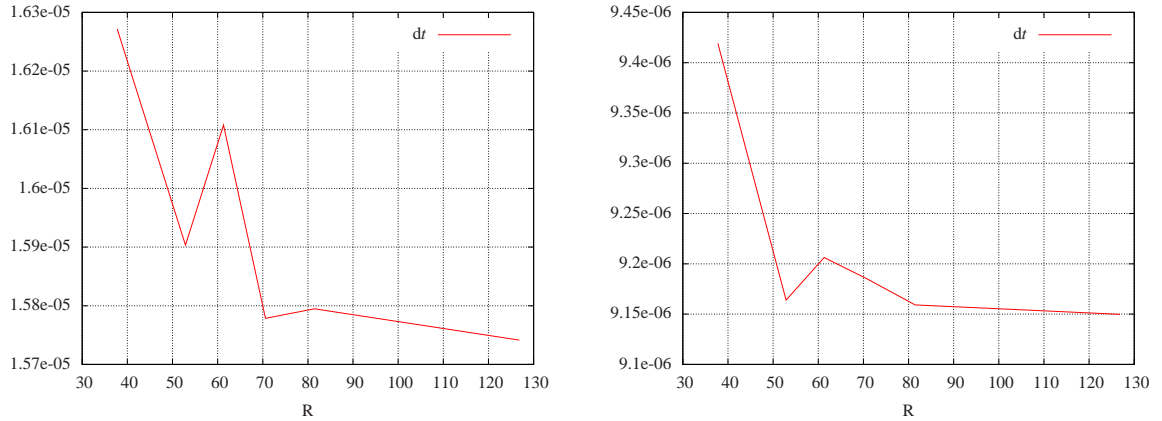
Figure 3.13: *Timestep. Left: case q=5, Right: case q=8.*

3.4 Other initial conditions

3.4.1 Oscillating dynamos

An increase of the initial magnetic field can lead to the oscillating dynamo in the case $q = 8$. Fig.(3.14) shows examples of this oscillating behavior. Two different initial conditions are
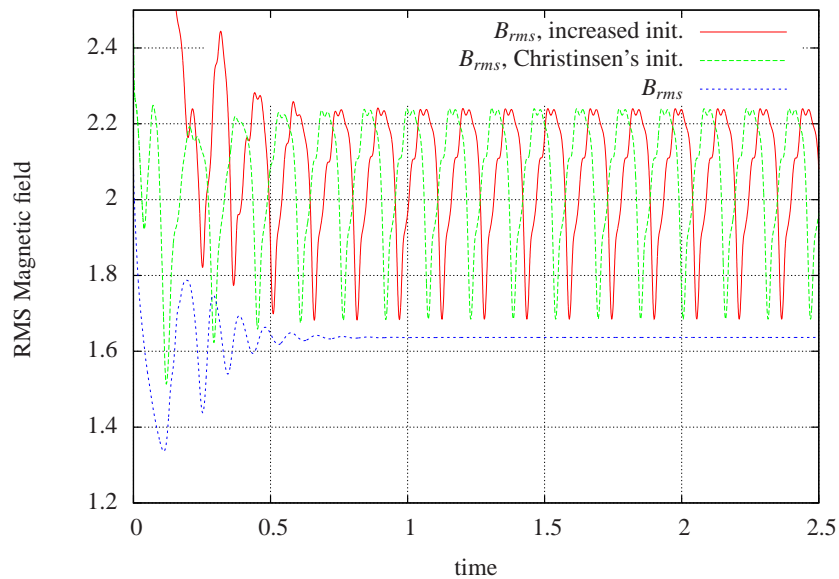
Figure 3.14: *Oscillating dynamos vs. stable, q=8. Green and red show dynamos with initial condition of Christensen et al. (2001) and for the strong field initial condition correspondingly. Blue line corresponds to the original initial condition eq.(3.32).*

(a) B_r (b) B_θ (c) B_φ

(d) u_r (e) u_θ (f) u_φ (g) T
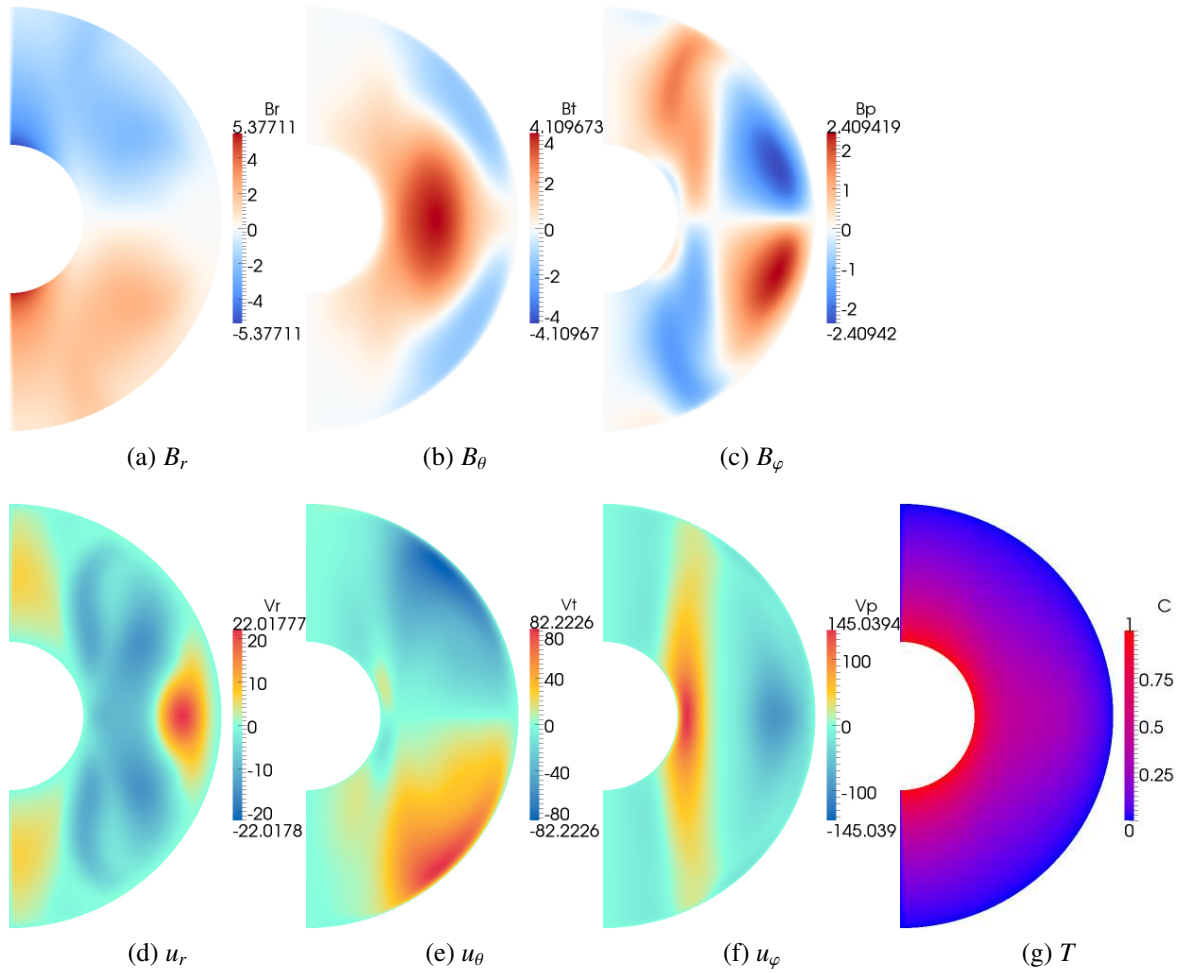
Figure 3.15: *Field structure of the case q = 8 for the strong field initial condition. Meridional sections of the solution.*

(a) B_r (b) B_θ (c) B_φ

(d) u_r (e) u_θ (f) u_φ (g) T
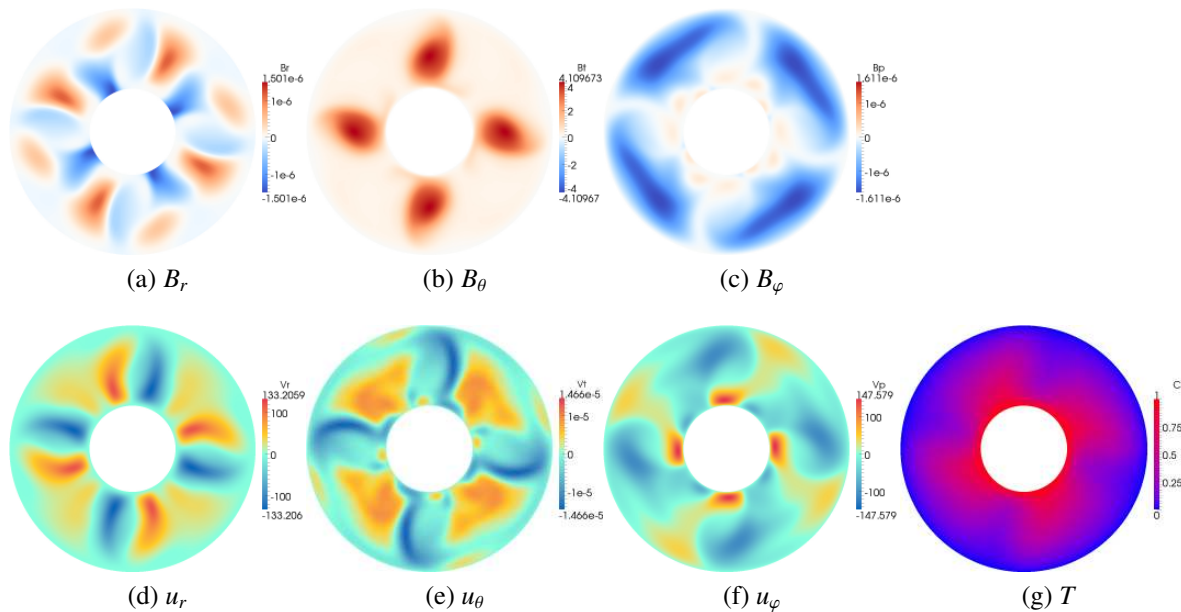
Figure 3.16: *Field structure of the case q = 8 for the strong field initial condition. Equatorial sections of the solution.*

used: (a) the magnetic field in eq.(3.32) multiplied by 8/3 (the strong field initial condition), (b) the initial condition of the "case 1" of Christensen et al. (2001) . In these two cases both energies, magnetic and kinetic, are oscillating with a constant amplitude. The angular drift periodically changes its direction. The field structure of such an oscillating solution with initial condition (a) is shown in figures (3.15) and (3.16), the snapshot is taken at the end of the run.

If the same increased initial condition 8/3×eq.(3.32) is used in the case $q = 5$, the dynamo is the same as before, see fig.(3.17). Thus the case $q = 8$ has two solutions, whereas $q = 5$ appears to be unique.

Time dependencies and spectra at the end of the simulations $q = 5$ and $q = 8$ with increased initial conditions are presented in figures (3.17, 3.18) and (3.19, 3.20).

(a)   (b)
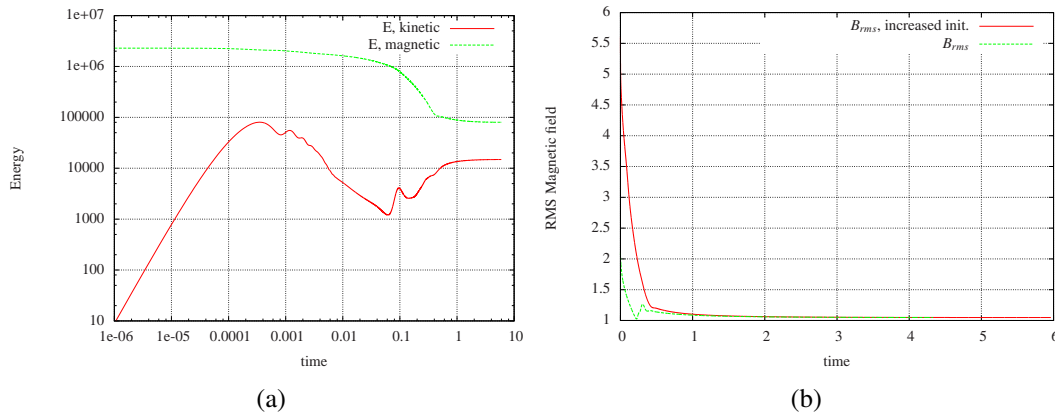
Figure 3.17: *Behaviour of the case $q = 5$ for the strong field initial condition. (a) Magnetic and kinetic energies vs. time on log-log scale. (b) Magnetic field vs. time on linear scale (green line corresponds to the original initial condition eq.3.32).*

(a)   (b)
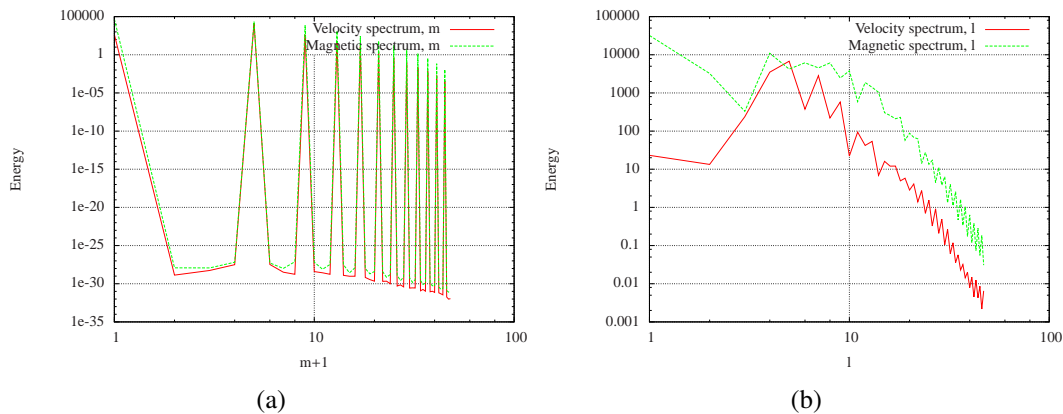
Figure 3.18: *Behaviour of the case $q = 5$ for the strong field initial condition. Kinetic (a) and magnetic (b) energy spectral components vs. spherical harmonic degree l and harmonic order m.*

(a)   (b)
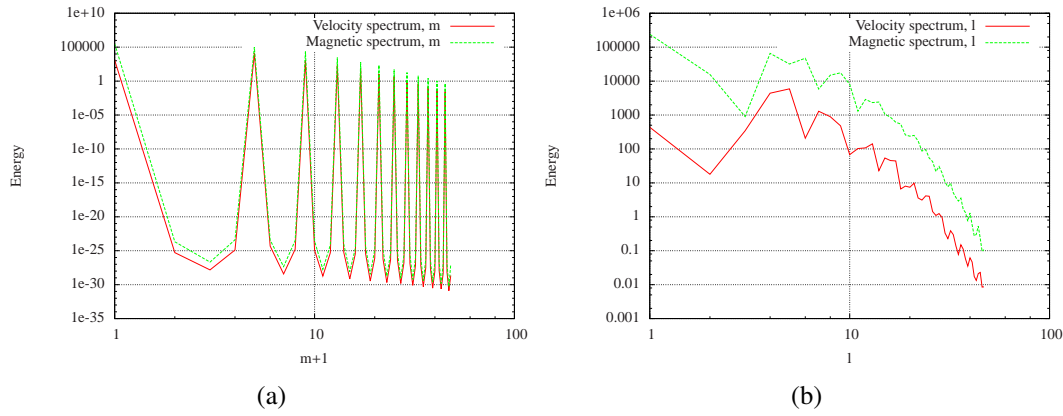
Figure 3.19: *Behaviour of the case q = 8 for the strong field initial condition. Kinetic (a) and magnetic (b) energy spectral components vs. spherical harmonic degree l and harmonic order m.*
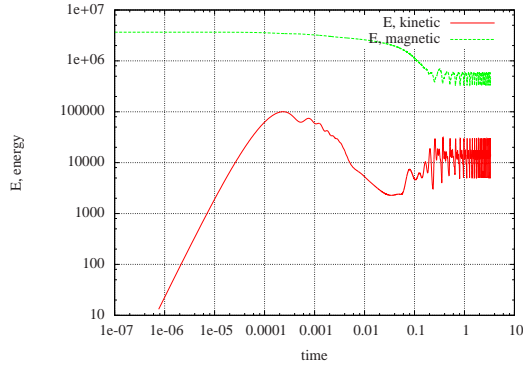
Figure 3.20: *Behaviour of the case q = 8 for the strong field initial condition. Magnetic and kinetic energies vs. time on log-log scale.*

3.4.2 Decaying magnetic field

Other forms of the initial magnetic field (even with energies similar to the energy of 3.32) can lead to decaying magnetic fields. E.g., we have tried the initial magnetic field (this field is written in physical coordinates in eq.D.3):

$$
\begin{cases}
T_2^0 = \dfrac{1}{\sqrt{2}} \dfrac{10}{3} \sin \pi (r - r_i), \\[2mm]
P_1^0 = \dfrac{4}{7} \dfrac{1}{\sqrt{2}} \left(\sin \left(2\pi \left(\dfrac{r - r_i}{r_o - r_i} - 0.25 \right) \right) + 1 \right).
\end{cases}
\tag{3.37}
$$

Fig.(3.21) shows results of the calculation with the parameters of the case $q = 5$, initial magnetic field (3.37), initial temperature (3.34), zero initial velocity field.

3.4.3 Variation of the initial magnetic energy

In this section the influence of the initial magnetic energy on the type of the solution was tested. The structure of the initial magnetic field was kept the same, different magnetic ener-
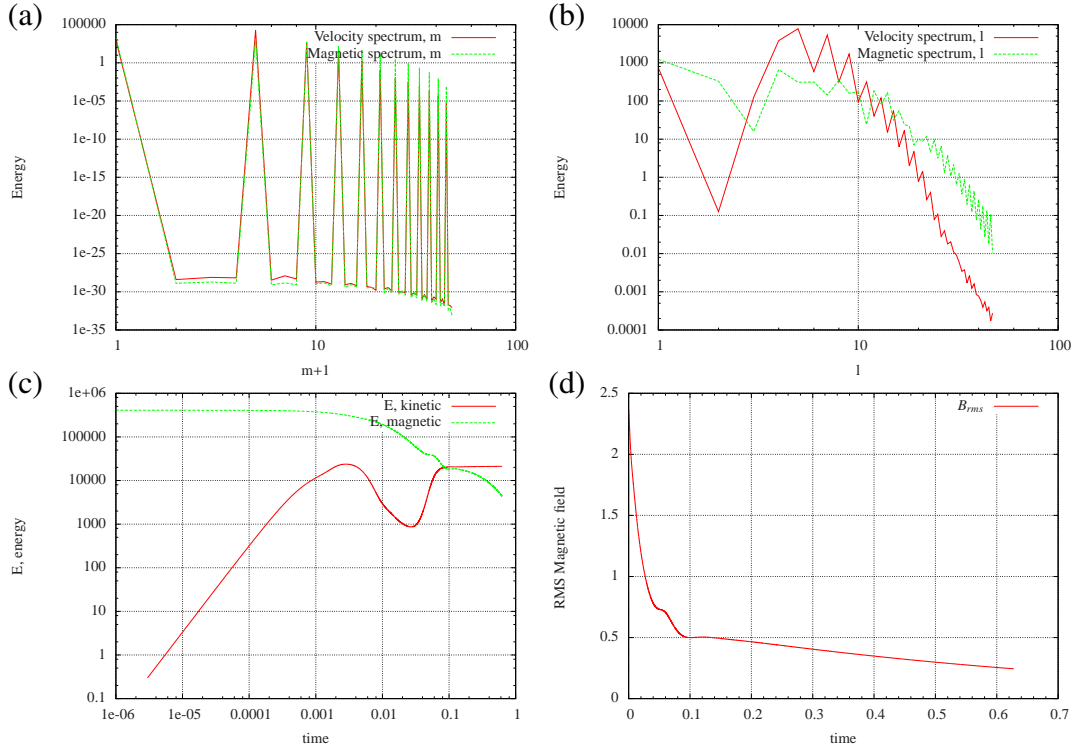
Figure 3.21: *Behaviour of the case $q = 5$ with the initial magnetic field (3.37) leading to subcritical behaviour. (a,b) Kinetic and magnetic energy spectral components vs. spherical harmonic order m and degree l. (c) Magnetic and kinetic energies vs. time on log-log scale. (d) Magnetic field vs. time on linear scale.*

gies were obtained by multiplication of the equation (3.32) by different prefactors (the ratio of the Toroidal and Poloidal components was not changed). Results are presented on the figure (3.22).
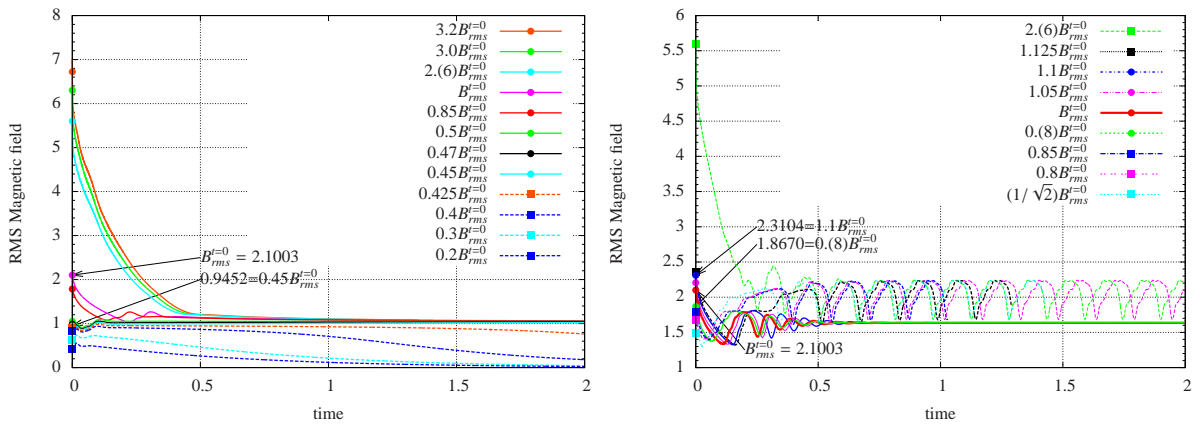
Figure 3.22: *Behaviour of the solution depending on the strength of the initial magnetic field. Left: $q = 5$, right: $q = 8$. Steady dynamos are denoted by circles and solid lines, oscillating or decaying - by squares and dashed lines.*

In the case $q = 8$ steady dynamos were started with the initial B_{rms} between 1.8670 and 2.3104 (prefactors 0.(8) and 1.1 times eq.(3.32); rms field of the eq.(3.32) is 2.1003). Outside

of this region only oscillating dynamos were obtained.

In the case $q = 5$ steady dynamos need initial B_{rms} above 0.9452. If the initial B_{rms} is weaker, the magnetic field fails to be self-generated. The upper boundary on initial magnetic energies suitable for steady dynamos was not found (much higher B_{rms} cause more complicated transients and require higher resolution than those was used for these runs: 80/42/37).

We conclude that this dynamo is, perhaps unsurprisingly, subcritical, just as the original benchmark dynamo is.

3.5   Insulating vs. Pseudo-Vacuum magnetic boundaries

It is interesting to compare Christensen's Case 1 with insulating boundaries and the case $q = 5$ (section 3.3.5) with pseudo-vacuum boundaries. To do so we start both runs from the same initial magnetic field (described in Christensen et al. (2001), Case 1)[2], although the initial condition will not satisfy pseudo-vacuum boundary condition. Both runs have exactly the same initial condition and parameters, only magnetic boundary conditions are different. The pseudo-vacuum condition is more strict than the insulating condition in the sense that it requires zero tangential magnetic field on boundaries. As the result, the magnetic energy is two times lower in the pseudo-vacuum case. The opposite behaviour is shown by the kinetic energy: it is thirty percent higher with pseudo-vacuum magnetic boundaries. The most prominent difference is in the direction of the drift (see the sign of the angular frequency ω) and its speed.

Although the initial condition for the $q = 5$ pseudo-vacuum simulation in this section is different from the described in sec.(3.3.5), the solution we have obtained is exactly the same. So we skip the detailed description of this run and refer to the sec.(3.3.5).

3.5.1   Christensen et al. (2001) Case 1 (insulating boundaries)

Parameters and boundary conditions are the same as in the Christensen et al. (2001) benchmark Case 1, in our non-dimensionalisation:

E	Ra	q	Ro
$0.5 \cdot 10^{-3}$	32.50	5	10^{-4}

Results of the integration are on the figure (3.23). Requested data of the simulation are in the table (3.3). The snapshot of the field in the steady region of the simulation is shown in figures (3.24) and (3.25).

---

[2]The initial magnetic field from the "Case 1" Christensen et al. (2001) has the direction opposite to the field in the eq.(3.32). This results in the inverse magnetic field in the steady state of the case $q = 5$ if Christensen's initial condition is used.

N	L	M	V_φ	B_θ	T	E_{mag}	E_{kin}	ω	dt
96	48	48	-38.0917	-3.4890	0.3733	228598.9	11230.8	-15.5068	2.6667e-05

Table 3.3: *Case 1 Christensen et al. (2001), output data. Boundaries are insulating.*

(a)

(b)

(c)

(d)
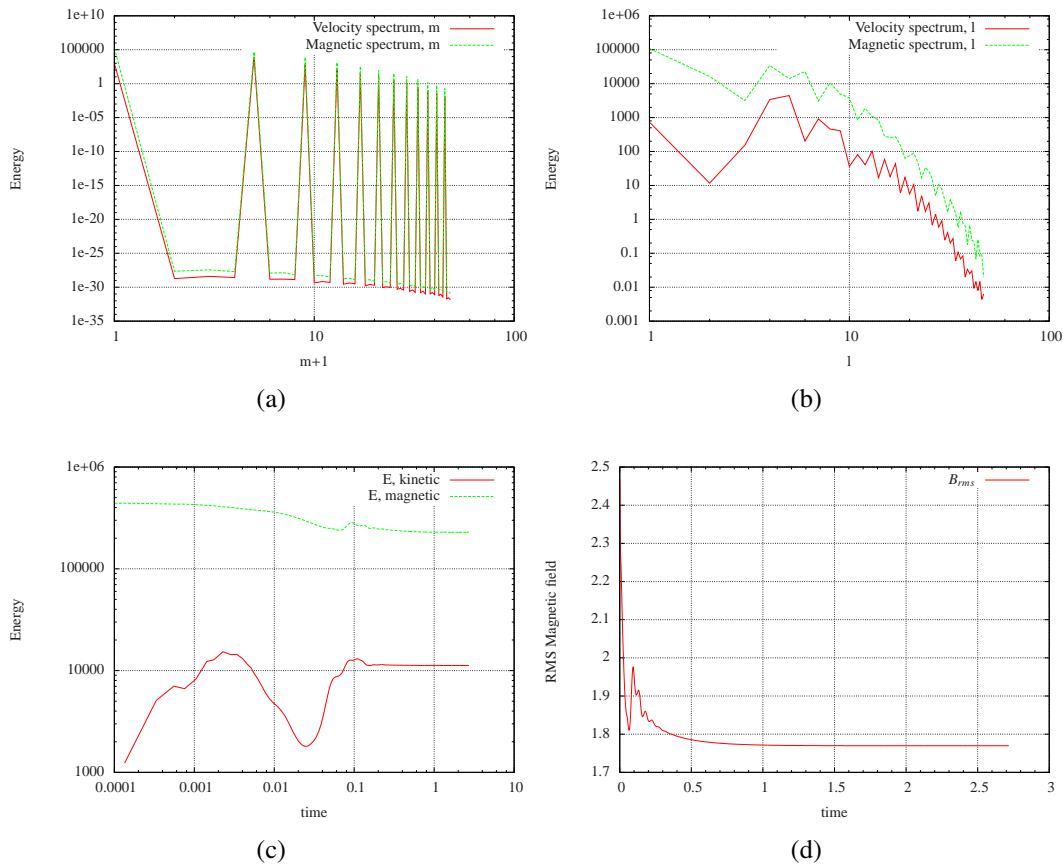
Figure 3.23: *Behaviour of the Case 1 Christensen et al. (2001). (a,b) Kinetic and magnetic energy spectral components vs. spherical harmonic degree l and harmonic order m. (c) Magnetic and kinetic energies vs. time on log-log scale. (d) Magnetic field vs. time on linear scale.*
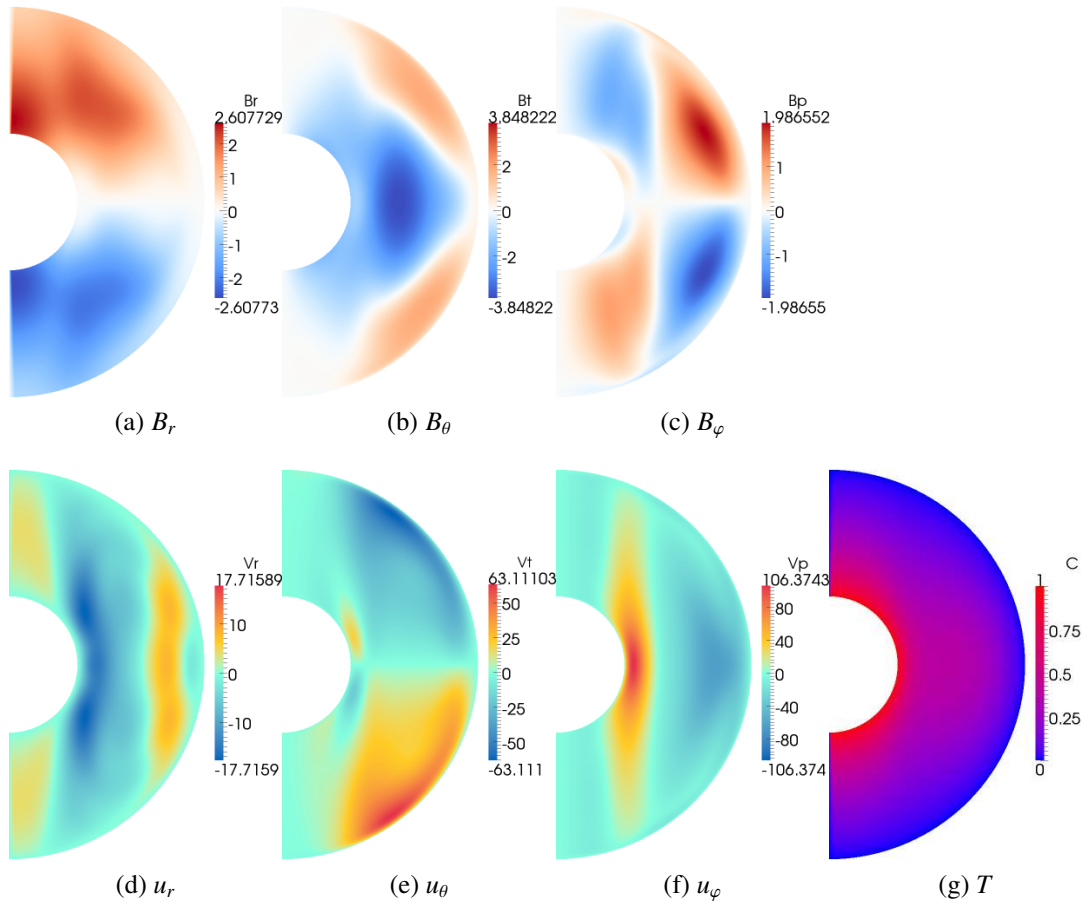
Figure 3.24: *The field structure of the Case 1 Christensen et al. (2001): q = 5, insulating boundaries. Meridional sections of the solution. The plane chosen for the sections includes the benchmark point (defined in seq.3.3.4).*
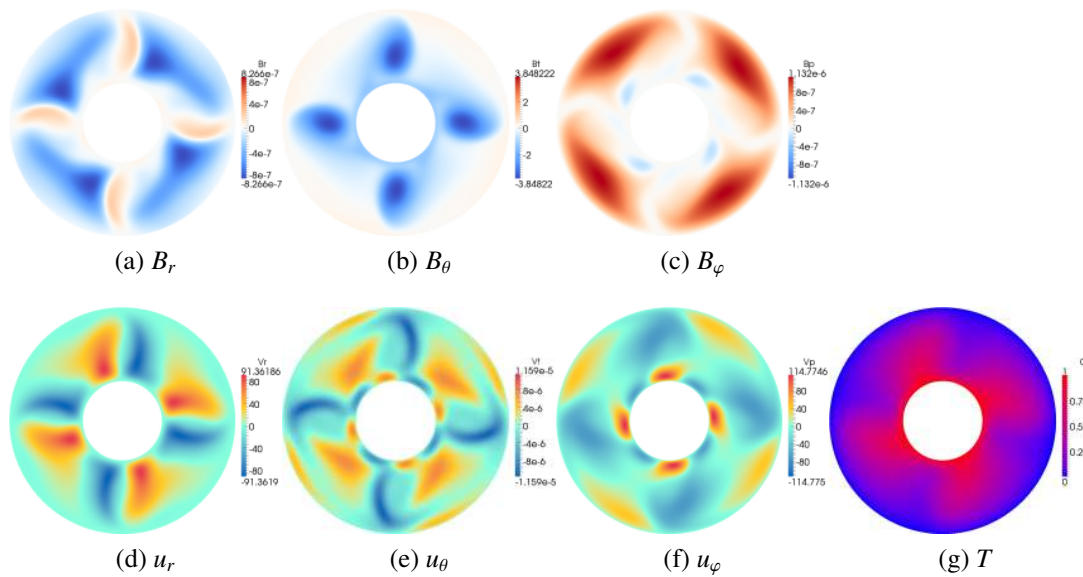
Figure 3.25: *The field structure of the Case 1 Christensen et al. (2001): q = 5, insulating boundaries. Equatorial sections of the solution. The plane chosen for the sections includes the benchmark point (defined in seq.3.3.4).*

3.5.2 Field on the outer boundary (insulating boundaries vs. pseudo-vacuum)

The radial magnetic field on the outer boundary for the cases described in the sections (3.3.5) and (3.5.1) is presented below.
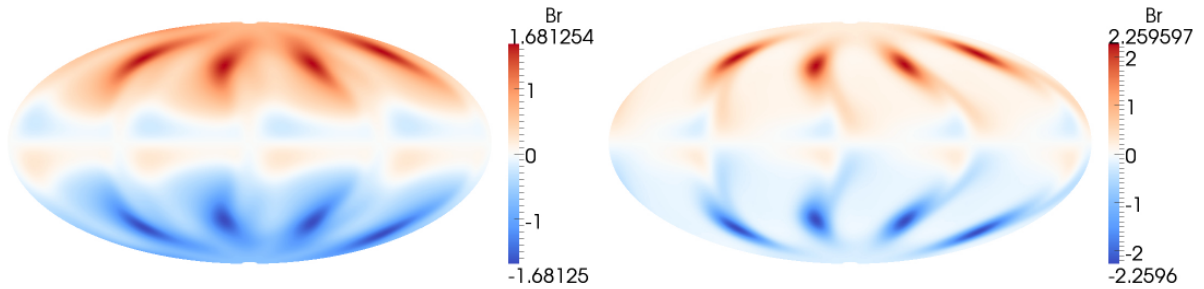
Figure 3.26: *B_r on the outer boundary. Left: insulating boundaries Right: Pseudo-vacuum boundaries.*

3.6 Conclusions

Two different set-ups which reach steady solutions with pseudo-vacuum boundary conditions are presented. Section (3.4) shows influence of the initial condition. The dynamos are subcritical and a proper initial magnetic field is required for the convergence to the steady regime. Solutions have fourfold and equatorial symmetries which can be useful to reduce cpu load during benchmarking. Case $q = 5$ converges slower than the $q = 8$ for the required precision, but it is less resolution-dependent. Properties of dynamos obeying pseudo-vacuum and insulating boundary conditions are largely different. Comparison (sections 3.5.1 and 3.3.5) shows that the switch between the boundary conditions affects the direction and the speed of the drift, repartition of the kinetic and magnetic energies, geometry of fields. Although it could be that subcritical dynamos are exceptionally highly sensitive to the boundary conditions. The $q = 5$ dynamo was used as a part of a benchmark (Jackson et al., 2014). All participants successfully found the solution within deviations of a few percent, including three local (finite element, finite volume) codes.

Chapter 4

Existence of dynamos driven by fluid injection through a porous boundary.

Experimental dynamos are usually driven or assumed to be driven: by differential rotation of their containers boundaries, by imposed temperature difference, due to unstable density distribution or mechanically by propellers. Injection of the fluid through the so-called "porous" boundary together with the suction on the other side could be another driving mechanism for an experimental dynamo. These conditions imply permeable boundaries where normal to them fluid velocities are non-zero and are used in applied fluid mechanics (e.g. in transpiration cooling or gaseous diffusion[1]). In this chapter we present the numerical approach for solving MHD equations with the porous boundary conditions. Also we show an examination of experimentally feasible injection-driven flows on a possibility to behave like a dynamo.

The figure 4.1 shows an idealized (for numerical representation) scheme of the experimental device which can drive a flow by an injection through the permeable boundaries. A real device will most probably include also a shaft on the rotation axis (to transfer rotational momentum and fluid for injection). This additional geometrical complication can not be solved with the spectral numerical code we are utilizing, therefore the effect of the shaft we admit as unessential.

---

[1]The transpiration cooling is a way of active heat protection (of e.g. blades in gas turbine, see Arai and Suidzu, 2013) during which a coolant passes through the wall and absorbs part of heat. Somewhat better cooling efficiency is obtained when a porous coating is attached onto the protected surface. The gaseous diffusion is used to produce enriched uranium by forcing its hexafluoride through semipermeable membranes.
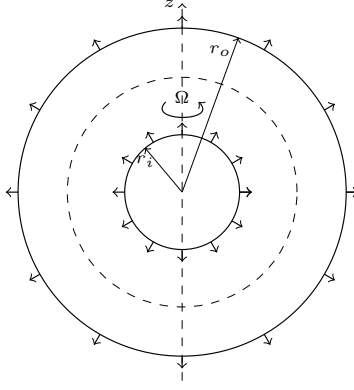
Figure 4.1: *Schematic representation of the rotating container with the injection-driven flow. Small arrows denote inlet and outlet flows.*

4.1 Equations

4.1.1 Hydrodynamic equations

Fluid is uniformly injected through the inner boundary with the speed $u_o r_o^2 / r_i^2$ and sucked from the outer boundary with the speed u_0 (fig. 4.1). The ratio of boundary fluid velocities is dictated by the incompressibility condition: the flow per unit surface remains constant on all surfaces closed around the inner core inside the fluid container. We decompose the fluid velocity $\mathbf{U}$ as $\mathbf{U} = \mathcal{I}\dfrac{\hat{\mathbf{r}}}{r^2} + \mathbf{u}$, where $\mathcal{I} = u_0 r_0^2$. The Laplacian $\boldsymbol{\nabla}^2 \dfrac{\hat{\mathbf{r}}}{r^2}$ is zero, hence the Navier-Stokes equation for the deviation $\mathbf{u}$ (eq.A.24 without magnetic and buoyancy forces) is:

$$\left(\frac{\partial}{\partial t} - \nu\boldsymbol{\nabla}^2\right)\mathbf{u} = \begin{array}{c} (\mathbf{u} + \mathcal{I}\frac{\hat{\mathbf{r}}}{r^2}) \times (\boldsymbol{\nabla}\times\mathbf{u}) - \\ 2\Omega\left(\hat{\mathbf{z}}\times\mathbf{u} + \frac{\mathcal{I}}{r^2}\sin\theta\hat{\varphi}\right) - \boldsymbol{\nabla}P \end{array}. \tag{4.1}$$

The variable P here is the modified pressure that stores information about conservative forces $\boldsymbol{\nabla}P$.

Using the outer radius of the shell r_o, the viscous diffusion time r_o^2/ν, and the velocity at outer boundary u_o as basic units, we define a non-dimensionalisation of eq.(4.2) .

$$\text{Length } r \to (r_o)\, r, \quad \text{Time } t \to r_o^2/\nu\, t, \quad \text{Velocity } u \to u_o\, u. \tag{4.2}$$

We substitute for variables using the non-dimensional forms eq.(4.2):

$$\left(\frac{\nu}{r_o^2}\frac{\partial}{\partial t} - \frac{\nu}{r_o^2}\boldsymbol{\nabla}^2\right)\mathbf{u}u_o = \frac{u_o^2}{r_o}(\mathbf{u} + \frac{\hat{\mathbf{r}}}{r^2})\times(\boldsymbol{\nabla}\times\mathbf{u}) - 2\Omega u_o\left(\hat{\mathbf{z}}\times\mathbf{u} + \frac{1}{r^2}\sin\theta\hat{\varphi}\right) - \frac{P_0}{r_o}\boldsymbol{\nabla}P, \tag{4.3}$$

then we divide through by $2\Omega u_o$:

$$\left(\frac{\nu}{2\Omega r_o^2}\frac{\partial}{\partial t} - \frac{\nu}{2\Omega r_o^2}\boldsymbol{\nabla}^2\right)\mathbf{u} = \frac{u_o}{2\Omega r_o}(\mathbf{u} + \frac{\hat{\mathbf{r}}}{r^2}) \times (\boldsymbol{\nabla} \times \mathbf{u}) - \left(\hat{\mathbf{z}} \times \mathbf{u} + \frac{1}{r^2}\sin\theta\hat{\varphi}\right) - \frac{P_0}{2\Omega u_o r_o}\boldsymbol{\nabla}P, \quad (4.4)$$

Finally, the non-dimensional Navier-Stokes equation for the injection is:

$$E\left(\frac{\partial}{\partial t} - \boldsymbol{\nabla}^2\right)\mathbf{u} = Ro\,(\mathbf{u} + \frac{\hat{\mathbf{r}}}{r^2}) \times (\boldsymbol{\nabla} \times \mathbf{u}) - \left(\hat{\mathbf{z}} \times \mathbf{u} + \frac{1}{r^2}\sin\theta\hat{\varphi}\right) - \boldsymbol{\nabla}\tilde{P}, \quad (4.5)$$

Only two non-dimensional parameters control the flow (see table 4.1)[2]. The term correspond-

Parameter	E	Ro
Definition	$\dfrac{\nu}{2\Omega r_o^2}$	$\dfrac{u_o}{2\Omega r_o}$

Table 4.1: *Non-dimensional parameters for injection driven flow (without magnetic field).*

ing to the pressure in eq.(4.5) disappears in the "curled" equation which is actually solved. We should not forget that **u** is the deviation from the basic flow through the shell $\hat{\mathbf{r}}/r^2$. The total non-dimensional flow is:

$$\mathbf{U} = \frac{\hat{\mathbf{r}}}{r^2} + \mathbf{u} \quad (4.6)$$

4.1.1.1 Additional terms due to the injection

The injection provides new non-linear terms for the Navier-Stokes equation. The non-linear terms in the pseudo-spectral code are calculated in physical space for each spherical coordinate individually. Components ($\hat{\mathbf{r}}$, $\hat{\theta}$, $\hat{\varphi}$) of terms due to the injection are presented in this section.

The Navier-Stokes equation for injection is:

$$E\left(\frac{\partial}{\partial t} - \boldsymbol{\nabla}^2\right)\mathbf{u} = Ro\,\mathbf{u} \times (\boldsymbol{\nabla} \times \mathbf{u}) - \hat{\mathbf{z}} \times \mathbf{u} + Ro\,\frac{\hat{\mathbf{r}}}{r^2} \times (\boldsymbol{\nabla} \times \mathbf{u}) - \frac{1}{r^2}\sin\theta\hat{\varphi} - \boldsymbol{\nabla}\tilde{P} \quad (4.7)$$

The inertial term corresponding to the injection is:

$$\frac{\hat{\mathbf{r}}}{r^2} \times (\boldsymbol{\nabla} \times \mathbf{u}) = \begin{pmatrix} 0 \\ -1/r^2 \cdot (\boldsymbol{\nabla} \times \mathbf{u})_\varphi \\ 1/r^2 \cdot (\boldsymbol{\nabla} \times \mathbf{u})_\theta \end{pmatrix}\begin{pmatrix} \hat{\mathbf{r}} & \hat{\theta} & \hat{\varphi} \end{pmatrix}. \quad (4.8)$$

Additional terms on the RHS in comparison with the "standard" Navier-Stokes equation are in table (4.2). We note that the forcing in radial direction is the same as before, but new

---

[2]Definitions of non-dimensional parameters E and Ro differ from those in other chapters. The outer radius r_o is used in the definition of E instead of the shell's thickness d, and Ro is the non-modified version of the Rossby number.

$$\hat{\mathbf{r}}: \quad 0$$
$$\hat{\theta}: \quad -Ro\, 1/r^2 \cdot (\boldsymbol{\nabla} \times \mathbf{u})_\varphi$$
$$\hat{\varphi}: \quad 1/r^2 \cdot [Ro\, (\boldsymbol{\nabla} \times \mathbf{u})_\theta - \sin\theta]$$

Table 4.2: *Components of additional terms in the Navier-Stokes equation due to the injection.*

horizontal forces are playing an important role. One driving term is $\dfrac{\sin\theta}{r^2}\hat{\varphi}$, it creates flow in $\hat{\varphi}$ direction. If the velocity perturbation $\mathbf{u}$ is zero everywhere, only this term is responsible for breaking the basic flow $\dfrac{1}{r^2}$. Other terms are important when the horizontal component of vorticity is non-zero. They appear due to the non-linear interaction between the basic flow $\dfrac{\hat{\mathbf{r}}}{r^2}$ and the perturbation $\mathbf{u}$.

4.1.2 Boundary conditions

The no-slip boundary condition is applied for the velocity perturbation $\mathbf{u}$. The only meaning is that the flow on the boundaries is exactly the basic flow $\hat{\mathbf{r}}/r^2$.

4.1.3 Equations with the magnetic field

The induction term of the induction equation (A.36) if the flow is driven by injection contains the basic flow $\dfrac{\hat{\mathbf{r}}}{r^2}$ and the perturbation $\mathbf{u}$. Besides that the Lorentz force appears in the Navier-Stokes equation in comparison with the purely hydrodynamical version (eq.4.5).

$$\begin{cases} \left(\dfrac{\partial}{\partial t} - \nu\boldsymbol{\nabla}^2\right)\mathbf{u} &= \quad (\mathbf{u} + \mathcal{I}\dfrac{\hat{\mathbf{r}}}{r^2}) \times (\boldsymbol{\nabla} \times \mathbf{u}) + \dfrac{1}{\rho_0\mu_0}(\boldsymbol{\nabla} \times \mathbf{B}) \times \mathbf{B} - \\ & \quad -2\Omega\left(\hat{\mathbf{z}} \times \mathbf{u} + \dfrac{\mathcal{I}}{r^2}\sin\theta\hat{\varphi}\right) - \boldsymbol{\nabla}P, \\ \left(\dfrac{\partial}{\partial t} - \eta\boldsymbol{\nabla}^2\right)\mathbf{B} &= \quad \boldsymbol{\nabla} \times ((\mathbf{u} + \mathcal{I}\dfrac{\hat{\mathbf{r}}}{r^2}) \times \mathbf{B}) \end{cases} \tag{4.9}$$

The same units as for the hydrodynamical version of equations are used for the non-dimensionalisation, additionally the definition for a unit magnetic field is applied.

$$\text{Length } r \to (r_o)\, r, \quad \text{Time } t \to r_o^2/\nu\, t, \quad \text{Magnetic } B \to (2\Omega\rho_0\mu_0\eta)^{\frac{1}{2}}\, B, \quad \text{Velocity } u \to u_o\, u. \tag{4.10}$$

Recalling that $\mathcal{I} = u_o r_o^2$, we substitute variables in eq.(4.9) by non-dimensional, divide the first eq. by $2\Omega u_o$ and multiply the second by r_o^2/η to get non-dimensional equations for the

injection driven MHD:

$$
\begin{cases}
E\left(\dfrac{\partial}{\partial t} - \boldsymbol{\nabla}^2\right)\mathbf{u} &= Ro\,(\mathbf{u} + \dfrac{\hat{\mathbf{r}}}{r^2}) \times (\boldsymbol{\nabla} \times \mathbf{u}) - \left(\hat{\mathbf{z}} \times \mathbf{u} + \dfrac{1}{r^2}\sin\theta\hat{\varphi}\right) - \boldsymbol{\nabla}\tilde{P} + \dfrac{1}{R_m}(\boldsymbol{\nabla} \times \mathbf{B}) \times \mathbf{B}, \\
\left(Pr_m\dfrac{\partial}{\partial t} - \boldsymbol{\nabla}^2\right)\mathbf{B} &= R_m\boldsymbol{\nabla} \times ((\mathbf{u} + \dfrac{\hat{\mathbf{r}}}{r^2}) \times \mathbf{B})
\end{cases}
\tag{4.11}
$$

The magnetic Reynolds number $R_m = \dfrac{u_o r_o}{\eta}$ is an extra parameter, that can be expressed via others:

$$
R_m = Ro \cdot Pr_m / E \tag{4.12}
$$

Table 4.3 gives definitions of chosen basic parameters.

E	Ro	Pr_m
$\dfrac{\nu}{2\Omega r_o^2}$	$\dfrac{u_o}{2\Omega r_o}$	$\dfrac{\nu}{\eta}$

Table 4.3: *Injection driven flow, basic parameters.*

4.1.3.1 Implementation in the code

The new term due to the injection on the right hand side of the induction equation (in comparison with the induction equation 2.1b used in other chapters) is:

$$
R_m\boldsymbol{\nabla} \times (\dfrac{\hat{\mathbf{r}}}{r^2} \times \mathbf{B}). \tag{4.13}
$$

The Navier-Stokes equations is the same as eq.(4.5), but with the Lorentz force.

4.1.4 Energy definitions

The non-dimensionalisation in equations (4.11) differs from the one which is originally used in previous chapters. Below we present definitions of energy which are changed accordingly. Dimensional variables are denoted with a hat.

Kinetic energy:

$$
\widehat{E}_{kin} = \frac{1}{2}\int \rho_0\widehat{\mathbf{u}}^2\mathrm{d}\widehat{V} = \frac{1}{2}\rho_0 r_o^3 u_0^2 \int \mathbf{u}^2\mathrm{d}V, \tag{4.14}
$$

$$
E_{kin} = \frac{1}{\rho_0 r_0^3 u_0^2}\widehat{E}_{kin} = \frac{1}{2}\int \mathbf{u}^2\mathrm{d}V. \tag{4.15}
$$

Viscous dissipation:

$$\widehat{D_\nu} = \int \rho_0 \nu (\widehat{\boldsymbol\nabla} \times \widehat{\mathbf{u}})^2 \mathrm{d}\widehat{V} = \rho_0 \nu r_0 u_0^2 \int (\boldsymbol\nabla \times \mathbf{u})^2 \mathrm{d}V, \tag{4.16}$$

$$D_\nu = \frac{1}{\rho_0 r_0^3 u_0^2} \frac{r_o^2}{\nu} \widehat{D_\nu} = \int (\boldsymbol\nabla \times \mathbf{u})^2 \mathrm{d}V. \tag{4.17}$$

Magnetic energy:

$$\widehat{E}_{mag} = \frac{1}{2\mu_0} \int \widehat{\mathbf{B}}^2 \mathrm{d}\widehat{V} = \frac{1}{2\mu_0} (2\Omega \rho_0 \mu_0 \eta) r_o^3 \int \mathbf{B}^2 \mathrm{d}V = \Omega \rho_0 \eta r_o^3 \int \mathbf{B}^2 \mathrm{d}V, \tag{4.18}$$

$$E_{mag} = \frac{1}{\rho_0 r_0^3 u_0^2} \widehat{E}_{mag} = \frac{\Omega \eta}{u_0^2} \int \mathbf{B}^2 \mathrm{d}V = \frac{1}{2} \frac{1}{RoR_m} \int \mathbf{B}^2 \mathrm{d}V. \tag{4.19}$$

Ohmic dissipation:

$$\widehat{D_\Omega} = \frac{\eta}{\mu_0} \int (\widehat{\boldsymbol\nabla} \times \widehat{\mathbf{B}})^2 \mathrm{d}\widehat{V} = \frac{\eta}{\mu_0} \frac{2\Omega \rho_0 \mu_0 \eta}{r_o^2} r_o^3 \int (\boldsymbol\nabla \times \mathbf{B})^2 \mathrm{d}V = 2\Omega \rho_0 \eta^2 r_o \int (\boldsymbol\nabla \times \mathbf{B})^2 \mathrm{d}V, \tag{4.20}$$

$$D_\Omega = \frac{1}{\rho_0 r_0^3 u_0^2} \frac{r_o^2}{\nu} \widehat{D_\Omega} = \frac{2\Omega \eta^2}{u_0^2 \nu} \int (\boldsymbol\nabla \times \mathbf{B})^2 \mathrm{d}V = \frac{1}{RoR_m Pr_m} \int (\boldsymbol\nabla \times \mathbf{B})^2 \mathrm{d}V. \tag{4.21}$$

A summary of the definitions of energy for injection driven flow is presented in the table (4.4).

E_{kin}	D_ν	E_{mag}	D_Ω
$\frac{1}{2} \int \mathbf{u}^2 \mathrm{d}V$	$\int (\boldsymbol\nabla \times \mathbf{u})^2 \mathrm{d}V$	$\frac{1}{2} \frac{1}{RoR_m} \int \mathbf{B}^2 \mathrm{d}V$	$\frac{1}{RoR_m Pr_m} \int (\boldsymbol\nabla \times \mathbf{B})^2 \mathrm{d}V$

Table 4.4: *Definitions of energies and powers for MHD equations with injection driven flow.*

4.2 Benchmarking

In this section we solve identical problems with two different codes (linear Hollerbach, 2000 and full 3D non-linear, Willis et al., 2007). We calculate only axisymetric components which simplify the choice of diagnostics and reduces the computational time. The flow in the runs with $Ro > 0$ is confirmed to be axisymmetric (the onset of non-axisymmetric motions with $Ro > 0$ is in fig. 4.6 later in the chapter). The ratio of inner and outer boundaries is chosen to be $r_i/r_o = 1/3$ in this chapter.

For an axisymmetric flow $\left(\dfrac{\partial}{\partial \varphi} = 0 \right)$:

$$\mathbf{u} = \boldsymbol{\nabla} \times \boldsymbol{\nabla} \times (P\mathbf{r}) + \boldsymbol{\nabla} \times (T\mathbf{r}) = -\boldsymbol{\nabla} \times \left(\frac{\partial P}{\partial \theta} \hat{\varphi} \right) - \frac{\partial T}{\partial \theta} \hat{\varphi} = \boldsymbol{\nabla} \times (A\hat{\varphi}/s) - \omega s \hat{\varphi}, \qquad (4.22)$$

where $s = r \sin \theta$.

This decomposition gives an easy geometrical interpretation of an axisymmetric flow. The first term gives the flow perpendicular to $\hat{\varphi}$ (meridional), the second term gives flow along $\hat{\varphi}$. The meridional circulation is represented by the potential $A = -(\partial P/\partial \theta) r \sin(\theta)$ with the corresponding flow $\mathbf{u}_m = \boldsymbol{\nabla} \times (A\hat{\varphi}/s)$. Angular velocity is $\omega = -\dfrac{1}{s} \dfrac{\partial T}{\partial \theta} = \dfrac{u_\varphi}{r \sin \theta}$.

Maximum values of these two flow scalars (ω & A) are measured in both codes. Parameters together with results from both codes are presented in table (4.5). The relative error varies from 10^{-6} to 10^{-3} showing a very good correspondence.

Figure (4.2) shows fields in the run with $E = 10^{-3}, Ro = 0.0975$. Meridional slices of the flow in the first row of the figure are obtained with the code of Willis et al. (2007), and in the second with that of Hollerbach (2000). It is easy to see that the fields are the same in both calculations.
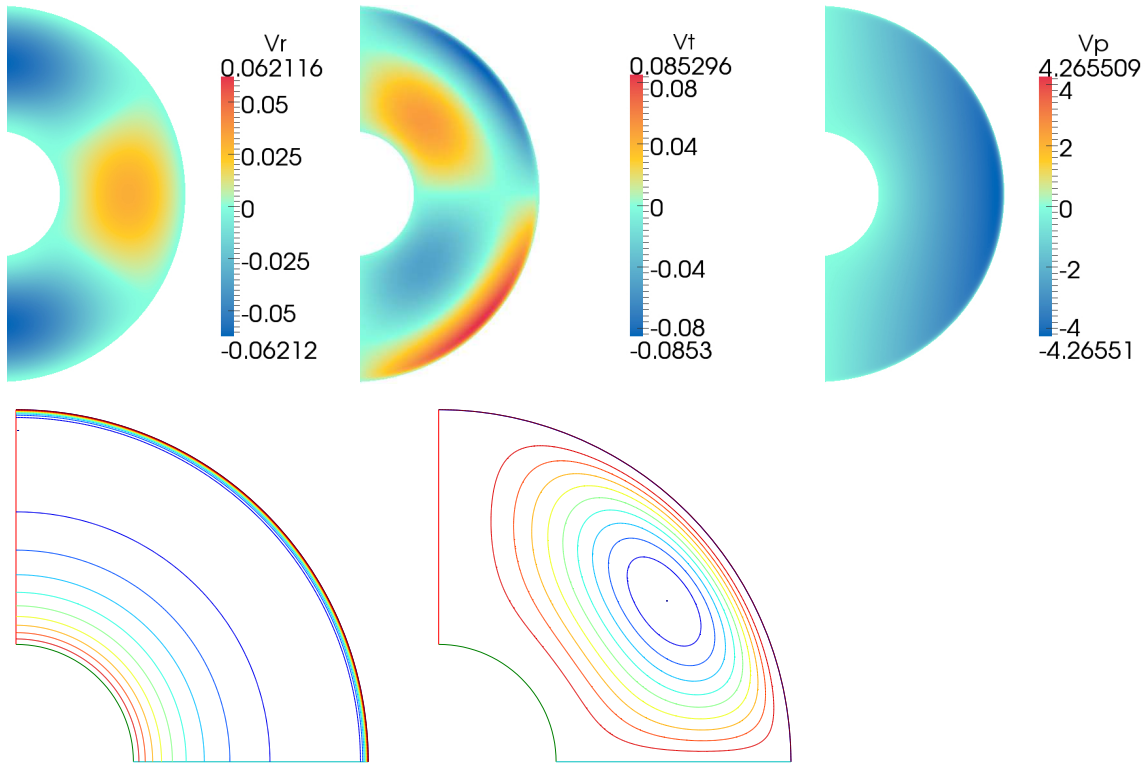
Figure 4.2: *Porous boundaries axisymmetric benchmark case, $E = 10^{-3}$, $Ro = 0.0975$. Meridional sections. 1st row: r, θ, φ components of velocity (code Willis et al., 2007), 2nd row (code Hollerbach, 2000): Angular velocity ω, Meridional circulation A .*

	$|\omega|_{max}$	$|A|_{max}$	N	L	M	E	Ro
Willis	4.4914378773685852	$6.69179162295804701 \cdot 10^{-003}$	96	48	16	10^{-3}	0.09745
Hollerbach	4.4893967684915967	$6.68909757932152627 \cdot 10^{-009}$	100	120	1		
rel.diff.	$4.5 \cdot 10^{-4}$	$4.03 \cdot 10^{-4}$					
Willis	8.6811240001888006	$2.36014334490133246 \cdot 10^{-002}$	96	48	1	10^{-3}	0.05
Hollerbach	8.6811422458514684	$2.36343000407229532 \cdot 10^{-002}$	100	120	1		
rel.diff.	$2.1 \cdot 10^{-6}$	$1.39 \cdot 10^{-3}$					
Willis	121.11849357953959	0.58941050973995213	96	48	1	10^{-3}	-0.001
Hollerbach	121.12584332266553	0.58957436214898873	100	120	1		
rel.diff.	$6.1 \cdot 10^{-5}$	$2.77 \cdot 10^{-4}$					
Willis	2.2029755546499574	$1.63955786129237730 \cdot 10^{-003}$	150	75	1	10^{-3}	0.2
Hollerbach	2.2029668587086988	$1.64046150084152164 \cdot 10^{-003}$	100	120	1		
rel.diff.	$3.9 \cdot 10^{-6}$	$5.5 \cdot 10^{-4}$					
Willis	19.551623771951391	$5.93446908797023998 \cdot 10^{-002}$	150	75	1	10^{-3}	-0.2
Hollerbach	19.508001331749799	$5.93501235334335381 \cdot 10^{-002}$	130	150	1		
rel.diff.	$2.2 \cdot 10^{-3}$	$9.15 \cdot 10^{-5}$					
Willis	4.3782131673540041	$6.36562102391098963 \cdot 10^{-003}$	150	75	1	10^{-3}	0.1
Hollerbach	4.3783378045838788	$6.36979245866310575 \cdot 10^{-003}$	100	120	1		
rel.diff.	$2.8 \cdot 10^{-5}$	$6.6 \cdot 10^{-4}$					
Willis	79.254841381579212	0.29656584283865622	150	75	1	10^{-3}	-0.1
Hollerbach	79.402441860700989	0.29660223913454165	130	150	1		
rel.diff.	$1.86 \cdot 10^{-3}$	$1.2 \cdot 10^{-4}$					
Willis	7.0211861690208313	$1.74414999773662323 \cdot 10^{-002}$	150	75	1	10^{-2}	0.05
Hollerbach	7.0213734850417158	$1.74471885965942972 \cdot 10^{-002}$	130	150	1		
rel.diff.	$2.6 \cdot 10^{-5}$	$3.2 \cdot 10^{-4}$					
Willis	37.688425266082703	0.27738709136641188	132	66	1	10^{-2}	0.1
Hollerbach	37.719307606159106	0.27745878728574014	100	120	1		
rel.diff.	$8.1 \cdot 10^{-4}$	$2.58 \cdot 10^{-4}$					
Willis	3.9293722773746782	$2.49977824115870002 \cdot 10^{-003}$	150	75	1	10^{-2}	0.1
Hollerbach	3.9294792052829783	$2.50080833941145053 \cdot 10^{-003}$	100	120	1		
rel.diff.	$2.7 \cdot 10^{-5}$	$4.11 \cdot 10^{-4}$					
Willis	26.601502634907398	0.16395900431014401	132	66	1	10^{-2}	-0.1
Hollerbach	26.607340986391495	0.16395854254979270	100	120	1		
rel.diff.	$2.19 \cdot 10^{-4}$	$2.8 \cdot 10^{-6}$					
Willis	7.0211861690208313	$1.74414999773662323 \cdot 10^{-002}$	150	75	1	10^{-2}	0.05
Hollerbach	7.0213734850417158	$1.74471885965942972 \cdot 10^{-002}$	100	120	1		
rel.diff.	$2.67 \cdot 10^{-5}$	$3.26 \cdot 10^{-4}$					
Willis	37.688425266082703	0.27738709136641188	132	66	1	10^{-2}	-0.05
Hollerbach	37.719307606159106	0.27745878728574014	100	120	1		
rel.diff.	$8.19 \cdot 10^{-4}$	$2.58 \cdot 10^{-4}$					

Table 4.5: *Benchmarking of injection flow codes: modified versions of Willis et al. (2007) and Hollerbach (2000). Maximum values of two flow scalars: angular velocity ω and meridional circulation A are measured. Numbers N, L, M represent resolutions. E and Ro are Ekman and Rossby numbers correspondingly.*

4.3 Onset of non-axisymmetric instabilities

We would like to find the subspace of Ro and E where non-axisymmetric motions are excited in the spherical shell with porous boundaries. To distinguish whether or not certain harmonics can grow, the linearized equations are sufficient.

The equations are solved in two steps. First, the solution for the $m = 0$ component $\tilde{\mathbf{u}}$ of the velocity deviation is obtained:

$$E\left(\frac{\partial}{\partial t} - \boldsymbol{\nabla}^2\right)\tilde{\mathbf{u}} \quad = \quad Ro\,(\tilde{\mathbf{u}} + \frac{\hat{\mathbf{r}}}{r^2}) \times (\boldsymbol{\nabla} \times \tilde{\mathbf{u}}) - \left(\hat{\mathbf{z}} \times \tilde{\mathbf{u}} + \frac{1}{r^2}\sin\theta\hat{\varphi}\right) - \frac{P_0}{2\Omega u_o r_o}\boldsymbol{\nabla}P. \quad (4.23)$$

Second, $\mathbf{u}$ is decomposed into axisymmetric and non-axisymmetric parts, i.e. $\mathbf{u} = \tilde{\mathbf{u}} + \mathbf{u}'$. For this we rewrite the non-linear term in the Navier-Stokes equation (4.5):

$$(\mathbf{u} + \frac{\hat{\mathbf{r}}}{r^2}) \times (\boldsymbol{\nabla} \times \mathbf{u}) = (\tilde{\mathbf{u}} + \mathbf{u}' + \frac{\hat{\mathbf{r}}}{r^2}) \times (\boldsymbol{\nabla} \times (\tilde{\mathbf{u}} + \mathbf{u}')) =$$
$$= (\tilde{\mathbf{u}} + \frac{\hat{\mathbf{r}}}{r^2}) \times (\boldsymbol{\nabla} \times \tilde{\mathbf{u}}) + \tilde{\mathbf{u}} \times \boldsymbol{\nabla} \times \mathbf{u}' + \mathbf{u}' \times \boldsymbol{\nabla} \times \tilde{\mathbf{u}} + \mathbf{u}' \times \boldsymbol{\nabla} \times \mathbf{u}' + \frac{\hat{\mathbf{r}}}{r^2} \times \boldsymbol{\nabla} \times \mathbf{u}'. \quad (4.24)$$

Linearising means removing the term $\mathbf{u}' \times \boldsymbol{\nabla} \times \mathbf{u}'$. Eventually, the equation for the perturbation for a given $\tilde{\mathbf{u}}$ is :

$$E\left(\frac{\partial}{\partial t} - \boldsymbol{\nabla}^2\right)\mathbf{u}' \quad = \quad \begin{aligned}&Ro\,(\tilde{\mathbf{u}} \times \boldsymbol{\nabla} \times \mathbf{u}' + \mathbf{u}' \times \boldsymbol{\nabla} \times \tilde{\mathbf{u}}) + Ro\,(\frac{\hat{\mathbf{r}}}{r^2}) \times (\boldsymbol{\nabla} \times \mathbf{u}') - \hat{\mathbf{z}} \times \mathbf{u}' - \\ &- \frac{P_0}{2\Omega u_o r_o}\boldsymbol{\nabla}P.\end{aligned} \quad (4.25)$$

This equation is linear in $\mathbf{u}'$ and can be solved independently for each harmonic. We are looking for the Ro-number when the growth rate of a single harmonic is zero, and all the others are decaying. Critical Rossby numbers and harmonic orders m are presented in table (4.6).

m	Ro	$-\lg E$	m	Ro	$-\lg E$	m	Ro	$-\lg E$	m	Ro	$-\lg E$
4	97.17	4.30	5	81.76	3.54	9	37.55	3.57	22	3.23	4.50
4	96.79	4.20	5	78.24	3.53	10	34.18	3.60	24	2.56	4.60
6	89.48	4.10	5	73.76	3.52	11	24.57	3.70	37	1.02	5.00
4	89.62	4.00	5	59.36	3.51	12	18.11	3.80	55	0.38	5.40
4	92.88	3.90	5	56.74	3.52	14	10.69	4.00			
4	99.28	3.80	9	44.65	3.53	15	8.34	4.10			
4	100.83	3.70	9	42.27	3.54	16	6.55	4.20			
5	93.05	3.60	9	40.43	3.55	18	5.16	4.30			

Table 4.6: *Results of the linear calculations for the onset of convection with the porous boundaries. The nomenclature -lg stands for $-\log_{10}$.*

Figure (4.3) shows critical values for the onset of non-axisymmetric flows. It is interesting that there is only a limited interval of the driving parameter Ro where non-axisymmetric
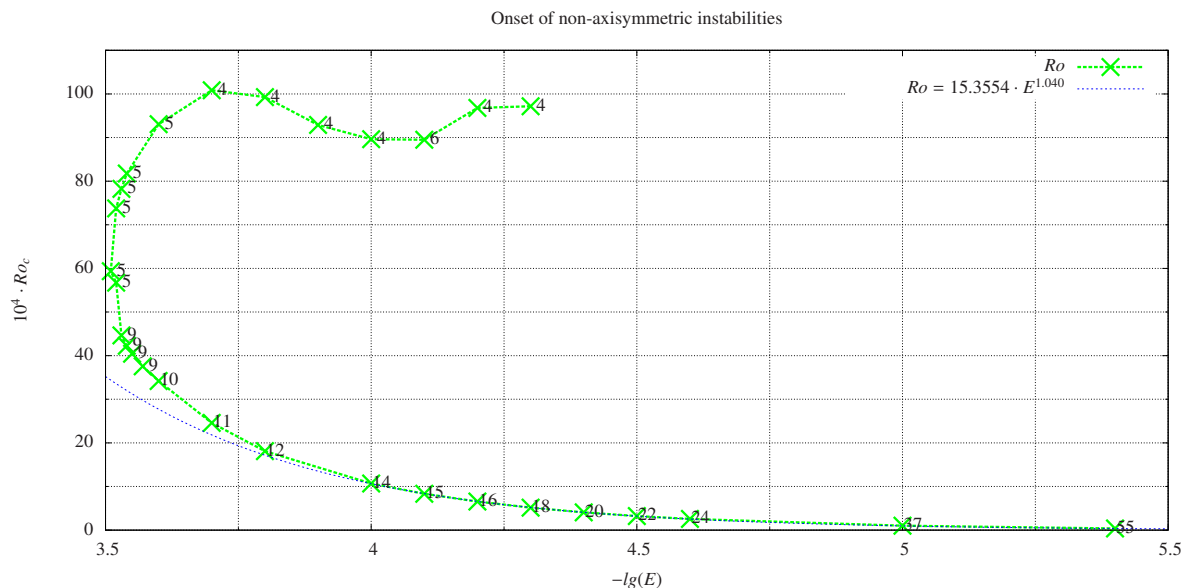
Figure 4.3: *The onset of non-axisymmetric instabilities: Ro vs E. Numbers on the plot signify orders m of the excited harmonics. Non-axisymmetric instabilities are excited in the half-subspace inside and right of the green curve. Shell geometry is defined by $r_i/r_o = 1/3$.*

motions are possible. Counter-intuitively, infinitely large injection of fluid secures axisymmetric motions. But it is understandable since a strong basic flow which is axisymmetric might suppress non-axisymmetric flows.

Figures (4.4) and (4.5) show dependencies of the order m of the critical harmonic on the Ekman number E and Rossby number Ro correspondingly. Only solutions from the bottom part of the curve of figure (4.3) are included there. Interestingly, the harmonic order m is proportional to the power of Ekman number $E^{-0.43}$ (fig.4.4). In the same region of the critical curve the Rossby number Ro is roughly proportional to the Ekman number E (fig.4.3).
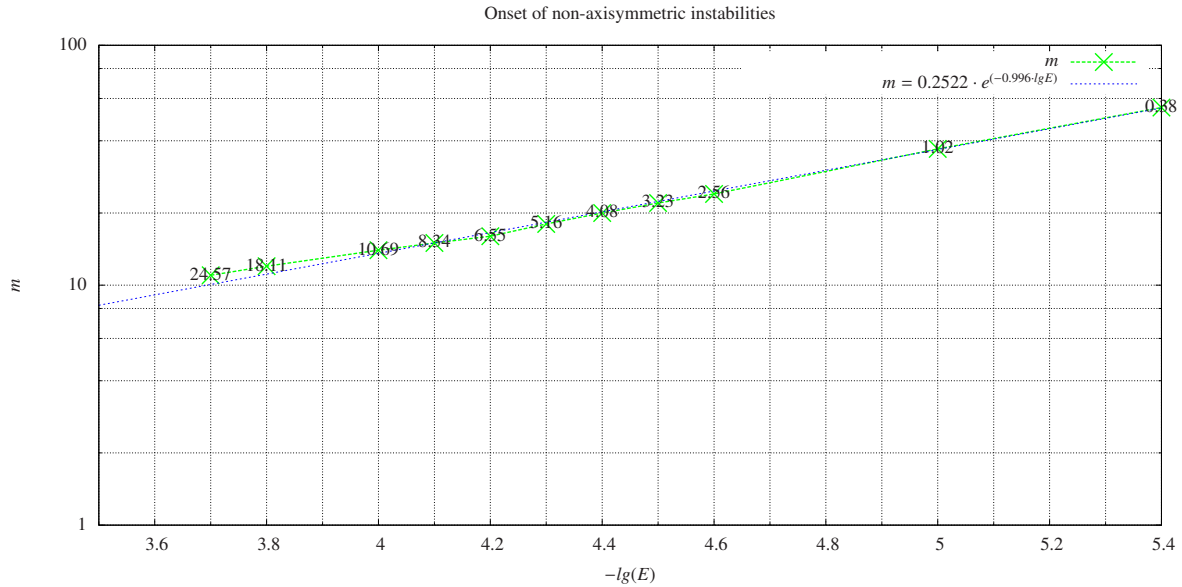
Figure 4.4: *The onset of non-axisymmetric instabilities: harmonic order m vs Ekman number E. Numbers on the plot show values of Ro when the first harmonic other than m = 0 is excited.*
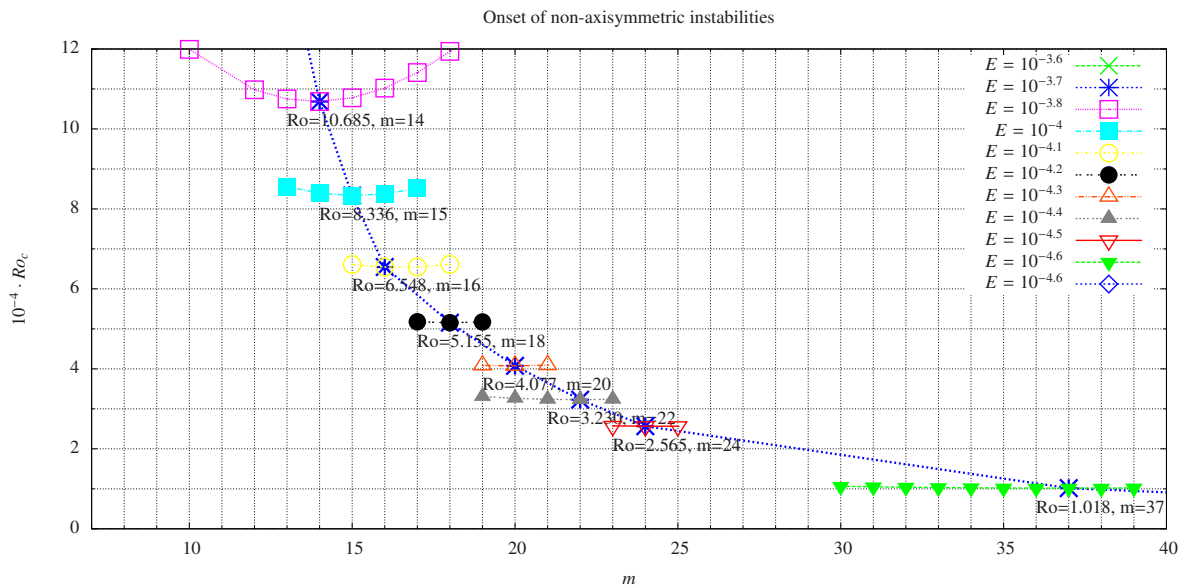
Figure 4.5: *The onset of non-axisymmetric instabilities: Rossby number Ro vs. order m of the first excited harmonic. Rossby numbers at which neighbouring harmonics have zero growth rate are also shown.*

4.4   Search for a dynamo

In the following two sections we will separately consider simulations with the axisymmetric velocity field (outside of the region enclosed by the blue curve in fig.4.6) and with velocity field where components *m* > 0 are excited.
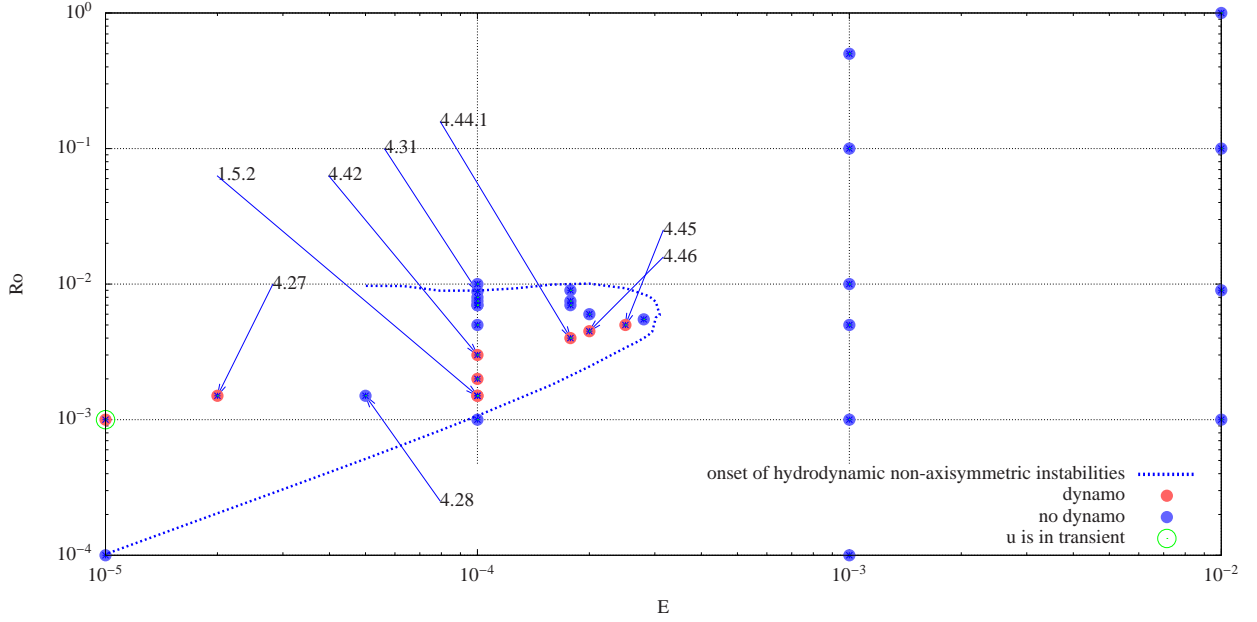
Figure 4.6: *Parametric study of the dynamo action. Numbers on the plot correspond to the names of the runs in the table. Initially* $\mathbf{u} = 0$, $\mathbf{B}$ *has energy in all harmonics.*

4.4.1 Kinematic dynamos with the axisymmetric velocity field

The Cowling's theorem prohibits existence of a self-sustained axisymmetric magnetic field, but doesn't have restrictions on the simplicity of the velocity field. First we investigate the parameter regime where non-axisymmetric components are hydrodynamically forbidden. Can an axisymmetric velocity field maintain dynamo action?

Supercritical dynamos are those which can grow from a tiny seed magnetic field (i.e. those which are linearly unstable, as opposed to subcritical dynamos, where non-linearities are important). Initially, when the magnetic field is small, the Lorentz force can be neglected preventing the feedback of the magnetic field on the velocity field. If growing modes of the magnetic field are absent, it is sufficient to say, that the supercritical dynamo is impossible. The advantage of the kinematic regime is that we don't need to worry about the amplitude of the initial magnetic field, it just needs to be distinct from zero.

Equations for the kinematic dynamo action (eq.4.11 without Lorentz force) are:

$$
\begin{cases}
E\left(\dfrac{\partial}{\partial t} - \boldsymbol{\nabla}^2\right)\mathbf{u} &= Ro\,(\mathbf{u} + \dfrac{\hat{\mathbf{r}}}{r^2}) \times (\boldsymbol{\nabla} \times \mathbf{u}) - \left(\hat{\mathbf{z}} \times \mathbf{u} + \dfrac{1}{r^2}\sin\theta\hat{\varphi}\right) - \dfrac{P_0}{2\Omega u_o r_o}\boldsymbol{\nabla}P, \\
\left(Pr_m\dfrac{\partial}{\partial t} - \boldsymbol{\nabla}^2\right)\mathbf{B} &= R_m\boldsymbol{\nabla} \times ((\mathbf{u} + \dfrac{\hat{\mathbf{r}}}{r^2}) \times \mathbf{B})
\end{cases}
$$
$$
R_m = Ro \cdot Pr_m/E
$$

(4.26)

The feature of an axisymmetric velocity field is that the m-modes of the magnetic field are decoupled. When $\mathbf{B} = \widetilde{\mathbf{B}}(\mathbf{r}, \theta)e^{im\varphi}$ and $\mathbf{u} = \mathbf{u}(\mathbf{r}, \theta)$, the non-linear term in the equation of the

induction is :

$$\mathbf{\nabla} \times ((\mathbf{u} + \frac{\hat{\mathbf{r}}}{r^2}) \times (\widetilde{\mathbf{B}}e^{im\varphi})) = e^{im\varphi} \left(\frac{im}{r \sin \theta} \hat{\varphi} + \mathbf{\nabla} \right) \times \left((\mathbf{u} + \frac{\hat{\mathbf{r}}}{r^2}) \times \widetilde{\mathbf{B}} \right). \quad (4.27)$$

Thus, the induction equation can be written for each m-mode separately.

Name	$E \cdot 10^{-4}$	$Ro \cdot 10^{-4}$	Pr_m	N	L	M	Rm	$E_{mag} \uparrow$	E_{kin}^{const}	F_{Lor}
4.05.r2.mhd	0.1	1	10.000	300	150	30	100.0	0	1	0
4.08.Rm400	1.0	10	40.000	170	86	20	400.0	0	1	0
4.09.Rm300	100.0	90	330.000	100	40	30	297.0	0	1	0
4.10.Rm300	100.0	1000	30.000	100	40	20	300.0	0	1	0
4.11.Rm300	10.0	1000	3.000	100	35	20	300.0	0	1	0
4.12.Rm300	10.0	5000	0.600	100	50	20	300.0	0	1	0
4.13.Rm300	10.0	100	30.000	100	50	20	300.0	0	1	0
4.14.Rm300	10.0	50	60.000	100	45	20	300.0	0	1	0
4.18.Rm300	100.0	10	3000.000	100	50	20	300.0	0	1	0
21h.m20.mhd	0.1	10	1.000	300	150	20	100.0	1	0	0
4.22	10.0	1	3000.000	150	76	20	300.0	0	1	0
4.23	10.0	10	300.000	100	50	20	300.0	0	1	0
4.24	1.0	100	3.000	180	90	30	300.0	0	1	0
4.26	100.0	10000	3.000	100	50	20	300.0	0	1	0
4.27	0.2	15	1.334	300	150	30	100.0	1	0	0
4.28	0.5	15	3.335	300	150	30	100.0	0	0	0
PorAbove1.5.2	1.0	15	5.000	300	150	150	75.0	1	1	1
PorAbove4.30	1.8	90	6.000	180	90	30	303.7	0	1	1
PorAbove4.31	1.0	88	3.500	180	90	30	308.0	0	1	1
PorAbove4.32	1.0	80	3.500	180	90	30	280.0	0	1	1
PorAbove4.33	1.0	70	4.300	180	90	30	301.0	0	1	1
PorAbove4.34	1.0	70	4.300	180	90	90	301.0	0	1	1
PorAbove4.36	1.0	75	2.000	180	90	90	150.0	0	1	1
PorAbove4.38	1.8	75	6.000	180	90	90	253.1	0	1	1
PorAbove4.40	1.8	70	7.700	200	100	100	303.1	0	1	1
PorAbove4.41	1.0	50	6.000	180	90	46	300.0	0	1	1
PorAbove4.42	1.0	30	10.000	180	90	46	300.0	1	1	1
PorAbove4.43	1.0	20	15.000	180	90	46	300.0	1	1	1
PorAbove4.44.1	1.8	40	13.000	200	100	70	292.4	1	1	1
PorAbove4.45	2.5	50	15.000	200	100	70	300.0	1	1	1
PorAbove4.46	2.0	45	13.400	200	100	70	301.5	1	1	1
PorAbove4.47	2.0	60	10.000	200	100	70	300.0	0	1	1
PorAbove4.48	2.8	55	17.000	200	100	70	333.9	0	1	1

Table 4.7: *Simulations with the purpose to check if a magnetic field can be produced by the fluid motions in the chosen parameter regime. Final state in a run is described in columns named $E_{mag} \uparrow$ and E_{kin}^{const}. Notation:*
if $E_{mag} \uparrow = 1$ magnetic field grows or steady non-zero (dynamo),
if $E_{kin}^{const} = 1$ kinetic energy is steady,
if $F_{Lor} = 1$ the Lorentz force is turned on.

The study in the parameter region where only axisymmetric velocities are possible is presented in fig.(4.6). Calculations outside of the area enclosed by the dashed curve have only axisymmetric velocity components . We could not find any dynamo there, although the fact that a dynamo can not exist when the injection produces only axisymmetric flow can not be excluded completely.

4.4.2   Dynamos with non-axisymmetric velocity field

It is fair to suppose that the magnetic field may more likely be self-sustained with a non-axisymmetric velocity. After the linear studies in the section (4.3) we know where this happens. Simulations in the table (4.7) are done both in kinematic regime (where it is easy to spot growing magnetic field regardless to the choice of the initial field) and with Lorentz force turned on (to find if the magnetic field saturates at non-zero level). Large R_m increases the probability for the magnetic field to stay in the simulation, although too high values are difficult to reach experimentally. Results of the calculation are plotted in fig.(4.6).

4.4.2.1   Case "PorAbove4.45"

The run that we denote by "PorAbove4.45" has parameters listed in the table (4.8).

E	Ro	Pr_m	N	L	M
$2.5 \cdot 10^{-4}$	$50 \cdot 10^{-4}$	15	200	100	70

Table 4.8*: Parameters of the run called "PorAbove4.45". N radial points, L harmonic degrees, M orders represent resolution. Lorentz force is turned on in the simulation.*

The total kinetic energy is equilibrated at the level 3208.5. The magnetic field was still evolving when the simulation has been stopped. At the last available state the magnetic energy composes a tiny proportion of the kinetic energy being 0.85 (see fig. 4.7). Magnetic energy outweighs kinetic only at smaller scales with spherical harmonic degree $l > 25$.

Energy spectra and time behaviour of individual magnetic harmonics are presented in figures (4.8) and (4.7) respectively. Excited harmonics are $m = 0$ and multiples of $m = 8$. Non-zero magnetic harmonics are also discrete and are listed below.

Non-zero velocity harmonic order	Non-zero magnetic harmonic order.
$m = 0, 8n$	$m \pm 1$.

Velocity is westward through the entire shell. The westward speed is maximal in the torus around the inner core in the middle of the shell at low latitudes (see fig.4.9). Two convecting cells are adjoint to the the surface causing upwelling in the polar regions and downwelling in the equatorial. These two convecting cells produce converging flows at equator beneath the
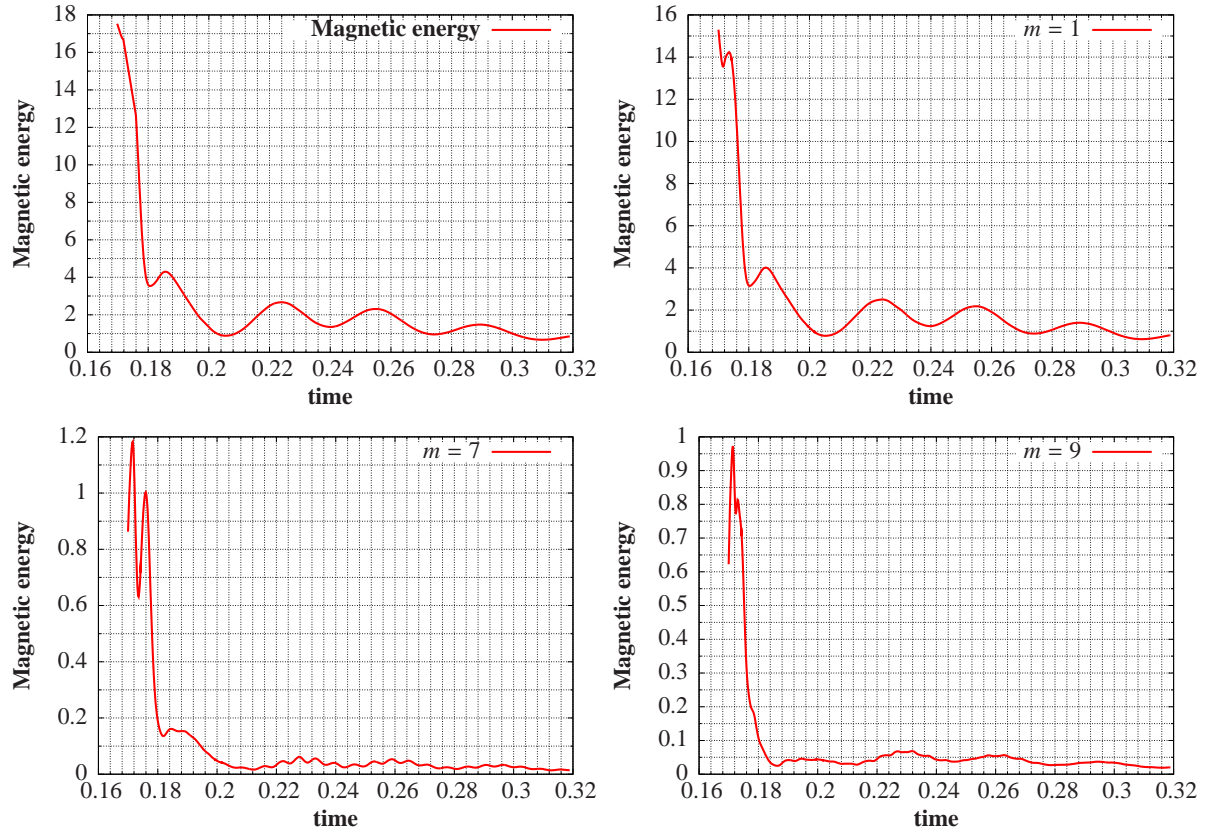
Figure 4.7*: Run "PorAbove4.45". Time evolution of the magnetic energy and its spectral components.*
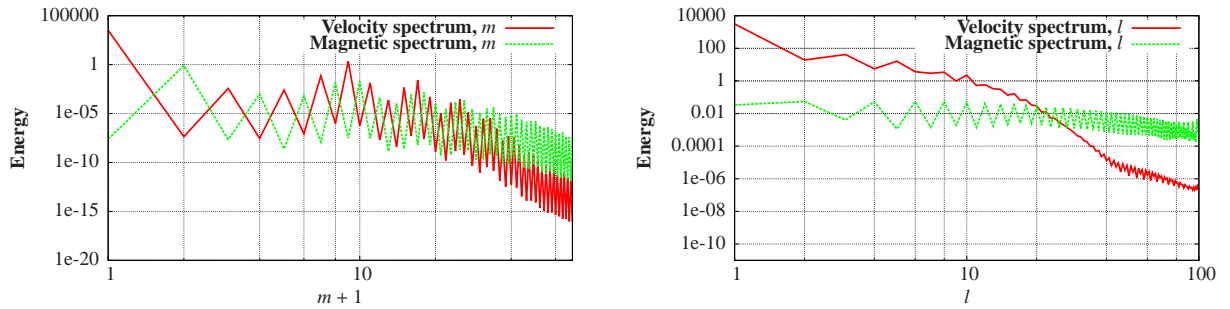
Figure 4.8*: Run "PorAbove4.45". Magnetic and kinetic energy spectra. Only $m = 0$ and $m = 8n$ kinetic energy components are $O(1)$.*

surface. The strongest magnetic field in the simulation is concentrated also in the equatorial region close to the outer boundary (see fig.4.10).

In the simulation magnetic field stays for relatively long time and even undergoes periods of growth, unlike in the simulations we mark as non-dynamos. But it is hard to say if the magnetic field stays if we integrate longer. In summary, a small magnetic energy and non-geophysical field geometry can't promise usefulness of this regime for experimental purposes.
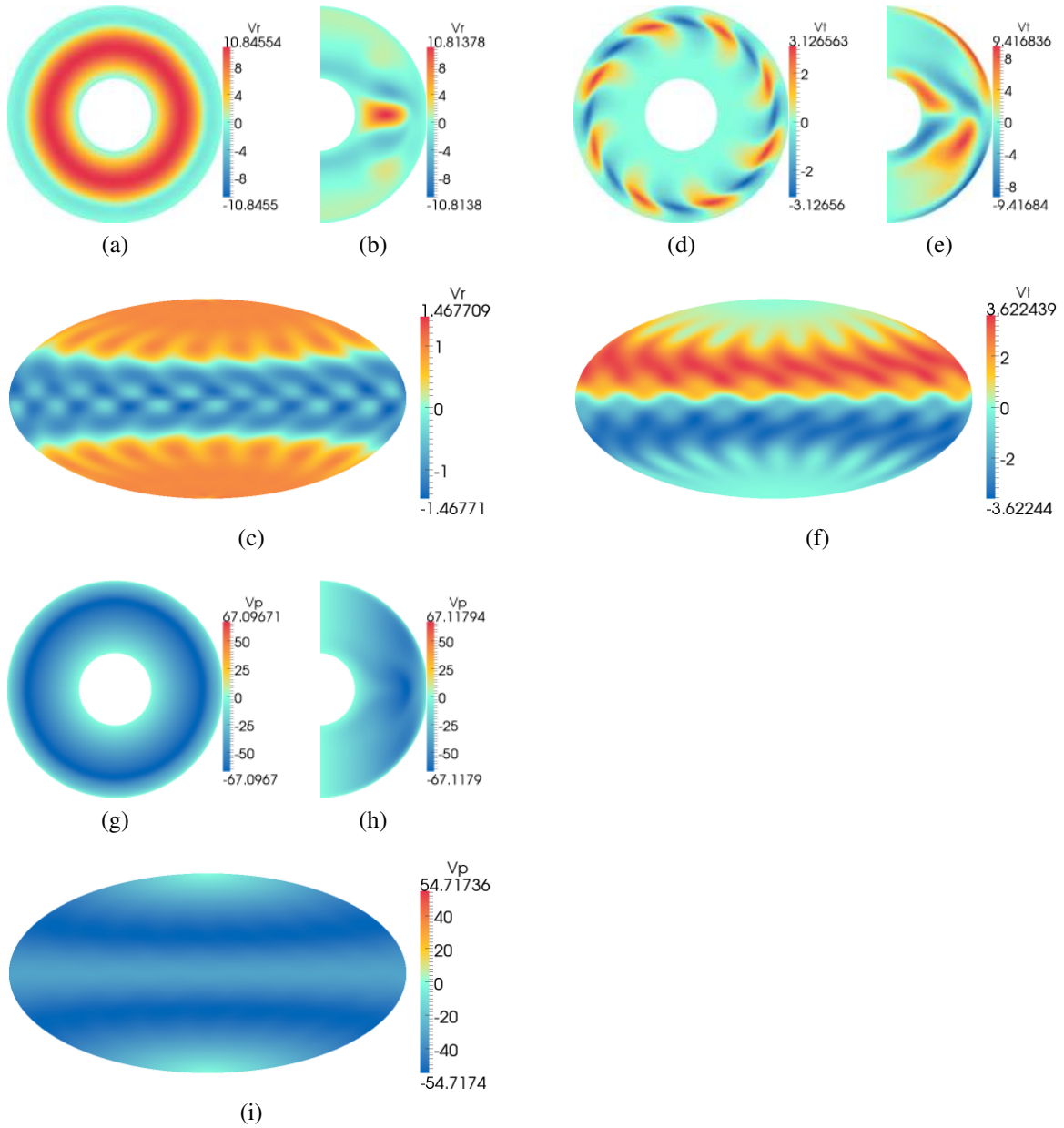
Figure 4.9: *Run "PorAbove4.45". Parameters are listed in the table (4.8). Velocity deviation field* **u**. *Equatorial slices: (a), (d), (g). Meridional slices: (b), (e), (h). Hammer projections of the spherical surface which is slightly below the surface: (c), (f), (i). Subscripts "$_p$" and "$_t$" denote φ and θ components respectively.*
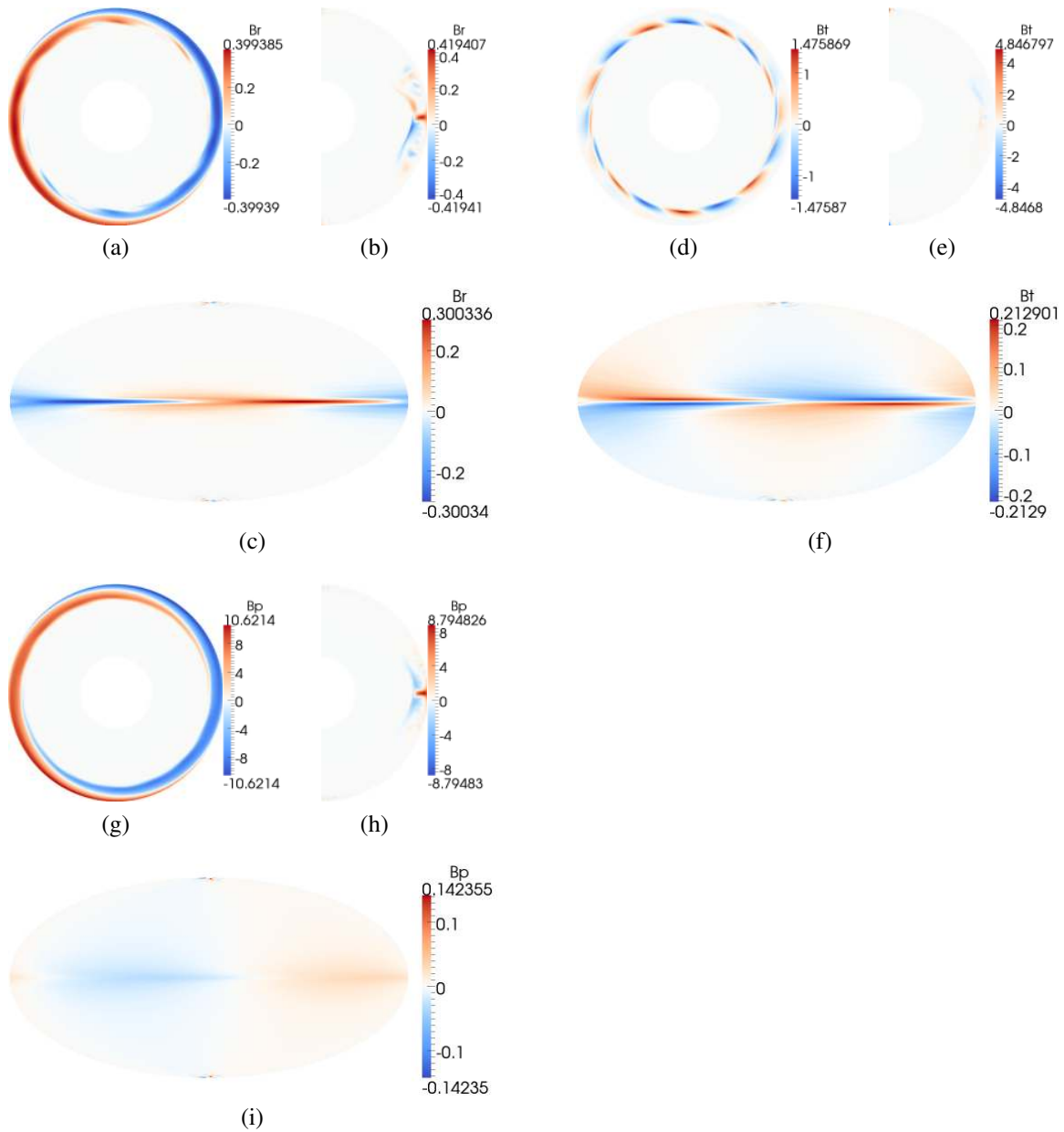
Figure 4.10: *Run "PorAbove4.45". Parameters are listed in the table (4.8). Magnetic field* **B**. *Equatorial slices: (a), (d), (g). Meridional slices: (b), (e), (h). Hammer projections of the outer boundary: (c), (f), (i). Subscripts "$_p$" and "$_t$" denote φ and θ components respectively.*

4.4.2.2 Case "PorAbove4.46"

The run that we denote by "PorAbove4.46" has parameters listed in the table (4.9). In comparison with the simulation discussed in the section (4.4.2.1) both Ekman number E and Rossby number Ro are decreased. This means that the regime is further away from the boundary in the parametric space $Ro - E$ beyond which only axisymmetric velocities are self-excited (see fig. 4.6).

E	Ro	Pr_m	N	L	M
$2.0 \cdot 10^{-4}$	$45 \cdot 10^{-4}$	13.4	200	100	70

Table 4.9: *Parameters of the run called "PorAbove4.46". N radial points, L harmonic degrees, M orders represent resolution. Lorentz force is turned on in the simulation.*

The total kinetic energy is equilibrated at the level 4040.3. In the end of the simulation magnetic energy is 8.6 being a tiny proportion of the kinetic energy (see fig.4.11). However,
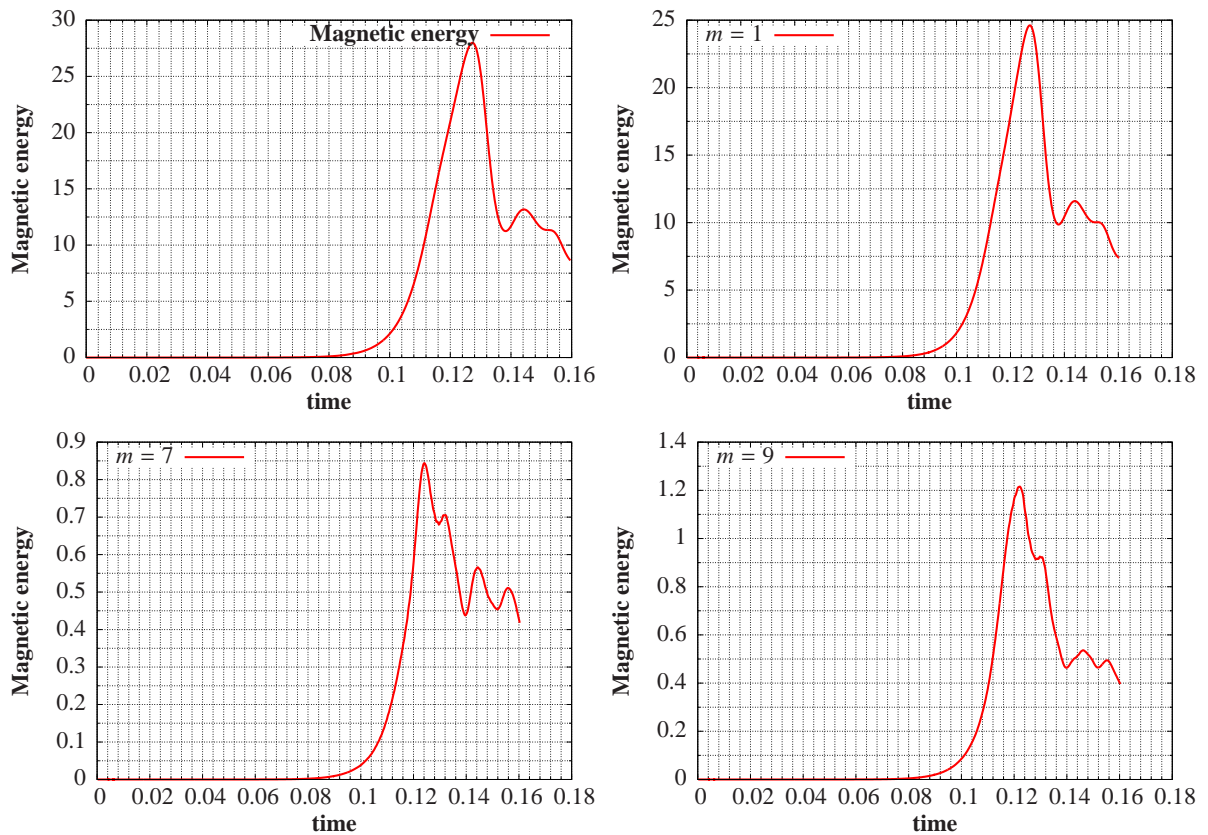
Figure 4.11: *Run "PorAbove4.46". Time evolution of the magnetic energy and its spectral components.*

the magnetic energy is 10 times larger than in the simulation "PorAbove4.45" (sec. 4.4.2.1). Magnetic spectral energy components are larger than kinetic at harmonic degrees $l > 20$. Energy spectra and time behaviour of individual magnetic harmonics are presented in figures (4.12) and (4.11) respectively.
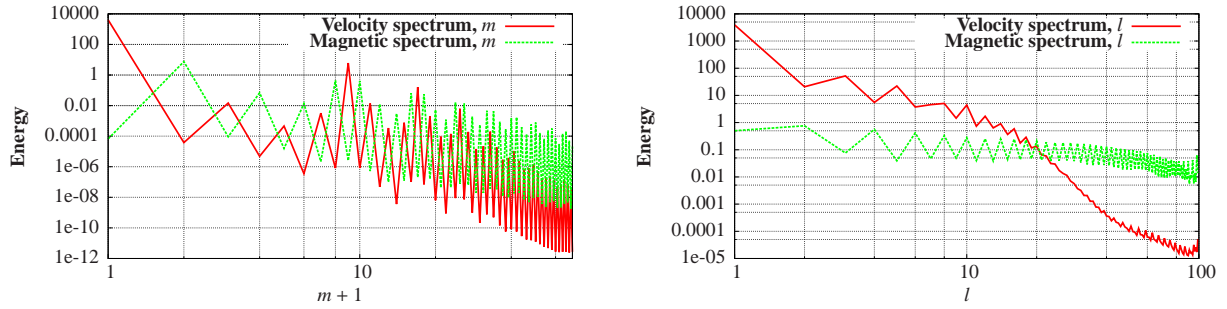
Figure 4.12: *Run "PorAbove4.46". Magnetic and kinetic energy spectra. Only $m = 0$ and $m = 8n$ kinetic energy components are $O(1)$.*

The velocity field resembles field of the run "PorAbove4.45" (sec. 4.4.2.1) since parameters are close. Non-zero harmonics are the same as in "PorAbove4.45" and are listed below.

Non-zero velocity harmonic order	Non-zero magnetic harmonic order.
$m = 0, 8n$	$m \pm 1$.

Velocity is very similar to the case "PorAbove4.45" (sec. 4.4.2.1): longitudinal velocity is westward through the entire shell and very axisymmetric, two symmetric about equator convective cells are present on the surface. The latitudinal velocity beneath the outer boundary is slightly different in comparison with the case "PorAbove4.45": additionally $m = 8$ components of the poleward flow appear at middle latitudes. The strongest magnetic field is again close to equator beneath the outer shell's boundary.

As in case "PorAbove4.45" (sec. 4.4.2.1) it is hard to say whether the magnetic field stays self-sustained forever in this regime. Magnetic field is small and non-geophysical, but it is order of magnitude larger than in the case "PorAbove4.45" with larger E and Ro.
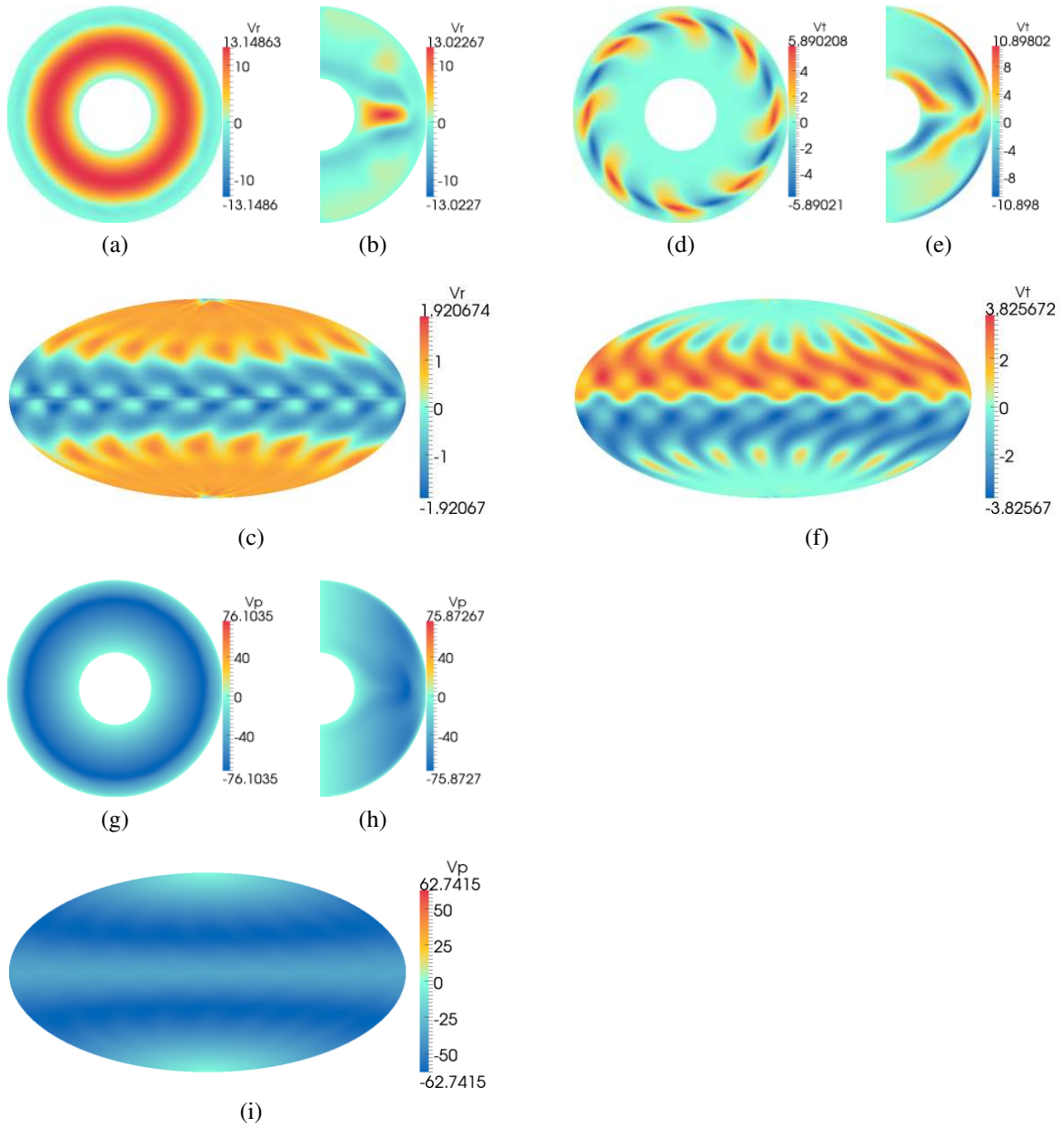
Figure 4.13: *Run "PorAbove4.46". Parameters are listed in the table (4.9). Velocity deviation field* **u**. *Equatorial slices: (a), (d), (g). Meridional slices: (b), (e), (h). Hammer projections of the spherical surface which is slightly below the surface: (c), (f), (i). Subscripts "$_p$" and "$_t$" denote φ and θ components respectively.*
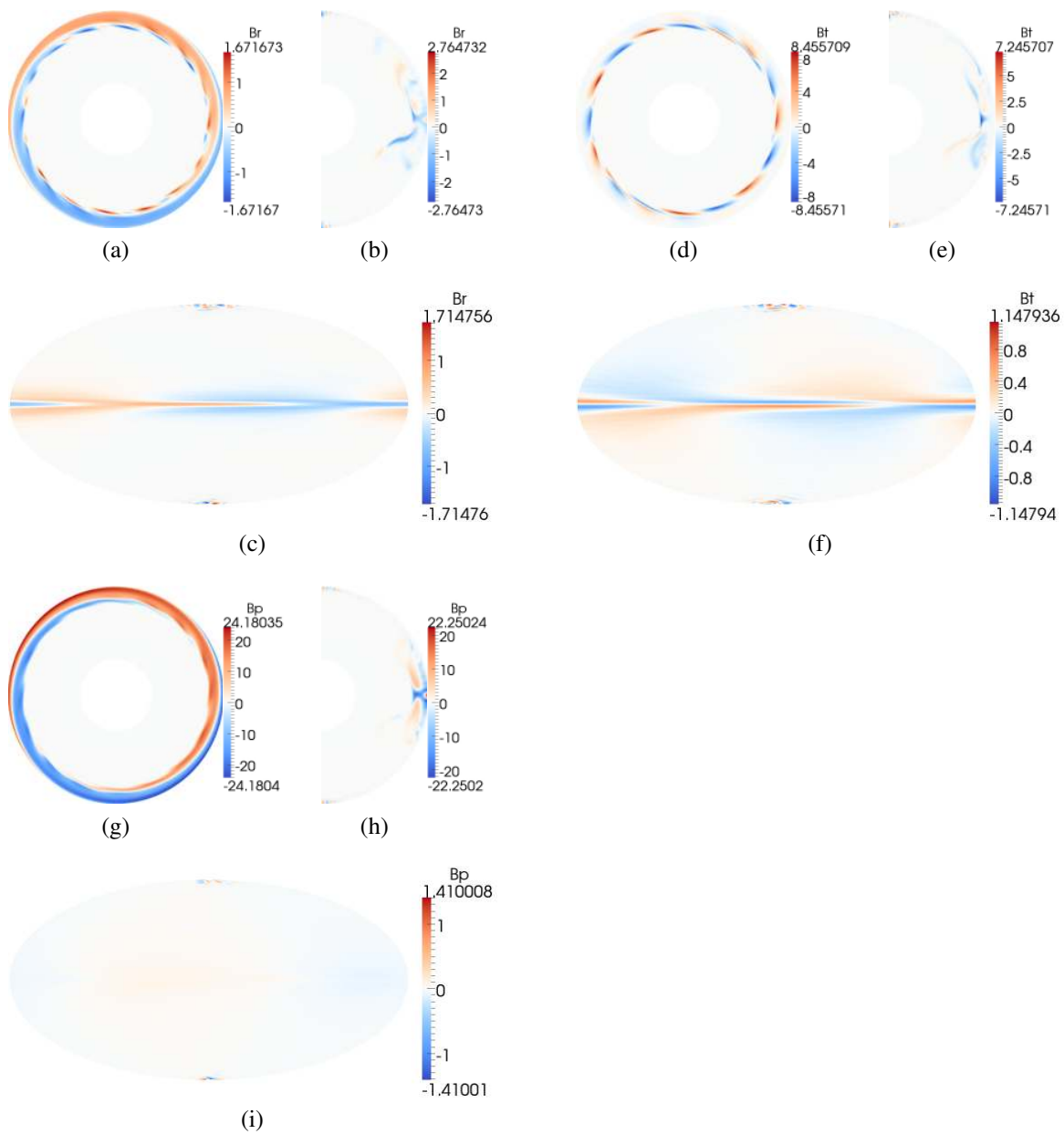
Figure 4.14: *Run "PorAbove4.46". Parameters are listed in the table (4.9). Magnetic field* **B**. *Equatorial slices: (a), (d), (g). Meridional slices: (b), (e), (h). Hammer projections of the outer boundary : (c), (f), (i). Subscripts "$_p$" and "$_t$" denote φ and θ components respectively.*

4.4.2.3   Case "PorAbove4.44.1"

The run that we denote by "PorAbove4.44.1" has parameters listed in the table (4.10). In comparison with the simulations "PorAbove4.45" and "PorAbove4.46" (sections 4.4.2.1 and 4.4.2.2) a lower Ekman number E and Rossby number Ro are chosen. From hydrodynamic considerations the flow is expected to be non-axisymmetric (see fig. 4.6).

E	Ro	Pr_m	N	L	M
$1.8 \cdot 10^{-4}$	$40 \cdot 10^{-4}$	13.0	200	100	70

Table 4.10: *Parameters of the run called "PorAbove4.44.1". N radial points, L harmonic degrees, M orders represent resolution. Lorentz force is turned on in the simulation.*

The total kinetic energy is equilibrated at the level 4850.5. Magnetic field was still evolving when the simulation has been stopped. At the last available state magnetic energy has the value 34.1 (see fig.4.15). Magnetic spectral energy components are larger than kinetic at
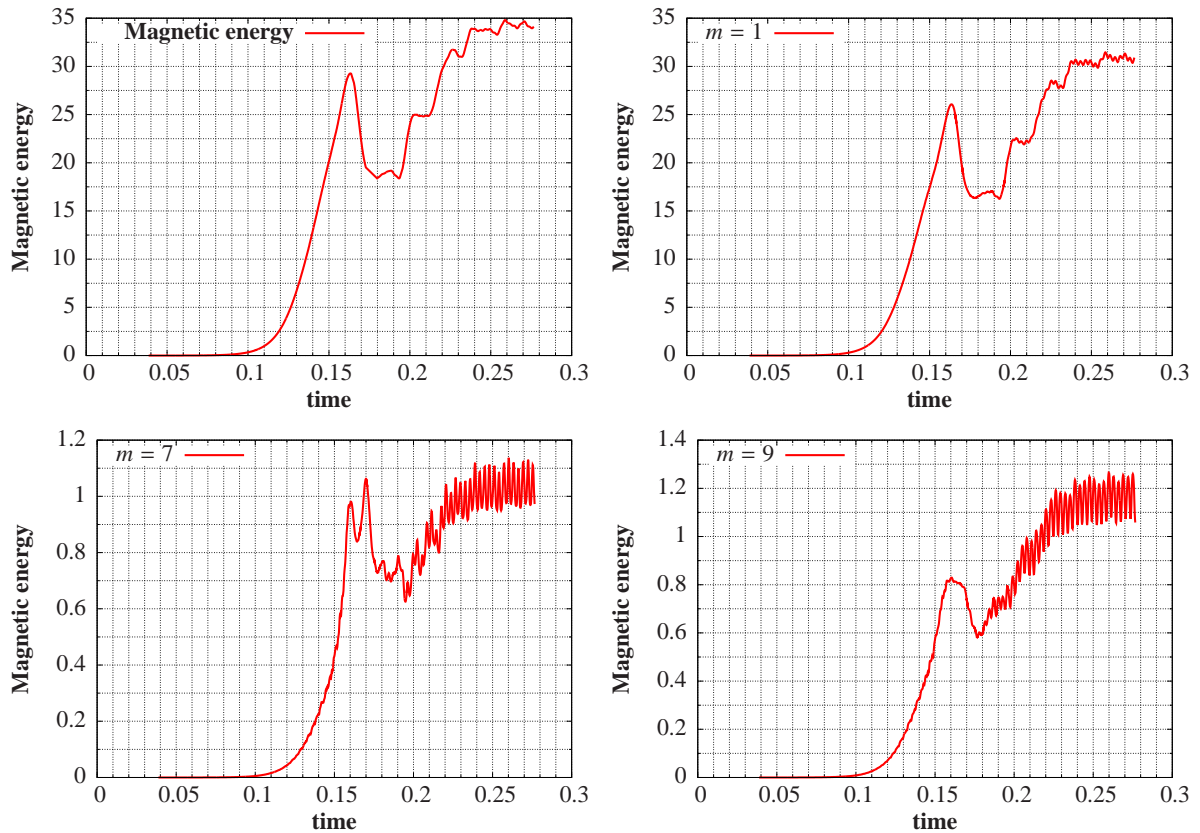
Figure 4.15: *Run "PorAbove4.44.1". Time evolution of the magnetic energy and its spectral components.*

harmonic degrees $l > 15$.

Energy spectra and time behaviour of individual magnetic harmonics are presented in figures (4.16) and (4.15) respectively.
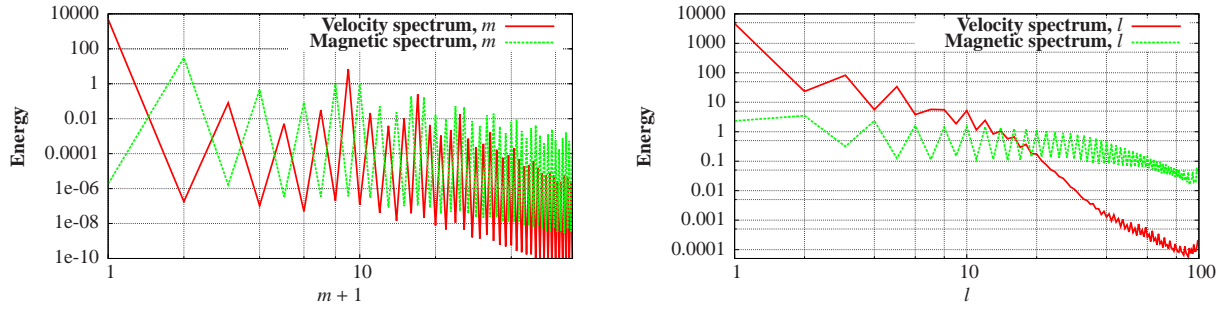
Figure 4.16: *Run "PorAbove4.44.1". Magnetic and kinetic energy spectra. Only $m = 0$ and $m = 8n$ kinetic energy components are $O(1)$.*

The geometry of the velocity and magnetic fields (see fig.4.18 and fig.4.17) resembles corresponding fields of runs "PorAbove4.45" and "PorAbove4.46" (sections 4.4.2.1 and 4.4.2.2). Non-zero harmonics are the same as in these runs and are listed below.

Non-zero velocity harmonics	Non-zero magnetic harmonics.
$m = 0, 8n$	$m \pm 1$.

At the last moments of the simulation the time derivative of the magnetic field is statistically close to zero giving a hope that we see a proper dynamo. Though, the magnetic field is concentrated at low latitudes beneath the outer boundary and doesn't resemble a geophysical field (see fig.4.18). The magnetic energy is small in comparison with the kinetic energy, but it is an order of magnitude larger than in the previous simulation "PorAbove4.46" and two orders of magnitude larger than in "PorAbove4.45" (sections 4.4.2.2 and 4.4.2.1).
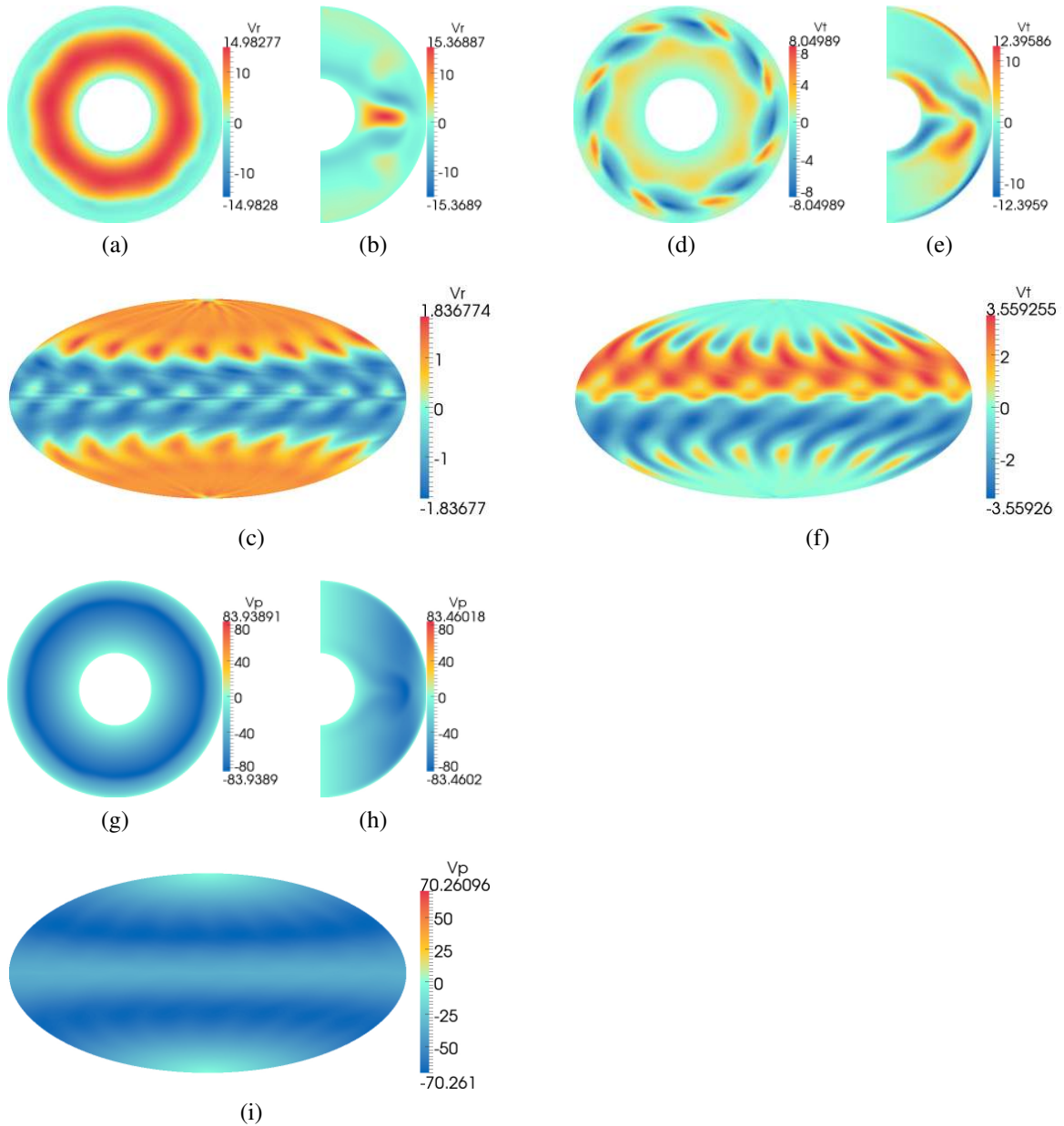
Figure 4.17: *Run "PorAbove4.44.1". Parameters are listed in the table (4.10). Velocity deviation field* **u**. *Equatorial slices: (a), (d), (g). Meridional slices: (b), (e), (h). Hammer projections of the spherical surface which is slightly below the surface: (c), (f), (i). Subscripts "$_p$" and "$_t$" denote φ and θ components respectively.*
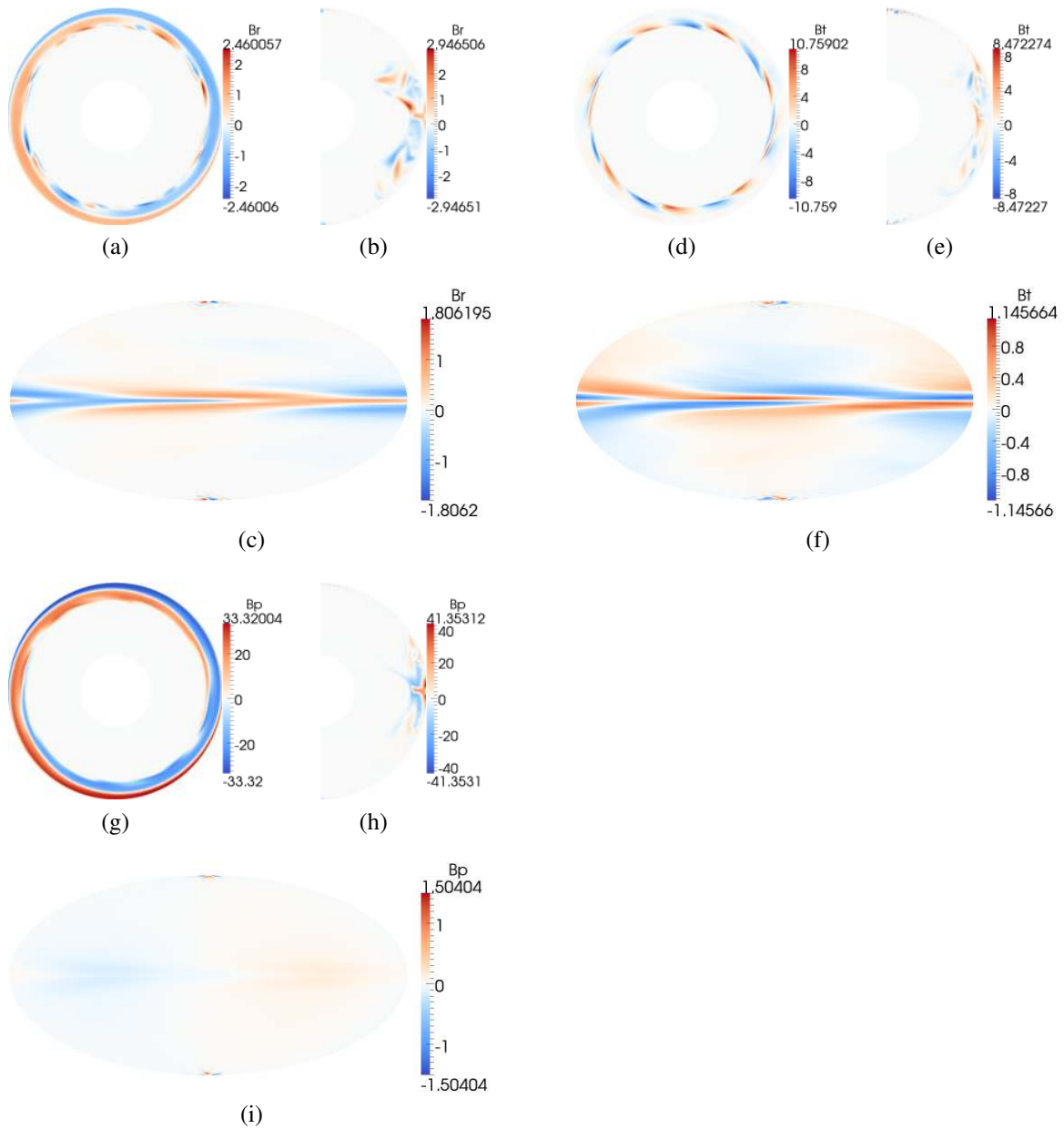
Figure 4.18: *Run "PorAbove4.44.1". Parameters are listed in the table (4.10). Magnetic field* **B**. *Equatorial slices: (a), (d), (g). Meridional slices: (b), (e), (h). Hammer projections of the outer boundary : (c), (f), (i). Subscripts "$_p$" and "$_t$" denote φ and θ components respectively.*

4.4.2.4 Case "PorAbove4.42"

The run that we denote by "PorAbove4.42" has parameters listed in the table (4.11). We moved into the regime with lower Ekman number E and Rossby number Ro in comparison with previous cases described in sections (4.4.2.1) – (4.4.2.3).

E	Ro	Pr_m	N	L	M
$1.0 \cdot 10^{-4}$	$30 \cdot 10^{-4}$	10.0	180	90	46

Table 4.11: *Parameters of the run called "PorAbove4.42". N radial points, L harmonic degrees, M orders represent resolution. Lorentz force is turned on in the simulation.*

The total kinetic energy is at the level 9289.7 at the last moment of the run. The magnetic field was still evolving with a tendency to grow when the simulation has been stopped. At the last available state magnetic energy has the value 0.45 (see fig.4.19). Surprisingly, magnetic
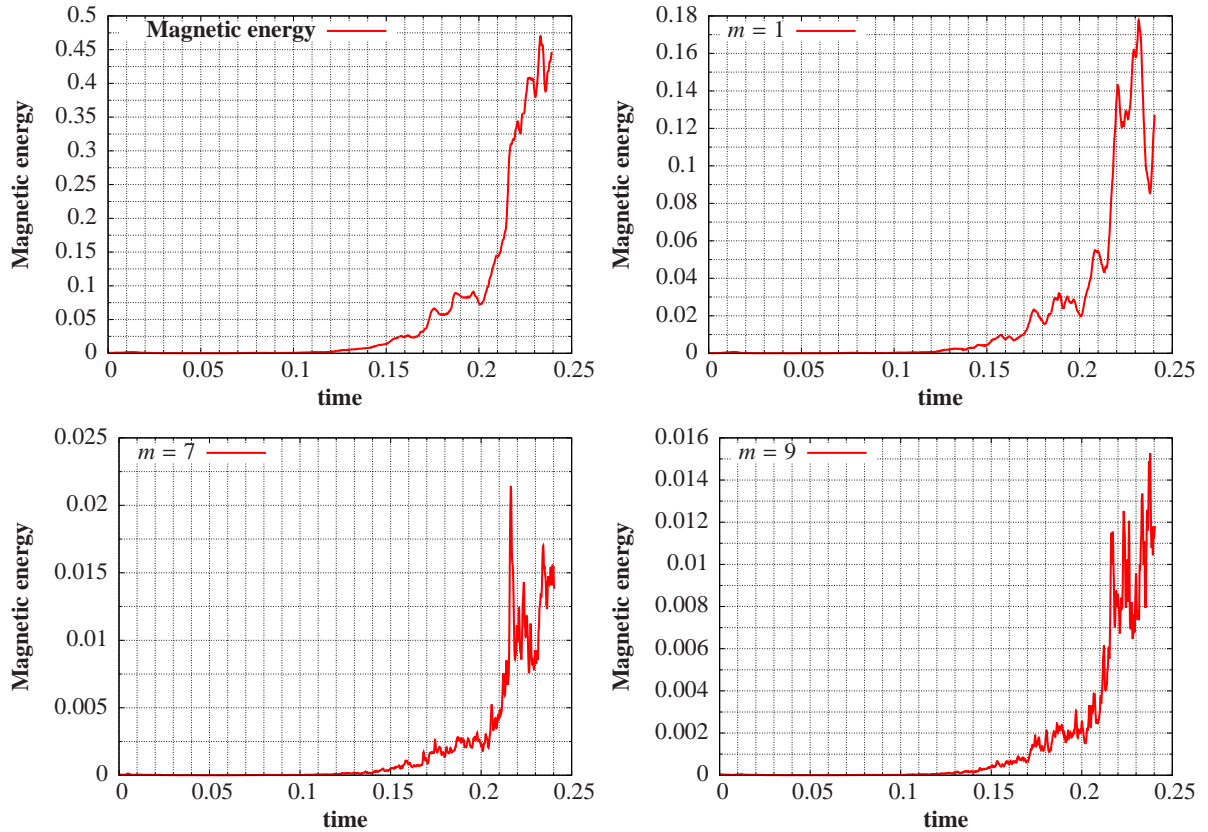
Figure 4.19: *Run "PorAbove4.42". Time evolution of the magnetic energy and its spectral components.*

field is much weaker than in the case "PorAbove4.44.1" with only slightly higher values of E, Ra and Pr_m.

In comparison with the runs in the previous sections the velocity field has less regular structure although it has similarities to those runs (sections 4.4.2.1 - 4.4.2.3). The longitudinal velocity is westward through the entire shell as in previous sections, but it contains significant non-axisymmetric components (see fig.4.21). The largest magnetic field concentrates outside

the tangent cylinder with the strongest toroidal field close to the outer boundary at low latitudes (see fig.4.22). Although in comparison with the runs in sections (4.4.2.1) - (4.4.2.3) the magnetic field is more evenly distributed throughout spherical surfaces.

Energy spectra and time behaviour of individual magnetic harmonics are presented in figures (4.20) and (4.19) respectively. The main difference with previously discussed simula-
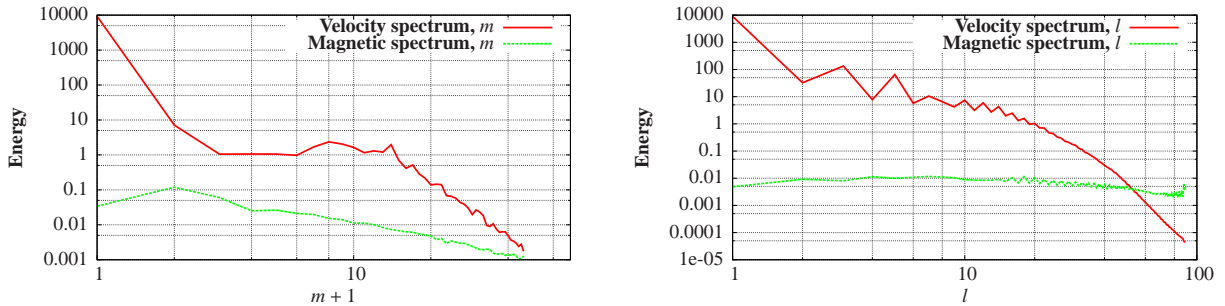
Figure 4.20: *Run "PorAbove4.42". Magnetic and kinetic energy spectra.*

tions is in continuous velocity and magnetic spectra. Magnetic spectral energy components are larger than kinetic at harmonic degrees $l > 53$. The magnetic energy spectrum in harmonic orders is everywhere below the kinetic spectrum.
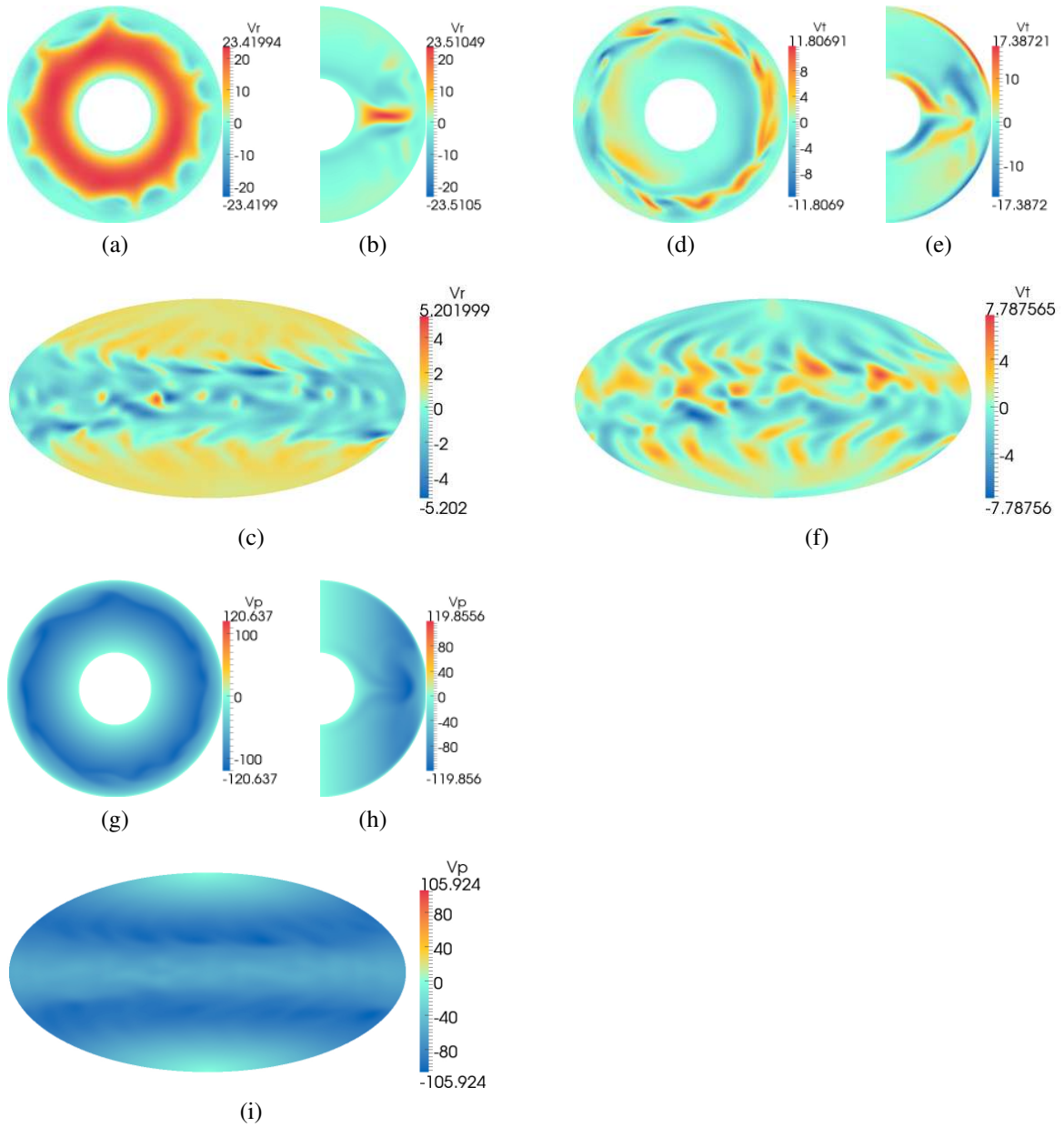
Figure 4.21: *Run "PorAbove4.42". Parameters are listed in the table (4.11). Velocity deviation field* **u**. *Equatorial slices: (a), (d), (g). Meridional slices: (b), (e), (h). Hammer projections of the spherical surface which is slightly below the surface: (c), (f), (i). Subscripts "$_p$" and "$_t$" denote φ and θ components respectively.*
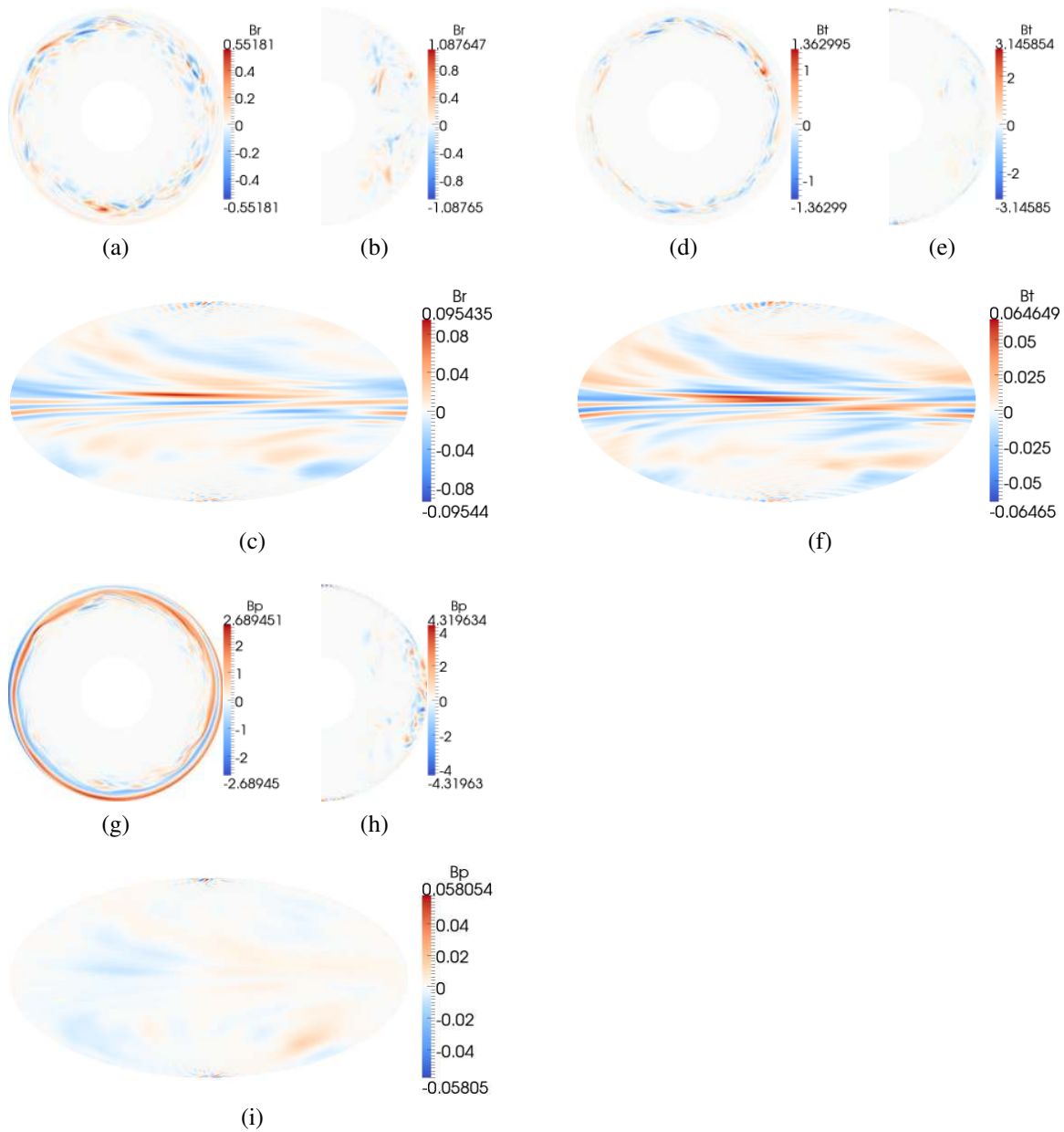
Figure 4.22: *Run "PorAbove4.42". Parameters are listed in the table (4.11). Magnetic field **B**. Equatorial slices: (a), (d), (g). Meridional slices: (b), (e), (h). Hammer projections of the outer boundary : (c), (f), (i). Subscripts "$_p$" and "$_t$" denote φ and θ components respectively.*

4.4.2.5 Case "PorAbove1.5.2"

The run that we denote by "PorAbove1.5.2" has parameters listed in the table (4.12). In comparison with the run "PorAbove4.42" we have moved down in Rossby number Ro closer to the boundary below which only axisymmetric velocity components are self-excited (see fig. 4.6)

E	Ro	Pr_m	N	L	M
$1.0 \cdot 10^{-4}$	$15 \cdot 10^{-4}$	5	300	150	150

Table 4.12: *Parameters of the run called "PorAbove1.5.2". N radial points, L harmonic degrees, M orders represent resolution. Lorentz force is turned on in the simulation.*

The total kinetic energy is equilibrated at the level 17379.0. The magnetic field had not finished growing when the simulation has been stopped. In the end of the simulation the magnetic energy has the value 3.6 and negative second time derivative suggesting that there will be an equilibrium state with a non-zero magnetic field (see fig.4.19). The value of energy
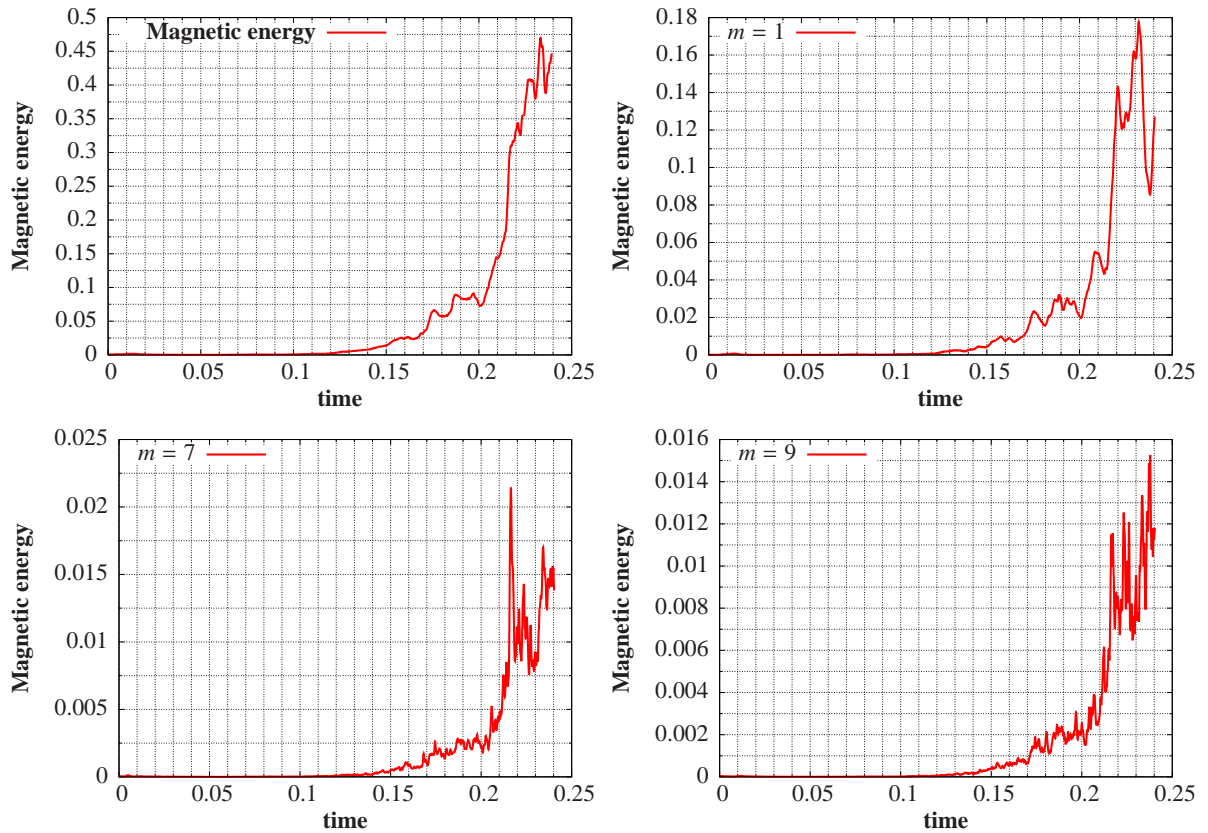
Figure 4.23: *Run "PorAbove1.5.2". Time evolution of the magnetic energy and its spectral components.*

is larger than in the run "PorAbove4.42" (sec. 4.4.2.4) with the same Ekman number and larger Rossby number Ro in spite of the fact that Pr_m is two times smaller here.

The velocity field is simple with multiples of harmonic order 14 and $m = 0$ excited. Non-zero magnetic harmonics are also discrete and are listed below.

Non-zero velocity harmonics	Non-zero magnetic harmonics.
$m = 0, 14n$	$m \pm 1$.

Energy spectra and time behaviour of individual magnetic harmonics are presented in figures (4.24) and (4.23) respectively. Magnetic spectral energy components are larger than kinetic at harmonic degrees $l > 42$.
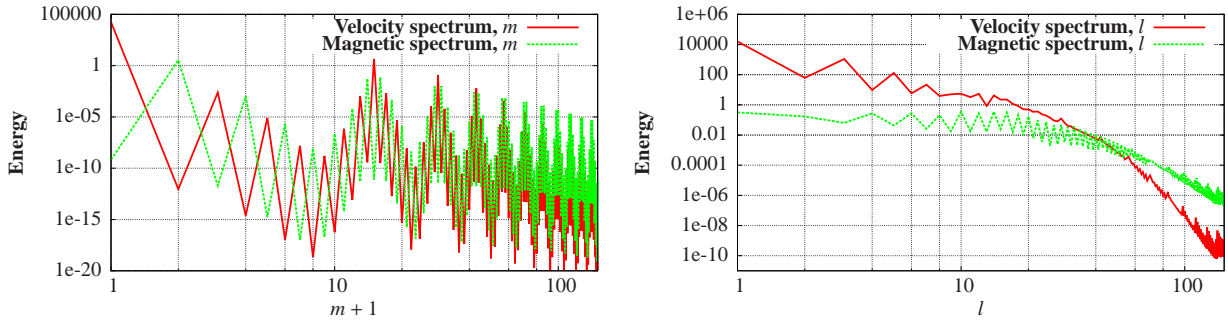
Figure 4.24: *Run "PorAbove1.5.2". Magnetic and kinetic energy spectra. Only m = 0 and m = 14n kinetic energy components are O(1).*

The lower Rossby number *Ro* than in the run "PorAbove4.42" (sec. 4.4.2.4) influences the position of the maximal longitudinal velocity. It happens at a smaller radius than in the previous cases (see e.g. the umbrella-shaped structure at the equator in fig.4.25h and fig.4.21h). Velocity is regular as in cases with lower Ekman number *E* (sections 4.4.2.1 – 4.4.2.3). In contrast to these cases there is a strong poleward flow at high latitudes.

The magnetic field is concentrated outside of the tangent cylinder where the flow shear is strong. For example, there is a region close to the outer boundary at low latitudes, where magnetic field is almost absent (see fig.4.26b,e,h). This corresponds to very small velocity perturbations (see fig.4.25b,e,h).
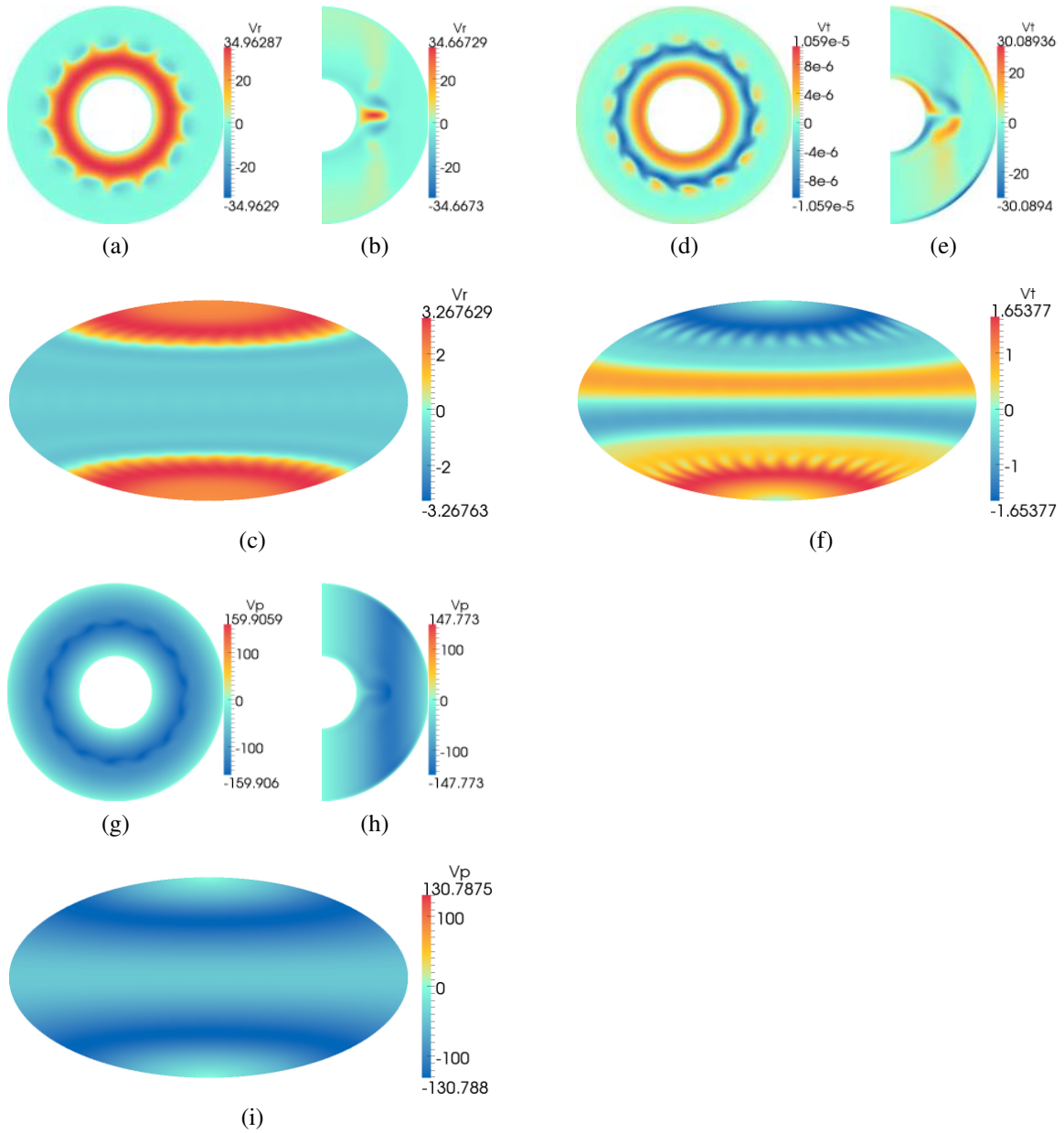
Figure 4.25: *Run "PorAbove1.5.2". Parameters are listed in the table (4.12). Velocity deviation field* **u**. *Equatorial slices: (a), (d), (g). Meridional slices: (b), (e), (h). Hammer projections of the spherical surface which is slightly below the surface: (c), (f), (i). Subscripts "$_p$" and "$_t$" denote φ and θ components respectively.*
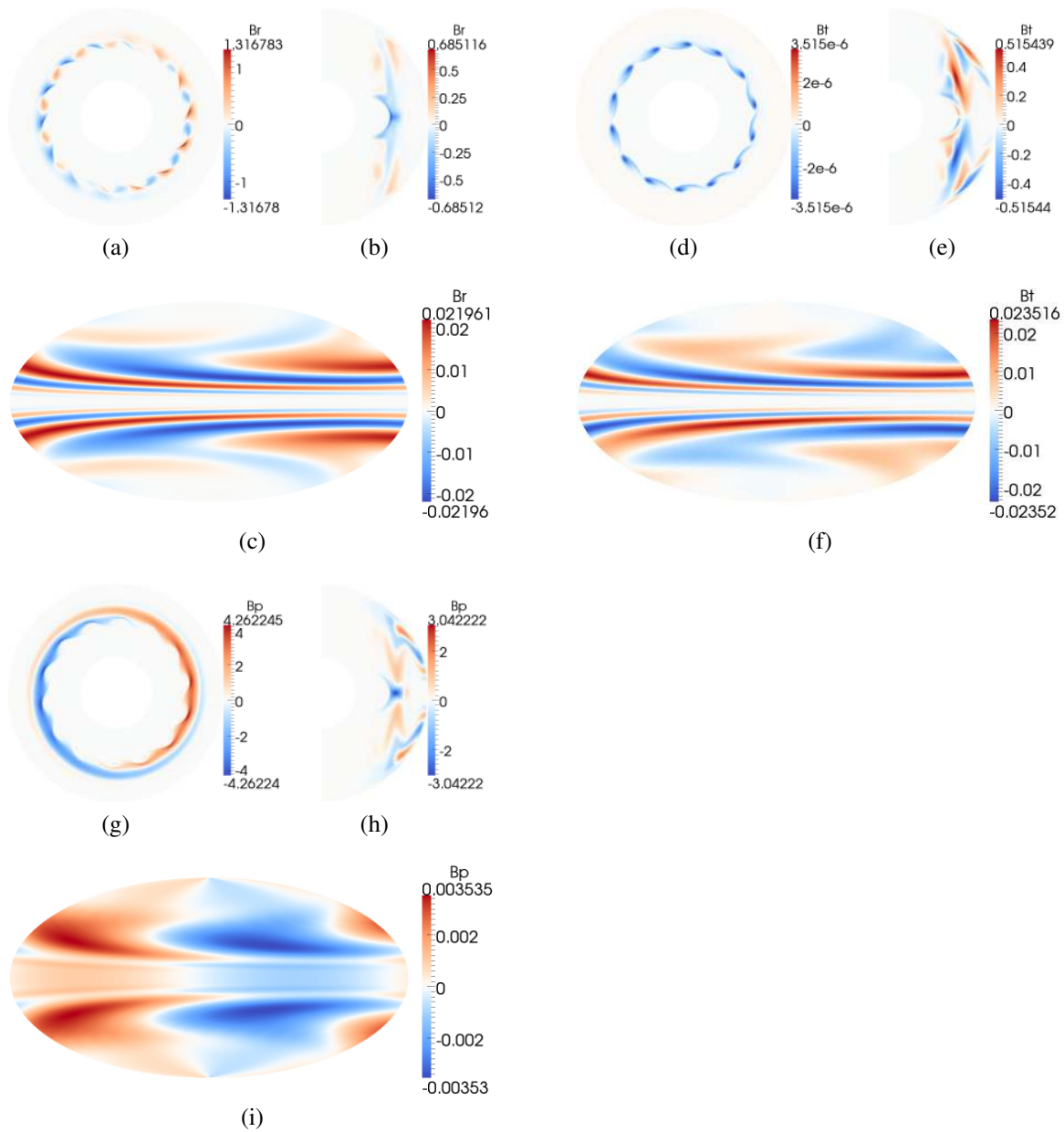
Figure 4.26: *Run "PorAbove1.5.2". Parameters are listed in the table (4.12). Magnetic field* **B**. *Equatorial slices: (a), (d), (g). Meridional slices: (b), (e), (h). Hammer projections of the outer boundary : (c), (f), (i). Subscripts "$_p$" and "$_t$" denote φ and θ components respectively.*

4.4.2.6 Case "PorAbove4.31"

The run that we denote by "PorAbove4.31" has parameters listed in the table (4.13). The run is very close to the boundary after which non-axisymmetric velocity components decay: the critical Rossby number Ro is $9 \cdot 10^{-3}$, whereas Ro for this run is $8.8 \cdot 10^{-3}$ (see figures 4.3 or 4.6). The Lorentz force is turned off in the simulation.

E	Ro	Pr_m	N	L	M
$1.0 \cdot 10^{-4}$	$88 \cdot 10^{-4}$	3.5	180	90	30

Table 4.13: *Parameters of the run called "PorAbove4.31". N radial points, L harmonic degrees, M orders represent resolution. Lorentz force is turned off in the simulation.*

The total energy of velocity perturbation is equilibrated at the level 1870.7. The magnetic field decayed almost to the numerical zero by the end of the simulation (see fig.4.27).
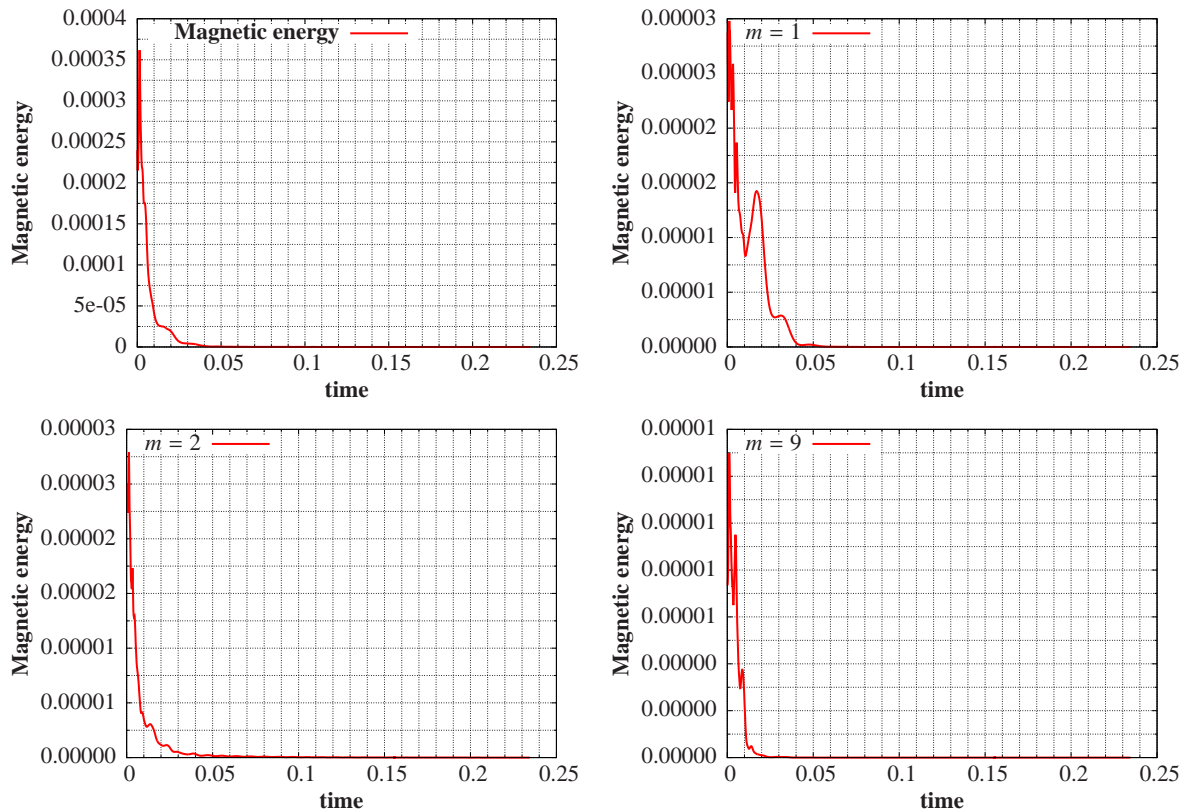
Figure 4.27: *Run "PorAbove4.31". Time evolution of the magnetic energy and its spectral components.*

The velocity field is simple with $m = 0$ and multiples $m = 4$ excited. The harmonic with the largest growth rate in the linear calculation at $Ro = 9 \cdot 10^{-3}$ is also $m = 4$ (fig. 4.3).

Non-zero velocity harmonics
$0, 4n$

These excited harmonics differ this case from the presented above runs with the same Ekman number E but lower Rossby numbers Ro, where multiples of $m = 14$ are excited ("PorAbove1.5.2", sec.4.4.2.5) or all harmonics are excited ("PorAbove4.42", sec.4.4.2.4). Energy spectra and time behaviour of individual magnetic harmonics are presented in figures (4.28) and (4.27) respectively.
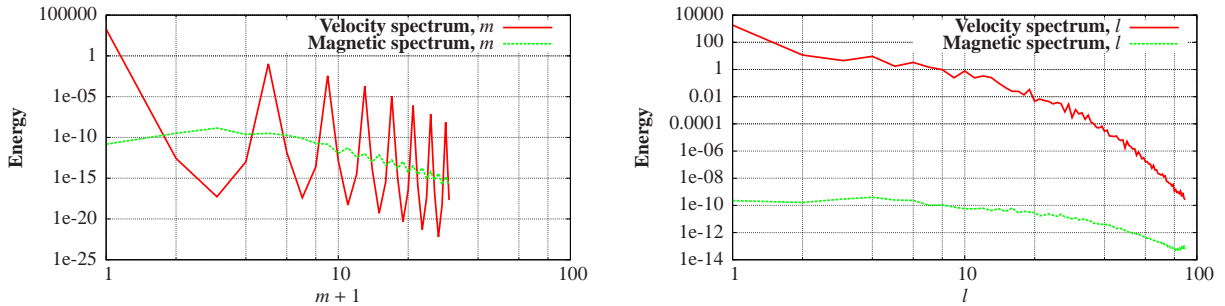
Figure 4.28: *Run "PorAbove4.31". Magnetic and kinetic energy spectra. Only $m = 0$ and $m = 4n$ kinetic energy components are $O(1)$.*

The longitudinal velocity is distinct from the runs where the magnetic field doesn't decay to zero: the umbrella-like structure in the middle of the shell is absent (compare e.g. fig.4.29h and fig.4.25h). The fluid injection with $Ro = 88 \cdot 10^{-4}$ is so strong that this structure would probably occur at the radius outside the shell. The equatorial upwelling that is associated with the "umbrella-like" structure is very thick and occupies almost all space between inner and outer radii of the shell.

Remnants of the decaying magnetic field are shown in fig.4.30.
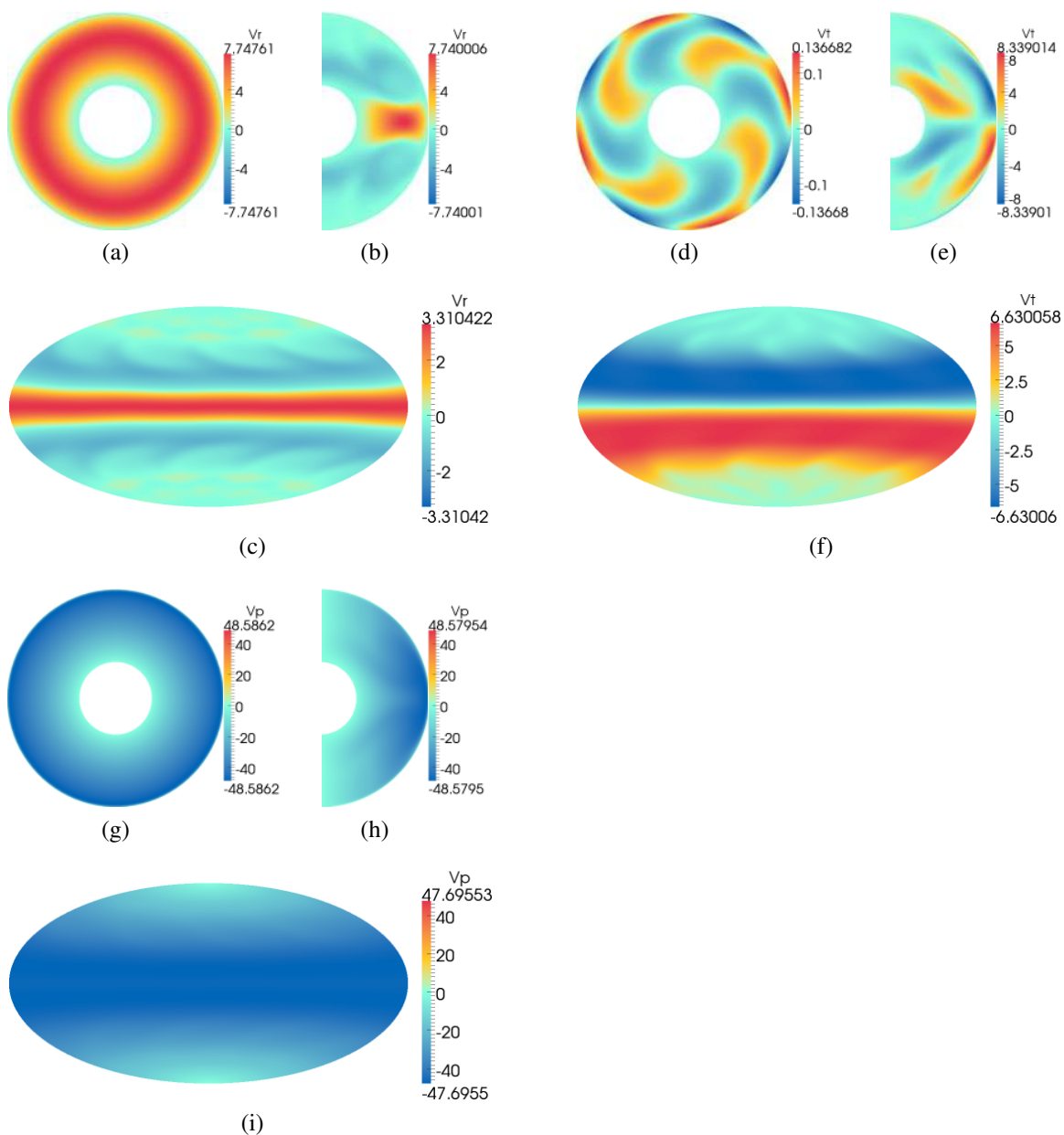
Figure 4.29: *Run "PorAbove4.31". Parameters are listed in the table (4.13). Velocity deviation field* **u**. *Equatorial slices: (a), (d), (g). Meridional slices: (b), (e), (h). Hammer projections of the spherical surface which is slightly below the surface: (c), (f), (i). Subscripts "$_p$" and "$_t$" denote φ and θ components respectively.*
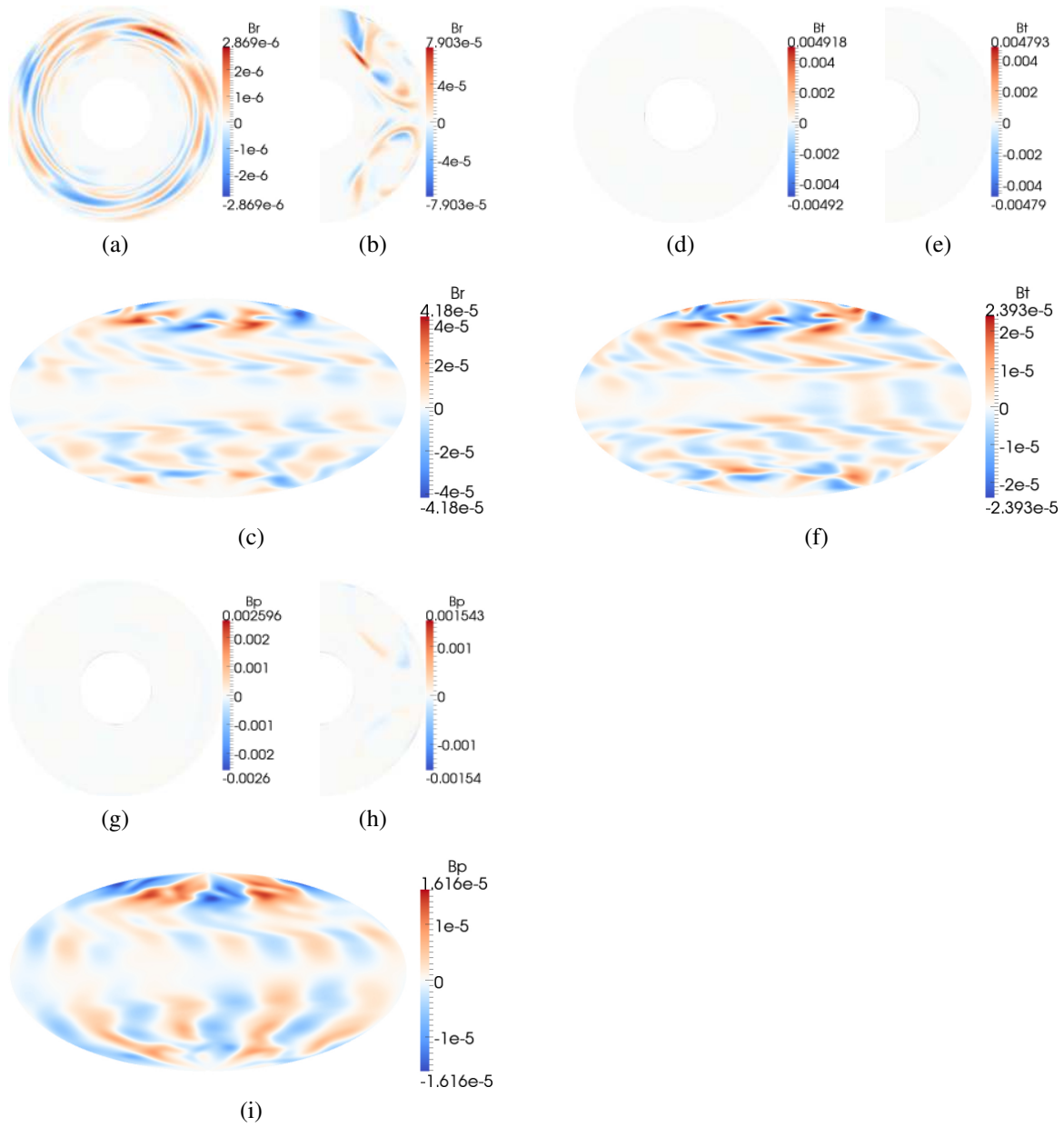
Figure 4.30: *Run "PorAbove4.31". Parameters are listed in the table (4.13). Magnetic field* **B**. *Equatorial slices: (a), (d), (g). Meridional slices: (b), (e), (h). Hammer projections of the outer boundary : (c), (f), (i). Subscripts "$_p$" and "$_t$" denote φ and θ components respectively.*

4.4.2.7 Case "PorAbove4.27"

The run that we denote by "PorAbove4.27" has parameters listed in the table (4.14). It has the lowest Ekman number E out of the presented cases. The Lorentz force was turned off in the run.

E	Ro	Pr_m	N	L	M
$0.2 \cdot 10^{-4}$	$15 \cdot 10^{-4}$	1.334	300	150	30

Table 4.14: *Parameters of the run called "PorAbove4.27". N radial points, L harmonic degrees, M orders represent resolution. Lorentz force is turned off in the simulation.*

The total energy of the velocity perturbation equilibrates at the value 44942. The magnetic energy was continuously growing in this run having no way to affect the velocity field (see fig.4.31).
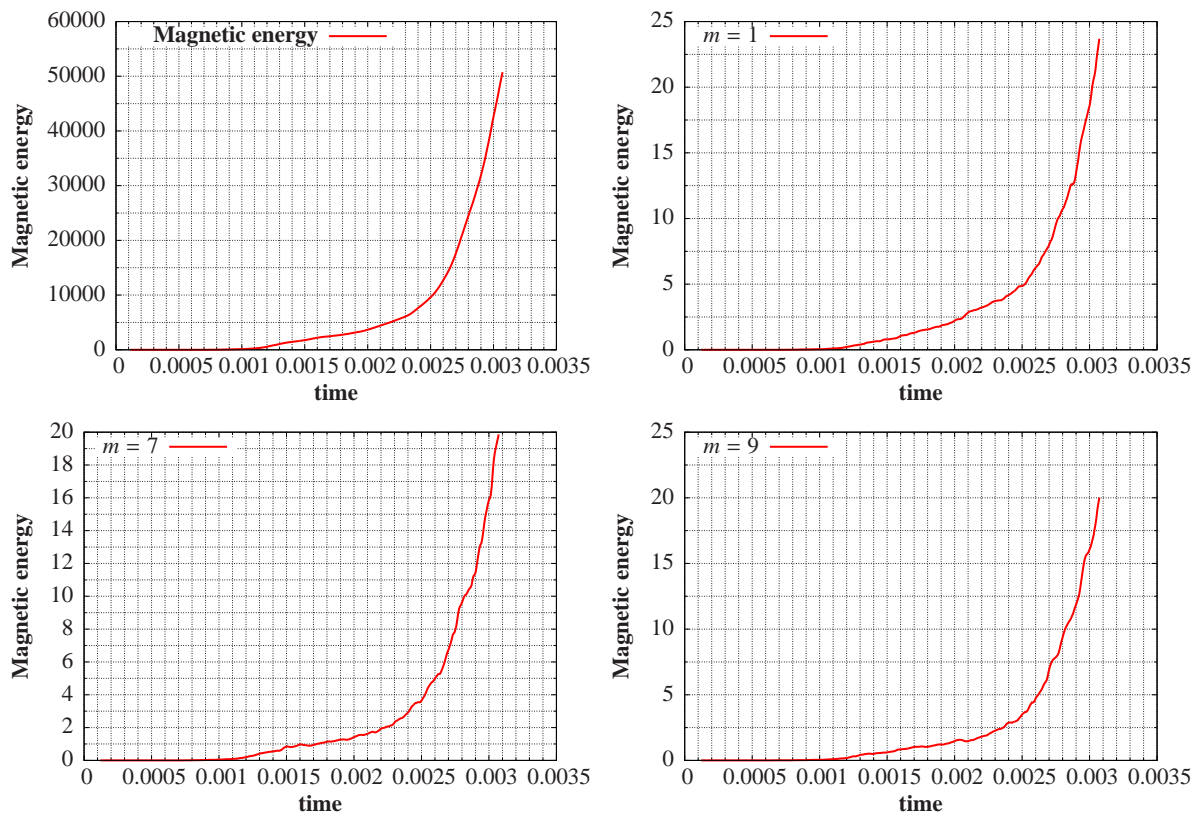
Figure 4.31: *Run "PorAbove4.27". Time evolution of the magnetic energy and its spectral components.*

All velocity and magnetic harmonics are excited. The velocity field has very fractured structure in comparison with previously discussed runs. The "umbrella-like" structure in the meridional projection of longitudinal flows is only partly present ("umbrella's" canopy is misshaped). The upwelling jet on equator in the deep layers of the shell (associated with the "umbrella") is narrow, short and is bent into a banana-shape unlike in other runs (see fig.4.33b).

In the same manner as the velocity field the magnetic field is very fractured. It is mostly concentrated in the middle and low latitudes outside of the tangent cylinder. The Lorentz force is turned off in the simulation, so the form and especially magnitude of the magnetic field is not physical. Even so, the growth of the magnetic field supports the guess that even with the complete equations it is self-sustained.
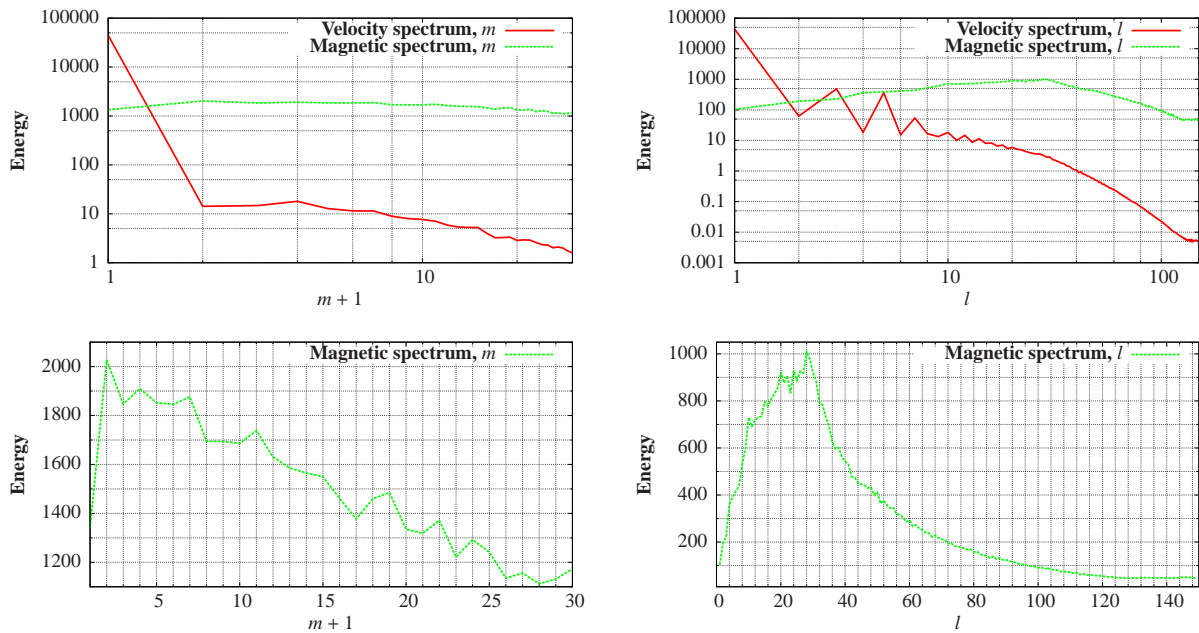
Figure 4.32*: Run "PorAbove4.27". Magnetic and kinetic energy spectra.*

Energy spectra and time behaviour of individual magnetic harmonics are presented in figures (4.32) and (4.31) respectively.
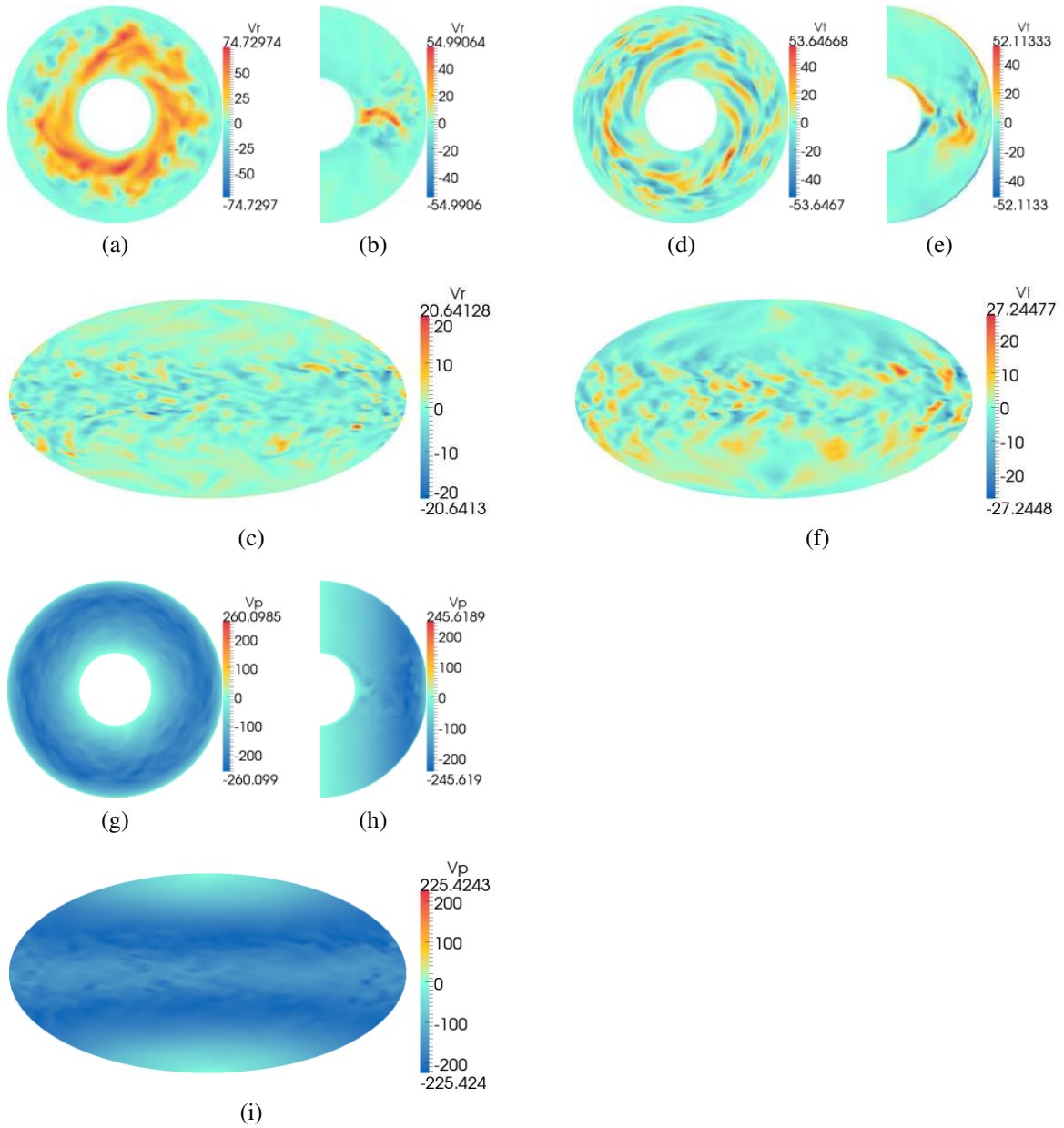
Figure 4.33: *Run "PorAbove4.27". Parameters are listed in the table (4.14). Velocity deviation field* **u**. *Equatorial slices: (a), (d), (g). Meridional slices: (b), (e), (h). Hammer projections of the spherical surface which is slightly below the surface: (c), (f), (i). Subscripts "$_p$" and "$_t$" denote φ and θ components respectively.*
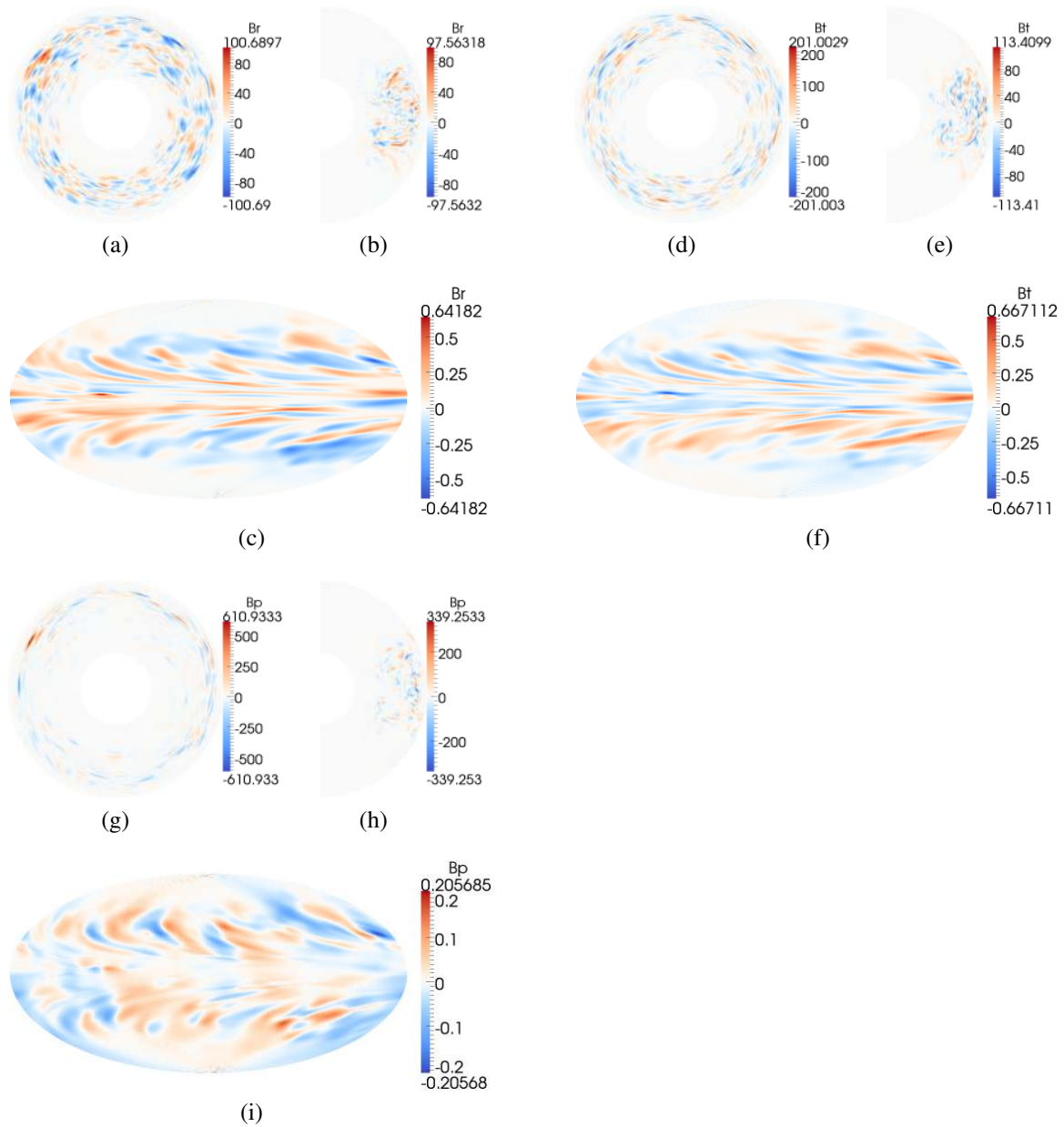
Figure 4.34: *Run "PorAbove4.27". Parameters are listed in the table (4.14). Magnetic field* **B**. *Equatorial slices: (a), (d), (g). Meridional slices: (b), (e), (h). Hammer projections of the outer boundary : (c), (f), (i). Subscripts "$_p$" and "$_t$" denote φ and θ components respectively.*

4.4.3   Conclusions

In this chapter we have described behaviour of conducting incompressible fluid in the rotating spherical shell in which it is injected through one porous boundary and drained off with the same rate from another boundary. First, we have investigated linearized purely hydrodynamical equations and found the region in the parametric space of Rossby-Ekman numbers Ro–E where non-axisymmetric motions are self excited (fig. 4.3).

Curiously, the system has non-trivial velocities only in a certain range of the injection strengths Ro. It is likely associated with the appearance of the "umbrella"-like structure in the middle of the shell. The fast fluid (faster than the injection) forms a jet on the equator that breaks at a certain length because of the viscosity. Equating viscous and injection terms:

$$-E\mathbf{\nabla}^2\mathbf{u} \sim Ro\,(\mathbf{u} + \frac{\hat{\mathbf{r}}}{r^2}) \times (\mathbf{\nabla} \times \mathbf{u}) \tag{4.28}$$

Then we can write a scale estimation of this equation:

$$\frac{E\,u}{l^2} \sim Ro\,(u + \frac{1}{r_{jet}^2})\frac{u}{l}, \tag{4.29}$$

where l is the length scale corresponding to the changes of $\mathbf{u}$. Reducing terms in the equation and equating u to zero to get non-dimensional radius until which jet exists:

$$r_{jet} \sim \sqrt{l}\,\sqrt{Ro/E}\,.^{3} \tag{4.30}$$

Indeed, comparing cases "PorAbove4.42" and "PorAbove1.5.2" with the same Ekman number E we see that the ratio of radii (where $u_r = 0$ at the tip of the equatorial jet) $1.4/1.0 = 1.4$ approximately equals to the square root of the ratio of the corresponding Rossby numbers $\sqrt{30/15} \approx 1.41$ (here we assume that the length scale l is the same in both cases).

If the Ekman number is larger than $E = 10^{-3.51}$, any positive Ro will create only axisymmetric motions. In other words it doesn't matter how much fluid we inject per unit time, there will not be self-excited non-axisymetric flows: the basic axisymmetric diverging flow $1/r^2$ guarantees decay of non-axisymmetric modes.

We have tested the capability of the axisymmetric regime to maintain a dynamo. Although there is no known theorem that prohibits dynamos with only axisymmetric velocity field, seed magnetic fields didn't succeed to become self-sustained with only axisymmetric velocity in the cases we have checked (see fig.4.6). But this result is foreseeable because the flow was not only axisymmetric but also steady.

We have found a definitive tendency for some non-axisymmetric injection-driven flows to self-reproduce magnetic field. However in cases where Lorentz force was turned on and

---

[3]With e.g. $Ro = 0$ the formula (4.30) predicts the tip of the jet inside the inner core, so it has some limited range of applicability.

the magnitude of the field was dictated by the interaction with the flow, the equillibrated regime turned out to contain little magnetic energy (less than 1% of kinetic energy even with large $Pr_m > 1$). Beyond that the geometry of the field has little to do with the geophysical situation. All this doesn't reveal the benefits of an experimental device with a similar type of driving for geophysical purposes. Nevertheless, we have explored only a tiny region of possible parameters, where the flows are simplest. Going to lower Ekman numbers could feature new flow regimes, but requires more computing resources.

An interesting direction for investigation is $Ro < 0$ where flow is injected from the outer boundary and drained off from the inner boundary. Our initial tests in this regime have shown that the flow in this case is highly unstable. It makes the task to draw a curve for the onset of non-axisymmetric modes much more difficult than for the $Ro > 0$. However this unstable converging flow promises more complicated and diverse velocity fields and accordingly more possibilities for dynamos.

Chapter 5

Convection-driven dynamos in rapidly rotating systems

5.1 Introduction

The geodynamo originates in a huge mass of liquid metal in the outer core of the Earth. Unlike thin films of the ocean or atmosphere (ratio of the thickness to the lateral size is order of 10^3), the dynamo region is truly three-dimensional. Moreover, the Earth rotates with enormous speeds (the rotational velocity $\Omega d \sim 0.5 \cdot 10^3$ km/hour in the core) in comparison to its viscous velocity scale $\nu/d \sim 10^{-12}$ km/hour (meaning that any information about the flow conveyed with viscosity will need a tremendous time to be transferred on length scales comparable to the size of the core) which gives rise to its very low Ekman

$$\text{Earth} \quad \begin{aligned} Ro &= 2 \cdot 10^{-10} \\ E &= 10^{-15} \\ Ra &= 10^{15} \\ q &= 2.5 \cdot 10^{-5} \end{aligned}$$

Table 5.1: *Earth's parameters from Sakuraba and Roberts (2009).*

number $E = \dfrac{\nu}{2\Omega d^2} \sim 10^{-15}$. The dissimilarity of scales shows that the flow is viscously coupled only on small distances. At the same time the magnetic diffusion is five orders of magnitude larger than the viscous diffusion. As a result both the induction and Navier-Stokes equations contain terms evolving on disparate length and timescales. Put simply, many aspects of the parameters (see Table 5.1) governing the Earth's dynamo are arranged in a way to make its numerical modelling a difficult exercise.

Nevertheless the aim in this chapter is to push numerical simulations into a regime as similar to the Earth as possible. Computer resources are restricted, but within these constraints parameters are chosen in an effort to match at least qualitatively those of the geodynamo. The hope is to be close enough to the asymptotic regime where further change in parameters is not necessary to achieve similarities with the Earth's core dynamics.

The low-viscosity simulations that we present in this chapter were conducted with the

practical aim of understanding the relation between magnetic structures appearing on the CMB and the internal behaviour of the MHD. In order that the reader may picture for themselves what is occurring inside a working dynamo, we depict relevant physical properties in a set of different projections. In addition, important integrated numerical characteristics are checked against existing theories.

5.2   Formulation of the modelling problem

We are going to solve the equations of core dynamics (in the form expressed by Willis et al., 2007) written in a rotating coordinate system for a conducting incompressible viscous fluid:

$$\begin{cases} \left(Ro\,\dfrac{\partial}{\partial t} - E\boldsymbol{\nabla}^2\right)\mathbf{u} & = & \mathbf{N}_u - \boldsymbol{\nabla}\hat{P}, \\[2mm] \left(\dfrac{\partial}{\partial t} - \boldsymbol{\nabla}^2\right)\mathbf{B} & = & \mathbf{N}_B, \\[2mm] \left(\dfrac{\partial}{\partial t} - q\boldsymbol{\nabla}^2\right)T & = & N_T, \end{cases} \qquad (5.1)$$

where

$$\begin{aligned} \mathbf{N}_u &= Ro\,\mathbf{u}\times(\boldsymbol{\nabla}\times\mathbf{u}) + (\boldsymbol{\nabla}\times\mathbf{B})\times\mathbf{B} + q\,Ra\,T\,\mathbf{r} - \hat{\mathbf{z}}\times\mathbf{u}, \\ \mathbf{N}_B &= \boldsymbol{\nabla}\times(\mathbf{u}\times\mathbf{B}), \\ N_T &= \varepsilon - \mathbf{u}\cdot\boldsymbol{\nabla}T, \end{aligned}$$

Incompressibility conditions are integrated into the solution technique through use of a poloidal-toroidal decomposition of the vector field. The modelled fluid is enclosed in a rotating spherical shell between radii r_i and r_o on which following boundary conditions are implemented:

- no slip and impenetrable at r_0 and $r_i/r_0 = c = 0.35$

- electrically insulating mantle, conducting inner core

- fixed heat flux on the CMB, and T on the ICB (*inner core boundary*)

The equations are non-dimensionalized in the following way:

$r \rightarrow d\,r, t \rightarrow d^2/\eta\,t, B \rightarrow (2\Omega\rho_0\mu_0\eta)^{\frac{1}{2}}\,B, T \rightarrow \Delta T\,T; \; d = r_o - r_i$

Non-dimensional parameters are defined as:

$Ro = \eta/(2\Omega d^2), \quad E = \nu/(2\Omega d^2), \quad Ra = g\,\alpha\,\Delta T\,d/(2\Omega\kappa), \quad q = \kappa/\eta$

The uniform internal heating is

$$\epsilon = 3q. \qquad (5.2)$$

All the numerical dynamos discussed in this chapter were started from the the steady solution of the Case 0 (simulations are defined in sec.5.2.2). For Case 0 itself the initial

condition was constructed from the steady solution of the dynamo benchmark (Christensen et al., 2001), but with the background temperature field replaced by[1]:

$$T = \frac{1}{2}(-r^2 + K/r + L) \tag{5.3}$$

with

$$K = \frac{2}{(1-c)^3} \text{ and } L = \frac{-1}{(1-c)^2}. \tag{5.4}$$

This temperature profile is a solution of the steady heat flux equation with internal heating (eq. 5.2). The following boundary conditions suit the initial temperature profile eq.(5.3) and were used in all runs:

$$r_i \left| \begin{array}{l} T = \frac{1}{2}\frac{c^2 + c + 2}{(1-c)c} = 5.434, \\ \frac{\partial T}{\partial r} = -\frac{2}{1-c} = -3.077. \end{array} \right.$$

In order to obtain a dynamo, the initial state requires a large magnetic field – tests for the parameters of Case 0 showed that it could not grow self-sustained manner from small numerical perturbations; the dynamo is subcritical. A long transient was therefore needed to reach a steady state from the artificial initial state in Case 0.

5.2.1 Numerical implementation: hardware, resolution, timestep

The employed resolution in all the runs is:

N 512 – 528,

L 256,

M 256,

where N is the number of radial points, L and M are the spherical harmonic degree and order respectively. The timestep was varied during the simulations, values from the final stages of the runs are presented in the table 5.2. The real time needed to move one timestep forward with 516 cores was approximately 6s on the Cray XE6. Some of the cases were executed in part on different machines and the radial resolution was adjusted to match the varying hardware framework. Thereby the radial decomposition was modified to match the number of cores on an integer number of nodes to balance the load of the CPUs and minimize the use of resources.

Case 0	$1.3 \cdot 10^{-6}$
Case 1	$1.5 \cdot 10^{-7}$
Case 2	$1.0 \cdot 10^{-8}$
Case 3	$2.0 \cdot 10^{-8}$
Case 4	$4.5 \cdot 10^{-8}$
Case 6	$2.1 \cdot 10^{-7}$

Table 5.2: *Final timesteps utilised in the simulations.*

---

[1]These coefficients are result of the dimensional profile $\frac{\partial T}{\partial r} = -\beta \left[(1-Q)\frac{r}{r_o} + Q\left(\frac{r_o}{r}\right)^2 \right]$ with $Q = 0.5$ (used by Sakuraba and Roberts, 2009, personal communication). L is chosen to make $T = 0$ at CMB in the initial temperature profile.

Simulations were executed on the computing facilities of the Swiss National Supercomputing Centre. The bulk of the computations were made on the Cray XE6 (Monte Rosa) and partly on the Cray XK7 (Tödi) using $512 - 528$ cores and 1Gb/core simultaneously. Postprocessing and visualisation were carried out on the IBMx3850 M2 (Julier) and the Dalco Supermicro System (Eiger). The detailed description of the machines is on the website of CSCS (www.cscs.ch).

5.2.2   List of simulations with parameters.

The control parameters for the seven runs discussed in this chapter are presented in table (5.3). The Rayleigh number (the driving parameter) was varied from $Ra = 219.7$ (as in Sakuraba and Roberts, 2009) up by a factor of 30 to $Ra = 6591.0$. The magnetic and thermal diffusivities were kept equal to each other in all runs. Hence, the Prandtl number $Pr = 1$ and the Roberts number $q = \kappa/\eta$ and the magnetic Prandtl number Pr_m are equal to each other as well. It is preferable to speak in terms of the magnetic Prandtl number, as it directly relates kinematic and magnetic phenomena. In a liquid metal the magnetic diffusivity is much larger than the viscous ($Pr_m \sim 10^{-7}$). If a magnetic field diffuses quickly (i.e. $Pr_m \ll 1$) it is difficult to maintain a dynamo with a large Ekman number (vs. Earth's core value, see e.g. Christensen and Wicht, 2007). The advantage of a numerical simulation is that we are free to choose the control parameters provided they are computationally feasible. In the simulations reported here, we made the magnetic diffusivities smaller than in liquid metals: $Pr_m = 0.20, 1.0, 0.05$ artificially enhancing the chance for a magnetic field to survive or even grow. Nevertheless $Pr_m = 0.05$ is rather low for contemporary numerical dynamo simulations.

The Ekman number is fixed at $E = 1.1834 \cdot 10^{-6}$ in agreement with the parameters used by Sakuraba and Roberts (2009), except for Case 4 that has a five times lower Ekman number. It means that effects of rotation in this case is larger. Case 0 is the simplest run in terms of required computational resources per diffusion time. In Cases 0, 1 and 2 only the Rayleigh number is altered. Case 1 has five times larger Ra and Case 2 has thirty times larger Ra than the Case 0.

In cases 3, 4 and 6 the magnetic Prandtl number Pr_m (or equivalently q since $Pr = 1$) was varied by a factor of 20 ranging between 1 and 0.05. Cases 4 and 6 are the most extreme cases having the highest $Ra = 6591$ and the lowest $Pr_m = 0.05$. Case 3 is the same as Case 0 except for its higher $Pr_m = 1$. The run called "HYDRO", as its name suggests, is a run with no magnetic field present and therefore no Lorentz force to change the flow. Otherwise the case "HYDRO" is the same as the Case 0.

Name	E	Ro	Ra	$q = Pr_m$
Case0	$1.1834 \cdot 10^{-6}$	$5.9172 \cdot 10^{-6}$	219.7	0.20
Case1	$1.1834 \cdot 10^{-6}$	$5.9172 \cdot 10^{-6}$	1098.5	0.20
Case2	$1.1834 \cdot 10^{-6}$	$5.9172 \cdot 10^{-6}$	6591.0	0.20
Case3	$1.1834 \cdot 10^{-6}$	$1.1834 \cdot 10^{-6}$	219.7	1.00
Case4	$0.2959 \cdot 10^{-6}$	$5.9172 \cdot 10^{-6}$	6591.0	0.05
Case6	$1.1834 \cdot 10^{-6}$	$23.6688 \cdot 10^{-6}$	6591.0	0.05
HYDRO	$1.1834 \cdot 10^{-6}$	$5.9172 \cdot 10^{-6}$	219.7	0.20

Table 5.3: *Parameters, low Ekman number runs. $Pr_m = q$ since $\nu/\kappa = 1$.*

5.3 Results of computations

5.3.1 Global diagnostics

Global diagnostics are derived by averaging in time and space fields ($\mathbf{u}$, $\mathbf{B}$, T and functions of these). This averaging diminishes the role of local irregularities, but it provides a means for quantitative analysis. In analogy to temperature being an average of the kinetic energy of chaotically moving particles, the global diagnostics reported here are first-order models of the enormously complex state of a MHD system.

Definitions of the diagnostics reported are collected in table (5.4). We report volume-

E_{mag}	E_{kin}	D_{mag}	D_{kin}	F_{Cor}/F_{Lor}	ΔT_{io}
$\dfrac{1}{2Ro}\int \mathbf{B}^2 dV$	$\dfrac{1}{2}\int \mathbf{u}^2 dV$	$\dfrac{1}{Ro}\int (\mathbf{\nabla}\times\mathbf{B})^2 dV$	$\dfrac{E}{Ro}\int (\mathbf{\nabla}\times\mathbf{u})^2 dV$	$\dfrac{\int |\hat{\mathbf{z}}\times\mathbf{u}| dV}{\int |(\mathbf{\nabla}\times\mathbf{B})\times\mathbf{B}| dV}$	$T_i - T_o$

R_m	R	Λ	l_u	l_B	m_u	m_B
$\sqrt{\dfrac{1}{V}\int \mathbf{u}^2 dV}$	$\dfrac{R_m}{Pr_m}$	$\dfrac{1}{V}\int \mathbf{B}^2 dV$	$\dfrac{\sum u_l^2 \cdot l}{2E_{kin}}$	$\dfrac{\sum B_l^2 \cdot l}{2RoE_{mag}}$	$\dfrac{\sum u_m^2 \cdot m}{2E_{kin}}$	$\dfrac{\sum B_m^2 \cdot m}{2RoE_{mag}}$

Table 5.4: *Definitions of reported global diagnostics.*

integrated magnetic and kinetic energies E_{kin} and E_{mag}, dissipation rates D_{kin} and D_{mag} (i.e. diffusion terms of the Navier-Stokes and induction equations multiplied by $\mathbf{u}$ and $\mathbf{B}$ correspondingly and integrated over the volume), ratios of the volume integrated Lorentz and Cori-

Name	t_1	t_2	Δt
Case0	1.096	1.453	0.358
Case1	0.270	0.329	0.059
Case2	0.056	0.062	0.006
Case3	0.070	0.076	0.006
Case4	0.068	0.073	0.005
Case6	0.201	0.234	0.033
HYDRO	1.303	1.590	0.288

Table 5.5: *The time-intervals $\Delta t = t_2 - t_1$ over which the global diagnostics are averaged.*

olis forces, differences between the mean temperatures on the outer and inner boundaries of the rotating container, as well as typical harmonic degrees (l_u and l_B) and orders (m_u and m_B) obtained by averaging over the energy spectra for both vector fields . These typical spherical harmonic degrees and orders of the field and flow provide information about local length scales of the fluid and the induced magnetic field. The time spans for diagnostics (Table 5.5) are chosen at the end of the runs, and are long enough to minimize statistical errors.

Name	E_{mag}	E_{kin}	E_{mag}/E_{kin}	D_{mag}	D_{kin}	D_{mag}/D_{kin}
Case0	8.71e+04	2.91e+04	2.99	3.41e+07	4.04e+07	0.84
Case1	7.50e+05	2.38e+05	3.15	8.66e+08	5.04e+08	1.72
Case2	1.22e+07	6.35e+06	1.93	6.30e+10	1.36e+10	4.65
Case3	3.53e+07	4.72e+05	74.84	3.03e+10	2.70e+09	11.22
Case4	4.46e+06	5.51e+05	8.10	6.31e+09	6.18e+08	10.21
Case6	4.43e+05	3.69e+05	1.20	5.94e+08	1.91e+08	3.11

Table 5.6: *Time-averages of global diagnostics at the final stages of runs, part 1. D is the dissipation power.*

Name	R	R_m	Λ	F_{Cor}/F_{Lor}	ΔT_{io}
Case0	315	63	0.07	76.6	2.37
Case1	902	180	0.61	12.9	1.66
Case2	4665	933	9.92	2.1	3.06
Case3	254	254	5.73	2.6	3.37
Case4	5492	274	3.61	3.1	3.33
Case6	4495	224	1.44	6.5	2.06

Table 5.7: *Time-averages of global diagnostics at the final stages of runs, part 2. R and R_m are Reynolds and magnetic Reynolds numbers correspondingly. Λ is the Elsasser number. ΔT_{io} is the difference between average temperatures on inner and outer boundaries. F_{Lor}/F_{Cor} is the ratio of integrated over the volume Coriolis and Lorentz forces.*

Name	l_u	m_u	l_B	m_B	k_u	k_B	k_u/k_B
Case0	37.18	26.18	6.44	3.88	45.47	7.52	6.05
Case1	51.60	32.12	13.30	7.23	60.78	15.14	4.01
Case2	36.57	21.40	31.50	17.28	42.37	35.93	1.18
Case3	26.85	16.92	12.99	7.05	31.73	14.78	2.15
Case4	50.32	27.48	14.27	7.05	57.33	15.91	3.60
Case6	34.62	21.29	15.24	8.19	40.64	17.31	2.35

Table 5.8: *Time-averages of global diagnostics at the final stages of runs, part 3. l_u and l_B are characteristic degrees of the flow and the magnetic field correspondingly. m_u and m_B are characteristic orders of the flow and the magnetic field correspondingly. $k = \sqrt{l^2 + m^2}$.*

The global diagnostics are presented in tables (5.6), (5.7) and (5.8). The magnetic energy is larger than the kinetic energy in all of the runs. In Case 6 the energies are almost equal. The magnetic energy of the Case 2 is about twice as big as the kinetic energy. Both cases 6

and 2 have very high Rayleigh number $Ra = 6591$. Case 4 has the same high Ra, but five times lower Ekman number $E = 0.2959 \cdot 10^{-6}$. The high rotation rate (or equivalently low viscosity and Ekman number) results in a ratio of the magnetic to kinetic energies of order 10. The magnetic energy is several times larger than the kinetic energy in the runs with lower $Ra = 219.7, 1098.5$. The highest ratio of magnetic to kinetic energies occurs in Case 3 because it has weaker magnetic diffusion compared to other cases ($Pr_m = q = 1$).

Dissipation rates ratios (D_{mag}/D_{kin}) vary from slightly less than unity in the Case 0 up to the order of ten in cases 3 and 4. The conductivity of the fluid in the Case 3 is high which one would expect to reduce the Ohmic dissipation and therefore the large ratio D_{mag}/D_{kin} seems at first sight surprising. But the magnetic energy itself is high in this case, so there are nevertheless large rates of magnetic dissipation.

An interesting tendency is found for the ratio of the lengthscales k_u/k_B (i.e. the ratio of magnetic to velocity length-scales). The highest ratio of about six is found for Case 0. The ratio k_u/k_B decreases as Ra increases. Case 2, which has the highest Rayleigh number Ra, has the lowest ratio of order unity. Considering a five time larger magnetic Prandtl number decreases the ratio k_u/k_B by a factor of three. Comparing cases 4 and 6 we find that the lowering of the Ekman number by a factor of 4 increases the ratio by a factor of 1.5. This is mainly due to the smaller velocity scales $1/k_u$ in the lower Ekman number run. But the absolute scale of the magnetic field $1/k_B$ also slightly increases in Case 4. This gives some hope that lower Ekman numbers will favour larger scales in the magnetic field.

The largest length scale for the velocity field is found in Case 3, with the highest $Pr_m = 1$, and $k_u \approx 32$. There is no pronounced dependence of the velocity length scale $1/k_u$ on the Rayleigh number. Comparing cases 0 through 2, the run with the highest $Ra = 6591$ (Case 2) has a slightly larger velocity length scale than in the run with $Ra = 219.7$ (Case 0). But at $Ra = 1098.5$ (Case 1), the flow length scale is the smallest obtained in all the runs.

The largest length scale for the magnetic field occurs in Case 0 with $k_b \approx 8$ and $m_B \approx 4$. The smallest length scale for the magnetic field $k_B \approx 32$ and $m_B \approx 17$ is found in Case 2 with its higher $Ra = 6591$. Other cases have similar magnetic length scales with k_B varying between 15 and 17 and m_B between 7 and 8.

It is worth noticing that the sum of the kinetic and magnetic energies grows like the power of the Rayleigh number Ra (fig. 5.1, left) if other parameters stay the same. The ratio F_{Cor}/F_{Lor} behaves in a different way: the influence of the Coriolis force compared to the Lorentz force drops almost linearly on the log-log scale when Ra grows (fig. 5.1, right). The total dissipation is nearly proportional to the total energy (fig. 5.2), what is natural since energy is mainly contained in the magnetic form and time is measured in magnetic diffusion units ($D \sim E/t$).

The partitioning between toroidal and poloidal energies and the conversion from one to another are crucial in a dynamo mechanism, therefore equillibrated levels may be important for understanding a dynamo's intrinsic properties. Ratios of the toroidal energy to the total

kinetic or magnetic energies are plotted on figure (5.3) with values reported in the table (5.9). If only the Rayleigh number Ra is changed, the toroidal part of the kinetic energy decreases along with the increase in Ra. The toroidal part of the magnetic energy behaves oppositely.
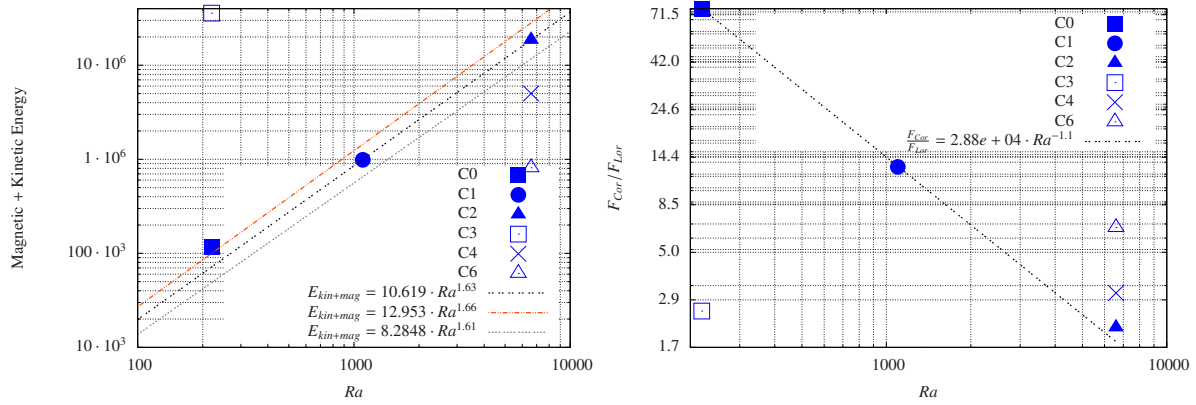
Figure 5.1: *Dependence of the total energy on the Rayleigh number Ra (left). Dependence of the ratio of integrated Lorentz and Coriolis forces on Ra (right). The best fit linear approximations and 3σ lines are shown. Only the Rayleigh number Ra varies in simulations which were used in the computation of the best fit line (cases 0 through 2).*
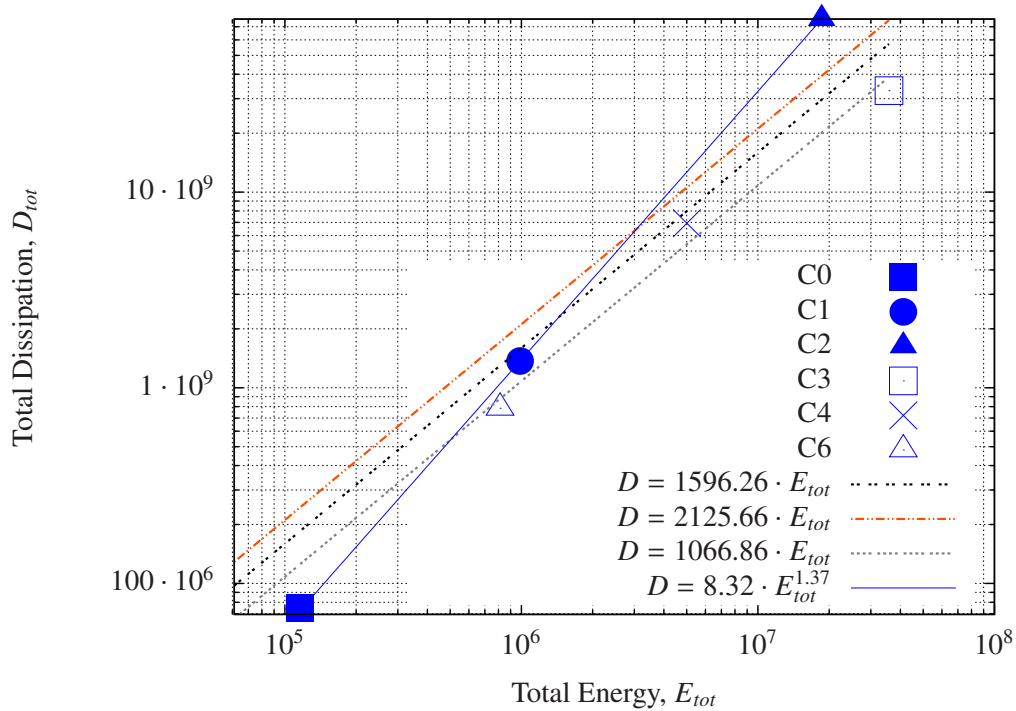
Figure 5.2: *The total dissipation (magnetic and kinetic) vs. total energy . The best fit linear approximations and 3σ lines are shown. The blue line is the best fit approximation for cases 0 through 2.*

Name	vel.	mag.
Case 0	0.8095	0.4384
Case 1	0.7126	0.5173
Case 2	0.6697	0.5595
Case 3	0.6903	0.5282
Case 4	0.6889	0.5482
Case 6	0.6808	0.6514
HYDRO	0.8281	

Table 5.9: *Ratios of the toroidal part of kinetic and magnetic energies to total energies.*
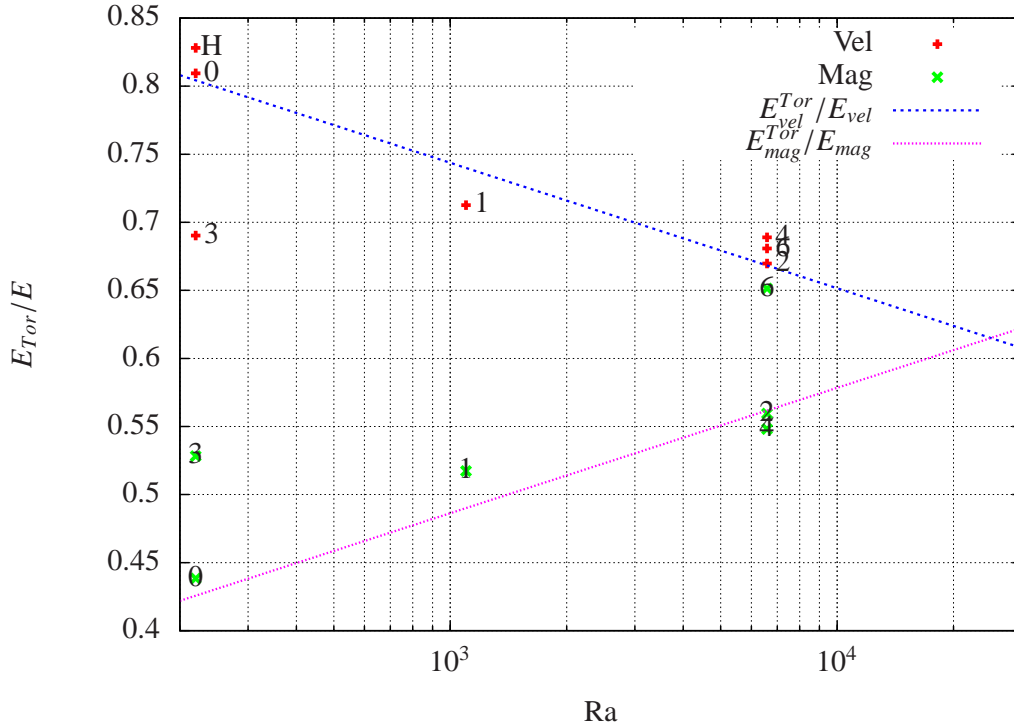
Figure 5.3: *Ratios of toroidal parts of the kinetic and magnetic energies to the total energies vs. Rayleigh number Ra. The least squares approximations are: $E_{mag}^{Tor}/E_{mag} = -0.04\ln(Ra) + 1.02$ and $E_{vel}^{Tor}/E_{vel} = 0.04\ln(Ra) + 0.21$.*

5.3.2 Energy of runs as a function of time

As described above, Case 0 was started from an initial condition with a prescribed strong magnetic field. Intermediate states of Case 0 were used as initial conditions for the other simulations. Such initial conditions are intrinsically inconsistent with the conditions of a new simulation and result in initial transients. Runs were integrated until their energies became statistically steady. Fig.(5.4) shows evolution of energies. The time-step is strongly dependent on the regime of a simulation which results in the different scales for the time (abscissa). Runs with higher Rayleigh number *Ra* have shorter advection timescales and equilibrate faster.

Time-dependencies of the ratio of the magnetic to the kinetic energies are presented in fig.(5.5). These ratios are more sensitive to the steadiness of the runs than the energies them-

(a) Case 0

(b) Case 1

(c) Case 2

(d) Case 3

(e) Case 4

(f) Case 6
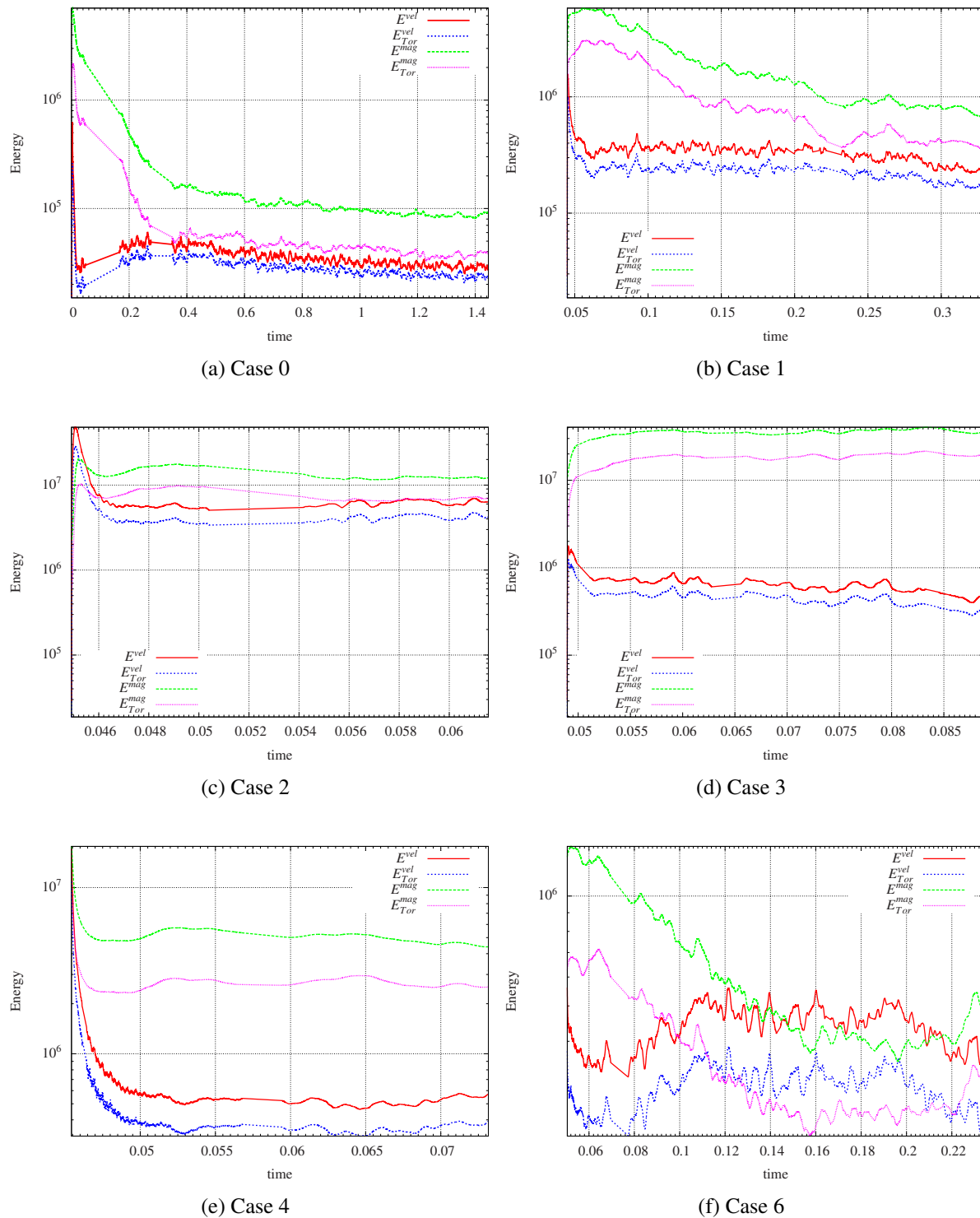
Figure 5.4: *Time evolution of the Magnetic and Kinetic energies, E_{kin} and E_{mag}, the toroidal part of energies is denoted by the superscript ^{Tor}. In all cases, the red line shows the total kinetic energy, the blue line shows the toroidal component of the kinetic energy, the green line shows the total magnetic energy and the magenta line shows the toroidal component of the magnetic energy.*

(a) Case 0

(b) Case 1

(c) Case 2

(d) Case 3

(e) Case 4

(f) Case 6
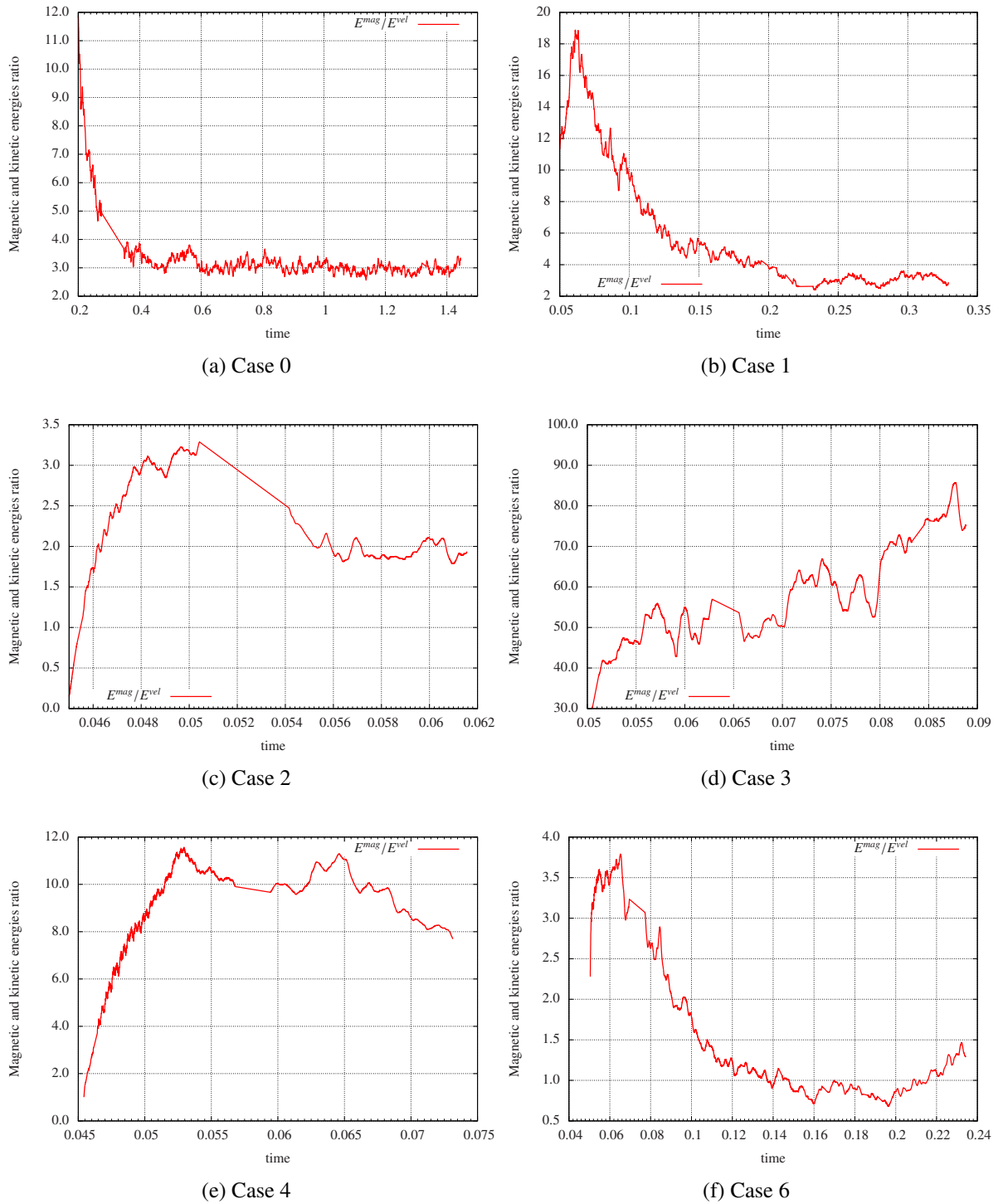
Figure 5.5: *Time evolution of the ratios of the magnetic and kinetic energies: E_{mag}/E_{kin}.*

selves. E.g. cases 3 , 4 and 6 are shown to be less equillibrated than other runs.

5.3.3   Energy spectra

Spatially random flows can be replaced by well-chosen coherent structures with virtually no impact on the kinetic energy spectrum but a huge influence on the generation of the magnetic field. An illustration of the non-uniqueness of spectra in the sense that two radically different flows can share the same spectrum can be found for instance in Tobias and Cattaneo (2008). Thus, an energy spectrum doesn't have a one-to-one correspondence to a flow. The fundamentally limited role played by spectra in dynamo theory should be remembered: a spectrum is an integrated property of fields, therefore it looses a portion of useful information. Nevertheless, the energy spectrum is an important instrument (e.g., in a turbulence theory and in understanding the transfer of energy between scales) and therefore time-averaged energy spectra for all our runs are presented in this section.

The usual way to utilise spectra in numerical simulations is as convenient measure of convergence. The numerical decomposition is essentially limited, however if the smallest scales contain much less energy (orders of magnitude less) than the largest scales, the simulation is thought to be well resolved.

A less prosaic way to use spectral representations in hydrodynamical theories was inspired by the influential work of Kolmogorov (1941). This outstanding example of dimensional analysis suggests that the

Name	R_m	R	l_{Ohmic}	$l_{Kolmogorov}$
Case0	63	315	22	74
Case1	180	902	49	164
Case2	933	4665	168	564
Case3	254	254	63	63
Case4	274	5492	67	638
Case6	224	4495	58	549
HYDRO		457		98

Table 5.10: *Estimations of the Kolmogorov ($R^{3/4}$) and Ohmic ($R_m^{3/4}$) harmonic degrees corresponding to lengthscales L_K and L_m.*

spectral slope (which we define as $d \log E(l)/d \log l$) of a turbulent isotropic flow is $-5/3$, meaning that the energy spectral density $E(l)$ is proportional to $l^{-5/3}$. This behaviour shows up most clearly in the so-called *inertial range* of scales, where viscosity has no affect. [2]

Several characteristic length scales divide magnetic and velocity spectrum in regions. Kol-

---

[2]The assumption of Kolmogorov is that spectral energy density of a chaotic turbulent flow in the inertial range (where lengthscales are sufficiently large to ignore viscosity) has self-similar scale-independent behaviour and depends only on the wave number k and dissipation of energy ϵ, i.e. $E(k) = C\epsilon^x k^y$ with non-dimensional constant C and powers x and y which can be found by dimensional analysis. The last equation in SI-units is $\frac{m^3}{s^2} = \left(\frac{m^2}{s^3}\right)^x \left(\frac{1}{m}\right)^y$. It follows from here that $\begin{cases} 3 = 2x - y \\ 2 = 3x \end{cases} \Rightarrow \begin{cases} y = -5/3 \\ x = 2/3 \end{cases}$. The resulting spectral slope is $-5/3$, in other words the energy which is associated with the scale L is proportional to the $L^{5/3}$ (or $k^{-5/3}$).

mogorov's length scale [3] L_K is $R^{-3/4}$ (where $R = (Ud)/\nu$ is the *Reynolds number*, it equals the rms velocity in our non-dimensionalisation), smaller scales are dominated by viscosity (correspondingly "-5/3" behaviour should be at scales $> L_K$). Similarly, at length scales smaller than $L_m = R_m^{-3/4}$ the Ohmic dissipation starts to be the dominant effect on the magnetic energy. Estimations of the spherical harmonic degrees corresponding to the length scales L_K and L_m in our dynamos are presented in the table (5.10).

We now discuss the spectra in fig.(5.6). In Case 0 we can clearly see an abrupt decrease of both the magnetic and kinetic energy at $l \approx 150$ (fig. 5.6a), approximately twice the value of L_K estimated in table (5.10). The Kolmogorov's length scale L_K can apparently only be resolved in the lowest $Ra = 219.7$ cases: 0, 3 and HYDRO. The entire kinetic spectra in the runs with higher Ra appear to be in the inertial range where they could be expected to show Kolmogorov's "$-5/3$", if magnetic forces are not too influential and if turbulence is isotropic enough at the length scale considered (and if no other reasons invalidate Kolmogorov's assumptions). It is shown below that the Kolmogorov's kinetic energy slope confidently matches the results from only one of our simulations.

Moving on to consider the magnetic energy spectrum, Moffatt (1961) has pointed out that in a kinematic regime, the magnetic spectrum slope in the interval between wave numbers $l_K = L_K^{-1} \ll l_m$ and $l_m = L_m^{-1}$ can equal the velocity spectrum slope minus two . This rule works only if the back-reaction of the magnetic field on the flow field is negligible. Giving Kolmogorov's turbulent slope "$-5/3$", the predicted slope of the magnetic field is "$-5/3 - 2 = -11/3$".

We have an interesting example where Kolmogorov's velocity and Moffatt's magnetic spectrum slopes seem to arise in our numerical experiments. The velocity spectrum presented in fig.(5.6a, Case 0) is in fact for two cases: when magnetic field is turned on and also when it is turned off (case HYDRO). Without a magnetic field the kinetic energy slope matches "$-5/3$". Including a dynamo generated magnetic field reduces the kinetic energy slope down to "$-4/3$". The associated magnetic spectrum slope is slightly less than the "$-11/3$" predicted by simply Moffatt (1961) theory to the Kolmogorov spectrum. However, if one takes into account that the kinetic energy slope is reduced in comparison with the purely hydrodynamic case, the theoretical prediction of the slope of the magnetic energy spectrum becomes "$-4/3 - 2 = -10/3$", what explains our results well.

The strongly driven Case 2 with $Pr_m = 0.2$ has a kinetic energy spectrum that is surpris-

---

[3]It is easy to get the expression $L_K = R^{-3/4}$ for the length scale at which viscosity becomes dominant in the same scale-analysis manner as for the Kolmogorov's spectrum. Let us suppose that the viscous cut-off length scale depends only on the dissipation of energy ϵ and the viscosity ν, i.e. dimensional $L_K^* = \epsilon^x \nu^y$. Checking the correctness of dimensions, we get in SI-units $m = (m^2/s^3)^x (m^2/s)^y$. The resulting equations for unknowns are $\begin{cases} 1 = 2x + 2y \\ 0 = 3x + y \end{cases} \Rightarrow \begin{cases} y = 3/4 \\ x = -1/4 \end{cases}$. Eventually, $L_K^* = \epsilon^{-1/4} \nu^{3/4}$. The dissipation of energy ϵ can be estimated by $\dfrac{U^2}{t} = \dfrac{U^2}{L/U} = \dfrac{U^3}{L}$. Then, $L_K^* = \left(\dfrac{\nu^3 L}{U^3}\right)^{1/4} = \dfrac{L}{R^{3/4}}$, and non-dimensional Kolmogorov's length-scale is $L_K = R^{-3/4}$.

ingly close to Kolmogorov's "$-5/3$". The predicted Kolmogorov scale $L_K = 564$ is far beyond the right boundary of the plot so obtaining a spectrum slope "$-5/3$" seems quite reasonable. Magnetic dissipation is predicted to dominate at length-scales above the wavenumber $l = 168$, and thereafter a magnetic energy slope that appears to be consistent with $-11/3$ is seen close to the right boundary of the plot.

In Case 1 I can't find any wide range where the slope "$-5/3$" appears. It is tempting to explain this by the action of the magnetic force. However, comparing F_{Cor}/F_{Lor} in the table (5.6) for the Case2 ($F_{Cor}/F_{Lor} = 2$) and Case1 ($F_{Cor}/F_{Lor} = 13$), we see that the Lorentz force is actually more influential in Case 2 where Kolmogorov's slope approximately survives.

Case 3 is exceptional, because $Pr_m = 1$ and correspondingly the magnetic and velocity dissipation length scales L_K and L_m are identical. The velocity spectral slope appears to change over the entire range and it is not obviously in correspondence with Kolmogorov's "$-5/3$". Moffat's predictions are not applicable since $L_K = L_m$.

Case 4 has the lowest Ekman number. The influence of the rotation should be the strongest amongst the runs under consideration. In this case we might expect a slope of the kinetic energy spectrum steeper than Kolmogorov's (we refer here to paragraphs below). The experiment demonstrates the contrary: the slope of the fig.(5.6, Case 4) is less steep than Kolmogorov's (this was also found early in Case 0, where again rotation was dominant). The magnetic spectrum is also less steep than Moffatt's classical $-11/3$ over a large part of the wave number range.

Case 6 has the lowest magnetic Prandtl number, i.e. highest magnetic diffusion. At the same time Ra takes its maximal value. A higher Ekman number distinguishes the Case 6 from the Case 4. The kinetic slope is in this case close to Kolmogorov's $-5/3$, but not exactly linear. The magnetic slope is also fairly close to Moffatt's "$-11/3$" over the range between $l = 40$ and $l = 200$.

Arguments for a kinetic energy spectrum slope "$-5/3$" come from the postulation of the isotropic turbulence. Rotation-dominated turbulence on the other hand has a preferential direction and involves another type of energy transfer between scales. Kinetic Energy spectrum slopes of "-2" have been proposed (Zhou, 1995; Morize et al., 2005). Dimensional arguments also exist for even steeper slopes[4]. The influence of rotation should be strongest in cases, when the Ekman number is the lowest (case 4) and where the driving is the weakest (favouring the Coriolis force rather than inertia; cases 0, 3 and HYDRO). But we find the kinetic energy spectrum slopes to be less steep in our low Ra, rotation-dominated, cases.

At scales larger than L_m Moffatt (1961) predicts a magnetic energy spectrum slope of "$1/3$", but we observe non-monotonic behaviour of spectra at larger length scales. Best fit lines with slope $\sim l^{1/3}$ are nevertheless shown in fig.(5.6). We find a $l^{1/3}$ slope seems reasonable only

---

[4]The dimensional argument for the turbulence subjected to a strong rotation comes from the hypothesis $E(l) \sim \Omega^x l^y$, or dimensionally $\frac{m^3}{s^2} = \left(\frac{1}{s}\right)^x \left(\frac{1}{m}\right)^y$. The resulting dependence is $E(l) \sim \Omega^2 l^{-3}$.

at very low degree before a maximum in the magnetic energy spectrum is obtained, usually around degree 10. Thereafter the slope turns over, and becomes increasingly negative with increasing degree.
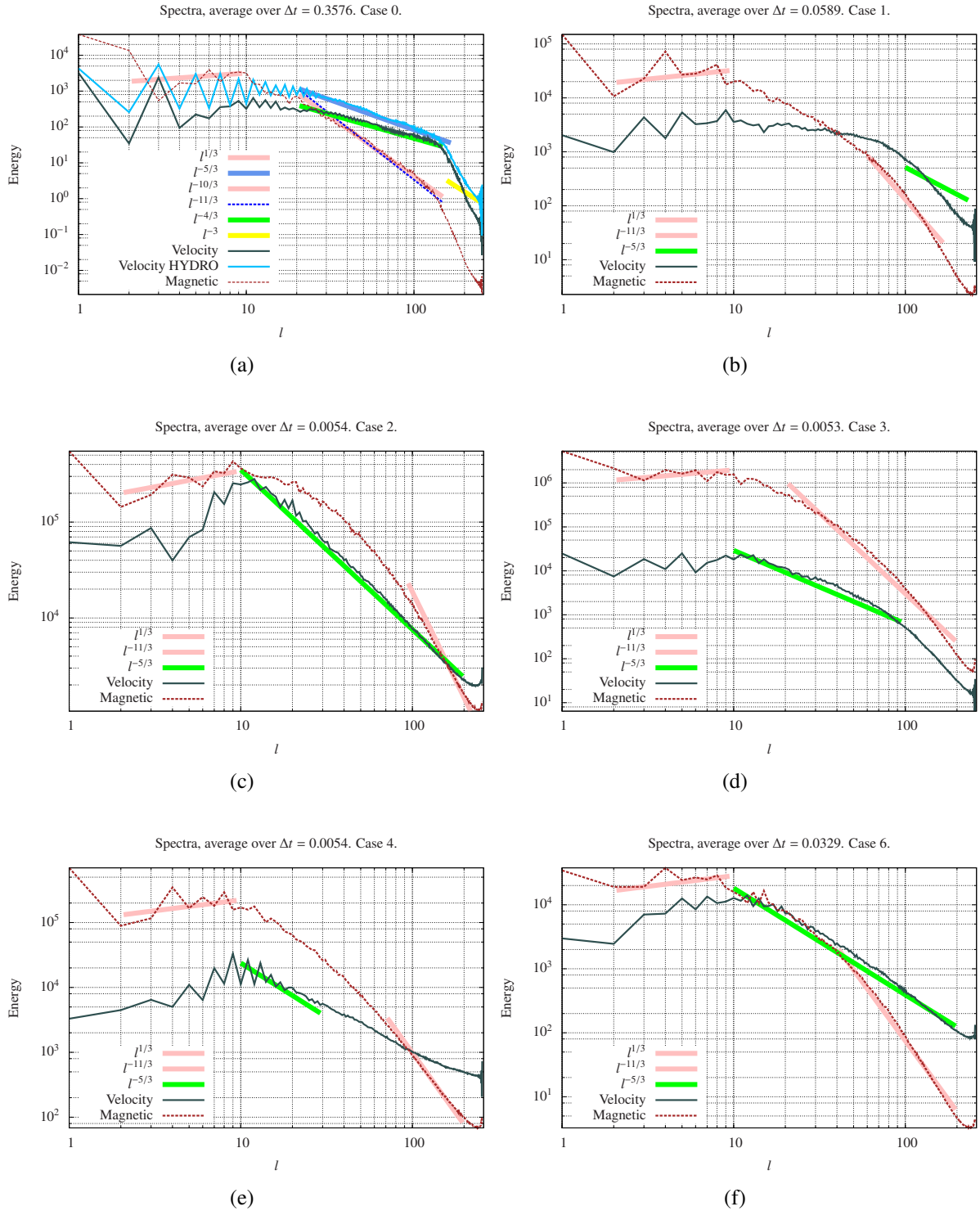
Figure 5.6: *Time-averaged (end of the run) magnetic and kinetic spectra (energy vs. l).*

5.3.4   Tests of existing rotating convection and dynamo scaling laws

Scaling laws are the expression of physical principles in homogeneous functions. A function $f(x)$ is homogeneous if $f(\alpha x) = \alpha^k f(x)$. A few power scaling laws can be explained theoretically but many are entirely empirical. Many phenomena that are encountered in the real world vary over an enormous range of scales, but nonetheless behave similarly. For large parameter ranges a log-log scale is usually adopted, and on this scale power laws are linear. In this section we present several previously proposed scaling laws from the literature and check their relevance for our MHD dynamo models.

5.3.4.1   Convection power scaling laws

The convective power or the work done by the buoyancy force is the source of energy in the Navier-Stokes equation. In thermally-driven convection (as opposed to e.g. magnetically-driven convection, when magnetic energy comes through the boundaries and drives flows) the convective power is the total useful energy which comes into the system. Eventually the energy produced by this power is distributed in kinetic and magnetic forms and vanishes by Ohmic and viscous dissipations and, due to the diffusion of magnetic energy, outwards from the shell (this later is a tiny part in comparison with other losses[5] , see table 5.11 and figure 5.8). If one has access to the convective power, the one can expect that the magnetic and kinetic energies satisfy some simple relations based on this power.

Aubert et al. (2009) proposes the following scaling laws (the best fit and 3σ lines):

$$Ro^{Aub} = (0.69, 1.31, 2.49)p^{0.42} \tag{5.5}$$

$$Lo/f_{Ohm}^{1/2} = (0.62, 1.17, 2.22)p^{0.34} \tag{5.6}$$

$$\tau_{diss}/\tau_{mag} = (0.11, 0.26, 0.65)R_m^{-1.0} \tag{5.7}$$

All values above (eq.5.5-5.7) are in Aubert et al. (2009)'s nondimensionalization. The definitions and conversions to our non-dimensionalization are introduced in the Appendix C.4.

The third scaling law eq.(5.7) doesn't involve the convective power. It relates the magnetic dissipation time in magnetic units d^2/η to the average speed of the fluid. The Ohmic

---

[5]The total magnetic energy dissipation is $\mathbf{B} \cdot \nabla^2 \mathbf{B} = -\mathbf{B} \cdot (\nabla \times [\nabla \times \mathbf{B}]) = \nabla \cdot (\mathbf{B} \times [\nabla \times \mathbf{B}]) - [\nabla \times \mathbf{B}]^2$ (identity $\mathbf{B} \cdot \nabla \times \mathbf{A} = \nabla \cdot (\mathbf{A} \times \mathbf{B}) + \mathbf{A} \cdot \nabla \times \mathbf{B}$ is used). Diffusion through shell boundaries is proportional to $\mathbf{P} = \int_{\partial V} \mathbf{B} \times [\nabla \times \mathbf{B}]d\mathbf{S} = \int_{\partial V} \mathbf{B} \times [\mathbf{E} + \mathbf{u} \times \mathbf{B}]d\mathbf{S} = -\int_{\partial V} \mathbf{E} \times \mathbf{B}d\mathbf{S}$. We have obtained the Umov-Poynting vector integrated over the surface of the shell. It represents directional energy flux density of an electromagnetic field. Diffusion flux energy losses $\mathbf{P}$ in contrast to other sinks of energy are scaled by the magnetic field on boundaries where it is smaller than inside. Consequently $\mathbf{P} \ll \int_V -[\nabla \times \mathbf{B}]^2 dV$, the Umov-Poynting flux is much less than Ohmic heat losses.

dissipation time in units of the magnetic diffusion time scale is:

$$\tau_{diss} = E_{mag}/D_{mag} = \frac{\int \mathbf{B}^2/2\mathrm{dV}}{\int \mathbf{B}\boldsymbol{\nabla}^2\mathbf{B}\mathrm{dV}} \sim \frac{B^2/2}{B^2/\ell_B^2} = \frac{\ell_B^2}{2} \tag{5.8}$$

Figure 5.7a shows how this proportionality $\tau_{diss} \sim \dfrac{\ell_B^2}{2}$ is satisfied in our simulations.

(a)   (b)
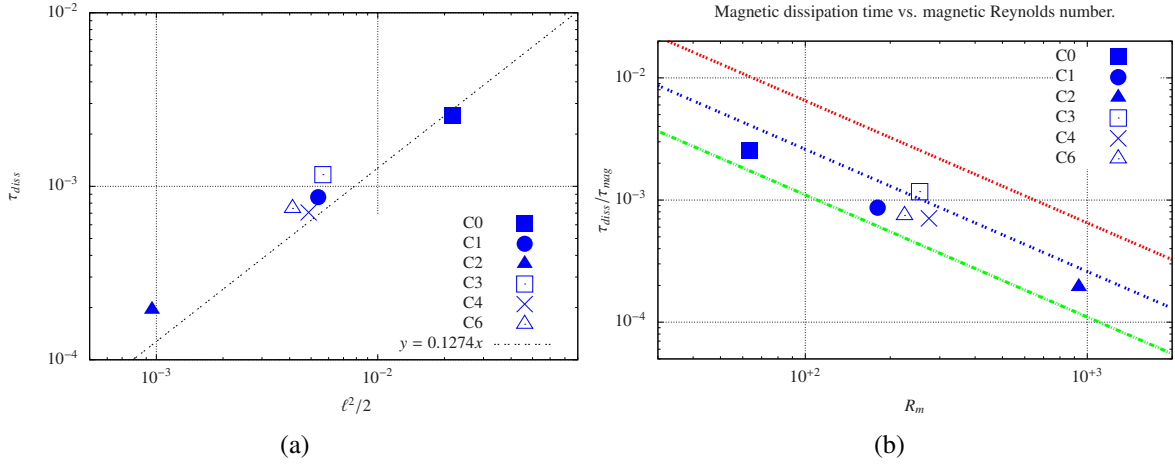
Figure 5.7: *(a) Dissipation time and its estimation via typical magnetic scale. (b) Correlation between magnetic dissipation time and magnetic Reynolds number.*

Experimental points for the dissipation time scaling law eq.(5.7) are shown in fig.(5.7b). Recalling the scaling $\tau_{diss} \sim \dfrac{\ell_B^2}{2}$ we conclude that $R_m \sim \ell_B^{-2} \sim m_B^2 + l_B^2$, that is to say the rms velocity is inversely proportional to the square of the mean length scale in the magnetic energy spectrum. In fact, two times smaller structures correspond to four times higher mean velocities according to $R_m \sim \ell_B^{-2}$.

Name	$D_{mag} + D_{kin}$	$\hat{p}$
Case0	$7.444e + 07$	$7.420e + 07$
Case1	$1.370e + 09$	$1.376e + 09$
Case2	$7.655e + 10$	$7.754e + 10$
Case3	$3.300e + 10$	$3.547e + 10$
Case4	$6.924e + 09$	$6.889e + 09$
Case6	$7.851e + 08$	$7.840e + 08$

Table 5.11: *Dissipation and the convective power. Values are slightly different due to the magnetic energy flux through the shell boundaries. $\hat{p}$ is the value of the convective power in our non-dimensionalization.*
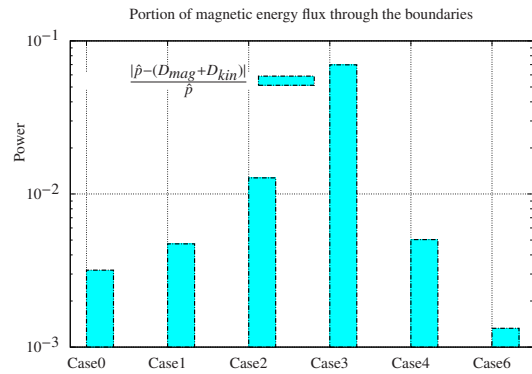
Figure 5.8: *Difference between the convection power and the sum of Ohmic and viscous dissipations normalised by the convective power.*

Aubert et al. (2009) provide an analytic formula for the convective power eq.(C.38) which does not work well for our dynamos. The internal heating is absent in the formula and this is likely to be the reason for discrepancy. Moreover fig.(5.9) shows that the convective power can not be satisfied by a linear relation of the form $p = \gamma Ra_Q$ (experimental points are not on the same line). The power law dependencies seem to be different for the low Ra dynamos and the high Ra dynamos. It might be because some of these dynamos are not at well-mixed (isentropic) state that Aubert et al. (2009) assume. We therefore resort to using the convection power $p \sim \frac{1}{V} \int_V u_r T r \mathrm{d}V$ calculated by the numerical integration over the shell volume V for input to the scaling laws fig.(5.10).
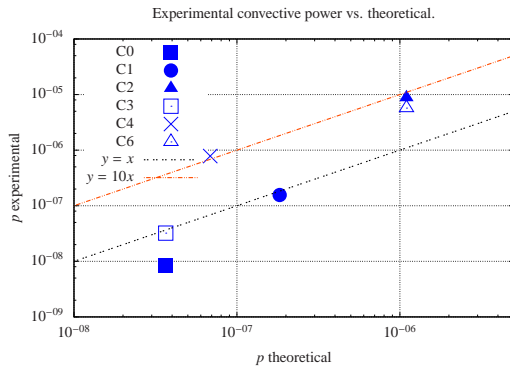
Name	p exper.	p analyt.
Case0	$8.420e - 09$	$3.659e - 08$
Case1	$1.560e - 07$	$1.829e - 07$
Case2	$8.800e - 06$	$1.098e - 06$
Case3	$3.220e - 08$	$3.658e - 08$
Case4	$7.820e - 07$	$6.860e - 08$
Case6	$5.700e - 06$	$1.098e - 06$

Figure 5.9: *Convection power: theoretical (γRa_Q) and values calculated from numerical experiments $\left(8Ro^2 qRa \frac{1}{V} \int_V u_r T r \mathrm{d}V \right)$, the values are in the units of Aubert et al. (2009).*

The convective power scaling laws suggested by Aubert et al. (2009) are generally satisfied by our dynamos. But note that the use of a log-log scale and large error allowances leave a lot of freedom for these scaling laws.

(a) *Ro* vs p (b) $Lo/f_{Ohm}^{1/2}$ vs p
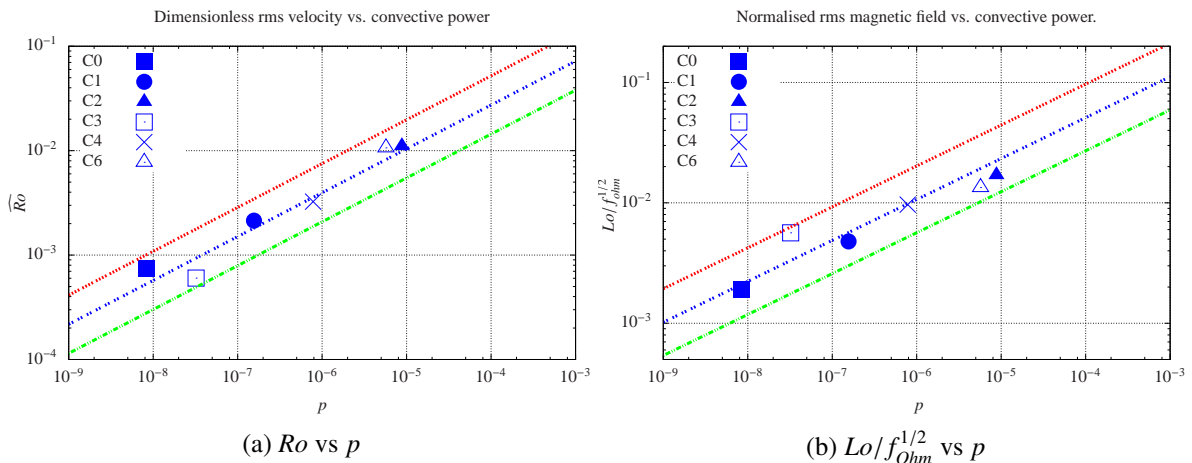
Figure 5.10: *Test of the Aubert et al. (2009) convective power scaling laws for the five dynamo cases reported in this chapter.*

5.3.4.2 Influence of the Lorentz force: Dynamic Elsasser number

Soderlund et al. (2012) have shown that a classical Elsasser number doesn't properly represent the ratio of the Lorentz and Coriolis forces when the magnetic Reynolds number R_m is high. The Elsasser number is defined as a non-dimensional estimate of the ratio of Coriolis and Lorentz forces:

$$\frac{1}{\mu_0}(\nabla \times \mathbf{B}) \times \mathbf{B} \quad \text{Lorentz force}$$
$$-2\rho(\Omega \times \mathbf{u}) \quad \text{Coriolis force}$$
(5.9)

The ratio of these forces can be evaluated in two different ways. If magnetic Reynolds number R_m is small (as happens when velocity is small or/and magnetic diffusion is large), then we can evaluate $\mathbf{u}$ as η/d and $\mathbf{B} \cdot \nabla$ as B/d. And the ratio of Lorentz to Coriolis forces in such assumption is the classical[6] Elsasser number (symbols on the rhs are in this case dimensional):

$$\Lambda = \frac{\frac{1}{\mu_0}B\frac{1}{d}B}{2\rho\Omega\frac{\eta}{d}} = \frac{B^2}{2\rho\mu_0\Omega\eta}$$
(5.10)

If on the other hand R_m is large, gradients are much larger and should be estimated using the length scale of the field's features, i.e. $(\nabla \times \mathbf{B}) \times \mathbf{B} \sim B^2/\ell_b$. In this case u_{rms} will be used as a typical velocity instead of the diffusion scale η/d:

$$\Lambda_d = \frac{\frac{1}{\mu_0}B\frac{1}{\ell_b}B}{2\rho\Omega u_{rms}} = \frac{B^2}{2\rho\mu_0\Omega u_{rms}\ell_b}$$
(5.11)

where

$$\ell_b = \frac{\pi d}{2\sqrt{l_b^2 + m_b^2}}$$
(5.12)

With our choice of non-dimensionalization, this results in a dynamic Elsasser number:

$$\Lambda_d = \frac{B^2}{u_{rms}\ell_b}$$
(5.13)

Soderlund et al. (2012) show an almost perfect one-to-one correlation between the ratio F_l/F_c and Λ_d for a collection of numerical dynamos. We have plotted the same correlation for our dynamos in fig.(5.12). The dynamic Elsasser number systematically slightly underestimates the ratio F_l/F_c for the presented simulations. This means that either $u_{rms} > \frac{1}{V}\int|\hat{\mathbf{z}} \times \mathbf{u}|dV$ or $B_{rms}^2/\ell_b < \frac{1}{V}\int|(\nabla \times \mathbf{B}) \times \mathbf{B}|dV$. The first inequality is obviously true simply because the magnitude of the vector $\mathbf{u}$ is larger or equal to it's component $|\hat{\mathbf{z}} \times \mathbf{u}|$. The second inequality is also true for our dynamos (see fig.5.11). It means that there is an important

---

[6]Classical Elsasser number is called also "imposed" in Soderlund et al. (2012) since it is usually used if a large scale magnetic field is imposed.

influence of magnetic scales smaller than ℓ_b.

Nevertheless, the ratio of Lorentz and Coriolis forces conforms to a linear relation $F_l/F_c = $ const $\cdot \Lambda_d$ very well, with const ≈ 2. The fact that all the studied dynamos obey the same simple rule tells us that the ratio between mean values of forces and the estimates are a geometrical property of magnetic and velocity fields that stays approximately constant in the region of parameters under consideration. We note in passing that the dynamos studied here have fairly modest R_m compared to those considered by Soderlund et al. (2012). At higher R_m the estimation of F_l/F_c by Λ_d is expected to be better.

Figure (5.12) shows that the traditional Elsasser number[7] $\Lambda = B^2$ severely overestimates the ratio F_l/F_c. It means that the estimation of the non-dimensional product $u_{rms}\ell_b$ in eq.(5.13) by unity = [unit velocity $\cdot$ unit length] to get the traditional Λ is not adequate for highly driven dynamos where u_{rms} is large in comparison with the typical wavenumber of magnetic diffusion[7] l_b.

Our conclusion is that the dynamic Elsasser number serves as a much better measure of the influence of the Lorentz force in comparison with the Coriolis force than does the traditional Elsasser number. The problem with using the dynamic Elsasser number in the context of a scaling law is in the nature of values in the definition: they are experimental. We don't know a rigorous or even approximate way to get the rms magnetic field or velocity from basic parameters (unless using other empirical scaling laws). Essentially, use of the dynamic Elsasser number doesn't bring the new predictive ability we desire from a scaling law.
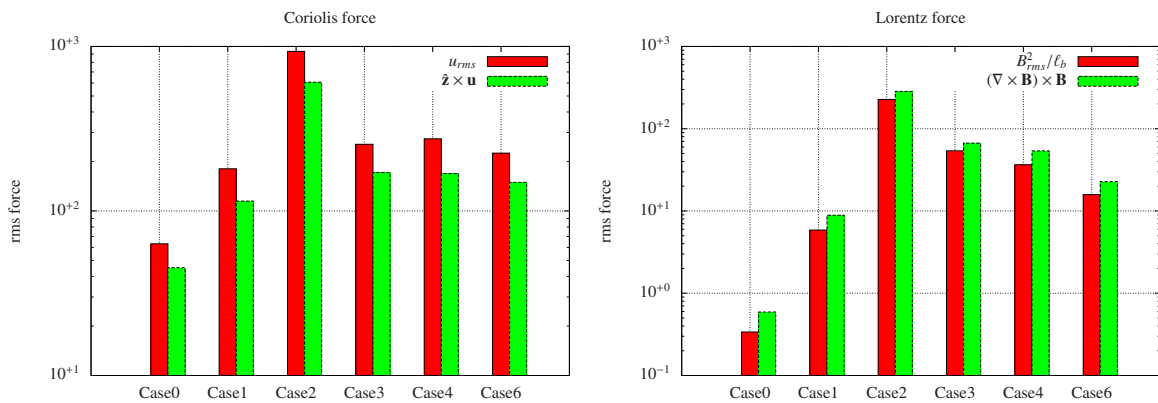
Figure 5.11: *Experimental rms Coriolis and Lorentz forces and their estimates.*

5.3.4.3 Heat transport scaling law

In this section we check properties of our dynamos against scaling laws recently proposed by Stelzer and Jackson (2013). A set of dynamos relevant for the Earth was chosen from a large database of numerical simulations in order to derive these scaling laws.

---

[7]The discussion is in terms of the non-dimensionalization chosen in section 5.2.
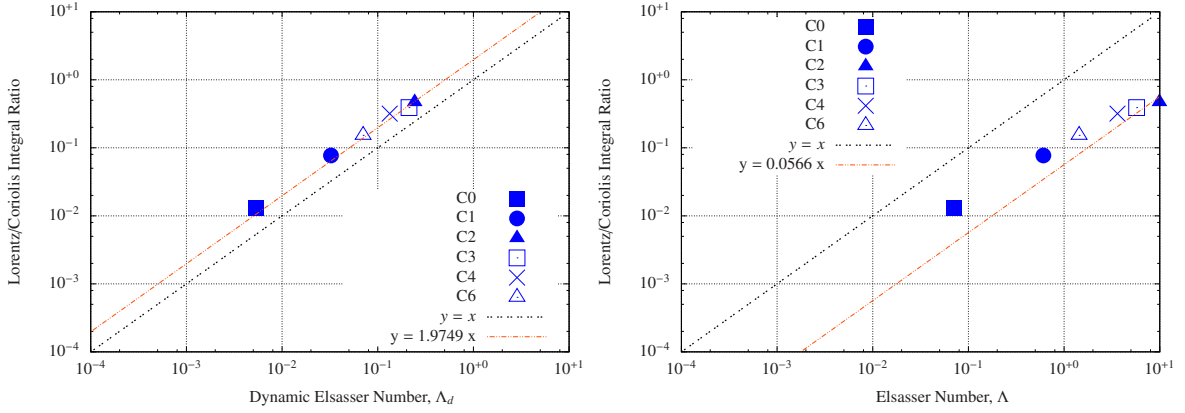
Figure 5.12: *Soderlund et al. (2012), Lorentz/Coriolis Integral Ratio F_L/F_C vs Dynamic Elsasser Number Λ_d. Dynamic Elsasser numbers plotted against the Lorentz to Coriolis force integral ratios for all dynamo models. The dashed black line indicates one-to-one correlation.*

Before obtaining the relevant scaling parameters, we need to define the following values: the modified Nusselt number Nu^* and the modified flux-based Rayleigh number Ra_Q^*. The dimensional total heat flux (radii with tildes are dimensional) is:

$$Q = -4\pi \widetilde{r}_o^2 \rho C_p \kappa \left. \frac{\partial T}{\partial r} \right|_{r_o} \frac{\Delta T}{d} \qquad (5.14)$$

where C_p is the heat capacity, κ is thermal diffusivity, ΔT and d are units of temperature and length correspondingly. As a measure of the total heat flux we use the thermal energy flux through the outer boundary of the convective shell[8]. The minus in eq.(5.14) appears because Q should be positive but $\frac{\partial T}{\partial r} < 0$, i.e. temperature decreases in the direction from the inner to the outer boundary of the convective shell.

The dimensional conductive heat flux is defined as:

$$Q_{cond} = 4\pi \widetilde{r}_o \widetilde{r}_i \rho C_p \kappa \frac{\Delta T}{d} \Delta T_{io} \qquad (5.15)$$

We have used definition of the conductive heat flux by Christensen and Aubert (2006) replacing ΔT by $\Delta T \Delta T_{io}$ to account for the fact that we are keeping heat flux instead of temperature constant on the outer boundary. ΔT_{io} is the non-dimensional experimental temperature difference between inner and outer boundaries of the convective shell, whereas ΔT is the dimensional temperature scale used for the non-dimensionalization .

---

[8]The heat flux equation is $\left(\frac{\partial}{\partial t} - q\nabla^2 \right) T = S_h - \mathbf{u} \cdot \nabla T$. In a quasi-stationary state $\int_V \frac{\partial T}{\partial t} dV = 0$, if no-slip boundary condition is applied $\int_V \mathbf{u} \cdot \nabla T dV = \int_{\partial V} \mathbf{u} T d\mathbf{S} = 0$ and the integrated heat flux equation is $-q \int_{r_i} \left. \frac{\partial T}{\partial r} \right|_{r_i} dS + S_h V = -q \int_{r_o} \left. \frac{\partial T}{\partial r} \right|_{r_o} dS$, or $Q_i + Q_{int} = Q_o$ the sum of heat from the internal heating and from inner core equals the heat leaving through the outer boundary. The total heat flux in a quasi-stationary case is either the left or the right side of the last equation. It is interesting that unlike in a heat engine, no heat energy is consumed during the operation of a dynamo in the Boussinesq approximation. Heat flows through the system without any losses due to mechanical work.

The convective heat flux is the difference between the total heat flux and the conductive heat flux.

$$Q_{conv} = Q - Q_{cond} = 4\pi\widetilde{r}_o\rho C_p\kappa\frac{\Delta T}{d}(-\widetilde{r}_o\frac{\partial T}{\partial r} - \widetilde{r}_i\Delta T_{io}) \tag{5.16}$$

The convective heat flux Q_{conv} is used in the definition of the modified Nusselt number Nu^*:

$$Nu^* = \frac{1}{4\pi\widetilde{r}_o\widetilde{r}_i}\frac{Q_{conv}d}{\rho C_p\kappa\Delta T} \cdot \frac{\kappa}{2\Omega d^2} = \left(-\frac{1}{c}\frac{\partial T}{\partial r} - \Delta T_{io}\right)Ro \cdot q \tag{5.17}$$

The conventional Nusselt number uses the total heat flux Q (definition from Christensen and Aubert, 2006):

$$Nu = \frac{1}{4\pi\widetilde{r}_o\widetilde{r}_i}\frac{Qd}{\rho C_p\kappa\Delta T} = -\frac{\widetilde{r}_o}{\widetilde{r}_i}\frac{\partial T}{\partial r}\bigg|_{r_o} = -\frac{1}{c}\frac{\partial T}{\partial r}\bigg|_{r_o} \tag{5.18}$$

The modified Rayleigh number defined by Christensen and Aubert (2006) is:

$$Ra^* = \frac{\alpha g\Delta T}{\Omega^2 d} = \frac{g\alpha\Delta T d}{2\Omega\kappa}\frac{\eta}{2\Omega d^2}\frac{\kappa}{\eta} = Ra \cdot Ro \cdot q \tag{5.19}$$

And the modified heat-flux based Rayleigh number also by Christensen and Aubert (2006) is:

$$Ra_Q^* = Ra^* \cdot Nu^* = \left(-\frac{1}{c}\frac{\partial T}{\partial r} - \Delta T_{io}\right) \cdot (Ro \cdot q)^2 \cdot Ra \tag{5.20}$$

The following scaling laws were suggested by Stelzer and Jackson (2013):

$$\begin{aligned} Ro^C = 2u_{rms}Ro &= 1.16 \cdot Ra_Q^{*0.44}P_m^{-0.13} \\ Lo/f_{Ohm}^{1/2} &= 0.60 \cdot Ra_Q^{*0.31}P_m^{0.16} \\ Nu^* &= 0.075 \cdot Ra_Q^{*0.51}E^{0.03} \end{aligned} \tag{5.21}$$

and these will now be compared with our numerical calculations. Ro^C is the Rossby number as defined by Stelzer and Jackson (2013) or Christensen and Aubert (2006). Figure 5.13 shows our attempt to test scaling laws eq.(5.21). An order of magnitude agreement is obtained, but the scalings appear less appropriate for our dynamos than for the database of numerical calculations chosen as the input to construct the scaling laws by Stelzer and Jackson (2013).

The reason for the disagreement could be due to the fact that the considered scaling laws were obtained for dynamos with constant temperature on the both sides of the convective shell, while our dynamos have constant heat flux on the outer boundary. For this reason the average temperature on the outer boundary was measured in the numerical experiments and used to calculate ΔT_{io}. The assumption that the change of the boundary condition makes little difference if ΔT_{io} is properly calculated could be too bold (indeed, Sakuraba and Roberts, 2009 shows a huge difference between dynamos with the fixed temperature and fixed heat flux), but it is the usual way to compare calculations with different temperature boundary conditions.

(a) Heat transport

(b) Flow velocity

(c) Magnetic field strength
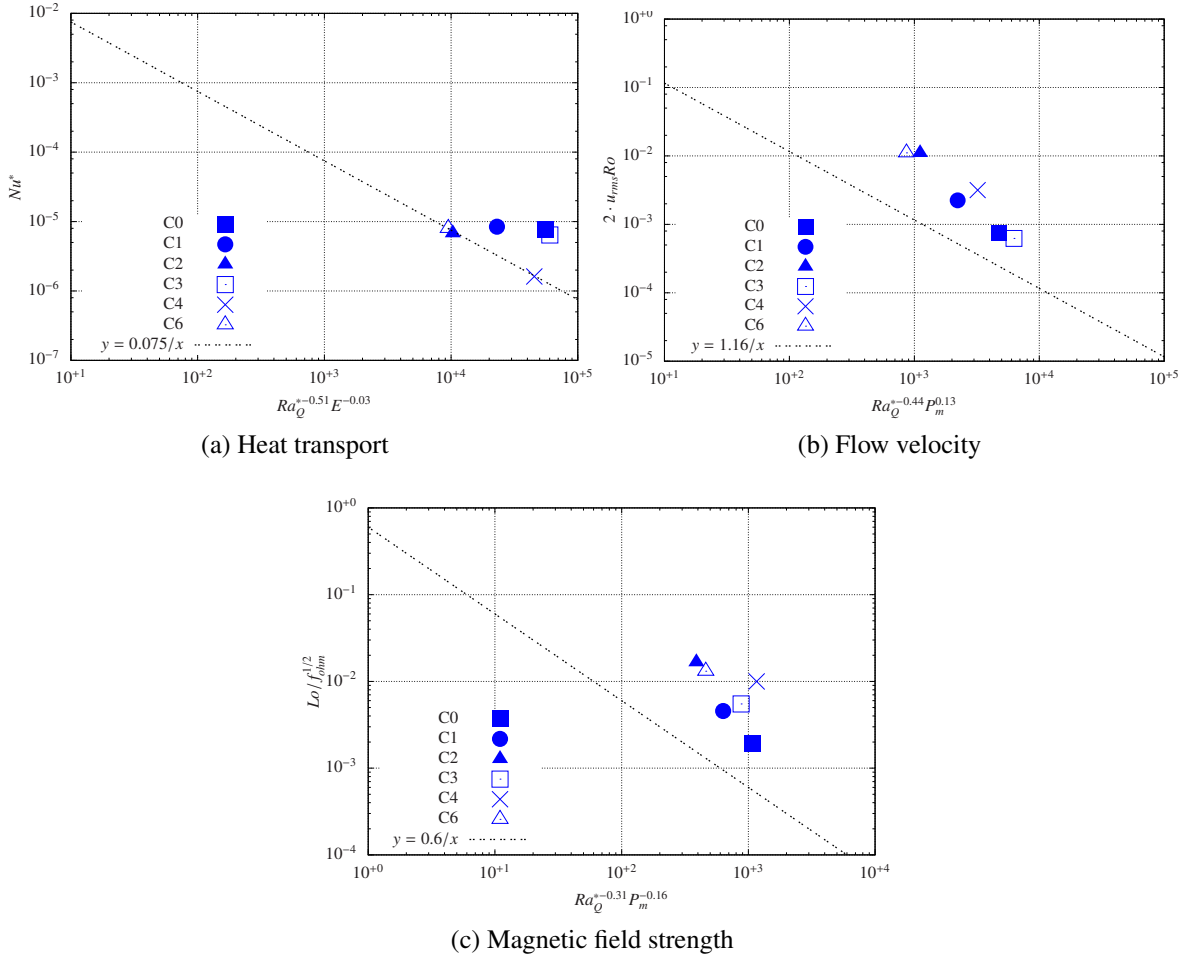
Figure 5.13: *Scaling laws of Stelzer and Jackson (2013), eq.(5.21). To ease comparison, scales of the axes are the same as in the original paper.*

5.3.4.4 Conclusions, scaling laws

The presented scaling laws can be divided into two classes: those empirically constructed from basic parameters (Stelzer and Jackson, 2013) and those based on some physical considerations but dependent on experimental measurements (Soderlund et al., 2012; Aubert et al., 2009).

Empirical scaling laws employ only dimensional considerations. The basic parameters are already non-dimensional, so any combination of $Ra^x q^y Ro^z E^j$ would have right dimensions. Having enough statistics, we can find best-fit values for x, y, z, j. But it is hard to believe that a sophisticated dynamo mechanism having several possible solutions for the same set of parameters (depending on the initial conditions and even a random numerical noise) should satisfy a mix of powers of static basic parameters. Particular scaling laws may possibly work only for certain dynamo regimes, started from particular initial conditions and have no relevance for other solutions. Dynamos can also be subject to regime changes (e.g. onsets of different types of convection) and moreover the hysteresis or history is important. It seems rather optimistic to believe that a simple empirical scaling law can provide general prediction, and it may simply be good fortune that they seem to work well over certain limited parameter ranges.

The Aubert et al. (2009) scaling laws in subsection 5.3.4.1 comply with our dynamos better than other presented scaling laws, when the experimental value of the convection power is used. These show importance of the value of the total mechanical power generated by the temperature field. A prior knowledge of the buoyancy power excludes the heat flux equation from the analysis. Temperature is not a passive constant and the experimental value for the convective power $\int T\mathbf{u} \cdot \mathbf{r}dr$ can be something more complicated than the suggested γRa_Q^*, i.e. a shell's geometry constant times the heat flux based Rayleigh number. We have found the theoretical formula for the buoyancy power inappropriate for our dynamos. The disadvantage of scaling laws by Aubert et al. (2009) is that two experimental values are related: buoyancy power vs. rms velocity or rms magnetic field; rms velocity vs. magnetic dissipation time. Although experimental points are exactly in the predicted places, the predictive ability is limited. Having one experimental value, another one can be fairly well estimated. But it is impossible using this approach to predict experimental properties having only the control parameters from the governing equations.

5.3.5 Structural features of dynamos and their components

The magnetic field on the outer boundary of the computational domain is of great importance in attempts to understand the mechanism underlying the generation of the Earth's magnetic field. The only segment of the magnetic field in the Earth's core which can in some way be observed from the planet's surface is the large scale poloidal field at the Core-Mantle-Boundary. The largest scale harmonics of this field can be obtained as a solution of the Laplace's equation in the non-conducting mantle given surface magnetic measurements. Any resemblance between the observable and simulated CMB fields could hint at similar internal structures.

It turns out that the Earth's magnetic field has components which are both equatorially symmetrical (ES) and antisymmetrical (EA, see fig. 5.14). Equatorially symmetrical low-latitude wave-like features are particularly strong and so far are not reliably explained in the literature.[9] Many previously published simulations display primarily equatorially antisymmetrical components. This could be on account of a very weak driving when one symmetry receives too little energy for excitation. With this in mind we have carried out runs with Ra varying more than an order of magnitude.

Beyond low latitude wave-like phenomena, high latitude magnetic field patches are particularly strong in the geomagnetic field. These features have stayed in approximately the same place during the time when direct observations have been available (the past four centuries). The position of these features corresponds roughly to the tangential cylinder containing the inner core and parallel to the rotational axis.

In this section we present the magnetic field structure at the outer boundary in all our

---

[9]These equatorially symmetrical wave-like features at low latitudes of the Earth's CMB structures could be an intrinsic property of dynamos in a certain parameters range, or for example a demonstration of an uneven temperature distribution on the CMB.

simulations. At least four snapshots per simulation are selected to illustrate the temporal variation of the surface magnetic field (secular variation).
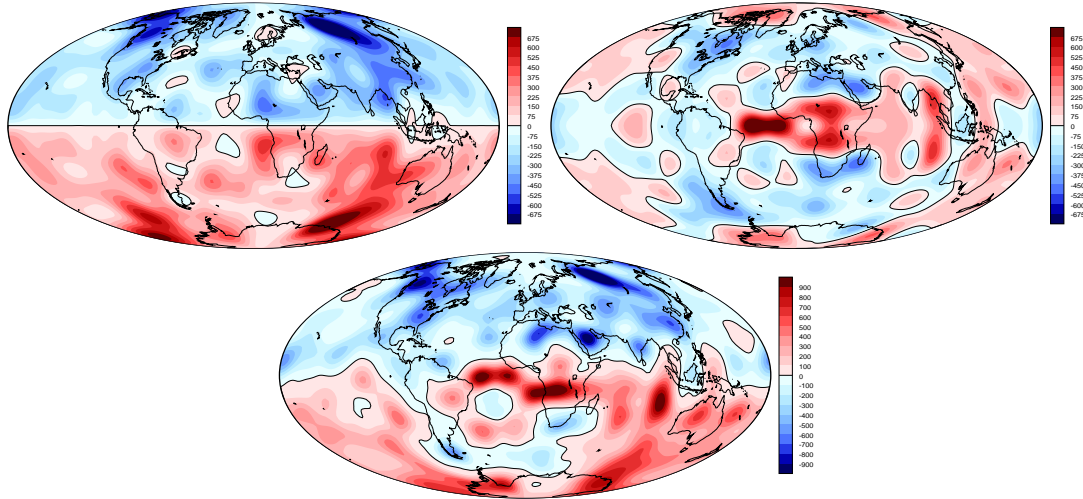
Figure 5.14: *B_r on the CMB, 2010 (EA,ES and both symmetries). Finlay (pers. com., 2010), see discussion in* Jackson (2003).

5.3.5.1 Case 0

Differences between successive snapshots in fig.(E.1) show westward motion of visible features, i.e. equatorial patches move in the direction opposite to the direction of the overall core rotation, similar to a crude characterization of the observable geomagnetic secular variation (although in this case the westward drift is mostly confined to the Atlantic hemisphere).

The field is weakest at the equator, and strongest where the tangent cylinder meets the surface. Low-latitudes contain periodically strong concentrations of the same sign as the dipolar field. This resembles geomagnetic field, but the Case 0 lacks an equatorial-symmetry (ES) component compared to the observations.

Case 0 has the same parameters as the constant heat flux case in Sakuraba and Roberts (2009). Indeed, comparing magnetic fields on the CMB, we see qualitatively similar fields in both cases, see fig.(5.15). The westward drift of the magnetic field is explained by Sakuraba and Roberts (2009) as advection of field by the thermally driven flow. Comparing the average flow speed at the equatorial region below the CMB and the speed of the magnetic pattern on the CMB, we arrive at the same conclusion (corresponding figures are in the section 5.3.10 and 5.3.6).

A weak eastward flow exists inside the tangent cylinder (fig. E.8) but flow disappears close to the rotational axis. The eastward direction in this region is dictated by the conservation of momentum taking into account westward average direction of the flow external to the tangent cylinder.

On the the surface of the core, the temperatures are distributed in such a way that the equator is the hottest location and the poles are colder.
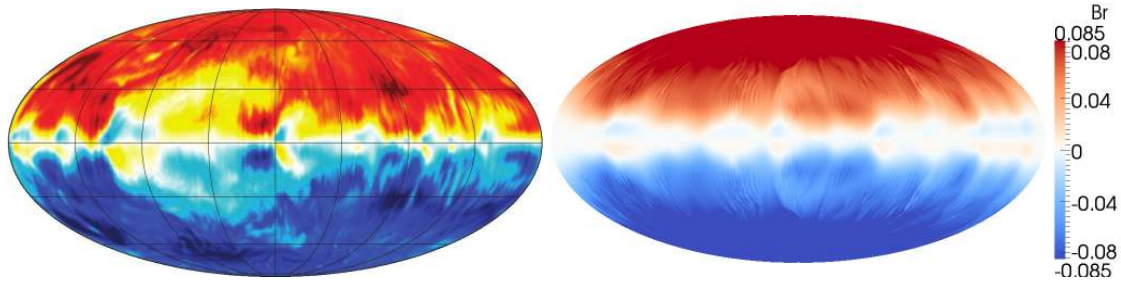
Figure 5.15: *Magnetic field at the CMB, model UHFM by Sakuraba and Roberts (2009) (left), parameters are the same as in Case 0 (right).*

5.3.5.2 Case 1

The Rayleigh number Ra is increased in comparison with Case 0. By virtue of the heightened convection the pattern of the magnetic field is less uniform and smaller scale (see fig.E.2). The EA (equatorially antisymmetric) field predominates, but one can see that some low-latitude patches have no counterpart in the other hemisphere.

Field patterns at the CMB become quickly unrecognisable as they are subject to strong advection which rapidly mixes them up, so it is tricky to see the predominant drift direction in a small number of snapshots. Time-longitude plots (fig. 5.34) however confirm that the drift is still systematically in the westward direction with similar speed to Case 0.

One can see a footprint of the tangent cylinder by the strengthening of the magnetic field in the form of a ring at high latitudes (fig. E.2, B_r). A very striking change in comparison with the Case 0 is that strong convection has now started inside the tangent cylinder. A vortex with eastward direction of flow is threaded on the axis of rotation (fig. E.10). The formation of the vortex is accompanied with the development of a large temperature gradient across the tangent cylinder (fig. E.10, temperature plots). A region of hot fluid inside the tangent cylinder is effectively isolated from the colder outer regions.

5.3.5.3 Case 2

The convection (fig. E.3) is even stronger and more developed than in the Case 1. Much more reverse magnetic field features are notable. Polar regions on the surface of the core contain magnetic field of the sign opposite to the main dipole. The convection is intense enough to break through the interface of the tangent cylinder (fig. E.12). Furthermore a column of hot fluid around the axis of rotation gives rise to plumes. This light material reaches the surface and forms a layer of relatively hot material directly below the CMB. The region of warm fluid on the surface of the core however remains at high latitudes, while the equator

remains relatively cold. Plumes already detached from the source of energy disappear with time through constant drain of heat to the mantle.

A strong vortex centered on the rotation axis has a retrograde (westward) direction. The distinct westward drift at low latitude as in cases 0 and 1 is absent in this case, as shown by the time-longitude plot 5.35.

5.3.5.4 Case 3

Case 3 has the same parameters as the Case 0 except it has five times higher magnetic Prandtl number $Pr_m = q = 1$. This means that the Ohmic dissipation of the magnetic field is much lower than in the Case 0. Less dissipation facilitates dynamo action. With high Pr_m it might be viable to carry out simulations in computationally less demanding parameter regimes and still obtain self-sustaining magnetic fields. Unfortunately the scenario with a high Pr_m is not a very realistic, since magnetic Prandtl numbers in liquid metals are tiny (order of 10^{-5}).

The interface of the tangent cylinder (fig. E.14) is not clearly delineated compared to the rest of the convective pattern as found, for example, in Case 0. On the other hand, there is a prominent concentration of high temperatures on the axis of rotation with a single large forking plume reaching the surface there. Unlike Case 0 where large temperature gradients are generated close to the outer surface, most temperature gradients in Case 3 are in the middle of the convective shell. Temperature gradients are the origin of buoyancy, accordingly the velocity field is locally intensified and magnetic field growth can be facilitated. As a consequence, the position of highest temperatures (adjacent to the location of highest temperature gradients) within the plume is well correlated with concentrations of the inverse magnetic field (negative field in the northern hemisphere, see fig. E.14, B_r).

Flows at the outer surface at high latitudes are overall eastward, flows deeper and closer to the axis of rotation are predominately westward except for a tiny vortex almost on the rotation axis (this inverse eastward vortex is a common feature of cases 1-6, in contrast to Case 0 where the fluid on the axis of rotation is at rest). The direction of the flow at low latitudes is mostly westward all the way down to the inner core.

The distribution of temperatures at the CMB (fig. E.4) is similar to Case 0: the equator is the hottest, regions around the poles are the coldest. Unlike in Case 0, the poles themselves have concentrations of high temperatures. A few thin polewards jets on the CMB spread concentrations of hot matter out from the equator (fig. E.4, V_t).

As in the simulations with higher Rayleigh number Ra, the magnetic field on the CMB (E.4, B_r) contains some ES field. High Pr_m favours frozen flux behaviour and the magnetic field follows complicated flow patterns more closely than in the other cases, breaking the EA symmetry of the basic dipole, since the flow itself contains an ES component.

5.3.5.5 Case 4

This is one of the most impressive and interesting simulations. The combination of the lowest Ekman and magnetic Prandtl numbers together with the highest Reynolds number is computationally highly demanding. It is appropriate to compare with cases 2 and 4, where Ra is the same. In contrast the Ekman number is five times lower, and the magnetic Prandtl number is four times lower in Case 4. The kinetic energy is almost ten times decreased in Case 4 vs. Case 2. The difference between magnetic fields is not so striking, although Case 4 has two times weaker magnetic field energy (see table 5.6).

There is a vortex with a strong westward flow on the axis of rotation inside the tangent cylinder (fig. E.16, V_φ). The vortex is correlated with the highest temperatures in the shell. Unlike in Case 2 where an analogous central eddy regularly produces hot plumes reaching the surface, the vortex in the Case 4 is more isolated and the rising plumes are less persistent and significantly colder than the core of the vortex. The tendency of the vortex flow to be isolated inside the tangent cylinder is in line with the strengthening of the Proudman-Taylor constraint at the lower Ekman number. Similar to a giant whirlwind the vortex moves randomly and rapidly. A central prograde thin eddy is again present in this run.

Like in all other cases with high Ra where convection inside the tangent cylinder is excited, the equator is colder than the poles (E.5). Consequences of the lower Ekman number are apparent on the CMB: high temperatures are significantly more concentrated on the poles and are much better isolated from low latitudes compared to Case 2. At the same time the temperature field of the Case 4 has periodic structures on the CMB nearby the equator. Warm matter is advected from the ICB by means of plumes that are strongly affected by diffusion. Eventually next to the surface thin latitudinal streams spread out warm fluid from equator to poles. An opposite equatorwards balancing flow is scattered, weak and doesn't have an apparent influence at low latitudes (see V_θ on the CMB, fig. E.5). By contrast in the Case 2 both directions of meridional flows at the outer boundary (equatorward and poleward) are equally strong, and this flow pattern is in charge of a flower-like structure composed of five or six petals at high and middle latitudes in the temperature field.

The magnetic field on the CMB has both EA and ES symmetries due to the vigorous convection. The equator contains a set of inverse field structures. These structures coincide with the latitudinal spreading out (poleward meridional flows). There is a strong positive magnetic flux concentration on the equator in the eastern hemisphere. This flux feature is strongest at t_1 and almost vanishes at t_4. This distinctive spot of radially directed intense magnetic field is caused by the single strong eruption of the magnetic field from the deep regions of the convective shell. The vortex in the tangent cylinder discussed above effectively generates magnetic field and it is responsible for the eruption (meridional snapshots of the magnetic field above the equatorial plane in fig. E.16 contain similar anomaly in the form of Cyrillic cursive "ge" or like γ). At time t_1 an outward flow of the same form accompanies the

magnetic field to the surface.

5.3.5.6 Case 6

This run is similar to Cases 4 and 2 having the same Rayleigh number *Ra*. In comparison to Case 2 the magnetic Prandtl number is lower (0.05 vs. 0.2). Compared with Case 4, the Ekman number is five times larger. The peculiarity of this run is that the strong central vortex inside the tangent cylinder (fig. E.18, V_φ) from Case 4 is absent. It is hard to discern the placement of the inner core by the distribution of longitudinal velocities in the plane above the equator. However similarities with the Case 4 are present: the highest temperatures and the strongest magnetic field are around the axis of rotation. The westward direction of flow in the tangent cylinder prevails, and the prograde tiny vortex almost on the rotational axis can be found as well.

The temperature has a maximum on the poles, while the equator is colder and contains a set of repeatable structures (fig. E.6). Like Case 4 these structures are associated with meridional jets.

The magnetic field on the CMB is mostly EA, but some ES field features are also present. There is a belt of inverse field at low latitudes, although positive magnetic field tends to dominate at low latitudes at some longitudes on both sides of the equator. This contributes to the equatorially symmetrical part of the magnetic field. The strong positive flux on the northern part of equator could be a contribution from the magnetic flux detached from the strong magnetic field concentration in the tangent cylinder and transported to the surface (the flux is seen at t=0.340429 and t=0.330822 above the equatorial plane).

5.3.6 Azimuthally averaged fields

We have already discussed the surface magnetic field and to some extent that inside the shell in section (5.3.5). To next obtain a picture of the general field structure as a function of depth into the shell and latitude, we here consider meridional sections. For this purpose fields were averaged in time and over longitude (figures 5.16 – 5.20). Some features resemble patterns observed on the surface, on the other hand additional variations become noticeable. Among other things the temperature pattern on the CMB at high Rayleigh numbers *Ra* significantly differs from that deeper in the shell. A thin layer of hot fluid at high and middle latitudes masks the surface from the interior (cases 2, 4 and 6). This layer contributes to the local latitudinal gradient of the temperature dT/dθ close to the outer boundary and seems intimately related to be responsible for the values of u_φ in adjacent regions[10]. Indeed, near equator at low latitudes there is a prominent prograde flow in cases 2 and 6. Tracing temperatures at the surface,

---

[10]To see that in certain conditions the latitudinal temperature gradient and zonal flow can be correlated, we consider the φ-component of the geostrophic equation $\nabla \times (qRaT\mathbf{r} = \hat{z} \times \mathbf{u})|_\varphi$, which gives $qRa(\nabla T)_\theta r = \dfrac{\partial u_\varphi}{\partial z}$.

we see that the temperatures have local minima on the equator in both cases. In contrast, the retrograde flow at equator in the Case 4 coincides with the local maximum of surface temperatures (see surface temperatures in fig. E.5).

Flow fields of Case 0 and of the similar non-magnetic case HYDRO are impressively different (fig. 5.16 and 5.17). The strong magnetic field on the tangent cylinder seems to control a sharp separation of the tangent cylinder region from the rest of the shell. Crossing the imaginary boundary of the tangent cylinder, we undergo a change from the prograde flow inside to generally retrograde flow (especially close to the equatorial plane) outside of it, in Case 0. In contrast, in the case HYDRO prograde flow remains on both sides of the tangent cylinder. The incorporation of the magnetic field also results in the redistribution of kinetic energy from deep regions towards the surface.

The magnetic field has maxima deep in the shell in all cases. Case 3 and Case 0 with the lowest Rayleigh number Ra have strong **B** on the tangent cylinder ($r \sin \theta \approx r_i$). This is especially clear in B_φ that has a strong local maximum right on the tangent cylinder in Case 0, and to a lesser extent in Case 3, especially in the northern hemisphere. Regardless of the fact that in Case 0 a roughly geostrophic flow inside the tangent cylinder does not contribute to dynamo action and can not convey the field towards the axis of rotation (the flow has a tiny radial component), the region $r \sin \theta < r_i$ contains a strong magnetic field. It is transported by diffusion from the tangent cylinder. This transport contributes to the simple dipolar component of the magnetic field. The magnetic field in the higher Rayleigh number runs (cases 1,2,4,6, figures 5.18 5.19 5.21 5.22) doesn't so obviously exhibit the presence of the tangent cylinder in contrast to the simulations with lower driving. The strongest magnetic field in these high-Ra cases tends to be on the rotation axis, rather than being localized on the tangent cylinder.

Another common property of low Rayleigh number runs (cases 3 and 0, fig. 5.20 and 5.16) are torous-like paired structures of the azimuthal magnetic field. These strong field concentrations are seen as intense spots in figures 5.16 and 5.20 (B_φ). The structures are almost on the surface in the Case 3 rather than in the Case 0 where they are deeper in the shell. Case 4 contains similar but weaker concentrations of the magnetic field. Cases 0 and 3 can be characterised by a low influence of the inertial forces (low Ra), in Case 4 rotational effects are intensified since E is low. The intense azimuthal field features might therefore be related to the stronger influence of rotation.

The prominent patches of inverse radial magnetic field around equator are nearly universal in our runs. The direction of the field in them is opposite to the dominant axial dipole. The exception is the Case 6, where the near equatorial region in both hemispheres contains positive magnetic field (averaged over longitude).

(a) B_r (b) B_φ (c) U_φ (d) T
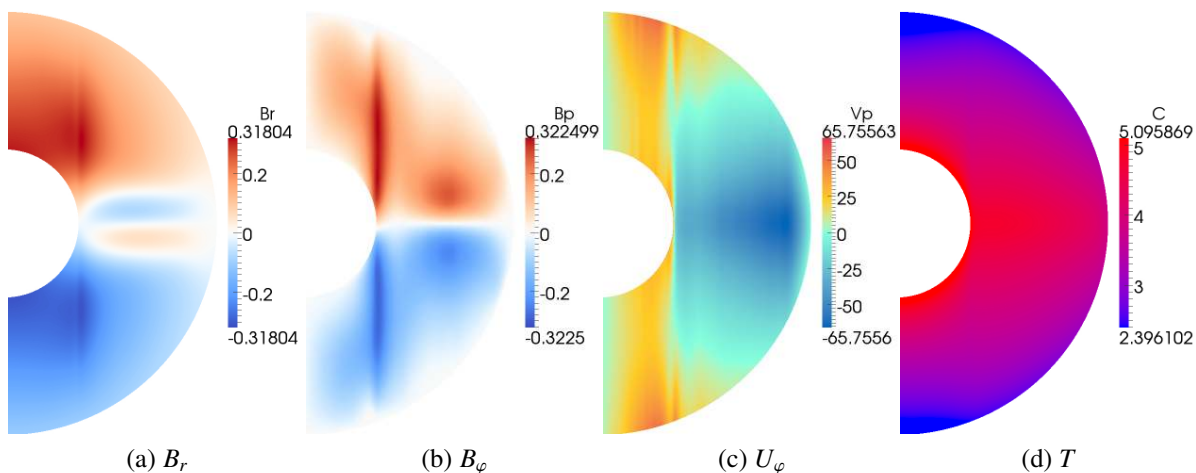
Figure 5.16: *Meridional sections of φ- and time- averaged fields. Case 0*

(a) T
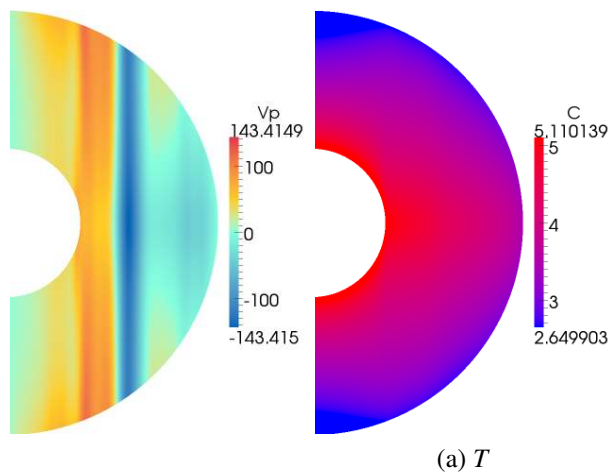
Figure 5.17: *Meridional sections of φ- and time- averaged fields. HYDRO*

(a) B_r (b) B_φ (c) U_φ (d) T
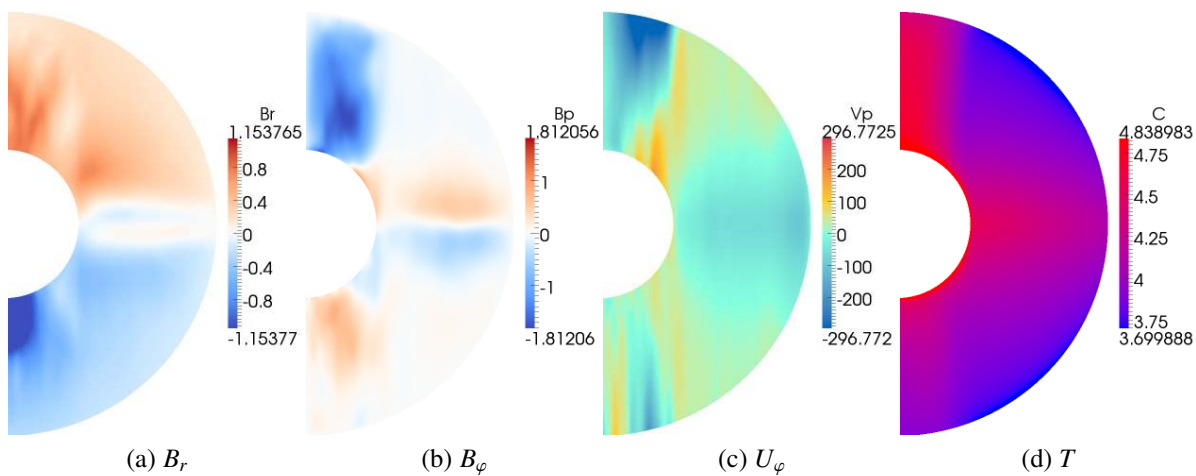
Figure 5.18: *Meridional sections of φ- and time- averaged fields. Case 1*

(a) B_r (b) B_φ (c) U_φ (d) T
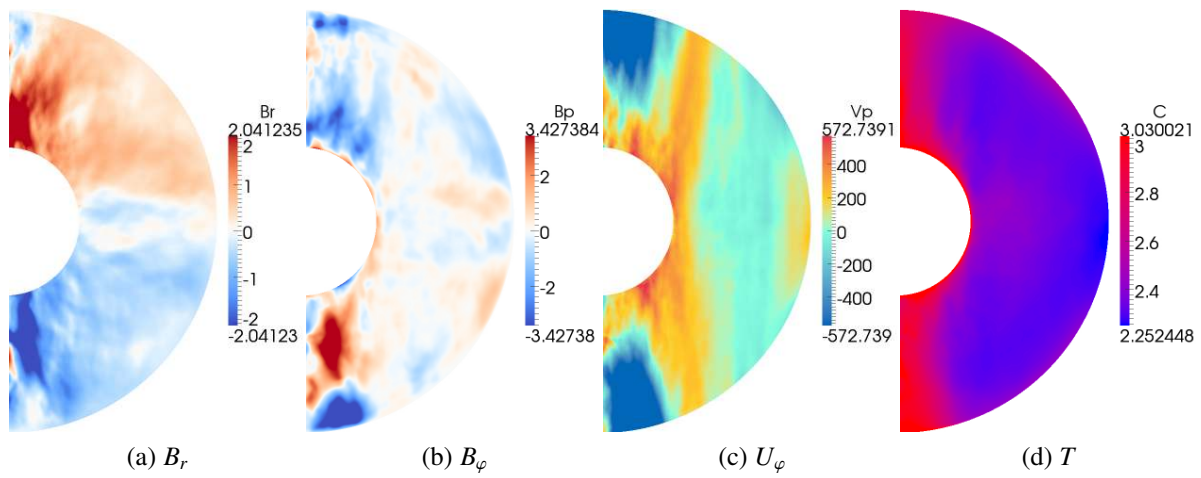
Figure 5.19: *Meridional sections of φ- and time- averaged fields. Case 2*

(a) B_r (b) B_φ (c) U_φ (d) T
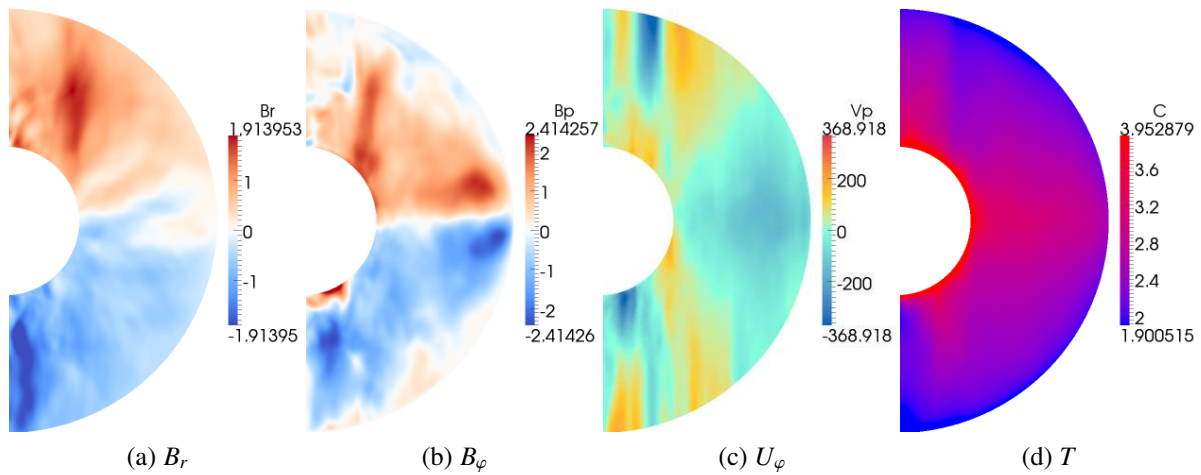
Figure 5.20: *Meridional sections of φ- and time- averaged fields. Case 3*

(a) B_r (b) B_φ (c) U_φ (d) T
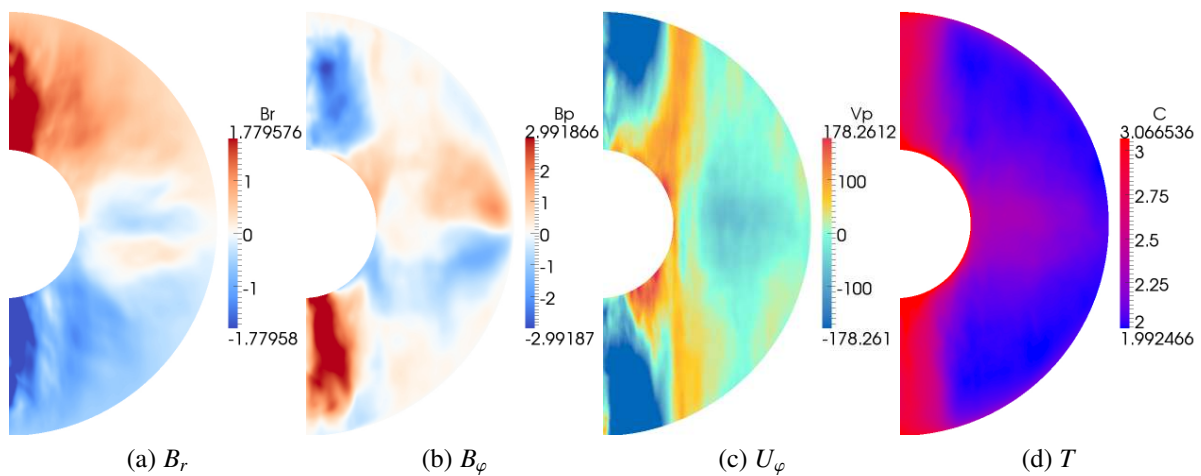
Figure 5.21: *Meridional sections of φ- and time- averaged fields. Case 4*

(a) B_r (b) B_φ (c) U_φ (d) T
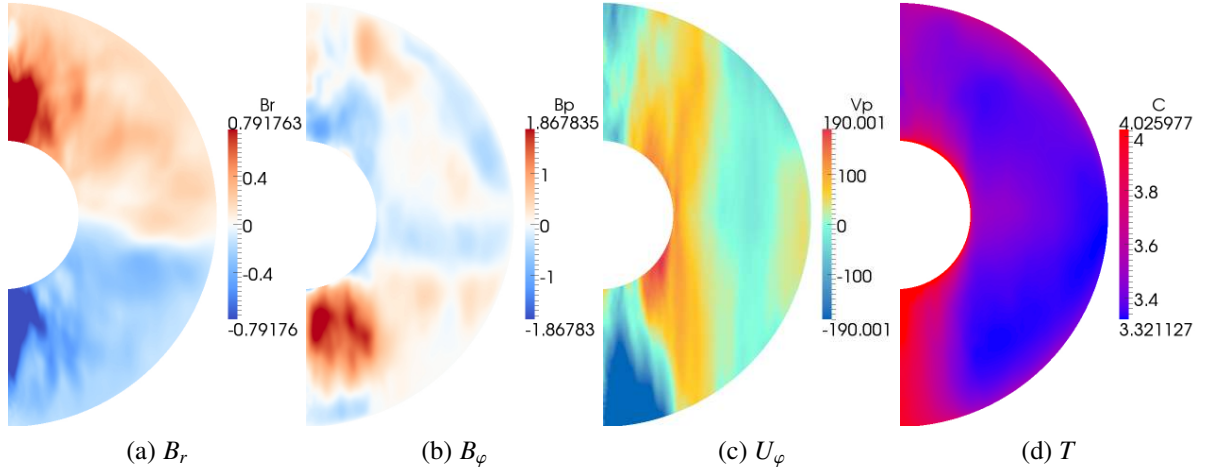
Figure 5.22: *Meridional sections of φ- and time- averaged fields. Case 6*

5.3.7   Azimuthal force balances

Let the square brackets $[\ ]_\varphi$ be the azimuthal averaging operator of the azimuthal component of a vector. Then applying it to the Navier-Stokes equation 2.1 we get:

$$Ro\,\frac{\partial}{\partial t}[\mathbf{u}_\varphi]_\varphi = \underbrace{Ro\,[\mathbf{u}\times(\boldsymbol{\nabla}\times\mathbf{u})]_\varphi}_{Advection} + \underbrace{[(\boldsymbol{\nabla}\times\mathbf{B})\times\mathbf{B}]_\varphi}_{Lorentz} + \underbrace{q\,Ra\,[T\,\mathbf{r}]_\varphi}_{Buoyancy} - \underbrace{[\hat{\mathbf{z}}\times\mathbf{u}]_\varphi}_{Coriolis} + \underbrace{[E\boldsymbol{\nabla}^2\mathbf{u}]_\varphi}_{Viscosity}. \quad (5.22)$$

Figures (5.23-5.28) show time- and longitude-averaged forces in φ-direction. As before, measurements are made at the end of the presented simulations. The time intervals are shorter than for diagnostics in section 5.3.1 due to higher computing resources required in this type of post-processing. The calculation of forces involves additional derivatives and non-linear operations. Inevitably, the structure of derived vector fields has smaller characteristic scales and it is significantly more complex than the initial fields.

The common feature of low Ra cases is a prograde Lorentz force at low latitudes (cases 0,1,3). These runs also show two branches of strong positive Coriolis force at low latitudes. To understand the influence of these two largest forces on the flow, we need to sum them up. The resulting force is prograde and has a much more uniform distribution than the individual forces. On the contrary, the flow itself is retrograde at low latitudes in low Ra cases. Azimuthal components of Lorentz and Coriolis forces in the chosen time span and at low latitudes "work" (are directed) on average against the flow.

Like the magnetic field itself, the Lorentz force can often be strong inside the tangent cylinder. The tendency seems to increase with the Rayleigh number, only Case 0 is a bit different where the strongest equatorial concentrations of the Lorentz force are comparable to those inside the tangent cylinder.

The advection is tiny in comparison with Coriolis and Lorentz forces. It is mostly concentrated on geostrophic cylinders parallel to the axis of rotation. The exception is Case 1 where

geostrophy is less apparent. The strength of the advection term increases with the Rayleigh number *Ra*.

The viscosity is concentrated mostly in a thin region along the inner and outer boundaries, where it works in order to match the no-slip boundary conditions. It can also be strong inside the tangent cylinder in cases when small scale convection is enhanced there. There is little convection inside the tangent cylinder in the Case 0 and it is reasonable that the viscosity is tiny inside the tangent cylinder, but strong on the cylinder itself. Actually, a sharp shear boundary layer on the tangent cylinder of viscosity plots is apparent for the low *Ra* runs (0, 1, 3), while on the contrary the transition is more gradual at higher Ra (2, 4, 6). The reason is that strongly driven dynamos have more energy in the flow, consequently deviations from the columnar constraint of the Proudman-Taylor theorem occur more easily.

It is obvious that at high Rayleigh numbers strong buoyancy increase convection rates. Flows become more turbulent and less structured. This influences the distributions of forces as well. Although it is still possible to discern the large structures of forces in the runs with the low *Ra*, at high *Ra* the patterns seem to be rather disordered.

(a) Lorentz   (b) Coriolis   (c) Advection   (d) −Viscous
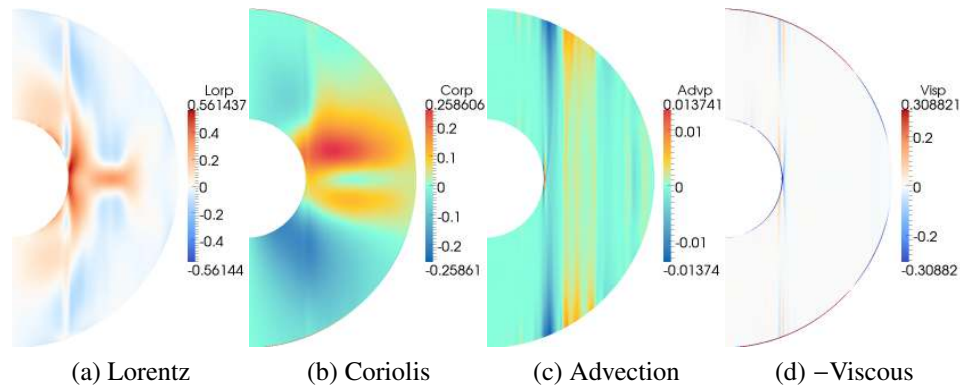
Figure 5.23: *Time- and longitude-averaged forces in the φ-direction in the meridional plane, Case0. Averaged between $t_1 = 1.4322$ and $t_2 = 1.45344$.*

(a) Lorentz   (b) Coriolis   (c) Advection   (d) −Viscous
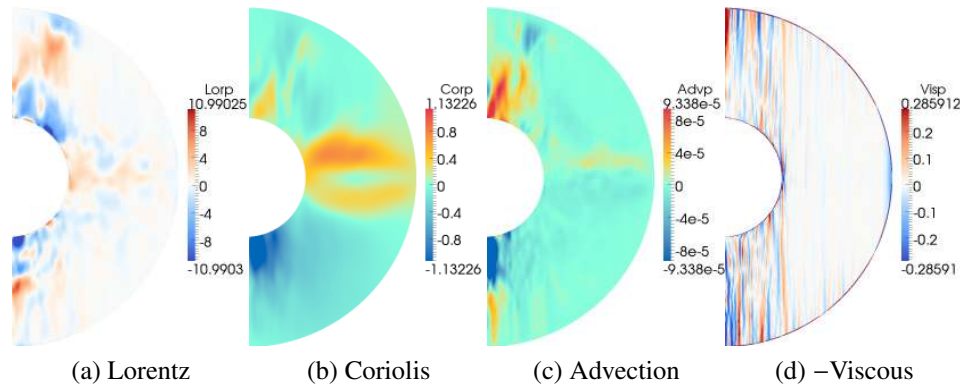
Figure 5.24: *Time- and longitude-averaged forces in the φ-direction in the meridional plane, Case1. Averaged between $t_1 = 0.295927$ and $t_2 = 0.297124$.*

(a) Lorentz   (b) Coriolis   (c) Advection   (d) −Viscous
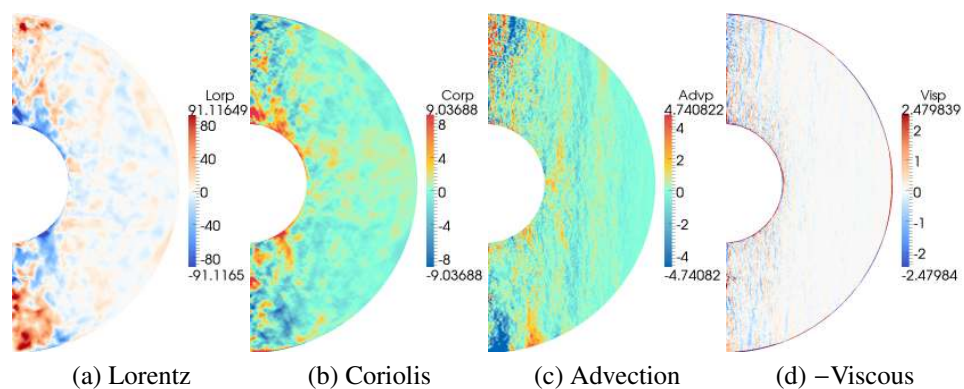
Figure 5.25: *Time- and longitude-averaged forces in the φ-direction in the meridional plane, Case 2. Averaged between $t_1 = 0.0613959$ and $t_2 = 0.0615897$.*

(a) Lorentz   (b) Coriolis   (c) Advection   (d) −Viscous
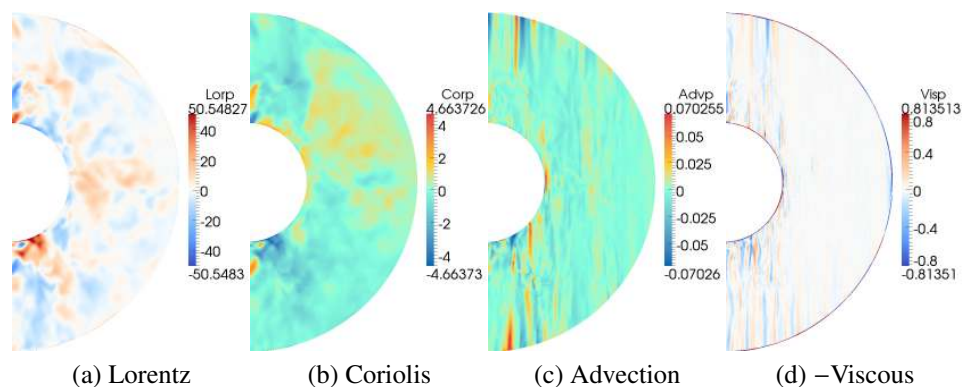
Figure 5.26: *Time- and longitude-averaged forces in the φ-direction in the meridional plane, Case 3. Averaged between $t_1 = 0.0888542$ and $t_2 = 0.0890833$.*

(a) Lorentz   (b) Coriolis   (c) Advection   (d) −Viscous
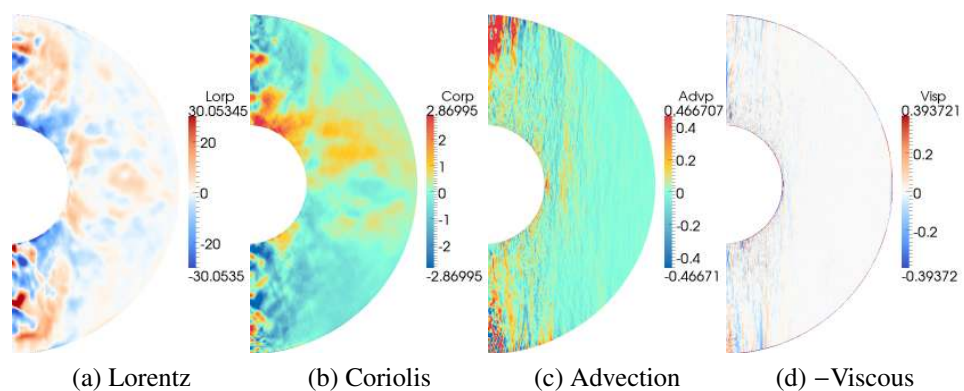
Figure 5.27: *Time- and longitude-averaged forces in the φ-direction in the meridional plane, Case 4. Averaged between $t_1 = 0.0725936$ and $t_2 = 0.0731656$.*

(a) Lorentz   (b) Coriolis   (c) Advection   (d) −Viscous
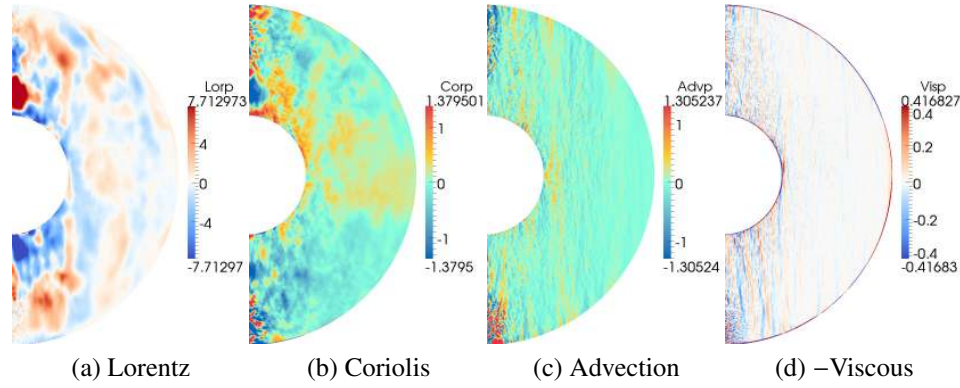
Figure 5.28: *Time- and longitude-averaged forces in the φ-direction in the meridional plane, Case6. Averaged between $t_1 = 0.241372$ and $t_2 = 0.243377$.*

5.3.8 Azimuthal kinetic energy balances

Inspired by Aubert (2005), we present sources and sinks of the "φ-component" of the kinetic energy. The azimuthal projection of the Navier-Stokes equation is multiplied by u_φ to get the time derivative of $u_\varphi^2/2$ on one side of the equation and terms which are of interest to us on the other side. The buoyancy force is excluded in such considerations. This is preferable since buoyancy is largely compensated by the pressure gradient, which is not calculated explicitly. Although the integral of the power produced by pressure over the cylindrical path $\oint u_\varphi (\boldsymbol{\nabla} P)_\varphi ds = \oint u_\varphi \frac{\partial P}{\partial s} ds = Pu_\varphi \big|_{\varphi_0}^{\varphi_0} - \oint P \frac{\partial u_\varphi}{\partial s} ds$ is not presented, it can be non-zero.

Although the Coriolis force can not produce energy, it has the strongest contribution to the balance of the kinetic energy in φ-direction. The Coriolis force rotates velocity. Its basic function is in transferring energy between different projections of a velocity.

The flow in the tangent cylinder of the Case 0 has little variations and is simply prograde. Therefore the force and its power should have similar pattern there (power is a flow times force). Comparing the power of the Lorentz force (fig.5.29) and the force itself (fig.5.23) inside the tangent cylinder we indeed see correspondence. On the contrary, the outer part of the shell of the Case 0 contains complicated flow. That is why averages of powers are not the same as multiplication of average forces by average velocities, i.e. $[u_\varphi \cdot F_\varphi] \neq [u_\varphi] \cdot [F_\varphi]$. So we have obtained surprising results: the average of forces that oppose the flow can produce positive contributions to the kinetic energy on average.

Furthermore an interesting effect appears with the Coriolis force. The power of the Coriolis force which produces the φ-component of the kinetic energy is columnar ($\frac{\partial}{\partial z} \approx 0$), although averages of azimuthal components of the force and flow are not apparently columnar. The power is $u_\varphi (\Omega \times \mathbf{u})_\varphi = u_\varphi [(\hat{r} \cos\theta - \hat{\theta} \sin\theta) \times \mathbf{u}]_\varphi = u_\varphi [u_\theta \cos\theta + u_r \sin\theta]$, this mix of velocity components apparently makes columnar structures more distinguishable.

The production of kinetic energy by advection and its dissipation by viscosity are increased in Case 6 in comparison with the Case 0. The influence of the Coriolis force on the production

of kinetic energy is, as in Case 0, more columnar than the force itself. Unlike in the Case 0, where the power of the Coriolis force is two orders of magnitude larger than the powers of other terms of the Navier-Stokes equation, in Case 6 production of Coriolis, Lorentz and Advection terms have the same order of magnitude.
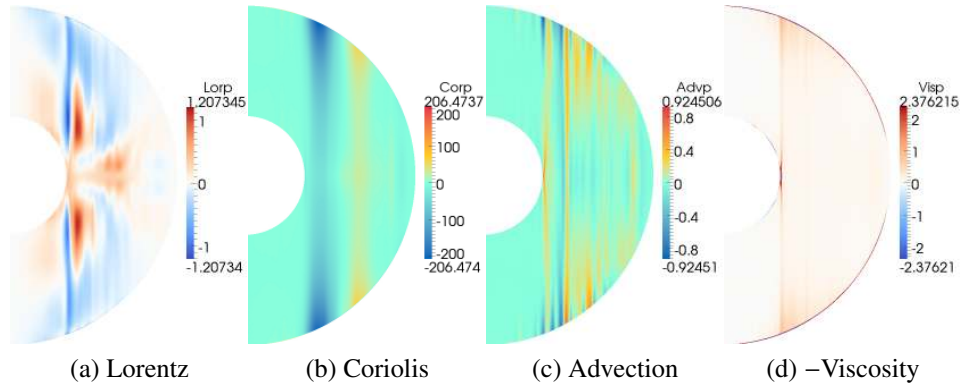
Figure 5.29: *Time- and longitude-averaged kinetic energy (u_φ^2) production components in the meridional plane, Case0. Averaged between $t_1 = 1.4322$ and $t_2 = 1.45344$.*
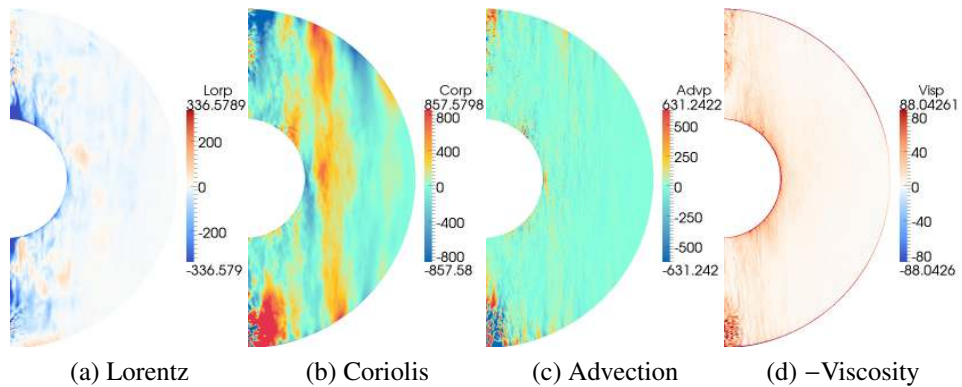
Figure 5.30: *Time- and longitude-averaged kinetic energy (u_φ^2) production components in the meridional plane, Case 6. Averaged between $t_1 = 0.241372$ and $t_2 = 0.243377$.*

5.3.9 Induction equation components

In this section various terms contributing to the azimuthal component of the induction equation are briefly analyzed, considering only Cases 0 and 6 for illustration. The goal here is to gain insight into the dynamo mechanisms at work, particularly concerning how the toroidal (azimuthal) component of the magnetic field is generated. Figures (5.31–5.32) show the φ-components of the advection $(\mathbf{u} \cdot \boldsymbol{\nabla})\mathbf{B}$, stretching $(\mathbf{B} \cdot \boldsymbol{\nabla})\mathbf{u}$ and diffusion terms of the induction equation. Of the particular interest is the relative influence of above-listed terms, their geometry and their arrangement in the shell.

The production of magnetic energy is performed by the stretching term. Intense generation of the magnetic field occurs on the tangent cylinder in the Case 0. Case 6 has an entirely

different mechanism, with the stretching term strongest inside the tangent cylinder. Moving from comparatively weak convection in Case 0 to the strongly driven Case 6, we observe smaller scale and more distributed structures. Nevertheless the columnarity of the induction process is notable even in the latter case.

In Case 6 the advection and stretching terms are comparable in strength. In Case 0 the stretching term is several times larger than the advection term.

(a) M_S (b) M_A (c) M_D
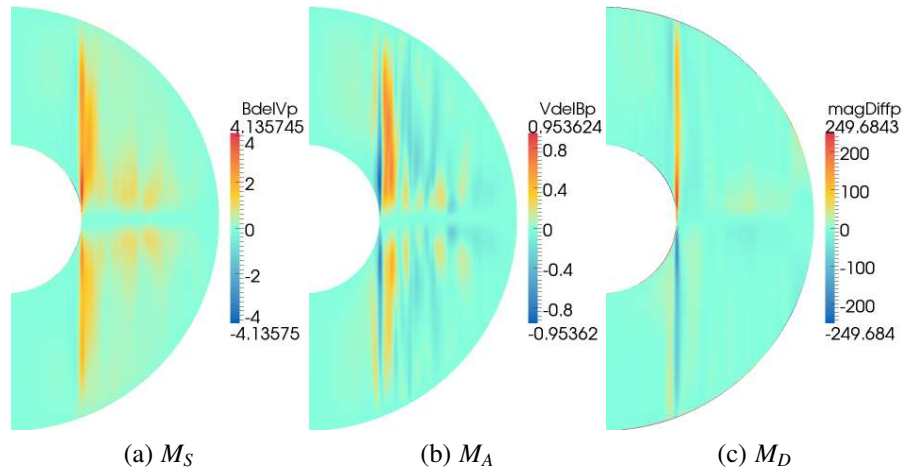
Figure 5.31: *Meridional sections, time-averaged. $M_s = [(\mathbf{B} \cdot \boldsymbol{\nabla})\mathbf{u}]_\varphi$, $M_A = [(\mathbf{u} \cdot \boldsymbol{\nabla})\mathbf{B}]_\varphi$, $M_D = [\boldsymbol{\nabla}^2\mathbf{B}]_\varphi$. Case 0.*

(a) M_S (b) M_A (c) M_D
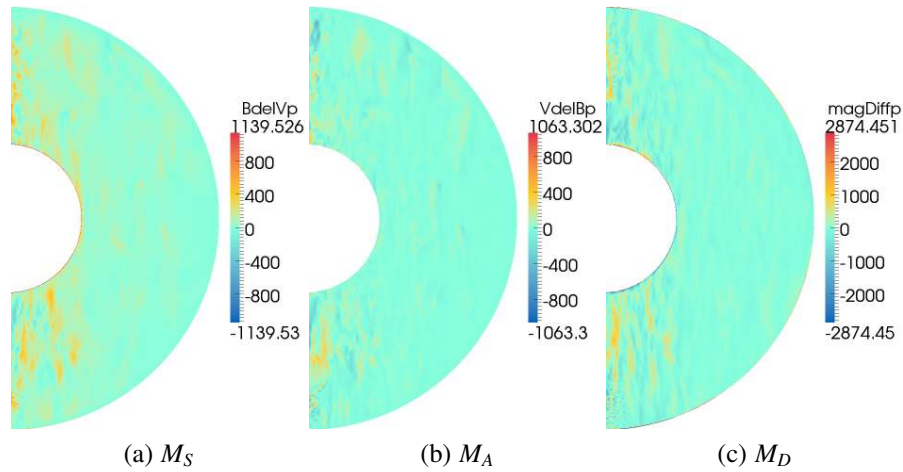
Figure 5.32: *Meridional sections, time-averaged. $M_s = [(\mathbf{B} \cdot \boldsymbol{\nabla})\mathbf{u}]_\varphi$, $M_A = [(\mathbf{u} \cdot \boldsymbol{\nabla})\mathbf{B}]_\varphi$, $M_D = [\boldsymbol{\nabla}^2\mathbf{B}]_\varphi$. Case 6.*

5.3.10   Time-longitude analysis of equatorial surface fields

In computer simulations we can easily substitute a space coordinate by time. Hereby one can see all the changes which happen during a certain time at a glance. For instance waves with constant propagation speed on a time-longitude plot will appear as regularly distributed

inclined stripes. On figures (5.33-5.35) simulation data are organised so that the equator is a horizontal coordinate and time is a vertical coordinate.

Striped structures in the time-longitude plots of Case 0 (fig.5.33) have an inclination corresponding to the velocity -42.8 ± 2.2 rad/mag.diff.time (minus sign indicates westward motion). Additionally, a similar temperature plot shows small scale and almost vertical structures corresponding to the velocity -11.6 ± 1.9 rad/mag.diff.time. The flow just below the surface has westward components varying from -6 to -50 rad/mag.diff.time (from fig. E.1). The same order of magnitude of the westward flow and of the westward motion of surface field structures suggests that on average the latter causes the former.

In Case 1 (fig. 5.34) with its stronger convection, the longitudinal speed of surface patterns is -51 ± 14 rad/mag.diff.time. At the selected time span stripes on the fig.(5.34) have slightly varied angles in different hemispheres (east-west) giving the large error bars. The smaller scale signal is absent here, unlike in the temperature field of Case 0. The range of westward velocities beneath the surface on equator is from -30 to -130 rad/mag.diff.time (from fig. E.2). Similarly to Case 0 the surface velocity of magnetic field structures falls in the same range of values as the surface flow, i.e. advection seems to be the primary cause of the westward moving features.

Case 2 has the most vigorous convection, and from its equatorial evolution (fig. 5.35) we are not able to extract any specific longitudinal drift direction of surface field features. One can measure both positive or negative tilt of stripes, resulting in velocities of structures up to ± 180 rad/mag.diff.time. The flow below the surface is also extremely variable having velocities from -650 to 720 rad/mag.diff.time (fig. E.3).

(a) B_r

(b) T

(c) B_t

(d) B_p
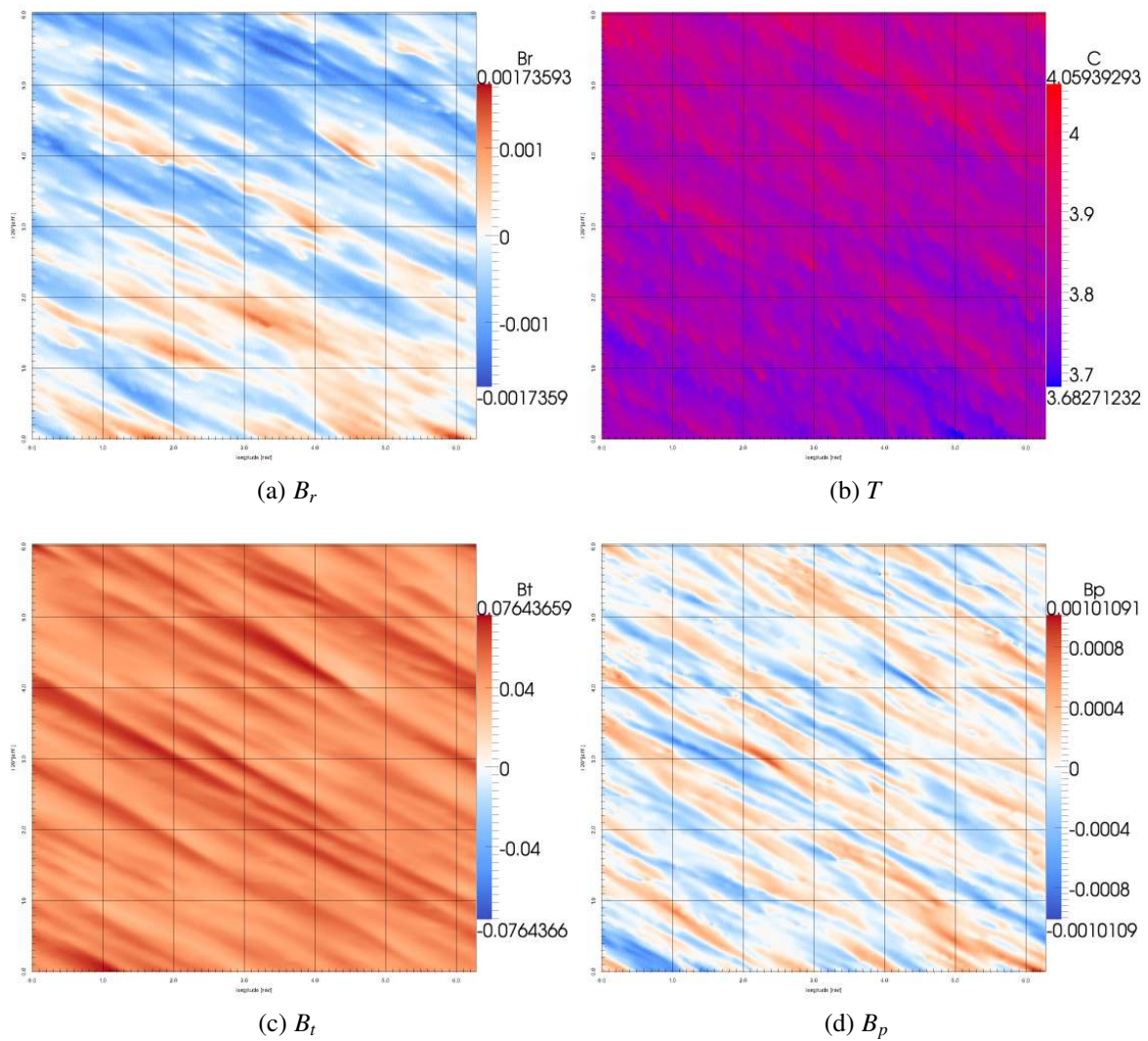
Figure 5.33: *Time-longitude plots at r_o at equator. Case 0. Horizontal axis is longitude. Vertical axis is time (major ticks are separated by 1/20 of a magnetic diffusion time). Time increases from the bottom to the top.*

(a) B_r

(b) T

(c) B_t

(d) B_p
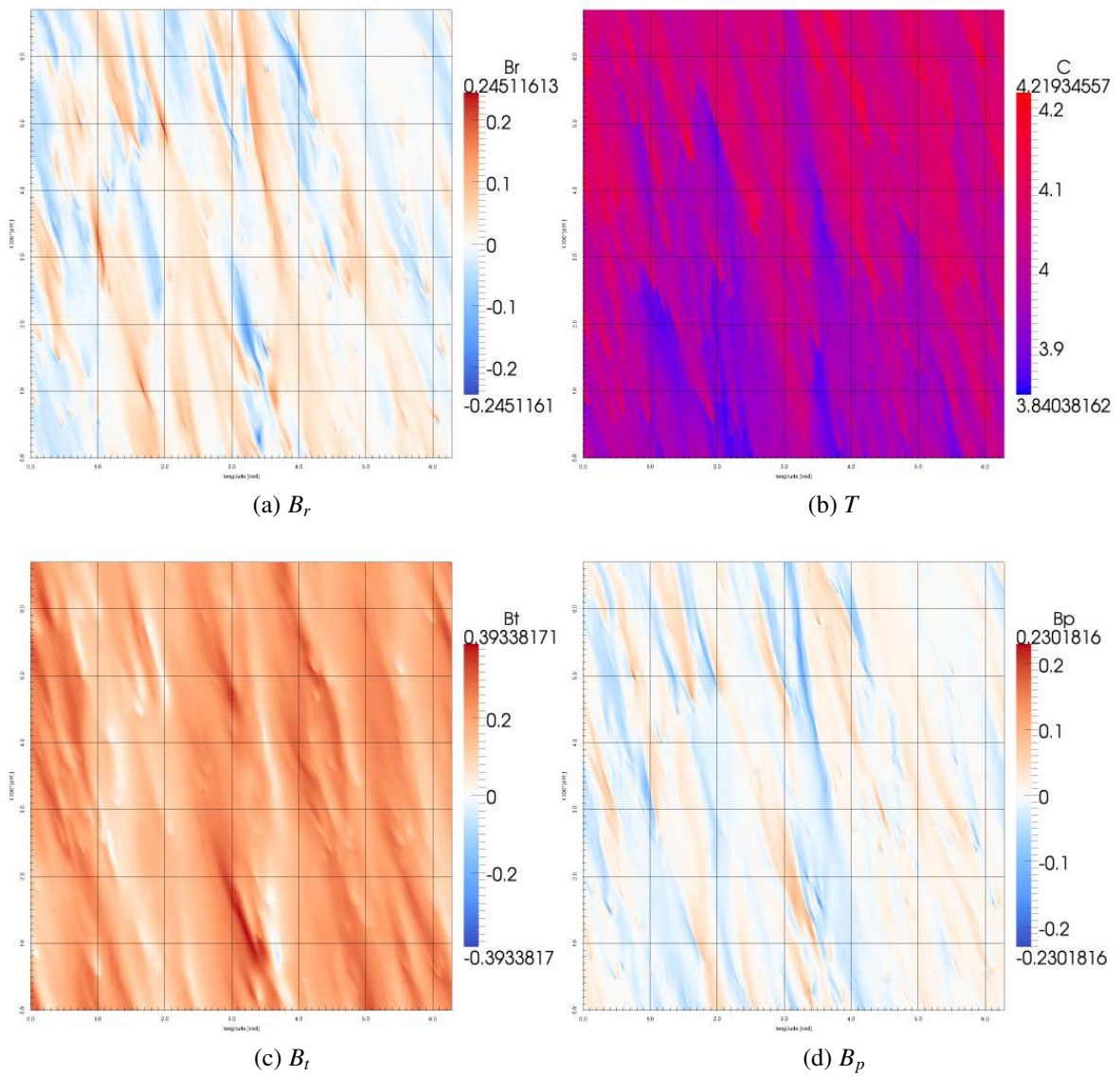
Figure 5.34: *Time-longitude plots at r_o at equator. Case 1. Horizontal axis is longitude. Vertical axis is time (major ticks are separated by 1/200 of a magnetic diffusion time). Time increases from the bottom to the top.*

(a) B_r

(b) T

(c) B_t

(d) B_p
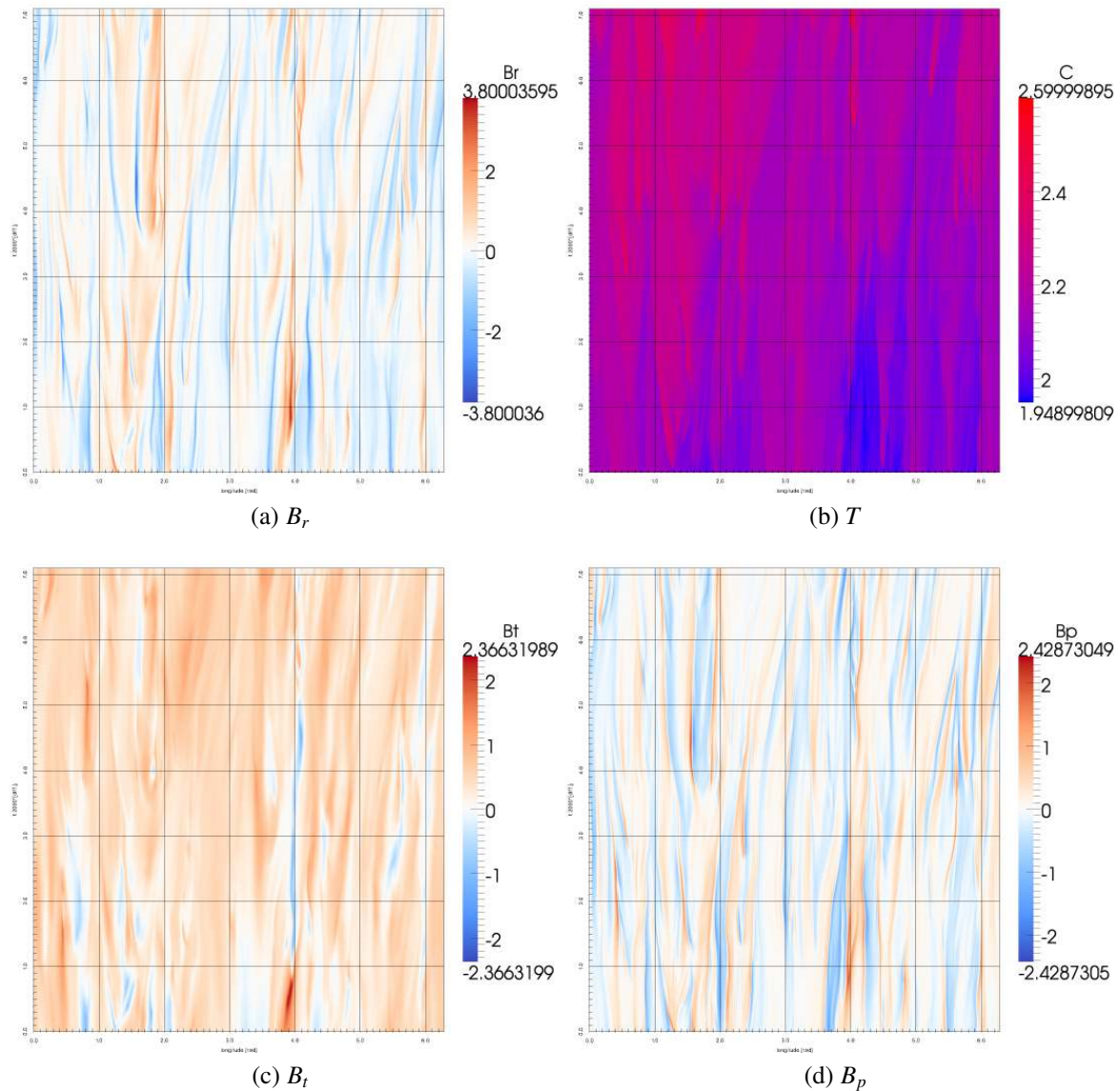
Figure 5.35: *Time-longitude plots at r_o at equator. Case 2. Horizontal axis is longitude. Vertical axis is time (major ticks are separated by 1/2000 of a magnetic diffusion time). Time increases from the bottom to the top.*

5.3.11   3D visualisations

The dynamo simulations discussed in this chapter involve an electrically conducting fluid undergoing highly entangled motions and generating complex magnetic fields. A viewer who is rebuilding in his imagination this 3D complexity from two-dimensional slices is in a situation reminiscent of the prisoner sitting in Plato's Cave. Here we try to drag the prisoner slightly nearer to the sunlight. Streamlines in all three space dimensions capturing more of the details of the true 3D field and examples are shown in figure (5.36).

(a) **u**   (b) **B**
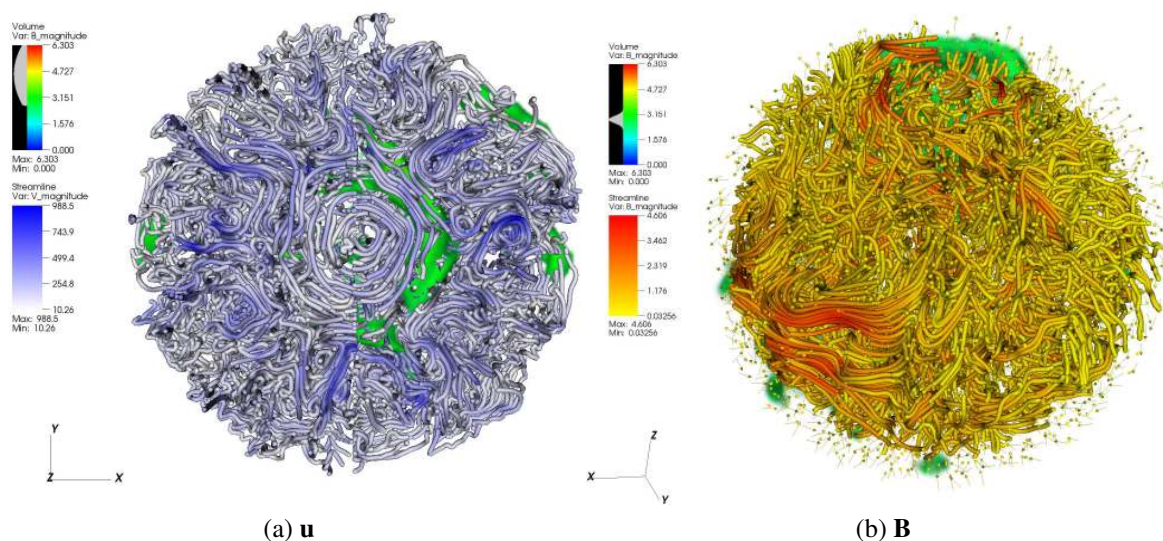
Figure 5.36*: Streamlines of the flow and the magnetic field, Case 1. a) Streamlines of the flow, view from the top b) Tangent to the magnetic field lines, side-view . Green background is a volume rendering of the magnetic field. The z-axis indicates the axis of rotation. Arrows illustrate direction of the surface magnetic field.*

Meandering lines of the magnetic field (on equator, left part of the **B**-plot, fig. 5.36) correspond to a vortex in the velocity field (dark blue stream-lines circle elongated in the direction perpendicular to the rotational axis direction , in the right-upper sector of the **u**-plot, fig. 5.36). The strong twisting of magnetic field lines produces significant amounts of radial field which is in turn observed as strong radial patches on the CMB.

The central vortex around the rotational axis forms circular-shaped streamlines. We can see how velocities are independent on different sides of the tangent cylinder. The fluid tolerates circular retrograde motions in the central regions of the shell. In the space outside the tangent cylinder the vigorous convection favours more complex flow geometries, but we can see the tendency to form loops where fluid travels from the tangent cylinder up to the surface and back down again, transporting hot material from the inner core to the outer core and cold material back again.

5.4 Discussion, Conclusions

In this chapter computationally demanding and intrinsically complicated convection-driven dynamo simulations at some of the lowest Ekman numbers yet reached have been presented. In terms of the analysis it is a real can of worms (to justify see 5.36). If parameters are such that the regime is very close to the onset of convection, the fluid and the magnetic field can in certain circumstances be expressed analytically. But in fully developed convection there is no obvious way to do so. The traditional aim of physics is to to simplify processes in the nature, avoid all incidental details and extract an idealised model. In any turbulent fluid we are therefore certainly in a difficult situation. Nonetheless, we have performed a list of diagnostic analyses and presented simulations in a detailed way with the aim of extracting the foremost persistent and coherent properties despite the partly accidental nature of individual features.

Self-sustaining large scale magnetic fields are obtained, even at high Rayleigh number and low magnetic Prandtl number, which is a result of importance in itself. The recipe for producing a dynamo is mostly a trial-and-error time-consuming process. But if we can even partly understand why a recipe to get a dynamo is successful, it is a great help for future experimenters. Moreover self-consistent "snapshots" of dynamos can be used to start future experiments directly in a scenario capable of self-producing a magnetic field, thus saving length transient periods.

Sections in the chapter were ordered in such a way that an amount of detail presented increased towards the end. The early sections (sec. 5.3.1–5.3.4) contain only volume or surface integrated properties such as energy, length scales and average temperatures. These are numerical values that are easy to compare with existing theories, e.g. scaling laws (sec. 5.3.4). We found that existing laws constructed from fundamental control parameters are not appropriate for the presented simulations. In contrast, laws which bind together experimental values work well, although they are not in the final analysis useful since neither of involved properties are known before carrying out the simulation.

Graphical representations are the only way to show numerical experiments in precise details and the rest of the chapter was devoted to them (sec. 5.3.5). We presented fields, forces and energies on different surfaces and even in three dimensions. Several interesting phenomena are noticed. The most obvious is the onset of convection inside the tangent cylinder at higher Rayleigh numbers Ra, which has the result of regulating the temperatures and fluid drift direction at the core's surface, although flows can become separated on different sides of the tangent cylinder if there is a sufficient rotation rate.

Most of the strong magnetic field features on the CMB originate on the tangent cylinder or within it and are expelled by strong flows up to the surface. An additional point is that the magnetic field for the most part is produced deep in the shell. It seems that it is important to understand the behaviour of the dynamo action inside the tangent cylinder region to obtain fundamental explanations of the origin of field features, even at low latitudes outside the

tangent cylinder.

Future investigations could, for example, involve extensions to include variations of boundary conditions (e.g. Earth-like heat flux pattern on the CMB and/or ICB), addition of a layer of light elements on the CMB (possible by the adjusting the internal heating profile) or in situ experiments such as artificial excitation of waves inside a working dynamo. For all these types of experiments the dynamos obtained and documented here could be a good starting point.

Chapter 6

Conclusions

Equipped with the pseudo-spectral dynamo code we have conducted several sets of numerical dynamo experiments and reported them in this thesis. We aimed to understand the origins of the features of the observable geomagnetic field and partly to investigate alternative ways of creating laboratory dynamos.

First, we have described several methods to benchmark codes with so-called pseudo-vacuum boundary conditions (chapter 3). For many dynamo codes these boundary conditions are advantageous since they can be easily implemented in non-spectral codes, and the benchmark may be convenient at the development stage for more complex and realistic BCs. Decay rates of decay modes in a sphere and in a spherical shell were deduced analytically. The solutions obtained with the modified version of our spectral code showed an excellent agreement with the analytical predictions. We have also found a recipe to achieve two dynamos with deterministic regular characteristics operating with the pseudo-vacuum BCs. We have reported essential properties of these dynamos, the dependence of the convergence on the resolution, and the required timesteps. These data were used in the community benchmark paper Jackson et al. (2014). Beyond that we have investigated the impact of initial conditions on the equilibrated state of the presented dynamos. As it turned out, the subcritical dynamos are very susceptible to even moderate changes in initial conditions, resulting in alternation of branches of the solution. We have also examined modifications in dynamos induced by the interchange of pseudo-vacuum and insulating boundary conditions (with otherwise equal parameters and initial conditions). It emerged that the solutions essentially deviate.

Continuing to discuss the importance of boundary conditions, we report that a driving mechanism, by the fluid injection, at first sight seemingly unconnected with our numerical code can be implemented by a simple modification of the boundary conditions (chapter 4). By virtue of this opportunity, we have investigated the possibility to create a laboratory dynamo driven by the fluid injection (from one boundary and draining off from another boundary in order to satisfy the fluid incompressibility condition). We have found a very particular behaviour of the flow when injection is from the inner boundary and uniform: the basic flow stabilises the system so much, that all non-axisymmetric perturbations die out if the basic flow is too

strong, too weak or the rotation is too slow. It is however more likely that non-axisymmetric fluid motions can act as a dynamo and generate magnetic fields. We have solved equations linearised about the basic flow to find that there is only a limited range of Rossby numbers (defined in tab.4.1) and limited from below Ekman numbers where non-axisymmetric motions are possible. Tests with the full set of MHD equations in the range of parameters where only axisymmetric fluid motions are feasible, failed to detect any self-sustained growth of magnetic field. On the other hand, we have observed the production of magnetic field in certain cases where non-axisymmetric flows are present. However the equilibrated energies turned out to be very low and the geometry of the resulting magnetic field therefore looked nothing like the geomagnetic field. Nevertheless, it should be remembered that we have investigated only a tiny region of parameters that is very close to the onset of non-axisymmetric flows. Going towards lower Ekman numbers would, for example, reveal more complicated and possibly favourable for dynamo fluid motions. In addition, we have found that inversion of the direction of the injection (with the base flow from the outer boundary towards the inner one) immediately produces complex unstable flows and this may be a fruitful course of the future investigations.

Turning back to the boundary conditions which are more related to the planetary phenomena, we have been inspired by the conclusion of Sakuraba and Roberts (2009) that the constant heat flux boundary condition contributes to the production of larger-scale magnetic fields, when Ekman number E is sufficiently low, in comparison to more commonly used constant-temperature boundary condition. The inability of the dynamo itself to adjust temperatures on the boundaries if a constant temperature is imposed leads to tiny-scale motions and correspondingly to small-scale magnetic fields, which are not relevant to the geomagnetic field. This constraint is easily removed if the radial derivative of temperature is controlled on the boundary (by imposing the constant heat flux) instead of temperature itself. We have repeated the calculation by Sakuraba and Roberts (2009) and have conducted six other calculations (chapter 5) increasing the driving parameter Ra (Rayleigh number) and varying Pr_m (ratio of viscous and magnetic diffusivities). It is tricky to obtain working dynamos with low values of Ekman number E (this leads to small length and time scales) and magnetic Prandtl number Pr_m (enhanced magnetic diffusion can shut the dynamo down). Yet, the lowest parameters we have used were $E \approx 3 \cdot 10^{-7}$ and $Pr_m = 0.05$ which are at the cutting edge of the geodynamo research today. After initial transients were passed in these dynamos, we have collected and reported their properties.

The bulk properties of our rapidly rotating dynamos were tested against a selection of scaling laws. The only scaling laws we found that adequately describe our dynamos are those that interrelate experimental values. Other scaling laws based on governing parameters and make predictions that are not well matched by our dynamos. Both types of scaling laws therefore have their weaknesses in practical applications and do not seem to bring new constraints or useful forecasts in the considered range of parameters.

The slope of an energy spectrum (energy vs. spherical harmonic degree) depends on whether or not friction or Ohmic losses are influential at the considered lengthscales. As discovered by Kolmogorov, in isotropic turbulence, the spectral density of energy grows as the length scale to the power of 5/3, at scales in inertial range, intermediate between large eddy- and small diffusive- scales. The preferential flow directions are constrained by the rotation and by magnetic field in the studied dynamos. Beyond that, Reynolds numbers are moderate in comparison with those in classical turbulence. Nevertheless, kinetic energy spectral slopes are close to Kolmogorov's. In fact, one of the calculations was conducted with the magnetic field turned off, and the slope was exactly as in the theory. When magnetic field is weak and diffusion term in induction equation dominates, the spectral density of magnetic energy grows faster than kinetic energy density, $E_{mag}(l) = l^2 \cdot E_{kin}(l)$, where l is the length scale (see Moffatt, 1961). Surprisingly, such magnetic spectral slopes were found in some of our dynamos, although magnetic field was influential.

Regarding the internal structure of the rapidly rotating dynamos, we have found that processes inside and on the tangent cylinder are essential to form geophysically relevant structures on the CMB. Furthermore, the temperature gradient between equator and poles, the choice of retro- or prograde flow under the surface are affected by the region of the shell inside the tangent cylinder and whether convection has onset there. Comparing the temporal behaviour of the surface magnetic field and flow velocities we have concluded that the drift of the magnetic field is mostly caused by the advection. The leading force balance in the bulk of the shell is between Coriolis and Lorentz forces. Moreover, comparing convection regimes with the same parameters, but with and without magnetic field we have found that the magnetic field substantially changes the flow and by no means can be considered as passive.

Before concluding, I would like to remark that a proper understanding of the geomagnetic field may require working out details of conditions specific for the Earth's core. For instance, as we have noted, solutions of MHD equations are strongly dependent on boundary and initial conditions. This gives rise to a straightforward conclusion that the proper treatment of geomagnetic field requires Earth-like (dictated by the mantle and solid inner core) boundary and initial conditions. Unfortunately we know little about the primordial conditions in the core of the young Earth, and likely would not wish to integrate from the very beginnings. Luckily, we can imagine that our current observations of the Earth's core, albeit incomplete, can constrain the initial conditions. Further complications of the model may also require accounting for the compressibility and inhomogeneity of the fluid, time-dependence of the BCs, oblate and bumpy boundaries, the volume distribution of the heat sources and even influences of external magnetic fields.

Continuing with the brute force approach of investigating the geodynamo forces us to gradually move the governing parameters towards Earth's core values. This will require extensive use of parallel computing resources, which involves adapting the codes to the constantly emerging new hardware technologies and aggressive performance optimisations. Going in this

direction will lead us into difficulties concerning how to interpret the results, since amount of data and complexity is likely to increase with e.g. the lowering of the Ekman number. This may also increase the importance of visualisation and of designing new intuitive human-computer interfaces for analysis of graphical representations. Besides that, the increase of storage requirements might force researchers to employ techniques such as post-processing on-the-fly.

The scenario in the previous paragraph requires burning gigawatt-hours of electricity and sharing millions of cpu-hours on parallel computers. Furthermore, investing a considerable amount of man-hours in rewriting, optimising and debugging a large, complex numerical codes is usually inevitable if utilisation of large resources is desired. It also seems that there are fundamental limitations on such a brute force direct modelling of such a huge natural object as the Earth's core (see e.g. the simple estimation of necessary resources on p. 9), and in this sense there is no hope to solve numerically the MHD equations with the Earth's core parameters. I would like to believe that an alternative analytical approach, probably in combination with simplified numerics, still presents an opportunity for giving to give important answers concerning the functioning of the geodynamo. For example, application of constraints (e.g. Taylor's constraint as in Livermore et al., 2011), physically consistent separation of small scales, usage of better algorithms of linear algebra and symmetries (e.g. as demonstrated by Pastukhov, 2000 for weakly-dissipative plasma in a different MHD application, an appropriate account for symmetries can permit the formulation of simplified equations which correctly capture large-scale dynamics) may be possibilities for reducing the required amount of computations.

Appendix A

Basic theory

A.1 Fluid flow equation (Navier-Stokes)

A.1.1 Newton's Law

The basic equation is Newton's 2nd law:

$$m\mathbf{a} = \mathbf{F} \tag{A.1}$$

for a fluid parcel with mass m, $\mathbf{a} = \dfrac{\mathrm{d}\mathbf{u}_{parcel}}{\mathrm{d}t}$ is acceleration of the parcel and $\mathbf{F}$ are forces acting on the parcel. This equation holds in an inertial reference frame .

If $\mathbf{u}(x, y, z, t)$ is a field of fluid velocities, we can trace the change in velocity of a fluid parcel by the following operation: [1]

$$\mathrm{d}\mathbf{u}_{\mathrm{parcel}} = \mathrm{dt}\frac{\partial}{\partial \mathrm{t}}\mathbf{u} + (\mathrm{d}\mathbf{x} \cdot \boldsymbol{\nabla})\mathbf{u},$$

where $\mathrm{d}\mathbf{x} = \mathbf{u} \cdot \mathrm{dt} + O(\mathrm{dt})$. Division of this equation by dt and taking the limit $\mathrm{dt} \to 0$ gives:

$$\frac{\mathrm{d}}{\mathrm{dt}}\mathbf{u}_{parcel} = \frac{\partial}{\partial t}\mathbf{u} + (\mathbf{u} \cdot \boldsymbol{\nabla})\mathbf{u} \quad = \frac{D}{Dt}\mathbf{u}.$$

Where the term $\mathbf{u} \cdot \boldsymbol{\nabla}\mathbf{u}$ takes into account the fact that at $t + \mathrm{dt}$ our parcel has moved to the position $\mathbf{x}_o + \mathbf{u}\,\mathrm{dt}$ where the fluid velocity is $\mathbf{u}_0 + (\mathrm{d}\mathbf{x} \cdot \boldsymbol{\nabla})\mathbf{u}$ at time t_0. At time t_1 the velocity should change by $\dfrac{\partial \mathbf{u}}{\partial t}(\mathbf{x}_0)$. This partial derivative is taken in $\mathbf{x}_0$, but the value is almost the same in the adjacent $\mathbf{x}_1$. In short, the velocity of the fluid parcel changes due to the movement to the new point $\mathbf{x}_1$ (where the value of the velocity field is different) and due to the change of the velocity field in time. By $D/Dt = \frac{\partial}{\partial \mathrm{t}} + \mathbf{u} \cdot \boldsymbol{\nabla}$ we have defined a new operator which gives us the acceleration of a fluid parcel from the velocity field $\mathbf{u}(x, y, z, t)$. Now we can substitute

---

[1] In a Cartesian coordinate system $\mathrm{d}\mathbf{x} \cdot \boldsymbol{\nabla}\mathbf{u} = (\mathrm{d}x\frac{\partial}{\partial x} + \mathrm{d}y\frac{\partial}{\partial y} + \mathrm{d}z\frac{\partial}{\partial z})\mathbf{u}$ which by definition of partial derivatives and from continuity of the field $\mathbf{u}(x, y, z, t)$ gives us the change in $\mathbf{u}$ in the direction $d\mathbf{x}$.

this operator into Newton's 2nd law (A.1): $m\dfrac{\mathrm{D}}{\mathrm{D}t}\mathbf{u} = \mathbf{F}$ and use the fact that $m = \rho V$ to write

$$\rho\frac{\mathrm{D}}{\mathrm{D}t}\mathbf{u} = \mathbf{F}, \tag{A.2}$$

where $\mathbf{F}$ now are the forces per unit volume.

A.1.2   Rotating reference frame

Consider a rotating co-ordinate system with constant angular rate $\mathbf{\Omega}$. We refer to the axes of this co-ordinate system as $\mathbf{i}$ and $\mathbf{j}$; $\mathbf{\Omega}$ is perpendicular to them. In an inertial coordinate system, where Newton's laws are obeyed, we can write:

$$\mathbf{r}_i = x\mathbf{i} + y\mathbf{j} \tag{A.3}$$

where x and y are coordinates in the rotating reference frame. Taking $\partial/\partial t$:

$$\dot{\mathbf{r}}_i = \dot{x}\mathbf{i} + \dot{y}\mathbf{j} + x\dot{\mathbf{i}} + y\dot{\mathbf{j}} \tag{A.4}$$

where $\dot{\mathbf{r}}_i = \dfrac{\partial \mathbf{r}_i}{\partial t}$. The axes $\mathbf{i}$ and $\mathbf{j}$ turn with the rate $\mathbf{\Omega}$, so $\dot{\mathbf{i}} = \mathbf{\Omega} \times \mathbf{i}$ and $\dot{\mathbf{j}} = \mathbf{\Omega} \times \mathbf{j}$. Then $x\dot{\mathbf{i}} + y\dot{\mathbf{j}} = \mathbf{\Omega} \times (x\mathbf{i} + y\mathbf{j}) = \mathbf{\Omega} \times \mathbf{r}_i$:

$$\dot{\mathbf{r}}_i = \dot{x}\mathbf{i} + \dot{y}\mathbf{j} + \mathbf{\Omega} \times \mathbf{r}_i = \mathbf{u}_r + \mathbf{\Omega} \times \mathbf{r}_i \tag{A.5}$$

where $\mathbf{u}_r$ is the velocity in the rotating reference frame. In equation (A.2) we are mainly interested in the acceleration, therefore taking a further derivative and using again equation (A.5):

$$\ddot{\mathbf{r}} = \dot{\mathbf{u}}_r + \mathbf{\Omega} \times \dot{\mathbf{r}}_i = \dot{\mathbf{u}}_r + \mathbf{\Omega} \times (\mathbf{u}_r + \mathbf{\Omega} \times \mathbf{r}_i)$$

Recall that $\mathbf{u}_r = \dot{x}\mathbf{i} + \dot{y}\mathbf{j}$, consequently $\dot{\mathbf{u}}_r = \ddot{x}\mathbf{i} + \ddot{y}\mathbf{j} + \dot{x}\dot{\mathbf{i}} + \dot{y}\dot{\mathbf{j}}$. Similarly to (A.4) we obtain $\dot{x}\dot{\mathbf{i}} + \dot{y}\dot{\mathbf{j}} = \mathbf{\Omega} \times \mathbf{u}_r$. The expression "$\ddot{x}\mathbf{i} + \ddot{y}\mathbf{j}$" is the desired acceleration in the non-inertial, rotating, frame, denoted $\mathrm{d}\mathbf{u}_r/\mathrm{d}t$ (this derivative is in the non-inertial frame, where axes are treated as fixed).

$$\ddot{\mathbf{r}} = \frac{\mathrm{d}\mathbf{u}_r}{\mathrm{d}t} + \mathbf{\Omega} \times \mathbf{u}_r + \mathbf{\Omega} \times (\mathbf{u}_r + \mathbf{\Omega} \times \mathbf{r}_i) = \frac{\mathrm{d}\mathbf{u}}{\mathrm{d}t} + 2\mathbf{\Omega} \times \mathbf{u}_r + \mathbf{\Omega} \times (\mathbf{\Omega} \times \mathbf{r}_i) \tag{A.6}$$

We can now substitute this into the left hand side of equation (A.2) to obtain an equation valid in a rotating reference frame

$$\frac{\mathrm{D}\mathbf{u}_r}{\mathrm{D}t} + 2\mathbf{\Omega} \times \mathbf{u}_r + \mathbf{\Omega} \times (\mathbf{\Omega} \times \mathbf{r}_i) = \frac{1}{\rho}\mathbf{F} \tag{A.7}$$

It is worth to mention that $\boldsymbol{\Omega} \times (\boldsymbol{\Omega} \times \mathbf{r}) = \boldsymbol{\nabla}(\frac{1}{2}|\boldsymbol{\Omega} \times \mathbf{r}|^2)$.

Hereinafter the subscript "r" that we used to indicate the velocity in a rotating reference frame will be omitted.

A.1.3   Forces

An electrically conducting fluid is affected by pressure, viscosity, gravity and electromagnetic (EM) forces. Pressure and viscosity are surface forces of a fluid self-interaction (in a continuous fluid by the Ostrogradsky-Gauss divergence theorem these surface forces can be converted into the volume form). Gravity and EM forces are external body forces.

A.1.3.1   Pressure and viscosity forces

Let T_{ij} be a stress tensor and n_j be a unit vector perpendicular to the surface element dS. The i-th component of the force exerted, by the surrounding fluid, on a blob of fluid with the surface S is:

$$\int_V F_i^{stress} \mathrm{dV} = \int_S T_{ij} n_j \mathrm{dS} = \int_V \frac{\partial T_{ij}}{\partial x_j} \mathrm{dV} \tag{A.8}$$

by Ostrogradsky-Gauss theorem[2].

Now we restrict attention to an incompressible fluid, for which

$$\boldsymbol{\nabla} \cdot \mathbf{u} = 0. \tag{A.9}$$

Following the definition of a Newtonian viscous fluid of a constant viscosity μ we write:

$$T_{ij} = -p\delta_{ij} + \mu\left(\frac{\partial u_j}{\partial x_i} + \frac{\partial u_i}{\partial x_j}\right). \tag{A.10}$$

So the stress-tensor is symmetric (i.e. $T_{ij} = T_{ji}$). The quantity p, called pressure, is simply minus the mean of the three normal stresses at a point:

$$p = -\frac{1}{3}(T_{ii}).$$

On substituting the definition of a Newtonian fluid eq.(A.10) into a component of the force equation (A.8):

$$F_i^{stress} = \frac{\partial T_{ij}}{\partial x_j} = \frac{\partial}{\partial x_j}\left(-p\delta_{ij} + \mu\left(\frac{\partial u_j}{\partial x_i} + \frac{\partial u_i}{\partial x_j}\right)\right) = -\frac{\partial p}{\partial x_i} + \mu\left(\frac{\partial}{\partial x_i}\frac{\partial u_j}{\partial x_j} + \frac{\partial^2 u_i}{\partial x_j^2}\right), \tag{A.11}$$

---

[2]From now on Einstein's notation is used where summation over $j = 1, 2, 3$ is understood by virtue of the repeated suffix.

here $\partial u_j/\partial x_j = \mathbf{\nabla} \cdot \mathbf{u} = 0$ by eq.(A.9), and $\partial^2 u_i/\partial x_j^2 = \mathbf{\nabla}^2 \mathbf{u}$, so we can write

$$\mathbf{F}^{stress} = -\mathbf{\nabla}p + \mu\mathbf{\nabla}^2\mathbf{u} \tag{A.12}$$

A.1.3.2   Gravitational force

The gravitational force per unit volume is

$$\mathbf{F}^{gravity} = \rho\mathbf{g} = -\rho\mathbf{\nabla}\Psi, \tag{A.13}$$

where Ψ is a gravitational potential, $\mathbf{\nabla}^2\Psi = 4\pi G\rho$. [3]

A.1.3.3   Electromagnetic force

The influence of electromagnetic forces on a fluid is described by the Lorentz force. By the definition of the magnetic field this force is

$$\tilde{\mathbf{F}} = q(\mathbf{u} \times \mathbf{B}), \tag{A.14}$$

where q is the charge of a particle moving with the velocity $\mathbf{u}$ and $\mathbf{B}$ is the value of the magnetic field at a point where the particle is. In a continuous medium with electric current density $\mathbf{J}$ and free charge density $\widetilde{\rho}$ [4] we can rewrite eq. (A.14) as

$$\mathbf{F}^{Lorentz} = \widetilde{\rho}(\mathbf{u} \times \mathbf{B}). \tag{A.15}$$

Now $\mathbf{F}^{Lorentz}$ is the force per unit volume. During the time dt a charge dq passes through the imaginary surface element dS. This charge can be counted either knowing the free charge density $\widetilde{\rho}$ and its velocity $\mathbf{u}$: dq $= \int \widetilde{\rho}\,\mathrm{d}\mathbf{S}\,\mathbf{u}\mathrm{d}t$, or equivalently by knowing the current density $\mathbf{J}$: dq $= \int \mathbf{J}\,\mathrm{d}\mathbf{S}\,\mathrm{d}t$. Since integration in both cases is over the variable t, and the same dq is counted and we can see that

$$\widetilde{\rho}\mathbf{u} = \mathbf{J}. \tag{A.16}$$

If we then substitute eq.(A.16) into (A.15): [5]

$$\mathbf{F}^{Lorentz} = \mathbf{J} \times \mathbf{B} = \frac{1}{\mu_0}(\mathbf{\nabla} \times \mathbf{B}) \times \mathbf{B} = \frac{1}{\mu_0}\left(-\mathbf{\nabla}\left(\frac{\mathbf{B}^2}{2}\right) + (\mathbf{B} \cdot \mathbf{\nabla})\mathbf{B}\right). \tag{A.17}$$

By use of $\mathbf{J} = \mathbf{\nabla} \times \mathbf{B}/\mu_0$ we assume that there are no displacement currents ($\partial\mathbf{D}/\partial t = 0$,

---

[3]By Gauss's law $\mathbf{\nabla} \cdot (\mathbf{g}(\mathbf{r})) = -\mathbf{\nabla} \cdot \mathbf{\nabla}\Psi \equiv -4\pi\rho \implies \mathbf{\nabla}^2\Psi \equiv 4\pi\rho$; e.g. inside a sphere of a constant density ρ, $\Psi = \frac{2}{3}\pi r^2 G\rho$; in a free space around mass M, $\Psi = -GM/r$. Using $\mathbf{\nabla}^2 f(r) = \frac{1}{r^2}\frac{\partial}{\partial r}(r^2\frac{\partial f}{\partial r})$ it is easy to check.

[4]To differentiate between the part of charge which is responsible for magnetic force and the net-charge, which is assumed to be zero in our fluid, the notation 'free charge' $\widetilde{\rho}$ is introduced here.

[5]Equality $\mathbf{a} \times (\mathbf{b} \times \mathbf{c}) = \mathbf{b}(\mathbf{a} \cdot \mathbf{c}) - \mathbf{c}(\mathbf{a} \cdot \mathbf{b})$ is used here: $(\mathbf{\nabla} \times \mathbf{B}) \times \mathbf{B} = -\mathbf{B} \times (\mathbf{\nabla} \times \check{\mathbf{B}}) = -(\mathbf{\nabla}(\check{\mathbf{B}} \cdot \mathbf{B}) - (\mathbf{B} \cdot \mathbf{\nabla})\check{\mathbf{B}})$; obviously $\mathbf{\nabla}(\check{\mathbf{B}} \cdot \mathbf{B}) = \frac{1}{2}(\mathbf{\nabla}(\check{\mathbf{B}} \cdot \mathbf{B}) + \mathbf{\nabla}(\mathbf{B} \cdot \check{\mathbf{B}})) = \mathbf{\nabla}(\frac{\mathbf{B}^2}{2})$

see section A.2).

Note that in this derivation we have assumed zero net-charge (the single fluid MHD approx, e.g. Treumann and Baumjohann, 1997), so the electric force $\mathbf{E}\rho_{nc}$ is zero and the electromagnetic force is adequately described by the magnetic component alone.

A.1.4 Boussinesq approximation

We now rewrite the equation for the fluid flow in a rotating reference frame eq.(A.7) with expressions for the forces from eq.(A.12), (A.13) & (A.17):

$$\rho\frac{\mathbf{D}\mathbf{u}}{\mathbf{D}t} = -2\rho(\mathbf{\Omega}\times\mathbf{u})-\rho\mathbf{\nabla}\left(\frac{1}{2}|\mathbf{\Omega}\times\mathbf{r}|^2\right)-\frac{1}{\mu_0}\mathbf{\nabla}\left(\frac{\mathbf{B}^2}{2}\right)+\frac{1}{\mu_0}(\mathbf{B}\cdot\mathbf{\nabla})\mathbf{B}-\rho\mathbf{\nabla}\Psi-\mathbf{\nabla}p+\mu\mathbf{\nabla}^2\mathbf{u}. \quad \text{(A.18)}$$

Note that in the viscosity term we have already the assumption of incompressibility ($\mathbf{\nabla}\cdot\mathbf{u} = 0$).

Next we define

$$p = p_0 + p_1, \quad \rho = \rho_0 + \rho_1, \quad -\mathbf{\nabla}(\Psi_0 - \Psi_1) = \mathbf{g}_0 + \mathbf{g}_1, \quad \text{(A.19)}$$

where the indices 0 denote the background state which is in hydrostatic balance $\rho_0\mathbf{g}_0 = \mathbf{\nabla}p_0$.

Since $|\mathbf{\Omega}\times\mathbf{u}|$, $|\frac{\mathbf{D}\mathbf{u}}{\mathbf{D}t}|$ & $\mathbf{\nabla}(\frac{1}{2}|\mathbf{\Omega}\times\mathbf{r}|^2)$ are much smaller than $|\mathbf{g}|$ and assuming $\rho_1 \ll \rho_0$, $|\mathbf{g}_1| \ll |\mathbf{g}_0|$ we neglect the product of these terms with ρ_1 and the rest of the second-order small terms and obtain

$$\rho_0\frac{\mathbf{D}\mathbf{u}}{\mathbf{D}t} = -2\rho_0(\mathbf{\Omega}\times\mathbf{u})-\rho_0\mathbf{\nabla}(\frac{1}{2}|\mathbf{\Omega}\times\mathbf{r}|^2)-\frac{1}{\mu_0}\mathbf{\nabla}\left(\frac{\mathbf{B}^2}{2}\right)+\frac{1}{\mu_0}(\mathbf{B}\cdot\mathbf{\nabla})\mathbf{B}+\rho_0\mathbf{g}_1+\rho_1\mathbf{g}_0-\mathbf{\nabla}p_1+\mu\mathbf{\nabla}^2\mathbf{u}.$$
$$\text{(A.20)}$$

Now we can move ρ_0 (it is assumed to be constant under the Boussinesq approximation adopted here) within the gradient operators and combine terms:

$$\rho_0\frac{\mathbf{D}\mathbf{u}}{\mathbf{D}t} = -2\rho_0(\mathbf{\Omega}\times\mathbf{u})-\mathbf{\nabla}\left(\frac{1}{2}\rho_0|\mathbf{\Omega}\times\mathbf{r}|^2+\frac{1}{\mu_0}\frac{\mathbf{B}^2}{2}+\rho_0\Psi_1+p_1\right)+\frac{1}{\mu_0}(\mathbf{B}\cdot\mathbf{\nabla})\mathbf{B}+\rho_1\mathbf{g}_0+\mu\mathbf{\nabla}^2\mathbf{u},$$
$$\text{(A.21)}$$

or:

$$\rho_0\frac{\mathbf{D}\mathbf{u}}{\mathbf{D}t} = -2\rho_0(\mathbf{\Omega}\times\mathbf{u})-\mathbf{\nabla}P+\frac{1}{\mu_0}(\mathbf{B}\cdot\mathbf{\nabla})\mathbf{B}+\rho_1\mathbf{g}_0+\mu\mathbf{\nabla}^2\mathbf{u}. \quad \text{(A.22)}$$

The thermal expansion coefficient α can be defined by:

$$\rho_1 = \rho_0\alpha(T_0 - T) \quad \text{(A.23)}$$

Thereby, eq. (A.22) takes the form:

$$\rho_0\frac{\mathbf{D}\mathbf{u}}{\mathbf{D}t} = -2\rho_0(\mathbf{\Omega}\times\mathbf{u})-\mathbf{\nabla}P+\frac{1}{\mu_0}(\mathbf{B}\cdot\mathbf{\nabla})\mathbf{B}-\alpha\rho_0\mathbf{g}_0(T - T_0)+\mu\mathbf{\nabla}^2\mathbf{u} \quad \text{(A.24)}$$

where T_0 is defined in section (A.3). Thus the fluid compressibility is neglected in eq. (A.24) except in the buoyancy term. This is the essence of the *Boussinesq approximation*. Sound waves become impossible on its account.

A.1.5 Continuity equation and incompressibility

From the conservation of mass we have

$$\boldsymbol{\nabla} \cdot (\rho \mathbf{u}) = -\frac{\partial \rho}{\partial t}. \tag{A.25}$$

If $\rho = \rho_0 + \rho_1$, where $\rho_0 = const$:

$$\boldsymbol{\nabla} \cdot (\rho_0 \mathbf{u}) + \boldsymbol{\nabla} \cdot (\rho_1 \mathbf{u}) = -\frac{\partial \rho_0}{\partial t} - \frac{\partial \rho_1}{\partial t}. \tag{A.26}$$

Then neglecting small terms and remembering that ρ_0 is constant we obtain,

$$\boldsymbol{\nabla} \cdot (\rho_0 \mathbf{u}) = 0. \tag{A.27}$$

This is known as the *anelastic approximation* which filters out sound waves. If ρ_0 does not vary with position, the continuity equation is even simpler:

$$\boldsymbol{\nabla} \cdot \mathbf{u} = 0. \tag{A.28}$$

This is called the *incompressibility condition*, it was assumed in the derivations above and is adopted throughout this thesis.

A.2 Electrodynamics and induction equation

The complete set of *Maxwell equations* is as follows:

$$\boldsymbol{\nabla} \times \mathbf{H} = \mathbf{J} + \frac{\partial \mathbf{D}}{\partial t}, \tag{A.29a}$$

$$\boldsymbol{\nabla} \cdot \mathbf{B} = 0, \tag{A.29b}$$

$$\boldsymbol{\nabla} \cdot \mathbf{D} = \rho_{nc}, \tag{A.29c}$$

$$\boldsymbol{\nabla} \times \mathbf{E} = -\frac{\partial \mathbf{B}}{\partial t}, \tag{A.29d}$$

where

H	is the magnetizing field,	**B**	is the magnetic field,
D	is the electric displacement field,	**E**	is the electric field.
J	is the current density,		

Ohm's law in a moving frame (for motions of the conductor much slower than the speed of light) is:

$$\mathbf{J} = \sigma(\mathbf{E} + \mathbf{u} \times \mathbf{B}), \tag{A.30}$$

where $\mathbf{u}$ is the velocity of a fluid parcel. σ is the coefficient of the linear dependence between a current density and an electric field (Ohm's law in a fixed reference frame), usually called the conductivity.

Furthermore, we consider only slow changes of the EM fields, so that displacement currents $\dfrac{\partial \mathbf{D}}{\partial t}$ can be neglected. By this operation EM-waves are filtered out. And eq.(A.29c) becomes redundant because it is not coupled to any other equation.

For non-ferromagnetic materials,

$$\mathbf{H} = \mathbf{B}/\mu_0. \tag{A.31}$$

Now we can combine (A.30) & (A.29a) together with the statement (A.31), to give:

$$\frac{1}{\mu_0}\mathbf{\nabla} \times \mathbf{B} = \sigma(\mathbf{E} + \mathbf{u} \times \mathbf{B}). \tag{A.32}$$

Taking $\mathbf{\nabla} \times$ of eq. (A.32), using Faraday's law (A.29d) and assuming that $\sigma = $ const, we obtain the so-called *magnetic induction* equation:

$$\frac{\partial \mathbf{B}}{\partial t} + \frac{1}{\sigma\mu_0}\mathbf{\nabla} \times (\mathbf{\nabla} \times \mathbf{B}) = \mathbf{\nabla} \times (\mathbf{u} \times \mathbf{B}). \tag{A.33}$$

Using the vector identity for $\mathbf{a} \times (\mathbf{b} \times \mathbf{c})$, we obtain $\mathbf{\nabla} \times (\mathbf{\nabla} \times \mathbf{B}) = \mathbf{\nabla}(\mathbf{\nabla} \cdot \mathbf{B}) - \mathbf{\nabla}^2\mathbf{B}$ and because of the solenoidal condition for the magnetic field (Maxwell's eq. A.29b coincides with the definition of a *solenoidal field*):

$$\mathbf{\nabla} \times (\mathbf{\nabla} \times \mathbf{B}) = -\mathbf{\nabla}^2\mathbf{B}. \tag{A.34}$$

In a similar way, using $\mathbf{\nabla} \cdot \mathbf{u} = 0$, $\mathbf{\nabla} \cdot \mathbf{B} = 0$ and the identity for $\mathbf{a} \times (\mathbf{b} \times \mathbf{c})$,

$$\mathbf{\nabla} \times (\mathbf{u} \times \mathbf{B}) = (\mathbf{B} \cdot \mathbf{\nabla})\mathbf{u} + \mathbf{u}(\mathbf{\nabla} \cdot \mathbf{B}) - (\mathbf{u} \cdot \mathbf{\nabla})\mathbf{B} - \mathbf{B}(\mathbf{\nabla} \cdot \mathbf{u}) = (\mathbf{B} \cdot \mathbf{\nabla})\mathbf{u} - (\mathbf{u} \cdot \mathbf{\nabla})\mathbf{B} \tag{A.35}$$

With eq. (A.34) and (A.35) the induction equation (A.33) can be rewritten in a more convenient form as:

$$\frac{\mathrm{D}\mathbf{B}}{\mathrm{D}t} = (\mathbf{B} \cdot \mathbf{\nabla})\mathbf{u} + \eta\mathbf{\nabla}^2\mathbf{B}, \tag{A.36}$$

where $\eta = \dfrac{1}{\mu_0\sigma}$ is known as the magnetic diffusivity.

A.3   Heat transport

In a quasi-steady process the change of heat δQ is:

$$\delta Q \equiv T \, \mathrm{d}S = (-\boldsymbol{\nabla} \cdot \mathbf{q} + \varepsilon) \cdot \mathrm{d}t, \tag{A.37}$$

where $\mathbf{q}$ is a heat-flux vector, ε is the rate of internal generation of heat per unit volume, S is an entropy per unit volume and T is the temperature.

Fourier's law of heat conduction is:

$$\mathbf{q} = -k\boldsymbol{\nabla}T, \tag{A.38}$$

if $k =$const then in a fluid we have:

$$T \frac{\mathrm{D}}{\mathrm{Dt}} S = k\boldsymbol{\nabla}^2 T + \varepsilon. \tag{A.39}$$

In Boussinesq approximation we treat ρ as a constant in all terms in the equations of motion except in the buoyancy force. Using the definition of the specific heat at constant pressure $C_p = T \left(\dfrac{\partial S}{\partial T} \right)_P$ we have,

$$\rho C_p \frac{\mathrm{D}}{\mathrm{Dt}} T - \alpha T \frac{\mathrm{D}}{\mathrm{Dt}} p = k\boldsymbol{\nabla}^2 T + \varepsilon \tag{A.40}$$

(see Jacobs, 1987 §1.3), where $\alpha = -\dfrac{1}{\rho} \left(\dfrac{\partial \rho}{\partial T} \right)_p$. Under the Boussinesq approximation ρ should be constant in eq.(A.40), so in this case we can take $\alpha = 0$ and we can rewrite eq. (A.40):

$$\rho C_p \frac{\mathrm{D}}{\mathrm{Dt}} T = k\boldsymbol{\nabla}^2 T + \varepsilon. \tag{A.41}$$

Next, consider an adiabatic background steady state T_0 which satisfies

$$\rho C_p \frac{\mathrm{D}}{\mathrm{Dt}} T_0 = 0. \tag{A.42}$$

Subtracting eq.(A.42) from eq.(A.41) and denoting $\Theta = T - T_0$, we obtain

$$\rho C_p \frac{\mathrm{D}}{\mathrm{Dt}} \Theta = k\boldsymbol{\nabla}^2 \Theta + \varepsilon. \tag{A.43}$$

Note that in the absence of fluid flow, $\mathbf{u} = 0$, a uniform internal heat source leads to a steady state temperature profile $\hat{\Theta}$ (see Chandrasekhar, 1961) which is solution of $0 = k\boldsymbol{\nabla}^2 \hat{\Theta} + \varepsilon$:

$$\hat{\Theta} = \frac{\beta}{2}(r_0^2 - r^2), \qquad \beta = \frac{\varepsilon}{3k}. \tag{A.44}$$

Background temperature deviation Θ can also be considered as a *co-density* including effects

of both temperature and light element perturbation (Braginsky and Roberts, 1995).

A.4   Summary of MHD equations for rotating convection

Gathering together equations (A.9), (A.24), (A.29b), (A.36), (A.43) we obtain:

$$
\begin{cases}
\qquad\qquad \boldsymbol{\nabla} \cdot \mathbf{u} \;=\; 0, \qquad \boldsymbol{\nabla} \cdot \mathbf{B} \;=\; 0, \\[4pt]
\rho_0 \dfrac{\mathrm{D}\mathbf{u}}{\mathrm{Dt}} \;=\; -2(\boldsymbol{\Omega} \times \mathbf{u})\rho_0 - \boldsymbol{\nabla}P + \dfrac{1}{\mu_0}(\mathbf{B}\cdot\boldsymbol{\nabla})\mathbf{B} - \rho_0\alpha\Theta\mathbf{g} + \nu\rho_0\boldsymbol{\nabla}^2\mathbf{u}, \\[4pt]
\dfrac{\mathrm{D}\mathbf{B}}{\mathrm{Dt}} \;=\; (\mathbf{B}\cdot\boldsymbol{\nabla})\mathbf{u} + \eta\boldsymbol{\nabla}^2\mathbf{B}, \\[4pt]
\rho_0 C_p \dfrac{\mathrm{D}}{\mathrm{Dt}}\Theta \;=\; k\boldsymbol{\nabla}^2\Theta + \varepsilon,
\end{cases}
\tag{A.46}
$$

where the *modified pressure P* is given (from eq.A.21) by:

$$
P = \left(\frac{1}{2}\rho_0 |\boldsymbol{\Omega}\times\mathbf{r}|^2 + \frac{1}{\mu_0}\frac{\mathbf{B}^2}{2} + \rho_0\Psi_1 + p_1 \right).
\tag{A.47}
$$

A commonly used non-dimensionalization of these equations (e.g. Christensen et al., 2001) is based on the length scale being the shell thickness $d = r_o - r_i$ where r_o is the radius of the outer shell and r_i is the radius of the inner shell, the viscous diffusion time scale d^2/ν and the temperature scale ΔT_0 which is difference in the temperature (imposed) at the top and bottom boundaries.

$$
\mathbf{r} \to d\mathbf{r}, \quad t \to \frac{d^2}{\nu}t, \quad \mathbf{u} \to \frac{\nu}{d}\mathbf{u}, \quad \Theta \to (\Delta T_0)\Theta, \quad \mathbf{B} \to (\rho_0\mu_0\eta\Omega)^{\frac{1}{2}}\mathbf{B}.
\tag{A.48}
$$

This yields:

$$
\begin{cases}
\qquad\qquad \boldsymbol{\nabla} \cdot \mathbf{u} = 0, \quad \boldsymbol{\nabla} \cdot \mathbf{B} = 0, \\[4pt]
E_1\left(\dfrac{\mathrm{D}\mathbf{u}}{\mathrm{Dt}}\right) + 2(\hat{\mathbf{z}}\times\mathbf{u}) \;=\; -\boldsymbol{\nabla}P + \dfrac{1}{Pr_m}(\mathbf{B}\cdot\boldsymbol{\nabla})\mathbf{B} + Ra_1 T\dfrac{\mathbf{r}}{r_0} + E\boldsymbol{\nabla}^2\mathbf{u}, \\[4pt]
\dfrac{\mathrm{D}}{\mathrm{Dt}}\mathbf{B} \;=\; (\mathbf{B}\cdot\boldsymbol{\nabla})\mathbf{u} + \dfrac{1}{Pr_m}\boldsymbol{\nabla}^2\mathbf{B}, \\[4pt]
\dfrac{\mathrm{D}}{\mathrm{Dt}}\Theta \;=\; \dfrac{1}{Pr}\boldsymbol{\nabla}^2\Theta + \dfrac{\varepsilon D^2}{\rho_0 C_p \Delta T_0}.
\end{cases}
\tag{A.49}
$$

with control parameters:

$$E_1 = \frac{\nu}{\Omega d^2} \qquad \text{Ekman Number,}$$

$$Ra_1 = \frac{\alpha g_0 \Delta T_0 d}{\nu \Omega} \qquad \text{Modified Rayleigh Number.}$$

$$Pr = \frac{\nu}{\kappa} \qquad \text{Prandtl Number,} \tag{A.50}$$

$$Pr_m = \frac{\nu}{\eta} \qquad \text{Magnetic Prandtl Number,}$$

$$\tilde{S} = \frac{\varepsilon d^2}{\rho_0 C_p \Delta T_0} \qquad \text{dimensionless internal heat,}$$

where $\kappa = \dfrac{k}{\rho_0 C_p}$.

A.4.1   Non-dimensionalization used for numerical calculations

In the numerical implementation used in this thesis an alternative non-dimensionalization is used (following Willis et al., 2007). This involves the scalings:

$$\text{Length } d = r_o - r_i, \quad \text{Time } t = d^2/\eta, \quad \text{Magnetic } B = (2\Omega\rho_0\mu_0\eta)^{\frac{1}{2}},$$

where r_i and r_o are radii of the inner and outer cores. It should be noted that time is scaled by the magnetic diffusivity η instead of ν in eq.(A.48). This scaling leads to the alternative dimensionless parameters (see, for example, Willis et al., 2007):

$$
\begin{array}{llcc}
\text{Magnetic Rossby number} & Ro = \eta/(2\Omega d^2) & = & \dfrac{E}{q\,Pr} = \dfrac{E_1}{2Pr_m}, \\[2mm]
\text{Ekman number} & E = \nu/(2\Omega d^2) & = & E_1/2, \\[2mm]
\text{Modified Rayleigh number} & Ra = g\,\alpha\,\Delta T_0\,d/(2\Omega\kappa) & = & \dfrac{2Ra_1}{Pr} = \dfrac{1}{2}Ra_1 \cdot \left(\dfrac{E}{q \cdot Ro}\right), \\[2mm]
\text{Roberts number} & q = \kappa/\eta & = & Pr_m/Pr.
\end{array}
\tag{A.51}
$$

If d^2/ν is taken for the timescale (as in eq.A.49) then Ro does not appear in the alternative governing equations. Also note that by setting $Pr_m = 1$, non-dimensionalisation by the viscous and magnetic timescales is equivalent, i.e.
we have

$$q = 1/Pr, \qquad Ro = E. \tag{A.52}$$

Similarly, if $q = 1$ thermal and magnetic timescales are equivalent and we have

$$q = 1, \qquad Ro = E/Pr. \tag{A.53}$$

Following Willis et al. (2007) the Navier-Stokes equation (A.49.2) can also be rearranged as follows:

$$E_1 \left(\frac{\partial \mathbf{u}}{\partial t} + (\mathbf{u} \cdot \mathbf{\nabla})\mathbf{u} \right) = -\mathbf{\nabla}P + \frac{1}{Pr_m}(\mathbf{B} \cdot \mathbf{\nabla})\mathbf{B} + Ra_1 T \frac{\mathbf{r}}{r_0} + E_1 \mathbf{\nabla}^2 \mathbf{u} - 2(\hat{\mathbf{z}} \times \mathbf{u}) \qquad \text{(A.54)}$$

if we then can use the identity to obtain $(\mathbf{u} \cdot \mathbf{\nabla})\mathbf{u} = -\mathbf{u} \times (\mathbf{\nabla} \times \mathbf{u}) + \frac{1}{2}\mathbf{\nabla}(\mathbf{u}^2)$. Noting that the term $\dfrac{\mathbf{B}^2}{2Pr_m}$ in the modified pressure can be combined with $\dfrac{(\mathbf{B} \cdot \mathbf{\nabla})\mathbf{B}}{Pr_m}$ and the pressure is now

$$\hat{P}_1 = P + \frac{E}{2}\mathbf{u}^2 - \frac{\mathbf{B}^2}{2Pr_m}. \qquad \text{(A.55)}$$

Giving

$$E_1 \left(\frac{\partial \mathbf{u}}{\partial t} - \mathbf{\nabla}^2 \mathbf{u} \right) = E_1 \, \mathbf{u} \times (\mathbf{\nabla} \times \mathbf{u}) - \mathbf{\nabla}\hat{P} + \frac{1}{Pr_m}(\mathbf{\nabla} \times \mathbf{B}) \times \mathbf{B} + Ra_1 T \frac{\mathbf{r}}{r_0} - 2(\hat{\mathbf{z}} \times \mathbf{u}). \qquad \text{(A.56)}$$

Then, finally, we can write the non-dimensional equations in the form used for numerical calculations in the thesis:

$$\begin{cases} \left(Ro\,\dfrac{\partial}{\partial t} - E\mathbf{\nabla}^2 \right)\mathbf{u} &=& \mathbf{N}_u - \mathbf{\nabla}\hat{P}, \\[2mm] \left(\dfrac{\partial}{\partial t} - \mathbf{\nabla}^2 \right)\mathbf{B} &=& \mathbf{N}_B, \\[2mm] \left(\dfrac{\partial}{\partial t} - q\mathbf{\nabla}^2 \right)\Theta &=& N_T, \end{cases} \qquad \text{(A.57)}$$

where

$$\begin{aligned} \mathbf{N}_u &= Ro\,\mathbf{u} \times (\mathbf{\nabla} \times \mathbf{u}) + (\mathbf{\nabla} \times \mathbf{B}) \times \mathbf{B} + q\,Ra\,\Theta\,\mathbf{r} - \hat{\mathbf{z}} \times \mathbf{u}, \\ \mathbf{N}_B &= \mathbf{\nabla} \times (\mathbf{u} \times \mathbf{B}), \\ N_T &= \varepsilon - \mathbf{u} \cdot \mathbf{\nabla}\Theta. \end{aligned} \qquad \text{(A.58)}$$

Appendix B

Numerical decomposition of governing equations

Before describing the numerical solution of equations (2.1), the representation of the fields in the relevant spherical shell geometry (i.e. as a function of radius and of position on a spherical surface) is first described. Details of how to perform simple operations using the chosen representations are given. Boundary conditions which depict various physical and geometrical constrains are also derived. In section (2.1.2.1) the equations are spectrally decomposed into a scalar form. In sections (2.1.2.2) and (2.1.2.3) the numerical scheme for solving the system of the resulting ordinary differential equations is described. This includes a description of the predictor-corrector and influence matrix methods.

B.1   Representation in the radial coordinate

Following Marti and Willis (2009), a function $p(r)$ can be represented by the values $p_n = p(r_n)$, where $p(r)$ is evaluated on the N radial points r_n. The position of the grid points is chosen to be the zeros of the Chebyshev polynomials.

Differentiation

Using a Taylor series expansion about the central point x_0, with k neighbouring points each side, we have

$$
\begin{aligned}
f(x_{-k}) &= f(x_0) + (x_{-k} - x_0)\,f'(x_0) + \tfrac{(x_{-k}-x_0)^2}{2!}\,f''(x_0) + \ldots \\
&\;\;\vdots \\
f(x_k) &= f(x_0) + (x_k - x_0)\,f'(x_0) + \tfrac{(x_k-x_0)^2}{2!}\,f''(x_0) + \ldots
\end{aligned}
\tag{B.1}
$$

This can be written in vectorial form as

$$\mathbf{f} = A\, \vec{df}, \quad \mathbf{d}f = A^{-1}\, \vec{f}, \quad \mathbf{f} = \begin{bmatrix} f(x_{-k}) \\ \vdots \\ f(x_k) \end{bmatrix}, \quad \mathbf{d}f = \begin{bmatrix} f(x_0) \\ f'(x_0) \\ f''(x_0) \\ \vdots \end{bmatrix}. \tag{B.2}$$

Radial derivatives can then be calculated using weights from the appropriate row of A^{-1}.

Integration

Integrating eqn.(B.1) the indefinite integral may be approximated about x_0 by

$$
\begin{aligned}
\int f(x)\, dx &= (x - x_0) f(x_0) + \tfrac{(x-x_0)^2}{2!} f'(x_0) + \tfrac{(x-x_0)^3}{3!} f''(x_0) + \dots \\
&= \begin{bmatrix} (x - x_0) & \tfrac{(x-x_0)^2}{2!} & \dots \end{bmatrix} A^{-1} \vec{f}.
\end{aligned}
\tag{B.3}
$$

A definite integral can therefore be approximated by

$$\frac{1}{2} \sum_n \int_{x_{n-1}}^{x_{n+1}} f(x)\, dx. \tag{B.4}$$

B.2   Spherical Harmonics

Laplace's equation $\nabla^2 f = 0$ in spherical coordinates is:

$$\frac{1}{r^2} \frac{\partial}{\partial r}\left(r^2 \frac{\partial f}{\partial r}\right) + \frac{1}{r^2 \sin\theta} \frac{\partial}{\partial \theta}\left(\sin\theta \frac{\partial f}{\partial \theta}\right) + \frac{1}{r^2 \sin^2\theta} \frac{\partial^2 f}{\partial \varphi^2} = 0. \tag{B.5}$$

By substituting $f(r, \theta, \varphi) = R(r) Y(\theta, \varphi)$ we separate variables:

$$\frac{d}{dr}(r^2 R') - \lambda R = 0, \tag{B.6}$$

$$\frac{1}{\sin\theta} \cdot \frac{\partial}{\partial \theta}\left(\sin\theta \frac{\partial Y}{\partial \theta}\right) + \frac{1}{\sin^2\theta} \cdot \frac{\partial^2 Y}{\partial \varphi^2} + \lambda Y = 0, \tag{B.7}$$

where λ is the constant of separation.

Continuous solutions of eq.(B.7) in $0 \le \theta \le \pi$, $0 \le \varphi \le 2\pi$, such that $Y(\theta, \varphi + 2\pi) \equiv Y(\theta, \varphi)$ are called *spherical functions*.

Equation (B.6) has the following solution:

$$R(r) = Ar^l + Br^{-(l+1)}, \tag{B.8}$$

where $\lambda = l(l + 1)$.

By further separation $Y = \Phi(\varphi)\Psi(\theta)$ in eq.(B.7):

$$\frac{1}{\sin\theta} \cdot \frac{d}{d\theta}(\Psi' \sin\theta) + (\lambda - \frac{\mu}{\sin^2\theta})\Psi = 0, \tag{B.9}$$

$$\Phi'' + \mu\Phi = 0. \tag{B.10}$$

For periodicity $\Phi(\varphi) = \Phi(\varphi + 2\pi)$ to hold we choose $\mu = m^2$, where m is an integer. Then, the solution of eq.(B.10) is:

$$\Phi(\varphi) = A\cos m\varphi + B\sin m\varphi. \tag{B.11}$$

And eq.(B.9) by the substitution $\xi = \cos\theta$ is transformed to the *associated Legendre equation*:

$$\frac{d}{d\xi}\left((1 - \xi^2)\frac{d\Psi}{d\xi}\right) + \left(l(l + 1) - \frac{m^2}{1 - \xi^2}\right)\Psi = 0, \tag{B.12}$$

substitutions $\mu = m^2$ and $\lambda = l(l + 1)$ were made here.

The solutions of this equation are *associated Legendre functions*:

$$\mathscr{P}_l^m = (1 - \xi^2)^{m/2}\frac{d^m}{d\xi^m}P_l(\xi), \tag{B.13}$$

where $P_l(\xi)$ are Legendre polynomials which are solutions of *Legendre equation*[1](it is obtained from eq.(B.12) when $m = 0$). Finite polynomial solutions of Legendre's equation are obtained only if l is an integer ≥ 0. Here m must be also integer, $0 \leq m \leq l$ (for more details see Riley et al., 2002; Arsenin, 1984). The integer m is called the *spherical harmonic order*, and l is the *spherical harmonic degree*.

The *spherical harmonic* (or fundamental spherical function) $Y_\alpha(\theta, \varphi)$ is defined using the associated Legendre polynomials $\mathscr{P}_l^m(\cos\theta)$ and including a cosine or sine dependence on the azimuthal wave-number m_α:

$$Y_\alpha = \mathscr{P}_{l_\alpha}^{m_\alpha}(\cos\theta)\left\{{\cos\atop\sin}\right\}_\alpha m_\alpha\varphi. \tag{B.14}$$

For convenience, a single Greek subscript will be used to denote spherical harmonics, $\alpha \equiv \{l_\alpha, m_\alpha, \{{\cos\atop\sin}\}_\alpha\}$.

Here spherical harmonics are defined as solutions of homogeneous differential equations, so they are defined within a constant factor and can be determined by normalisation. Schmidt quasi-normalisation is used in this study. Together with the property of orthogonality:

$$\int_0^{2\pi}\int_0^\pi Y_\alpha Y_{\alpha_1}\sin\theta\,d\theta d\varphi = \left\{\begin{array}{cc}\dfrac{4\pi}{2l_\alpha + 1} & \alpha = \alpha_1 \\ 0 & \alpha \neq \alpha_1\end{array}\right\}, \tag{B.15}$$

---

[1]Solutions of the Legendre equation are usually presented by the Rodrigues' formula $P_l(\xi) = \frac{1}{2^l l!} \cdot \frac{d^l}{d\xi^l}[(\xi^2 - 1)^l]$.

and the associated Legendre functions, $\mathscr{P}_l^m(\xi)$, satisfy:

$$\int_{-1}^1 [\mathscr{P}_l^m(\xi)]^2 \, d\xi = \frac{2(2-\delta_{m0})}{2l+1}. \tag{B.16}$$

It is useful to notice:

$$\boldsymbol{\nabla}^2 Y_\alpha = -\frac{l_\alpha(l_\alpha+1)}{r^2} Y_\alpha. \tag{B.17}$$

This is easy to check using the definition of Laplace's operator in spherical coordinates from eq.(B.5) and equation (B.9) for $\mathscr{P}_l^m(\cos\theta)$.

In addition, the spherical harmonics form a complete set in that any reasonable function (i.e. one that is likely to be met in a physical situation) of spherical coordinates r, θ, φ can be expanded as a sum of such functions,

$$f(r,\theta,\varphi) = \sum_{l=0}^\infty \sum_{m=0}^l a_{lm}(r) \mathscr{P}_{l_\alpha}^{m_\alpha}(\cos\theta) \left\{{\cos \atop \sin}\right\}_\alpha m_\alpha \varphi = \sum_\alpha a_\alpha(r) Y_\alpha(\theta,\varphi). \tag{B.18}$$

The coefficients $a_\alpha(r)$ are calculated using (B.15) :

$$a_\alpha(r) = \frac{2l_\alpha+1}{4\pi} \int_{-1}^1 \int_0^{2\pi} Y_\alpha(\theta,\varphi) f(\theta,\varphi) d(\cos\theta). \tag{B.19}$$

B.3 Vector spherical harmonics and the toroidal poloidal decomposition

In this section the magnetic field **B** is used as an example of how a solenoidal field can be represented by poloidal-toroidal decomposition.

Since the magnetic field is solenoidal (eq.A.29b),

$$\boldsymbol{\nabla} \cdot \mathbf{B} = 0,$$

we can express **B** as a sum of toroidal and poloidal vector components,

$$\mathbf{B} = \mathbf{T} + \mathbf{P}, \tag{B.20a}$$

$$\mathbf{T} = \boldsymbol{\nabla} \times (T(r,\theta,\varphi)\,\mathbf{r}), \tag{B.20b}$$

$$\mathbf{P} = \boldsymbol{\nabla} \times \boldsymbol{\nabla} \times (P(r,\theta,\varphi)\,\mathbf{r}). \tag{B.20c}$$

It is useful to note here that $\mathbf{T} \perp \mathbf{r}$, because $\boldsymbol{\nabla} \times \mathbf{r} = 0$. Using the vector identity for the curl of a vector multiplied by a scalar field, $\mathbf{T} = \boldsymbol{\nabla} \times (T\,\mathbf{r}) = \boldsymbol{\nabla}T \times \mathbf{r} + T\,\boldsymbol{\nabla} \times \mathbf{r} = \boldsymbol{\nabla}T \times \mathbf{r}$, which is obviously perpendicular to **r**.

Both the toroidal and poloidal scalars, T and S, can then be expanded as an infinite series of spherical harmonic terms,

$$T(r, \theta, \varphi) = \sum_{l=1}^{\infty} \sum_{m=0}^{l} \tau_l^m(r) \mathscr{P}_l^m(\cos\theta) \, \cos(m\varphi) + \tau_l^m(r) \mathscr{P}_l^m(\cos\theta) \, \sin(m\varphi), \quad \text{(B.21)}$$

$$P(r, \theta, \varphi) = \sum_{l=1}^{\infty} \sum_{m=0}^{l} p_l^m(r) \mathscr{P}_l^m(\cos\theta) \, \cos(m\varphi) + p_l^m(r) \mathscr{P}_l^m(\cos\theta) \, \sin(m\varphi). \quad \text{(B.22)}$$

In single Greek subscript notation this can be expressed in the more compact manner:

$$T = \sum_{\alpha} \tau_\alpha(r) Y_\alpha(\theta, \varphi), \quad \text{(B.23a)}$$

$$P = \sum_{\alpha} p_\alpha(r) Y_\alpha(\theta, \varphi). \quad \text{(B.23b)}$$

Vector spherical harmonics are obtained by the substitution of equations (B.23a, B.23b) into (B.20b, B.20c).

$$\mathbf{T}_\alpha = \boldsymbol{\nabla} \times (\tau_\alpha(r) Y_\alpha(\theta, \varphi) \, \mathbf{r}), \quad \text{(B.24)}$$

$$\mathbf{P}_\alpha = \boldsymbol{\nabla} \times \boldsymbol{\nabla} \times (p_\alpha(r) Y_\alpha(\theta, \varphi) \, \mathbf{r}). \quad \text{(B.25)}$$

And the vector components are given (see Bullard and Gellman, 1954; Gibbons, 2001) by:

$$
\begin{aligned}
[\mathbf{T}_\alpha]_r &= 0, & [\mathbf{P}_\alpha]_r &= l_\alpha(l_\alpha + 1)\frac{p_\alpha(r)}{r} Y_\alpha, \\
[\mathbf{T}_\alpha]_\theta &= \frac{\tau_\alpha(r)}{\sin\theta}\frac{\partial Y_\alpha}{\partial\varphi}, & [\mathbf{P}_\alpha]_\theta &= \left(\frac{p_\alpha(r)}{r} + \frac{\mathrm{d}p_\alpha(r)}{\mathrm{d}r}\right)\frac{\partial Y_\alpha}{\partial\theta}, \\
[\mathbf{T}_\alpha]_\varphi &= -\tau_\alpha(r)\frac{\partial Y_\alpha}{\partial\theta}, & [\mathbf{P}_\alpha]_\varphi &= \frac{1}{\sin\theta}\left(\frac{p_\alpha(r)}{r} + \frac{\mathrm{d}p_\alpha(r)}{\mathrm{d}r}\right)\frac{\partial Y_\alpha}{\partial\varphi}.
\end{aligned}
\quad \text{(B.26)}
$$

A general vector (not necessarily solenoidal) can be represented in a decomposition of scaloidal, spheroidal and toroidal vector harmonics (Backus, 1986):

$$\mathbf{G} = \sum_{\alpha} \left(q_\alpha \mathbf{q}_\alpha + s_\alpha \mathbf{s}_\alpha + t_\alpha \mathbf{t}_\alpha\right), \quad \text{(B.27)}$$

with

$$
\begin{aligned}
\mathbf{q}_\alpha &= Y_\alpha \frac{\mathbf{r}}{r} & &= & [Y_\alpha, 0, 0], \\
\mathbf{s}_\alpha &= \frac{1}{\sqrt{l_\alpha(l_\alpha+1)}}\boldsymbol{\nabla}_h(rY_\alpha) & &= & \frac{1}{\sqrt{l_\alpha(l_\alpha+1)}}\left[0, \frac{\mathrm{d}Y_\alpha}{\mathrm{d}\theta}, \frac{1}{\sin\theta}\frac{\partial Y_\alpha}{\partial\varphi}\right], \\
\mathbf{t}_\alpha &= \frac{1}{\sqrt{l_\alpha(l_\alpha+1)}}\mathbf{r}\times\boldsymbol{\nabla}_h(Y_\alpha) & &= & \frac{1}{\sqrt{l_\alpha(l_\alpha+1)}}\left[0, -\frac{1}{\sin\theta}\frac{\partial Y_\alpha}{\partial\varphi}, \frac{\partial Y_\alpha}{\partial\theta}\right].
\end{aligned}
\quad \text{(B.28)}
$$

This representation will be referred to here as a '*qst-decomposition*' and is used in the numerical scheme presented below for calculating the Coriolis term and non-linear terms in the momentum and induction equations. Even though **u** and **B** are solenoidal, their cross products are generally not, although because finally $\mathbf{\nabla}\times$ is applied, the end result can be treated as a PT-decomposed vector.

If **G** is a general solenoidal vector, conditions on the radial functions $q_\alpha(r)$, $s_\alpha(r)$, $t_\alpha(r)$ can be obtained to make the expansions in eq.(B.20b) and eq.(B.27) equivalent. A direct comparison of equations (B.26) and (B.28) reveals

$$
\begin{aligned}
\mathbf{q}_\alpha &= l_\alpha(l_\alpha + 1)\frac{p_\alpha(r)}{r}, \\
\mathbf{s}_\alpha &= \sqrt{l_\alpha(l_\alpha + 1)}\frac{1}{r}\frac{\mathrm{d}}{\mathrm{d}r}(rp_\alpha(r)), \\
\mathbf{t}_\alpha &= -\sqrt{l_\alpha(l_\alpha + 1)}\tau_\alpha(r),
\end{aligned}
\tag{B.29}
$$

when $\mathbf{\nabla} \cdot \mathbf{G} = 0$.

B.4   Matrix representation of linear operators

Linear equations may be written in the matrix form

$$
L\,\vec{p} = M\,\mathbf{q} + \mathbf{s}.
\tag{B.30}
$$

L and M are $N \times N$ matrices representing linear operators. If **q** and **s** are known then the right-hand side is simple to evaluate. Consider the equation

$$
L\,\mathbf{p} = \mathbf{q},
\tag{B.31}
$$

where **p** is unknown. If the matrix operators are formed by linear combinations of the weights in eq. (B.2), using only k neighbouring points to each side, they are banded. Boundary conditions are formed in the same way and are placed in the end rows. The equation then can be solved by forward-backward substitution, using the banded LU-factorisation of L (see Press, 2007).

Appendix C

Non-dimensionalisations

C.1 Christensen et al. (2001)

In this section we present formulas to convert values between non-dimensionalisations used in Christensen et al. (2001) and the non-dimensionalisation used in our code (defined in sec.2.1). Table (C.1) presents definitions of these non-dimensionalisations, and table (C.2) has formulas for the conversion between them. Parameters of the Case 1 and Case 2 from Christensen et al. (2001) are converted in tables (C.3) and (C.4) correspondingly. For the conversion we need to know the geometry of the shell $c = r_i/r_o = 0.35$. Table (C.5) converts diagnostics between non-dimensionalisations.

Christensen et al. (2001):		used in thesis:	
Ekman number	$E = \nu/(\Omega d^2)$,	Ekman number	$E = \nu/(2\Omega d^2)$,
Rayleigh number	$Ra = \dfrac{\alpha\, g\, \Delta T\, d}{\nu\Omega}$,	Mod. Rayleigh number	$Ra = \dfrac{g\, \alpha\, \Delta T\, d}{2\Omega\kappa}$
Prandtl number	$P = \nu/\kappa$,	Roberts number	$q = \kappa/\eta$,
Magnetic Prandtl number	$P_m = \nu/\eta$,	Magnetic Rossby number	$Ro = \eta/(2\Omega d^2)$.
Length	$r \to (d = r_o - r_i)\, r$,	Length	$r \to (d = r_o - r_i)\, r$,
Time	$t \to d^2/\eta\, t$,	Time	$t \to d^2/\nu\, t$,
Magnetic	$B \to (2\Omega\rho_0\mu_0\eta)^{\frac{1}{2}}\, B$,	Magnetic	$B \to (\Omega\rho_0\mu_0\eta)^{\frac{1}{2}}\, B$,
Co-density	$\Theta \to \Delta T\, \Theta$,	Co-density	$\Theta \to \Delta T\, \Theta$.

Table C.1: *Definitions of the Christensen et al. (2001) and our non-dimensionalisations.*

E	Ra	q	Ro
$\dfrac{1}{2} \cdot E^C$	$\dfrac{1}{2} \cdot \dfrac{Ra^C}{r_o/d} \cdot P$	$\dfrac{P_m}{P}$	$\dfrac{1}{2} \cdot \dfrac{E^C}{P_m}$

Table C.2: *Conversion of Christensen et al. (2001) non-dimensional parameters (denoted by ^{C}) to the non-dimensionalisation used in our code.*

Christensen et al. (2001)	E^C	Ra^C	P_m	Pr
	10^{-3}	100	5	1
Thesis	E	Ra	q	Ro
	$0.5 \cdot 10^{-3}$	32.50	5	10^{-4}

Table C.3: *Conversion of the parameters of* **Case 1** *in Christensen et al. (2001) to the non-dimensionalisation used in this thesis.*

Christensen et al. (2001)	E^C	Ra^C	P_m	Pr
	10^{-3}	110	5	1
Thesis	E	Ra	q	Ro
	$0.5 \cdot 10^{-3}$	35.75	5	10^{-4}

Table C.4: *Conversion of the parameters of* **Case 2** *in Christensen et al. (2001) to the non-dimensionalisation used in this thesis.*

	Thesis		Christensen et al. (2001)		
	Formula	Value	Formula	Convert.	Value
E_{kin}	$\frac{1}{2}\int_{V_s} \mathbf{u}^2 dV$	$1.1230827 \cdot 10^4$	$\frac{1}{2V_s}\int_{V_s} \mathbf{u}^2 dV$	$\cdot(Pr_m^2 \cdot V_s)^{-1}$	30.7719154
E_{mag}	$\frac{1}{2Ro}\int_{V_s} \mathbf{B}^2 dV$	$2.2859984 \cdot 10^5$	$\frac{1}{2V_s EPm}\int_{V_s} \mathbf{B}^2 dV$	$\cdot(Pr_m^2 \cdot V_s)^{-1}$	626.352354

Table C.5: *An example of conversion of diagnostics. Values are calculated with our code and converted in Christensen et al. (2001) non-dimensionalisation. The volume of the shell $V_s = 4/3\pi(r_o^3 - r_i^3) = 14.59880136$, where $r_i = 7/13$, $ro = 20/13$.*

C.2   Harder and Hansen (2005)

For the pseudo-vacuum benchmark exercise in the chapter (3) we have used dynamos described in Harder and Hansen (2005). The MHD equations in this paper have the form:

$$
\begin{cases}
\left(\dfrac{\partial}{\partial t} - Pr\boldsymbol{\nabla}^2\right)\mathbf{u} &= \boldsymbol{\nabla} \cdot \left(\dfrac{Pr}{q}\mathbf{BB} - \mathbf{uu}\right) + Pr\,Ra^{HH}\,T\,(\mathbf{r}/r_o) - \dfrac{Pr}{E}\hat{\mathbf{z}} \times \mathbf{u} - \boldsymbol{\nabla}\hat{P}, \\[2ex]
\left(\dfrac{\partial}{\partial t} - \dfrac{1}{q}\boldsymbol{\nabla}^2\right)\mathbf{B} &= \boldsymbol{\nabla} \times (\mathbf{u} \times \mathbf{B}), \\[2ex]
\left(\dfrac{\partial}{\partial t} - \boldsymbol{\nabla}^2\right)T &= -\mathbf{u} \cdot \boldsymbol{\nabla}T.
\end{cases}
\tag{C.1}
$$

We denote variables in non-dimensionalisation defined in Harder and Hansen (2005) by ^{HH}. The tensor product is defined as:

$$
\mathbf{uu} = \frac{\mathrm{d}}{\mathrm{d}x_j}(u_i u_j) = \mathbf{u}(\boldsymbol{\nabla} \cdot \mathbf{u}) + (\mathbf{u}\boldsymbol{\nabla})\mathbf{u}.
\tag{C.2}
$$

Units are defined as:

$$
\text{Length } r \to (d = r_o - r_i)\, r, \quad \text{Time } t \to \frac{d^2}{\kappa}\, t, \quad \text{Magnetic } B \to \frac{\sqrt{\rho_0 \mu_0 \nu \eta}}{d}\, B, \quad \text{Co-density } T \to \Delta T\, T. \tag{C.3}
$$

The control parameters are defined below:

$$
\begin{aligned}
\text{Rayleigh number} \quad Ra^{HH} &= \frac{g_0 \, \alpha \, \Delta T \, d^3}{\kappa \nu}, \\
\text{Ekman number} \quad E &= \nu/(2\Omega d^2), \\
\text{Prandtl number} \quad Pr &= \nu/\kappa, \\
\text{Roberts number} \quad q &= \kappa/\eta.
\end{aligned}
\tag{C.4}
$$

Now we can derive formulas for the conversion between non-dimensionalisations in Harder and Hansen (2005) and the one adopted in this thesis (see eq.2.1). The dimensional fields should be the same irrespective to the non-dimensionalisation of original values, thus:

$$
\sqrt{2\Omega\rho_0\mu_0\eta} \, B = \frac{\sqrt{\rho_0\mu_0\nu\eta}}{d} \, B^{HH},
\tag{C.5}
$$

$$
B = \sqrt{\frac{\nu}{2\Omega d^2}} \, B^{HH} = \sqrt{E} \, B^{HH}.
\tag{C.6}
$$

Magnetic energy in Ashley's non-dimensionalisation E_{mag} is:

$$
E_{mag} = \frac{1}{2\,Ro} \int B^2 \, dV.
\tag{C.7}
$$

Then, it is convenient to express magnetic field in Willis et al. (2007) units in terms of magnetic energy:

$$
B^A_{rms} = \sqrt{\frac{2\,Ro\,E_M}{V}} = \sqrt{\frac{2\,E\,(Pr\,q)^{-1}\,E_{mag}}{4/3\pi(r_o^3 - r_i^3)}}.
\tag{C.8}
$$

Further, magnetic field B^{HH} in Harder and Hansen (2005) units in terms of magnetic energy E_{mag} in Willis et al. (2007) units (comes out of the simulation) is:

$$
B^{HH}_{rms} = \sqrt{\frac{3\,E_{mag}}{2\pi(r_o^3 - r_i^3)\,Pr\,q}}.
\tag{C.9}
$$

C.3 Jones et al. (2003)

In this section we convert control parameters from Jones et al. (2003) to the non-dimensionalisation adopted in this thesis (see eq.2.1). The MHD equations in the form of Jones et al. (2003) are:

$$
\left\{
\begin{aligned}
E\left(\frac{\partial}{\partial t} - \nabla^2\right)\mathbf{u} + \hat{\mathbf{z}} \times \mathbf{u} &= -\nabla p + ER\Theta\mathbf{r} + \Lambda[(\mathbf{B} \cdot \nabla)\mathbf{b} + (\mathbf{b} \cdot \nabla)\mathbf{B}], \\
\left(P_m\frac{\partial}{\partial t} - \nabla^2\right)\mathbf{b} &= \nabla \times (\mathbf{u} \times \mathbf{B}), \\
\left(Pr\frac{\partial}{\partial t} - \nabla^2\right)\Theta &= \mathbf{r} \cdot \mathbf{u}.
\end{aligned}
\right.
\tag{C.10}
$$

They were non-dimensionalized as follows:

$$\text{Length } r \rightarrow r_o \, r, \qquad \text{Time } t \rightarrow \frac{r_0^2}{\nu} \, t,$$
$$\text{Mag}_1 \, b \rightarrow \frac{B_0 \nu}{\eta} \, b, \quad \text{Mag}_2 \, B \rightarrow B_0 \, B, \quad \text{Temperature } \Theta \rightarrow \frac{\beta r_0^2 \nu}{\kappa} \, \Theta. \tag{C.11}$$

The dimensionless parameters in the equations are:

$$
\begin{aligned}
\text{Elsasser number} \quad \Lambda &= \frac{B_0^2}{2\Omega\mu\rho_0\eta}, \\
\text{Prandtl number} \quad Pr &= \frac{\nu}{\kappa}, \\
\text{Magnetic Prandtl number} \quad P_m &= \frac{\nu}{\eta}, \\
\text{Ekman number} \quad E &= \frac{\nu}{2\Omega r_0^2}, \\
\text{Modified Rayleigh number} \quad R &= \frac{\gamma\alpha\beta \, r_0^6}{\kappa\nu}.
\end{aligned}
\tag{C.12}
$$

It is easy to check that equations (C.10) can be converted to dimensional, if we multiply 1st eq. by $2\Omega \, \nu/r_0$, the 2nd by $\eta/(r_0^2/B_0)$ and the last by $\nu\beta$. This brings us to the following form of dimensional equations:

$$
\begin{cases}
\left(\dfrac{\partial}{\partial t} - \nu \, \boldsymbol{\nabla}^2\right)\mathbf{u} + 2\Omega \, \hat{\mathbf{z}} \times \mathbf{u} = \begin{aligned}&-2\Omega \, \dfrac{\nu}{r_0} \, \boldsymbol{\nabla}p + \gamma\alpha \, \Theta\mathbf{r} \\ &+ \dfrac{1}{\mu\rho_0} \, [(\mathbf{B} \cdot \boldsymbol{\nabla})\mathbf{b} + (\mathbf{b} \cdot \boldsymbol{\nabla})\mathbf{B}]\end{aligned}, \\
\left(\dfrac{\partial}{\partial t} - \eta\boldsymbol{\nabla}^2\right)\mathbf{b} = \boldsymbol{\nabla} \times (\mathbf{u} \times \mathbf{B}), \\
\left(\dfrac{\partial}{\partial t} - \kappa\boldsymbol{\nabla}^2\right)\Theta = \beta\mathbf{r} \cdot \mathbf{u}.
\end{cases}
\tag{C.13}
$$

Bringing both Jones et al. (2003) and our (eq.2.1) MHD equations in the same form and comparing coefficients before dimensionalised $\boldsymbol{\nabla}^2\mathbf{u}$, we get conversion between Ekman numbers in our and Jones et al. (2003) non-dimensionalisations:

$$Ed^2\frac{d}{\eta} \cdot \frac{2\Omega\eta}{d} = E^J \, r_o^2 \frac{r_o}{\nu} \, 2\Omega\frac{\nu}{r_o}, \tag{C.14}$$

$$E = E^J\frac{r_o^2}{d^2}. \tag{C.15}$$

Here superscripts ^{J} denote variables in the non-dimensionalisation of Jones et al. (2003). In the same way equating coefficients in front of the term $\Theta\mathbf{r}$, we get the Rayleigh number:

$$E^J R^J \frac{\kappa}{\beta r_0^2 \nu} \frac{1}{r_0} 2\Omega \frac{\nu}{r_0} = q\, Ra \frac{1}{\Delta T} \frac{1}{d} 2\Omega \frac{\eta}{d}, \tag{C.16}$$

$$Ra = \frac{\Delta T}{\beta} \frac{d^2}{r_0^4} E^J \cdot R^J. \tag{C.17}$$

then,

$$Ra = \frac{\Delta T}{\beta} \frac{d^2}{r_0^4} \cdot E^J \cdot R^J = \frac{\beta d^2}{\beta} \frac{d^2}{r_0^4} \cdot E^J \cdot R^J = \frac{d^4}{r_0^4} \cdot E^J \cdot R^J. \tag{C.18}$$

The Elsasser number Λ is needed for the imposed field, and corresponds to the root-mean-square value of the magnetic field in our non-dimensionalisation. The Roberts number is $q = Pr_m/Pr$, and the modified Rossby number is $Ro = E/Pr_m$.

C.4 Aubert et al. (2009), scalings

Scaling laws obtained by Aubert et al. (2009) are converted to our non-dimensionalization in this section. Definitions of parameters for scaling laws eq.(5.5-5.7) are:

$Ro^{Aub} = u_{rms}^{Aub}$	is the dimensionless rms velocity,
$Lo = B_{rms}^{Aub}$	is the dimensionless magnetic field,
$R_m = u_{rms}$	is the magnetic Reynolds number and it equals the rms velocity in our non-dimensionalization,
$\tau_{diss}/\tau_{mag} = E_{mag}/D_{mag}$	τ_{mag} is the magnetic dissipation time d^2/η which is unit in our non-dimensionalization,
E_{mag}	is the total magnetic energy in the shell (our non-dimensionalization),
D_{mag}	is the ohmic dissipation of magnetic energy (our non-dimensionalization),
$p = 8Ro^2\, qRa \frac{1}{V} \int_V u_r T r\,\mathrm{dV}$	is the buoyancy power defined in Aubert et al. (2009)'s non-dimensionalization via values in our units (see eq.C.40 and eq.C.41),
f_{Ohm}	is the fraction of the Ohmic dissipation (C.42).

Aubert et al. (2009) have used following units for non-dimensionalization of MHD equations:

$$\text{Length } r \to (d = r_o - r_i)\, r, \quad \text{Time } t \to \Omega^{-1}\, t, \quad \text{Magnetic } B \to (\rho_0\mu_0)^{\frac{1}{2}}\Omega d\, B, \tag{C.19}$$
$$\text{Co-density } C \to F/(4\pi d^3 \Omega)\, \Theta.$$

Co-density is constructed in the following way:

$$C = \alpha \rho \Theta + \Delta \rho \xi'. \tag{C.20}$$

The first term in the right hand side of the equation eq.(C.20) is thermal buoyancy, second term is chemical buoyancy. C is measured in $[kg/m^3]$ in SI. Θ is temperature deviation field. $\Delta \rho$ is density difference between light and heavy components, which contributes to chemical convection.

   The use of two-terms in the co-density (C.20) is irrelevant for the numerical solution since it doesn't influence the equations solved numerically. The only reason to have the chemical term in the definition of co-density is to show that all possible mechanisms can be modelled by Boussinesq MHD equations.

Dimensionless parameters used by Aubert et al. (2009):

$$
\begin{aligned}
\text{mass anomaly based Rayleigh number} \quad & Ra_Q = \frac{g_0 F}{4\pi \rho_0 \Omega^3 d^4}, \\
\text{Ekman number} \quad & E^{Aub} = \nu/(\Omega d^2), \\
\text{magnetic Prandtl number} \quad & P_m = \frac{\nu}{\lambda}, \\
\text{Prandtl number} \quad & Pr = \frac{\nu}{\kappa}.
\end{aligned}
\tag{C.21}
$$

$F = F_i + F_o$ is the measure of the mass flux $[kg/s]$,

$F_i = \displaystyle\int_{S_i} \kappa \left.\frac{dC}{dr}\right|_{r_i} dS$ is the positive mass flux on the inner boundary,

$F_o = \displaystyle\int_{S_o} \kappa \left.\frac{dC}{dr}\right|_{r_o} dS$ is the mass flux going out of the outer boundary.

Due to the definition of codensity eq.(C.20) the mass flux and the heat flux are integrated into one value which can be called equally correct heat flux or mass flux. Let's denote by H the measure of heat flux in our non-dimensionalization (defined by Willis et al., 2007).

$$H_i = -q \int_{S_i} \left.\frac{dT}{dr}\right|_{r_i} dS, \tag{C.22}$$

$$H_o = -qS_o \left.\frac{dT}{dr}\right|_{r_o}. \tag{C.23}$$

H_i is positive if heat goes inside the shell, H_o is positive if heat goes outside of the outer boundary of the shell. Heat flux is controlled so that it is always the same everywhere on the outer boundary, and integration sign is omitted in eq.(C.23).

Let's integrate the heat flux equation in the Willis et al. (2007)'s non-dimensionalization over the volume of the shell. As a result we will get the energy balance in the system:

$$H_i - H_o + VS_{int} = 0 \tag{C.24}$$

with the internal heat S_{int}.

We are interested in the non-dimensional value measuring heat flux:

$$H = H_i + H_o = 2H_o - S_{int}V = q(-2 \cdot 4\pi r_o^2 \left.\frac{\partial T}{\partial r}\right|_{r_o} - 3\frac{4}{3}\pi(r_o^3 - r_i^3)) = \tag{C.25}$$

$$-4\pi q(2r_o^2 \left.\frac{\partial T}{\partial r}\right|_{r_o} + (r_o^3 - r_i^3)) = \frac{\pi q}{2}\frac{d}{r_o}h. \tag{C.26}$$

We use relation $S_{int} = 3q$ and eq.(C.24).

Non-dimensional parameter h is:

$$h = -8\pi\frac{r_o}{d}\left(2r_o^2 \left.\frac{\partial T}{\partial r}\right|_{r_o} + (r_o^3 - r_i^3)\right) = 8\pi\frac{c^3 + 3}{(1 - c)^4} = 428.435. \tag{C.27}$$

We use fixed temperature gradient on the outer boundary of the shell

$$\left.\frac{\partial T}{\partial r}\right|_{r_o} = -\frac{2}{1 - c} = -3.077. \tag{C.28}$$

and shell's geometry $c = r_i/r_o = 0.35$, $r_o - r_i = 1$.

The dimensional mass flux F is proportional to H with the coefficient $\eta\Delta T d\alpha\rho$:

$$F = F_i + F_o = \eta H\Delta T d\alpha\rho. \tag{C.29}$$

Now we can find relation between Ra_Q and Ra in our (following Willis et al. (2007)) non-dimensionalization. Navier-Stokes equations in our (eq.C.31) and Aubert et al. (2009) (eq.C.30) forms are:

$$\frac{\partial \mathbf{u}}{\partial t} = Ra_Q\frac{\mathbf{r}}{r_o}C + \dots \tag{C.30}$$

$$Ro\frac{\partial \mathbf{u}}{\partial t} = qRaT\mathbf{r} + \dots \tag{C.31}$$

Equating buoyancy terms in the dimensional form:

$$2\Omega\frac{\eta}{d} qRa\frac{T}{\Delta T}\frac{\mathbf{r}}{d} = \Omega^2 d Ra_Q\frac{\mathbf{r}}{r_o}\alpha\rho T\left(\frac{4\pi d^3\Omega}{F}\right). \tag{C.32}$$

Here we have equated right hand sides of dimensionalized equations eq.(C.31) and eq.(C.30)

with left hand sides being $\dfrac{\partial \mathbf{u}}{\partial t}$. Then simplifying and using eq.(C.29) and eq.(C.26),

$$Ra_Q = \frac{1}{2\pi}\frac{\eta q r_o}{\Delta T \alpha \rho d^6 \Omega^2} F Ra = \frac{1}{2\pi}\frac{\eta q r_o}{\Delta T \alpha \rho d^6 \Omega^2}\eta H \Delta T d\alpha\rho Ra = \tag{C.33}$$

$$= \frac{1}{2\pi}\frac{\eta^2 q H r_o}{d^5 \Omega^2} Ra = \frac{2H}{\pi q}\frac{r_o}{d}(Roq)^2 Ra = h(Roq)^2 Ra. \tag{C.34}$$

Finally, the relation between our Rayleigh number and Rayleigh number of Aubert et al. (2009) is:

$$Ra_Q = h(Ro \cdot q)^2 Ra \tag{C.35}$$

with $h = 428.435$.

Now we calculate the power parameter p. For this $f_i = F_i/F = H_i/H$ is needed:

$$f_i = \frac{r_o^2 \left.\dfrac{\partial T}{\partial r}\right|_{r_o} + (r_o^3 - r_i^3)}{2r_o^2 \left.\dfrac{\partial T}{\partial r}\right|_{r_o} + (r_o^3 - r_i^3)} = 1 - \frac{2}{3 + c^3} = 0.343. \tag{C.36}$$

The formula eq.(C.36) was simplified with the use of temperature gradient from the eq.(C.28). The parameter γ defined in Aubert et al. (2009) is:

$$\gamma = \frac{3(r_o - r_i)^2}{2(r_o^3 - r_i^3)r_o}\left[f_i\left(\frac{3}{5}\frac{r_o^5 - r_i^5}{r_o^3 - r_i^3} - r_i^2\right) + (1 - f_i)\left(r_o^2 - \frac{3}{5}\frac{r_o^5 - r_i^5}{r_o^3 - r_i^3}\right)\right] = 0.278. \tag{C.37}$$

Non-dimensional (in Aubert et al., 2009 units) theoretical convective power (integral of the buoyancy term times u_r) per unit volume is p:

$$p = \gamma Ra_Q = 118.904(Roq)^2 Ra. \tag{C.38}$$

The unit of the convective power per unit volume is $\rho_0 d^2 \Omega^3$ in Aubert's non-dimensionalization and $\rho_0 \eta^3/d^4$ in Willis et al. (2007)'s (since power has the dimension of $\rho_0 u\dfrac{\partial u}{\partial t}$). Hence,

$$p\rho_0 d^2 \Omega^3 = p^{our}\rho_0 \eta^3/d^4, \tag{C.39}$$

$$p^{our} = \frac{1}{8}(\eta/(2\Omega d^2))^{-3}p = \frac{p}{8Ro^3}. \tag{C.40}$$

Here we need to mention that buoyancy power per unit volume in our non-dimensionalization is

$$p^{our} = \frac{qRa}{Ro}\frac{1}{V}\int_V u_r T r \mathrm{d}V. \tag{C.41}$$

This formula is a modification of eq.(C.31). Leaving on the left-hand side $\mathbf{u}\dfrac{\partial \mathbf{u}}{\partial t}$ we get the power from the buoyancy term.

Dissipation fraction

$$f_{ohm} = D_{mag}/(Vp^{our})$$ (C.42)

should be independent of a non-dimensionalization.

$$V = \frac{4}{3}\pi(r_o^3 - r_i^3)$$ (C.43)

is the volume of the shell, D_{mag} is the integrated magnetic dissipation in Willis et al. (2007)'s units.

Conversion of the magnetic field:

$$B^{Aub}(\rho\mu)^{1/2}\Omega d = B^{our}(\rho\mu)^{1/2}(2\Omega\eta)^{1/2},$$ (C.44)

$$B^{Aub} = B^{our}\left(\frac{2\eta}{\Omega d^2}\right)^{1/2} = 2B^{our}Ro^{1/2}.$$ (C.45)

Conversion of the velocity:

$$u^{Aub}\Omega d = u^{our}\frac{\eta}{d},$$ (C.46)

$$u^{Aub} = 2u^{our}Ro,$$ (C.47)

$$u_{rms}^{Aub} = 2\frac{\sqrt{2E_{kin}}}{V}Ro.$$ (C.48)

Appendix D

Alternative forms of selected initial magnetic fields

It may be convenient to write down magnetic fields used for initial conditions in numerical experiments discussed in this thesis in both spectral and physical coordinates.

In Christensen et al. (2001) the initial field of Case 1 is written in physical coordinates. Although it has a simple formulation in terms of poloidal and toroidal scalars (non-dimensionalisation as in eq.2.3 and definition of spherical harmonic decomposition as in sec.B.3):

$$
\begin{cases}
T_2^0 = \dfrac{1}{\sqrt{2}} \dfrac{10}{3} \sin \pi (r - r_i), \\[2ex]
P_1^0 = \dfrac{1}{\sqrt{2}} \dfrac{5}{16} r \, (8 r_o - 6r - 2 \dfrac{r_i^4}{r^3}).
\end{cases}
\tag{D.1}
$$

[1] Equation (3.37) defines the initial magnetic field which leads to decaying solution described in sec.3.4.2. In physical space this equation can be written in the form:

$$
\begin{aligned}
B_r &= \frac{4}{7\sqrt{2}} \frac{2}{r} \left(\sin \left(2\pi \left(\frac{r - r_i}{r_o - r_i} - 0.25 \right) \right) + 1 \right) \cos \theta, \\
B_\theta &= -\frac{4}{7\sqrt{2}} \frac{\sin \theta}{r} \left(\sin \left(2\pi \left(\frac{r - r_i}{r_o - r_i} - 0.25 \right) \right) + \frac{2\pi r}{r_o - r_i} \cos \left(2\pi \left(\frac{r - r_i}{r_o - r_i} - 0.25 \right) \right) + 1 \right), \quad \text{(D.3)} \\
B_\phi &= \frac{1}{\sqrt{2}} 5 \sin \left(\pi (r - r_i) \right) \sin 2\theta.
\end{aligned}
$$

---

[1]First few Legendre polynomials are:

$$
\begin{aligned}
P_0(x) &= 1, \\
P_1(x) &= x, \\
P_2(x) &= \frac{1}{2}(3x^2 - 1).
\end{aligned}
\tag{D.2}
$$

They are needed to convert initial fields from physical space to real and vice versa.

Appendix E

Rapidly rotating dynamos: snapshots

Snapshots of the dynamos, which are described in chapter (5), are collected below.

E.1 The surface of the shell, snapshots

E.1.1 Case 0

(a) $t_1 = 1.4269$

(b) $t_2 = 1.43485$

(c) $t_3 = 1.44557$

(d) $t_4 = 1.45344$

(e) $t_4 = 1.45344$

(f) $t_4 = 1.45344$

(g) $t_4 = 1.45344$

(h) $t_4 = 1.45344$
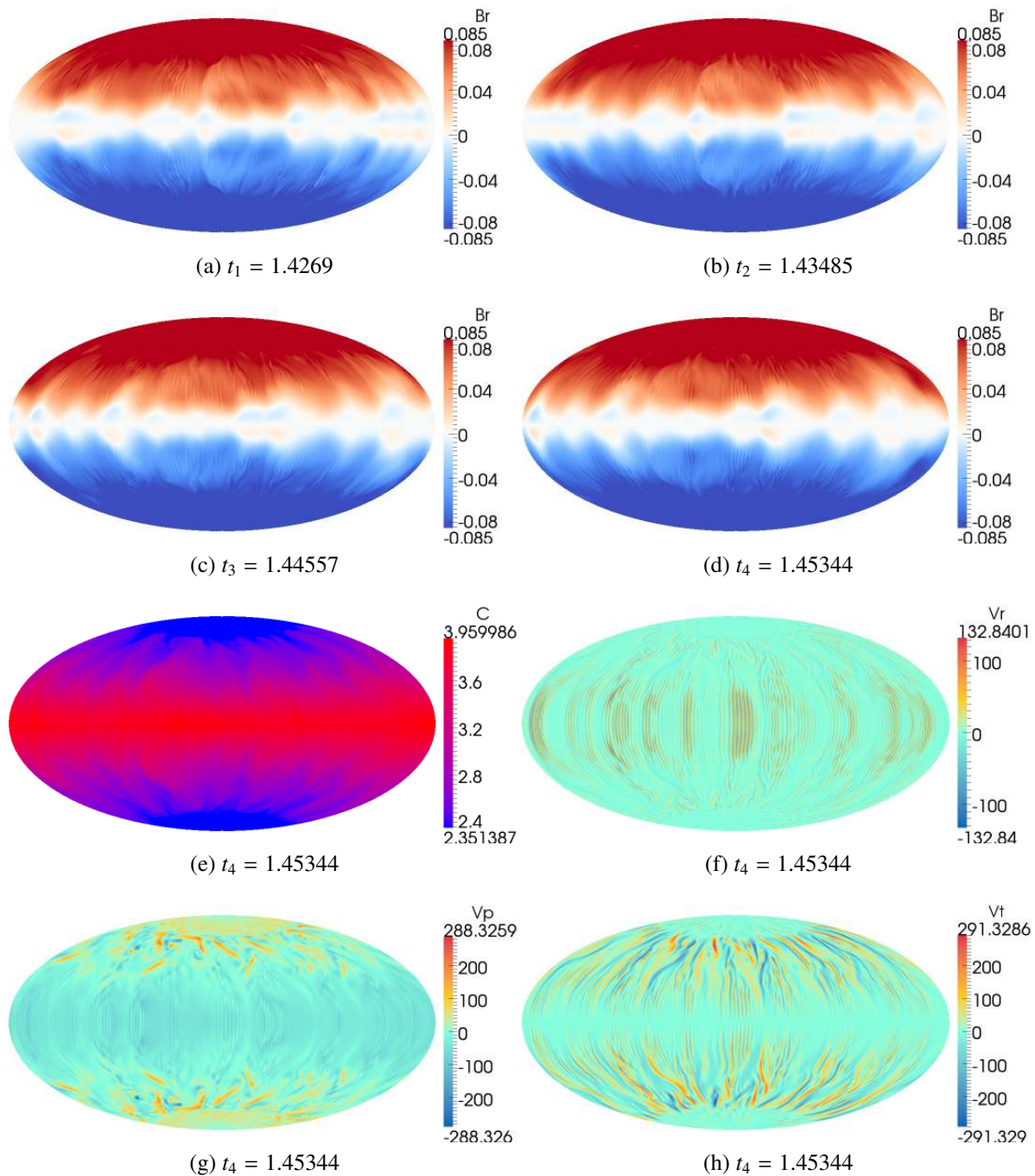
Figure E.1: *Fields on the CMB, velocity is below the surface, Case 0. The fields "C" and "V" denote temperature T and velocity **u**; subscripts "$_p$" and "$_t$" denote φ and θ components respectively.*

E.1.2 Case 1

(a) $t_1 = 0.316417$

(b) $t_2 = 0.320847$

(c) $t_3 = 0.325246$

(d) $t_4 = 0.329283$

(e) $t_4 = 0.329283$

(f) $t_4 = 0.329283$

(g) $t_4 = 0.329283$

(h) $t_4 = 0.329283$
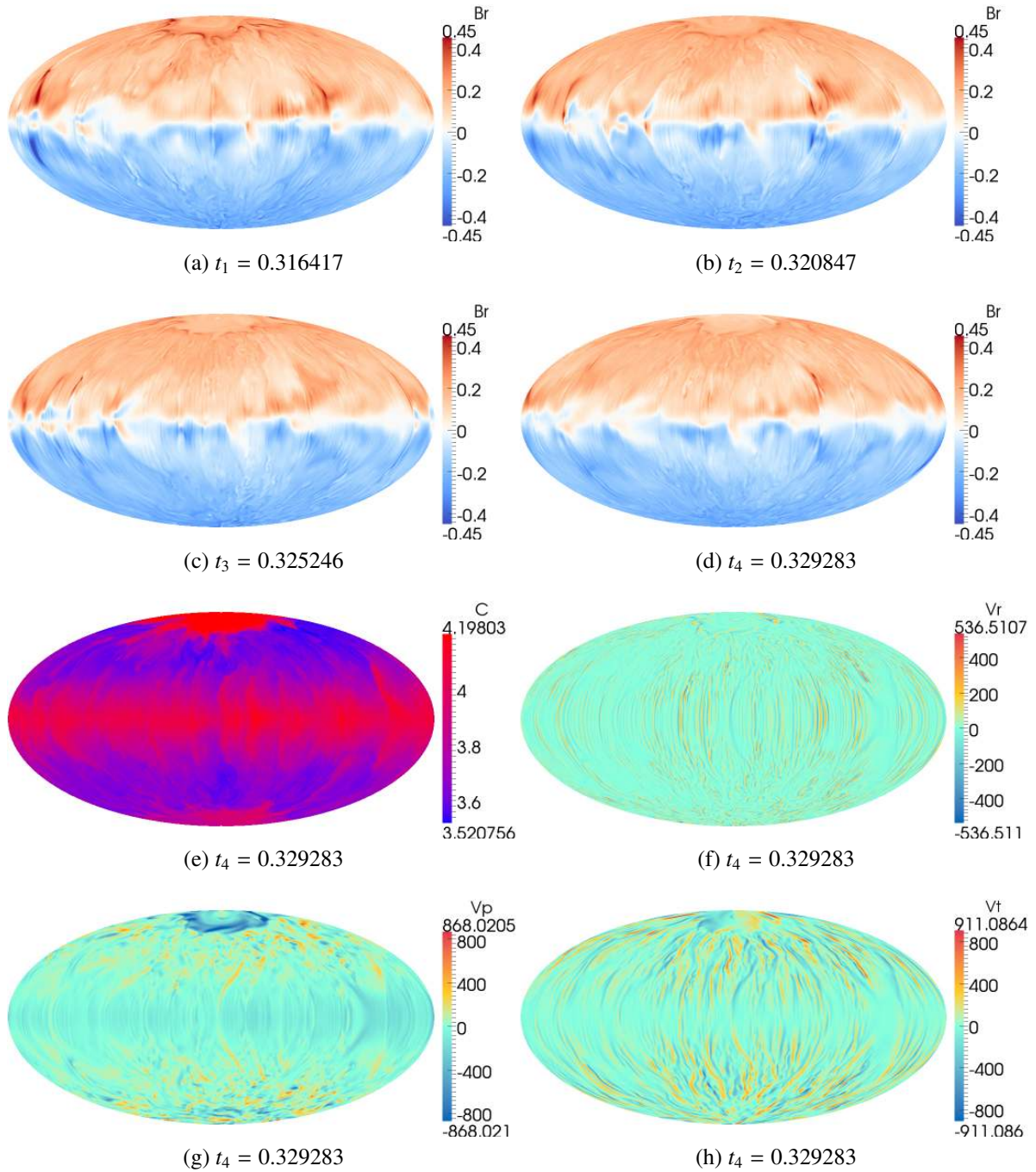
Figure E.2: *Fields on the CMB, velocity is below the surface, Case 1. The fields "C" and "**V**" denote temperature T and velocity* **u***; subscripts "$_p$" and "$_t$" denote φ and θ components respectively.*

E.1.3   Case 2

(a) $t_1 = 0.0605766$

(b) $t_2 = 0.0609511$

(c) $t_4 = 0.0612439$

(d) $t_5 = 0.0613967$

(e) $t_5 = 0.0613967$

(f) $t_5 = 0.0613967$

(g) $t_5 = 0.0613967$

(h) $t_5 = 0.0613967$
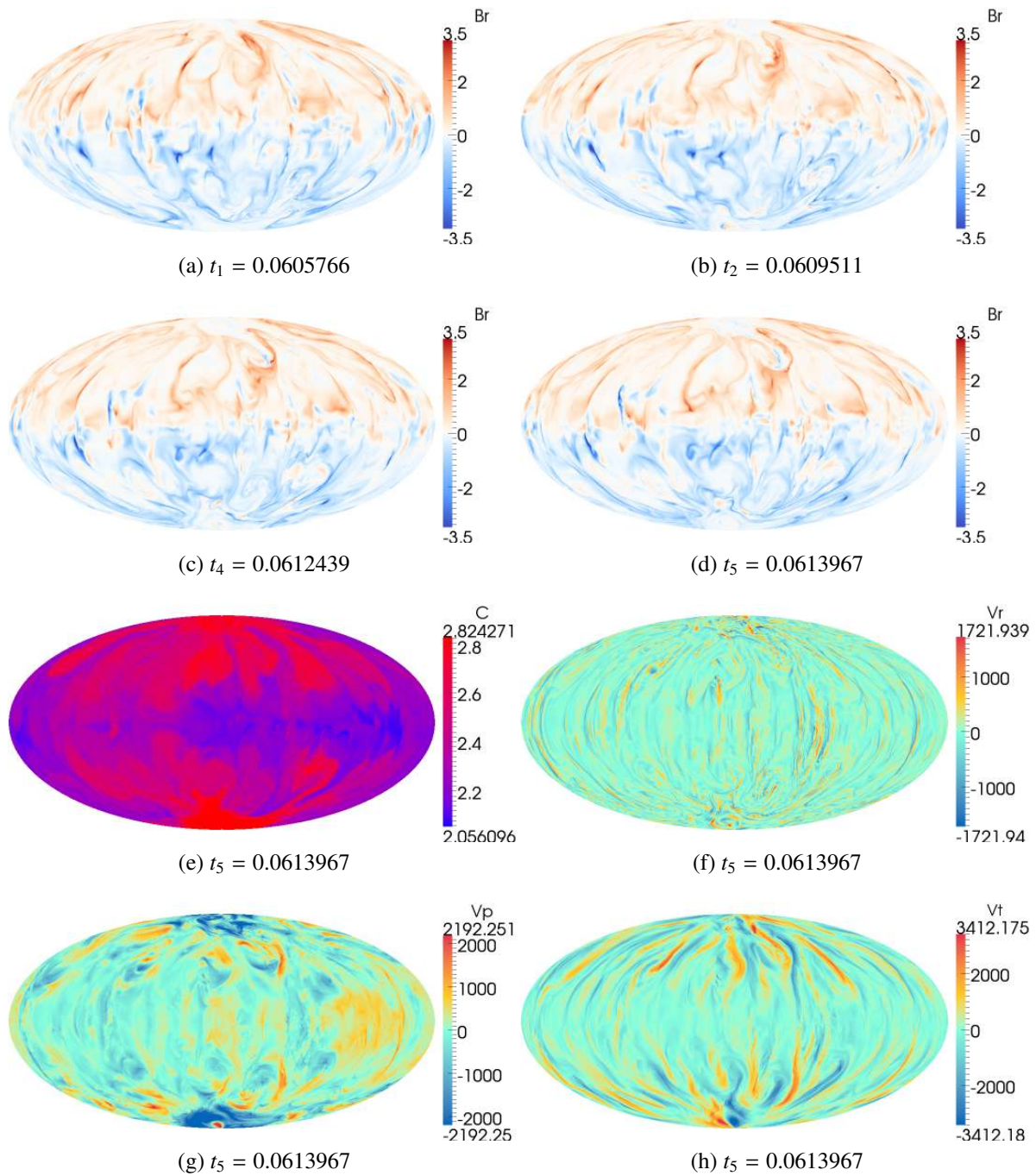
Figure E.3: *Fields on the CMB, velocity is below the surface, Case 2. The fields "C" and "V" denote temperature T and velocity* **u***; subscripts "$_p$" and "$_t$" denote φ and θ components respectively.*

E.1.4   Case 3

(a) $t_1 = 0.0972422$

(b) $t_2 = 0.0977636$

(c) $t_4 = 0.0984726$

(d) $t_5 = 0.0992703$

(e) $t_5 = 0.0992703$

(f) $t_5 = 0.0992703$

(g) $t_5 = 0.0992703$

(h) $t_5 = 0.0992703$
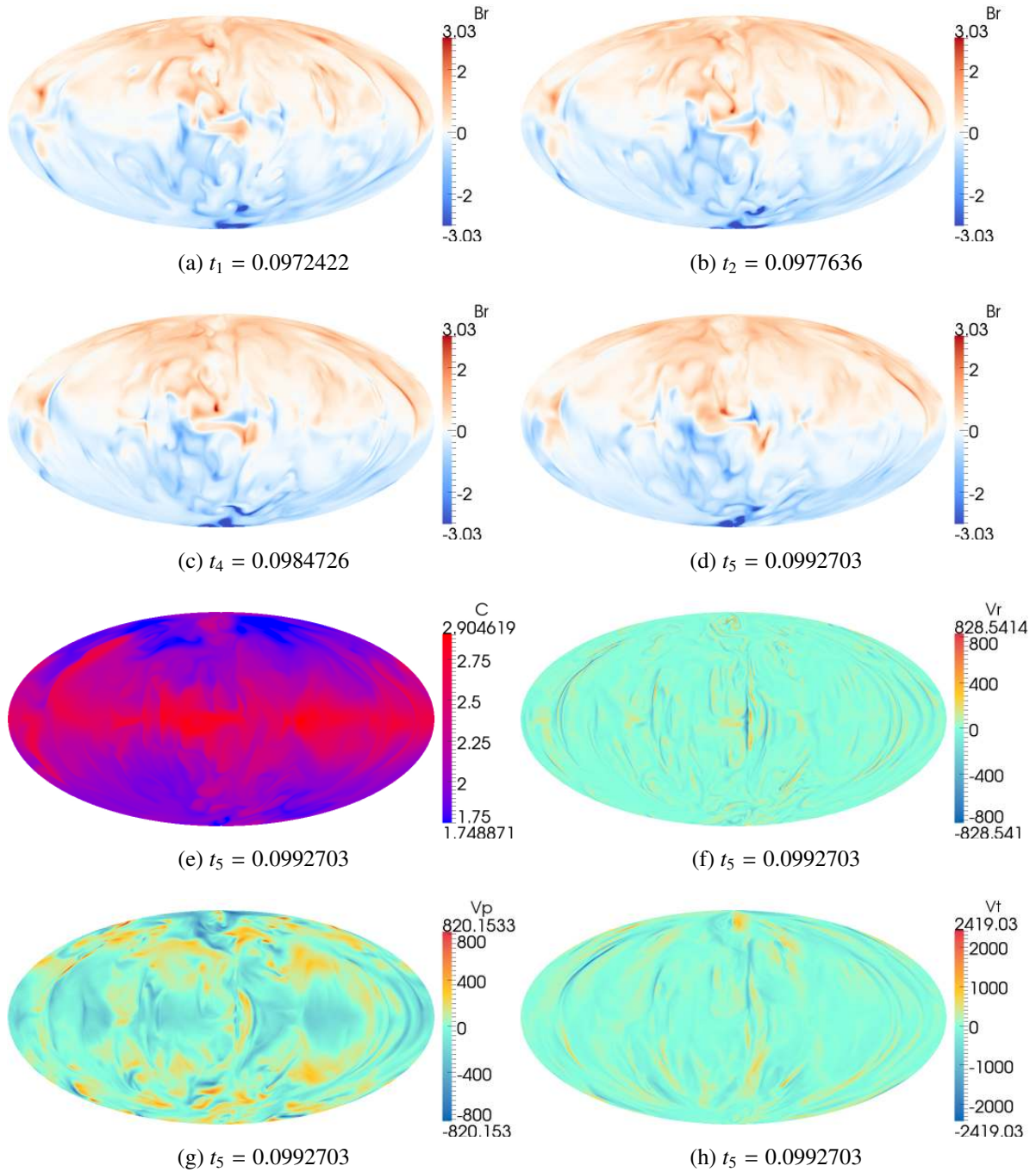
Figure E.4: *Fields on the CMB, velocity is below the surface, Case 3. The fields "C" and "**V**" denote temperature T and velocity* **u**; *subscripts "$_p$" and "$_t$" denote φ and θ components respectively.*

E.1.5 Case 4

(a) $t_1 = 0.0684313$

(b) $t_2 = 0.0702145$

(c) $t_3 = 0.0712324$

(d) $t_4 = 0731656$

(e) $t_3 = 0.0712324$

(f) $t_1 = 0.0684313$

(g) $t_1 = 0.0684313$

(h) $t_1 = 0.0684313$
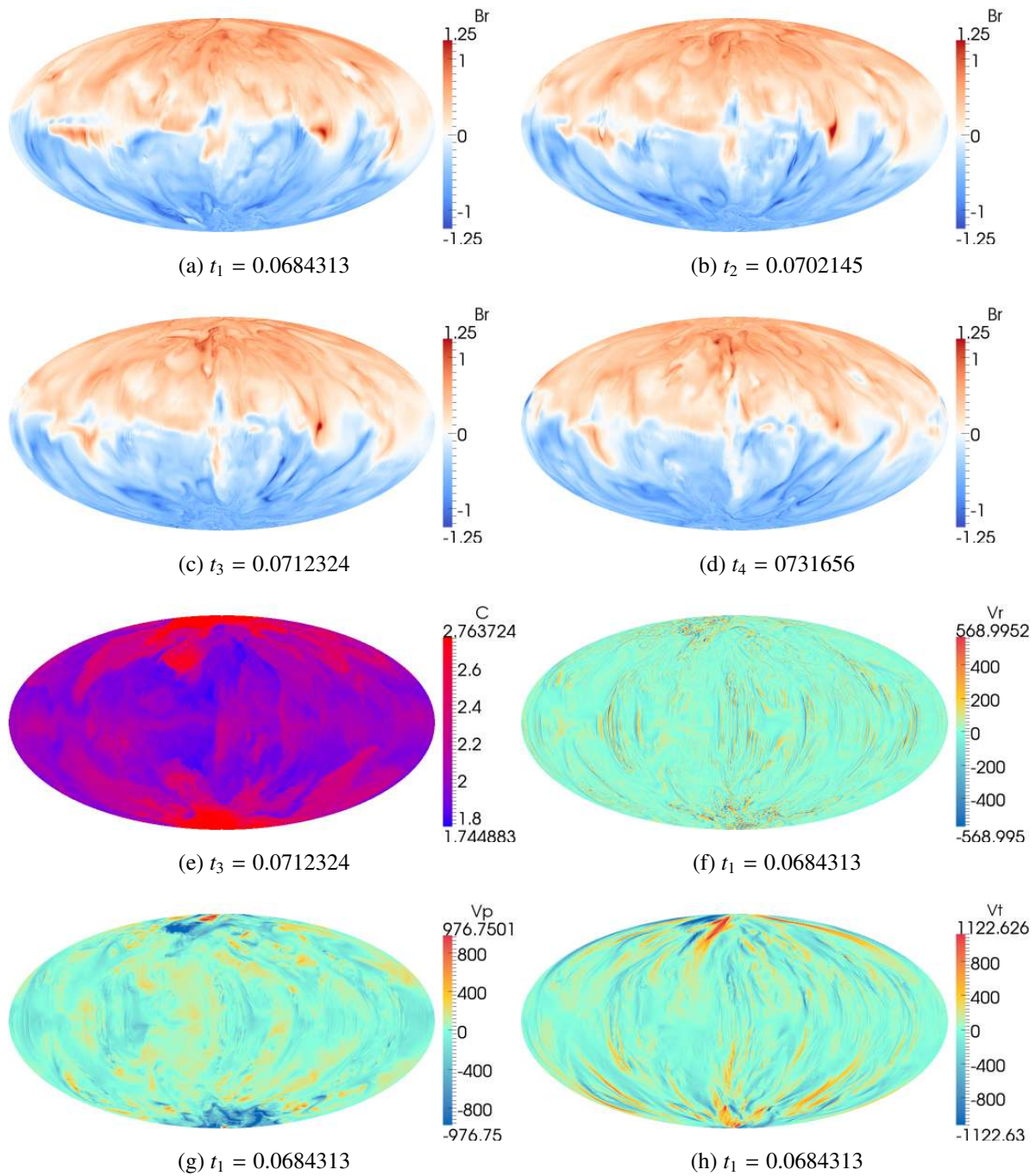
Figure E.5: *Fields on the CMB, velocity is below the surface, Case 4. The fields "C" and "**V**" denote temperature T and velocity* **u***; subscripts "$_p$" and "$_t$" denote* φ *and* θ *components respectively.*

E.1.6 Case 6

(a) $t_1 = 0.272893$

(b) $t_3 = 0.285452$

(c) $t_4 = 0.316841$

(d) $t_5 = 0.322532$

(e) $t_6 = 0.326925$

(f) $t_7 = 0.330822$

(g) $t_8 = 0.333401$

(h) $t_9 = 0.340429$
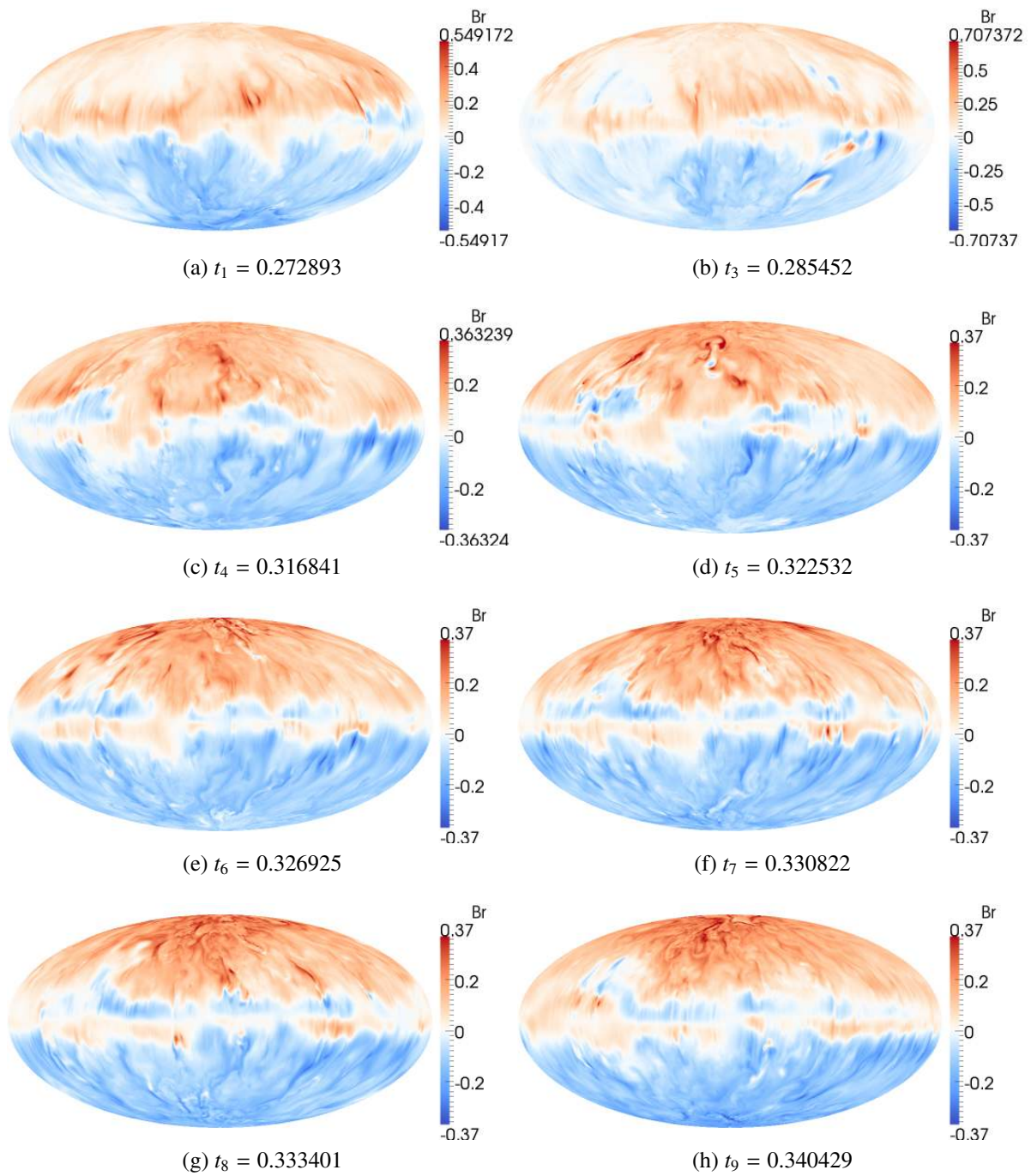
Figure E.6: *Radial magnetic fields on the CMB, Case 6.*

(a) $t_9 = 0.340429$

(b) $t_9 = 0.340429$

(c) $t_9 = 0.340429$

(d) $t_9 = 0.340429$
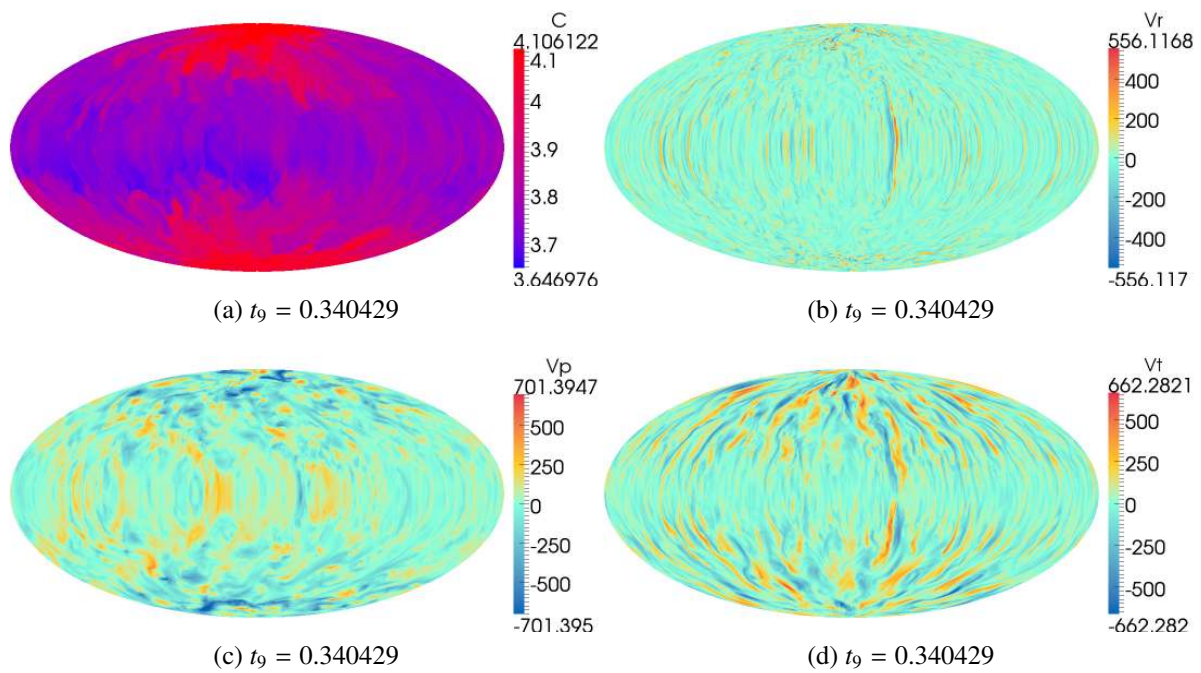
Figure E.7*: Fields on the CMB, velocity is below the surface, Case 6. The fields "C" and "**V**" denote temperature T and velocity* **u***; subscripts "$_p$" and "$_t$" denote φ and θ components respectively.*

E.2 Fields in the plane normal to the rotational axis

A rotating fluid container is an anisotropic system having preferential direction. The behaviour of the system along the rotational axis Ω is not the same as in the normal direction. Owing to Proudman-Taylor theorem, which has an impact[1] on dynamics of rotating MHD even if non-potential forces apart from Coriolis are not negligible, a columnar structure of the flow is preferred. Cross-sections of such columns are seen in equatorial sections and in sections parallel thereto. The behaviour and the influence of internal non-observable fields on the surface magnetic field are discussed in the section (5.3.5) above.

It is worth to know, that "three o'clock" on a cross-section matches the left and right edges of a hammer plot (the type of surface projections in the appendix E.1). The clockwise direction corresponds to right-to-left on a hammer plot. In the same manner the position of "nine o'clock" synchronises with the middle of a hammer plot. Summing up, we look at cross-sections from the north pole in such a way that the zero meridian is on the right edge. Hammer plots spread from zero meridian (left edge) via 180°E (middle) to 0°W (right edge).

---

[1]The Proudman-Taylor theorem is valid when Ekman and Rossby numbers are small, i.e. Coriolis force dominates.

E.2.1 Case 0

(a) $t_1 = 1.4269$ (b) $t_2 = 1.43485$ (c) $t_3 = 1.44557$ (d) $t_4 = 1.45344$

(e) $t_1 = 1.4269$ (f) $t_2 = 1.43485$ (g) $t_3 = 1.44557$ (h) $t_4 = 1.45344$

(i) $t_1 = 1.4269$ (j) $t_2 = 1.43485$ (k) $t_3 = 1.44557$ (l) $t_4 = 1.45344$

(m) $t_1 = 1.4269$ (n) $t_2 = 1.43485$ (o) $t_3 = 1.44557$ (p) $t_4 = 1.45344$
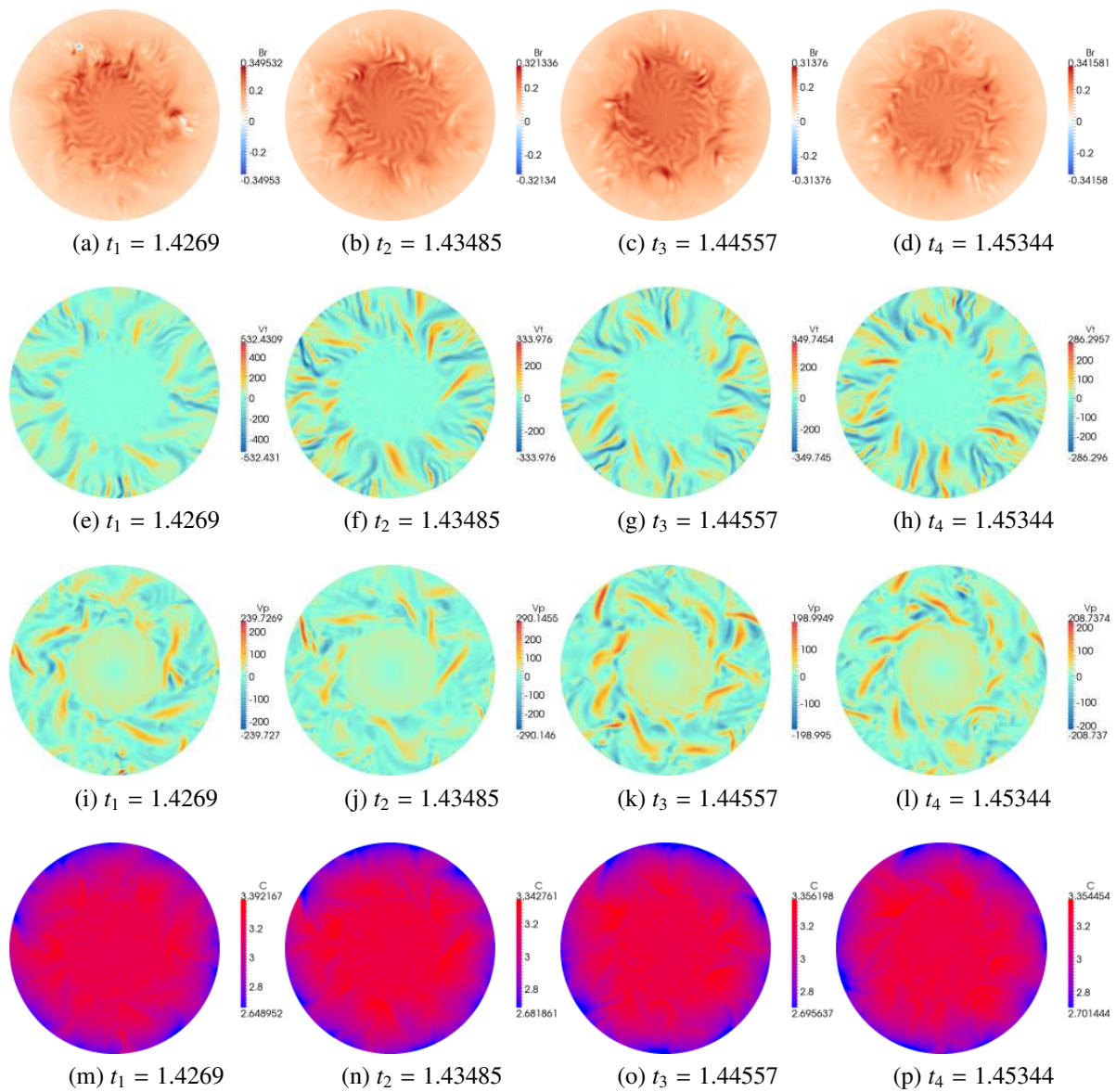
Figure E.8: *Fields in the plane $z = r_i + 0.5$, Case 0. The fields "C" and "**V**" denote temperature T and velocity* **u***; subscripts "$_p$" and "$_t$" denote φ and θ components respectively.*

(a) $t_1 = 1.4269$ (b) $t_2 = 1.43485$ (c) $t_3 = 1.44557$ (d) $t_4 = 1.45344$

(e) $t_1 = 1.4269$ (f) $t_2 = 1.43485$ (g) $t_3 = 1.44557$ (h) $t_4 = 1.45344$

(i) $t_1 = 1.4269$ (j) $t_2 = 1.43485$ (k) $t_3 = 1.44557$ (l) $t_4 = 1.45344$

(m) $t_1 = 1.4269$ (n) $t_2 = 1.43485$ (o) $t_3 = 1.44557$ (p) $t_4 = 1.45344$
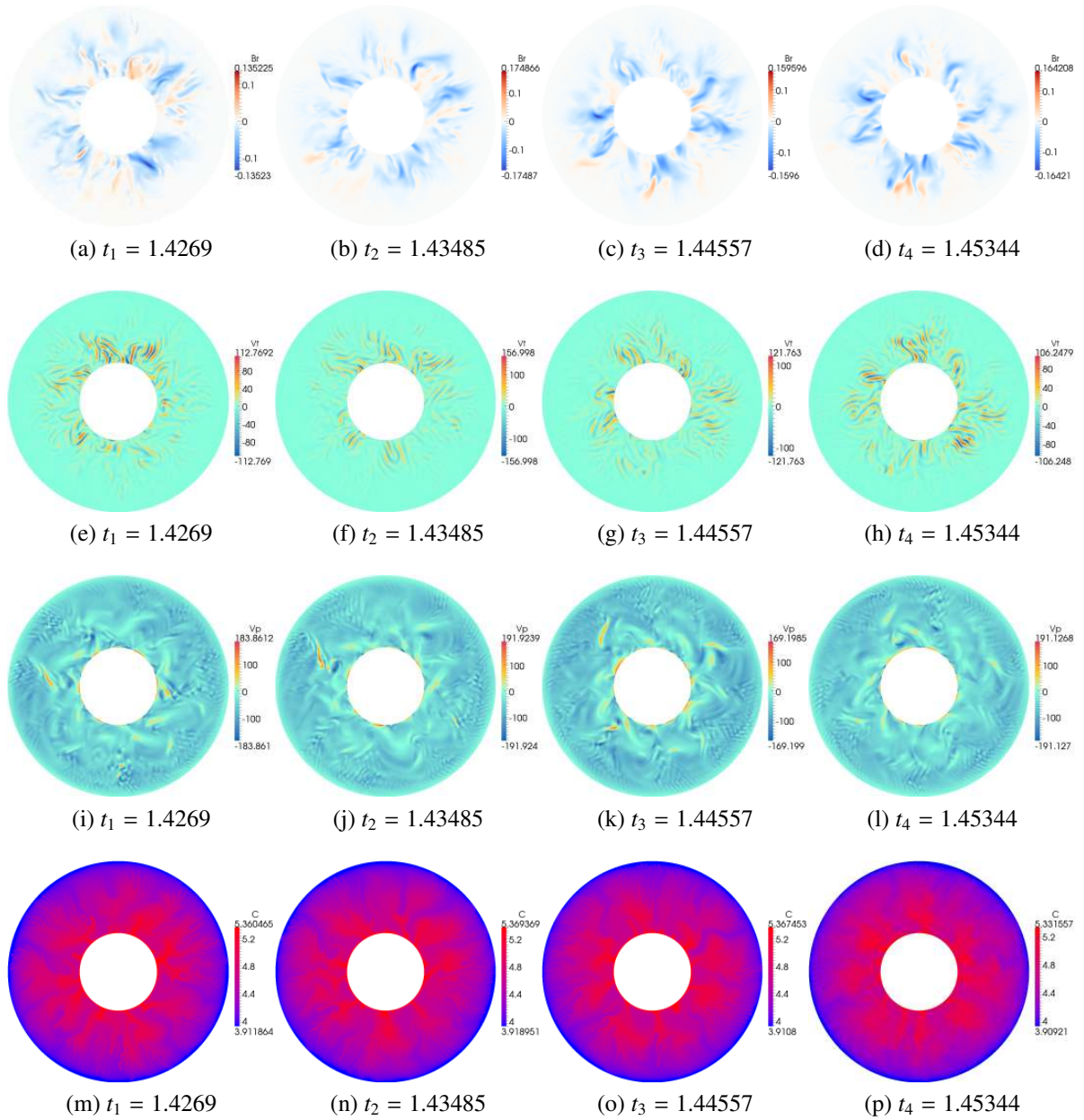
Figure E.9: *Fields in the plane z=0.0, Case 0. The fields "C" and "V" denote temperature T and velocity* $\mathbf{u}$*; subscripts "$_p$" and "$_t$" denote φ and θ components respectively.*

E.2.2   Case 1

(a) $t_1 = 0.316417$ (b) $t_2 = 0.320847$ (c) $t_3 = 0.325246$ (d) $t_4 = 0.329283$

(e) $t_1 = 0.316417$ (f) $t_2 = 0.320847$ (g) $t_3 = 0.325246$ (h) $t_4 = 0.329283$

(i) $t_1 = 0.316417$ (j) $t_2 = 0.320847$ (k) $t_3 = 0.325246$ (l) $t_4 = 0.329283$

(m) $t_1 = 0.316417$ (n) $t_2 = 0.320847$ (o) $t_3 = 0.325246$ (p) $t_4 = 0.329283$
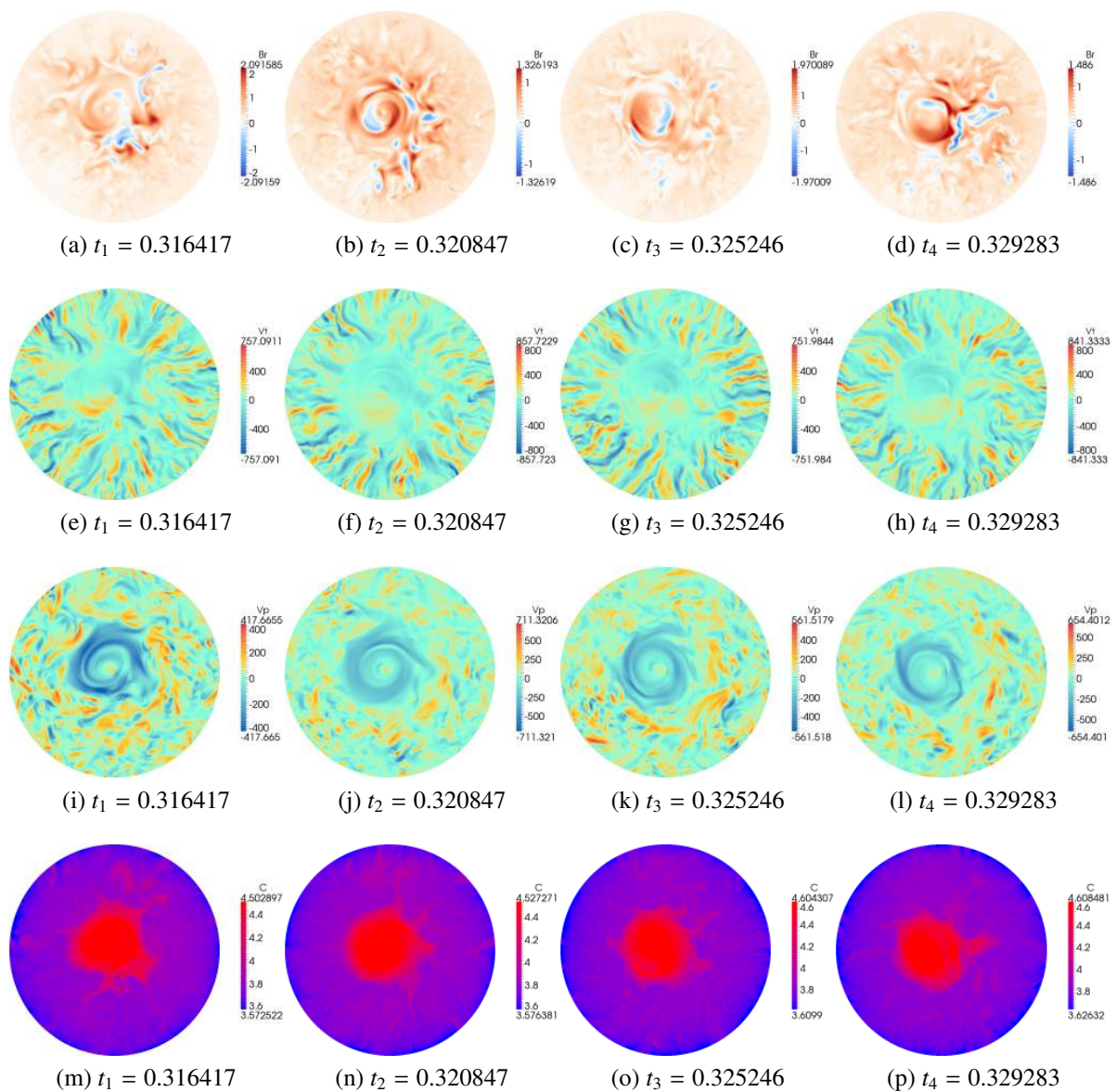
Figure E.10: *Fields in the plane $z = r_i + 0.5$, Case 1. The fields "C" and "V" denote temperature T and velocity* **u***; subscripts "$_p$" and "$_t$" denote φ and θ components respectively.*

(a) $t_1 = 0.316417$ (b) $t_2 = 0.320847$ (c) $t_3 = 0.325246$ (d) $t_4 = 0.329283$

(e) $t_1 = 0.316417$ (f) $t_2 = 0.320847$ (g) $t_3 = 0.325246$ (h) $t_4 = 0.329283$

(i) $t_1 = 0.316417$ (j) $t_2 = 0.320847$ (k) $t_3 = 0.325246$ (l) $t_4 = 0.329283$

(m) $t_1 = 0.316417$ (n) $t_2 = 0.320847$ (o) $t_3 = 0.325246$ (p) $t_4 = 0.329283$
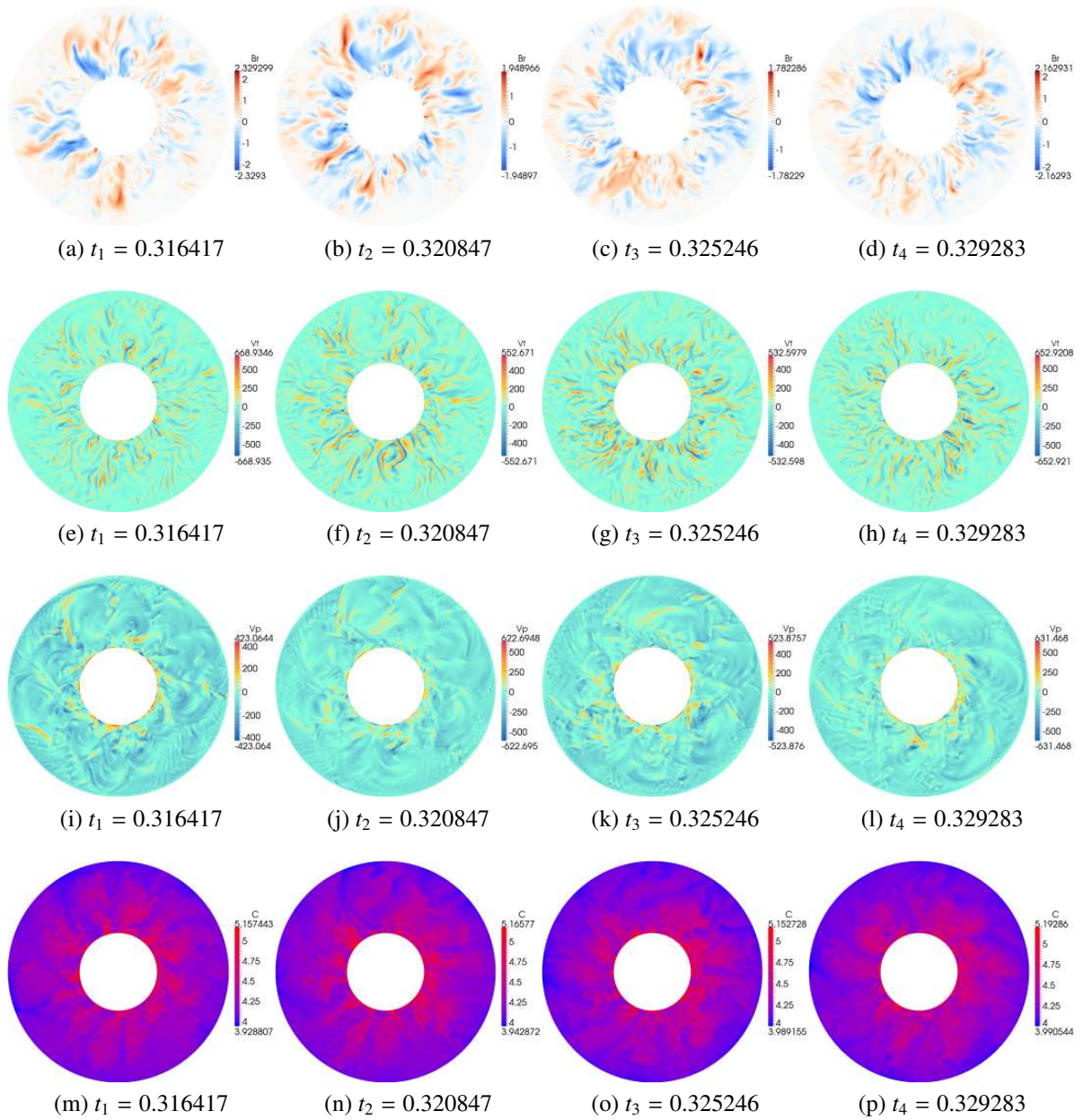
Figure E.11: *Fields in the plane z=0.0, Case 1. The fields "C" and "$\mathbf{V}$" denote temperature T and velocity $\mathbf{u}$; subscripts "$_p$" and "$_t$" denote φ and θ components respectively.*

E.2.3 Case 2

(a) $t_1 = 0.0605766$ (b) $t_2 = 0.0609511$ (c) $t_4 = 0.0612439$ (d) $t_5 = 0.0613967$

(e) $t_1 = 0.0605766$ (f) $t_2 = 0.0609511$ (g) $t_4 = 0.0612439$ (h) $t_5 = 0.0613967$

(i) $t_1 = 0.0605766$ (j) $t_2 = 0.0609511$ (k) $t_4 = 0.0612439$ (l) $t_5 = 0.0613967$

(m) $t_1 = 0.0605766$ (n) $t_2 = 0.0609511$ (o) $t_4 = 0.0612439$ (p) $t_5 = 0.0613967$
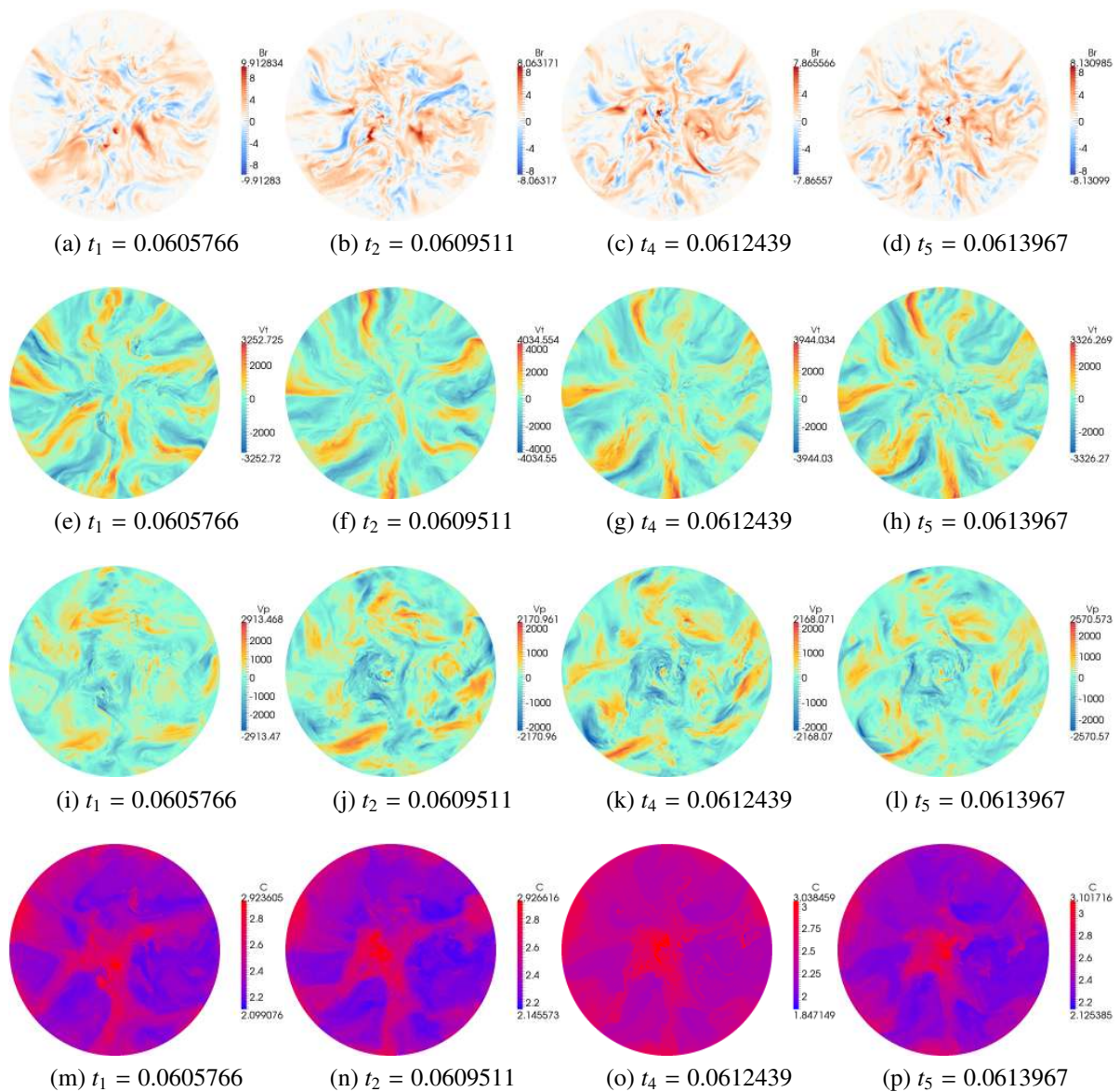
Figure E.12: *Fields in the plane $z = r_i + 0.5$, Case 2. The fields "C" and "V" denote temperature T and velocity $\mathbf{u}$; subscripts "$_p$" and "$_t$" denote φ and θ components respectively.*

(a) $t_1 = 0.0605766$ (b) $t_2 = 0.0609511$ (c) $t_3 = 0.0612439$ (d) $t_4 = 0.0613967$

(e) $t_1 = 0.0605766$ (f) $t_2 = 0.0609511$ (g) $t_3 = 0.0612439$ (h) $t_4 = 0.0613967$

(i) $t_1 = 0.0605766$ (j) $t_2 = 0.0609511$ (k) $t_3 = 0.0612439$ (l) $t_4 = 0.0613967$

(m) $t_1 = 0.0605766$ (n) $t_2 = 0.0609511$ (o) $t_3 = 0.0612439$ (p) $t_4 = 0.0613967$
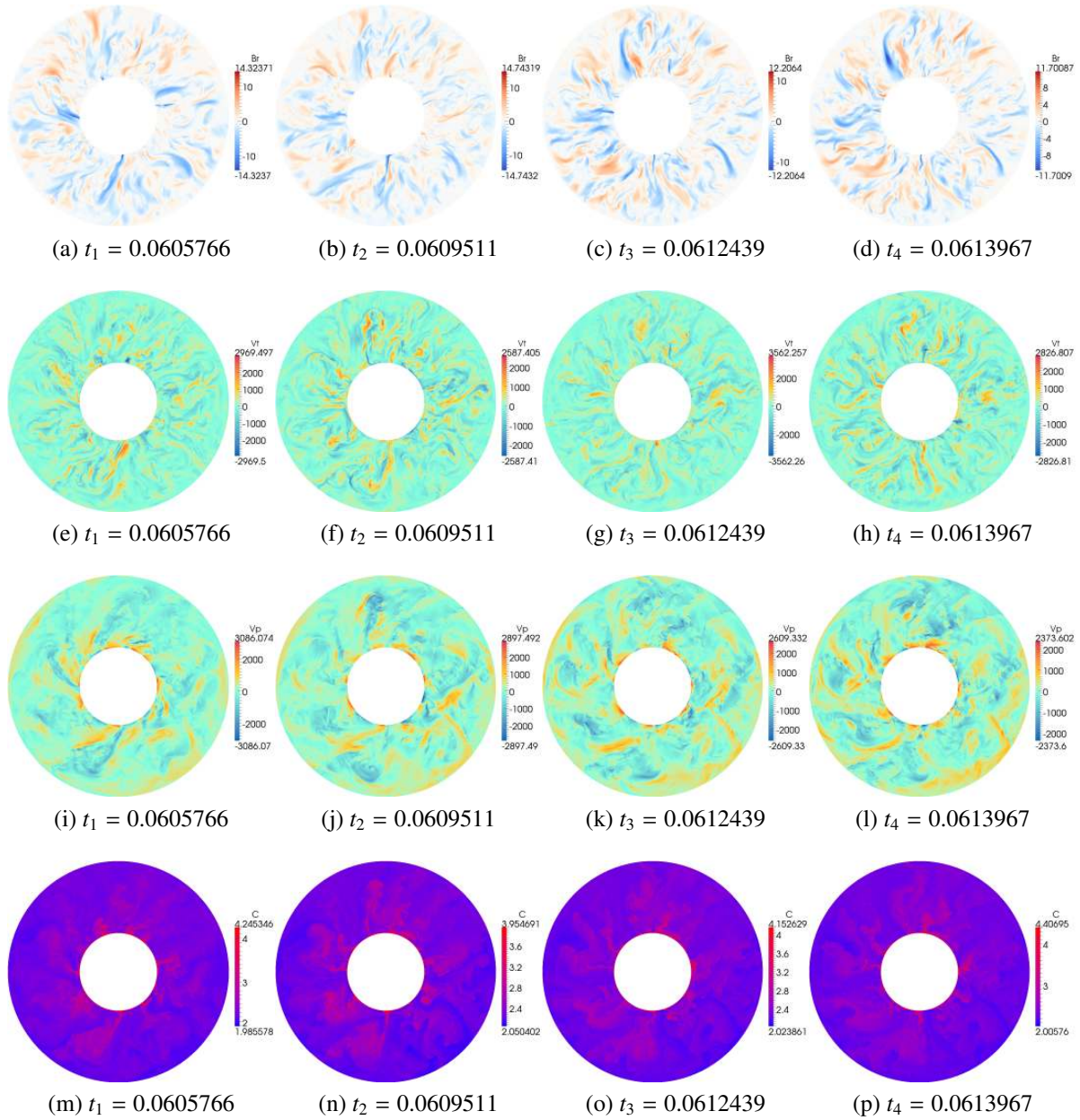
Figure E.13: *Fields in the plane z=0.0, Case 2. The fields "C" and "V" denote temperature T and velocity* **u***; subscripts "$_p$" and "$_t$" denote φ and θ components respectively.*

E.2.4 Case 3

(a) $t_1 = 0.0972422$ (b) $t_2 = 0.0977636$ (c) $t_4 = 0.0984726$ (d) $t_5 = 0.0992703$

(e) $t_1 = 0.0972422$ (f) $t_2 = 0.0977636$ (g) $t_4 = 0.0984726$ (h) $t_5 = 0.0992703$

(i) $t_1 = 0.0972422$ (j) $t_2 = 0.0977636$ (k) $t_4 = 0.0984726$ (l) $t_5 = 0.0992703$

(m) $t_1 = 0.0972422$ (n) $t_2 = 0.0977636$ (o) $t_4 = 0.0984726$ (p) $t_5 = 0.0992703$
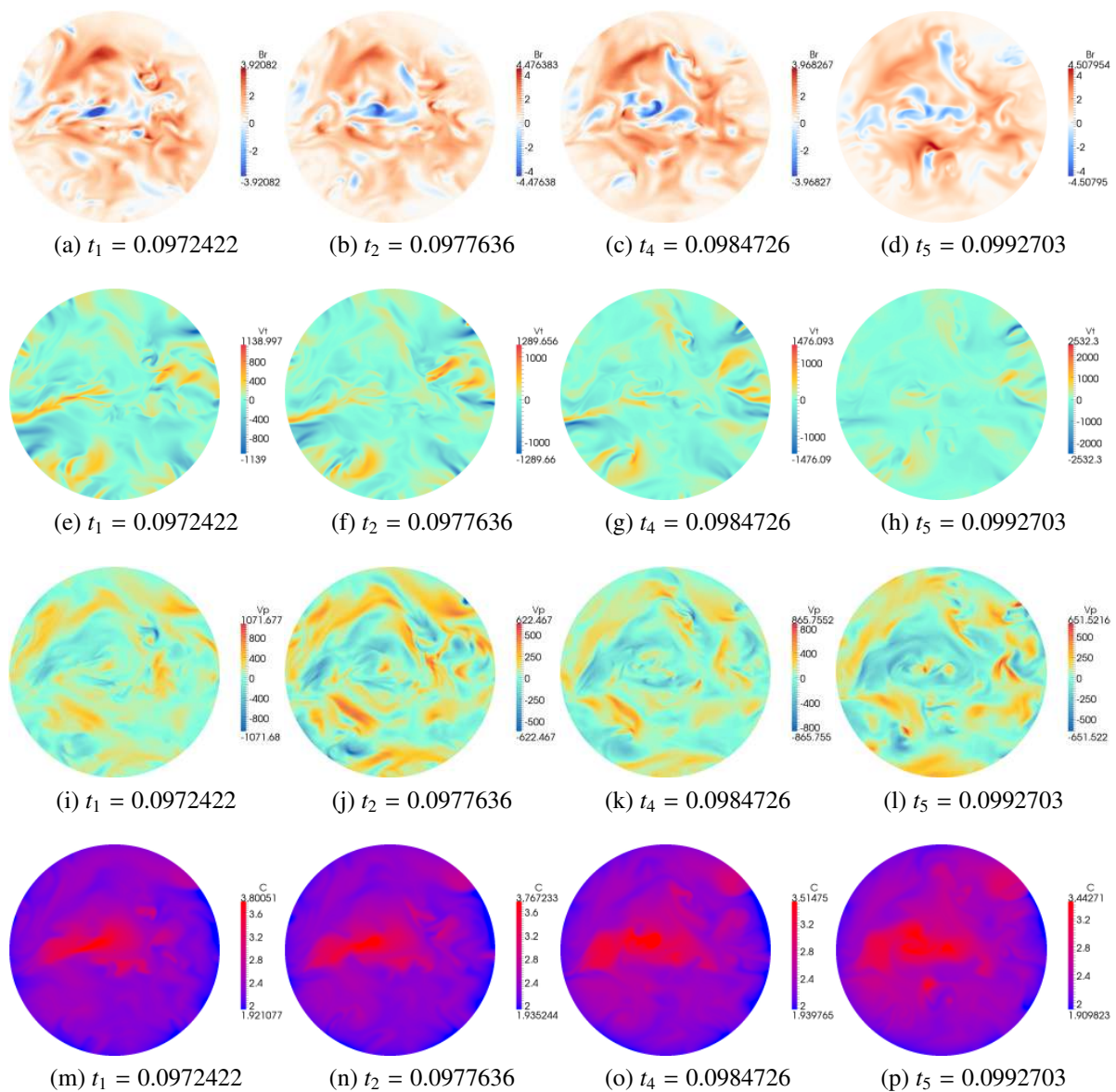
Figure E.14: *Fields in the plane $z = r_i + 0.5$, Case 3. The fields "C" and "V" denote temperature T and velocity $\mathbf{u}$; subscripts "$_p$" and "$_t$" denote φ and θ components respectively.*

(a) $t_1 = 0.0972422$ (b) $t_2 = 0.0977636$ (c) $t_4 = 0.0984726$ (d) $t_5 = 0.0992703$

(e) $t_1 = 0.0972422$ (f) $t_2 = 0.0977636$ (g) $t_4 = 0.0984726$ (h) $t_5 = 0.0992703$

(i) $t_1 = 0.0972422$ (j) $t_2 = 0.0977636$ (k) $t_4 = 0.0984726$ (l) $t_5 = 0.0992703$

(m) $t_1 = 0.0972422$ (n) $t_2 = 0.0977636$ (o) $t_4 = 0.0984726$ (p) $t_5 = 0.0992703$
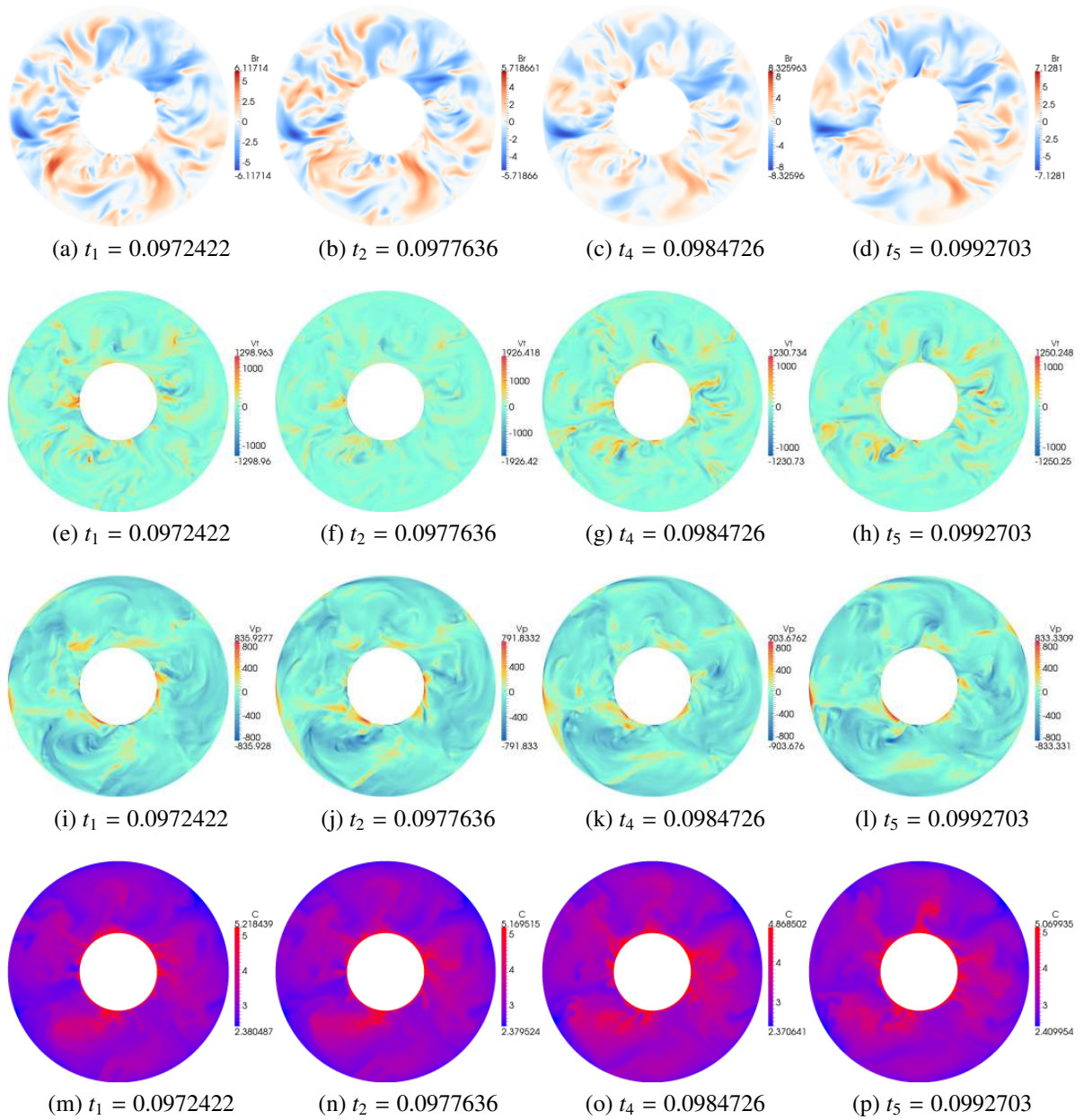
Figure E.15: *Fields in the plane z=0.0, Case 3. The fields "C" and "V" denote temperature T and velocity* **u***; subscripts "$_p$" and "$_t$" denote φ and θ components respectively.*

E.2.5   Case 4

(a) $t_1 = 0.0684313$ (b) $t_2 = 0.0702145$ (c) $t_3 = 0.0712324$ (d) $t_4 = 0731656$

(e) $t_1 = 0.0684313$ (f) $t_2 = 0.0702145$ (g) $t_3 = 0.0712324$ (h) $t_4 = 0731656$

(i) $t_1 = 0.0684313$ (j) $t_2 = 0.0702145$ (k) $t_3 = 0.0712324$ (l) $t_4 = 0731656$

(m) $t_1 = 0.0684313$ (n) $t_2 = 0.0702145$ (o) $t_3 = 0.0712324$ (p) $t_4 = 0731656$

(q) $t_1 = 0.0684313$ (r) $t_2 = 0.0702145$ (s) $t_3 = 0.0712324$ (t) $t_4 = 0731656$
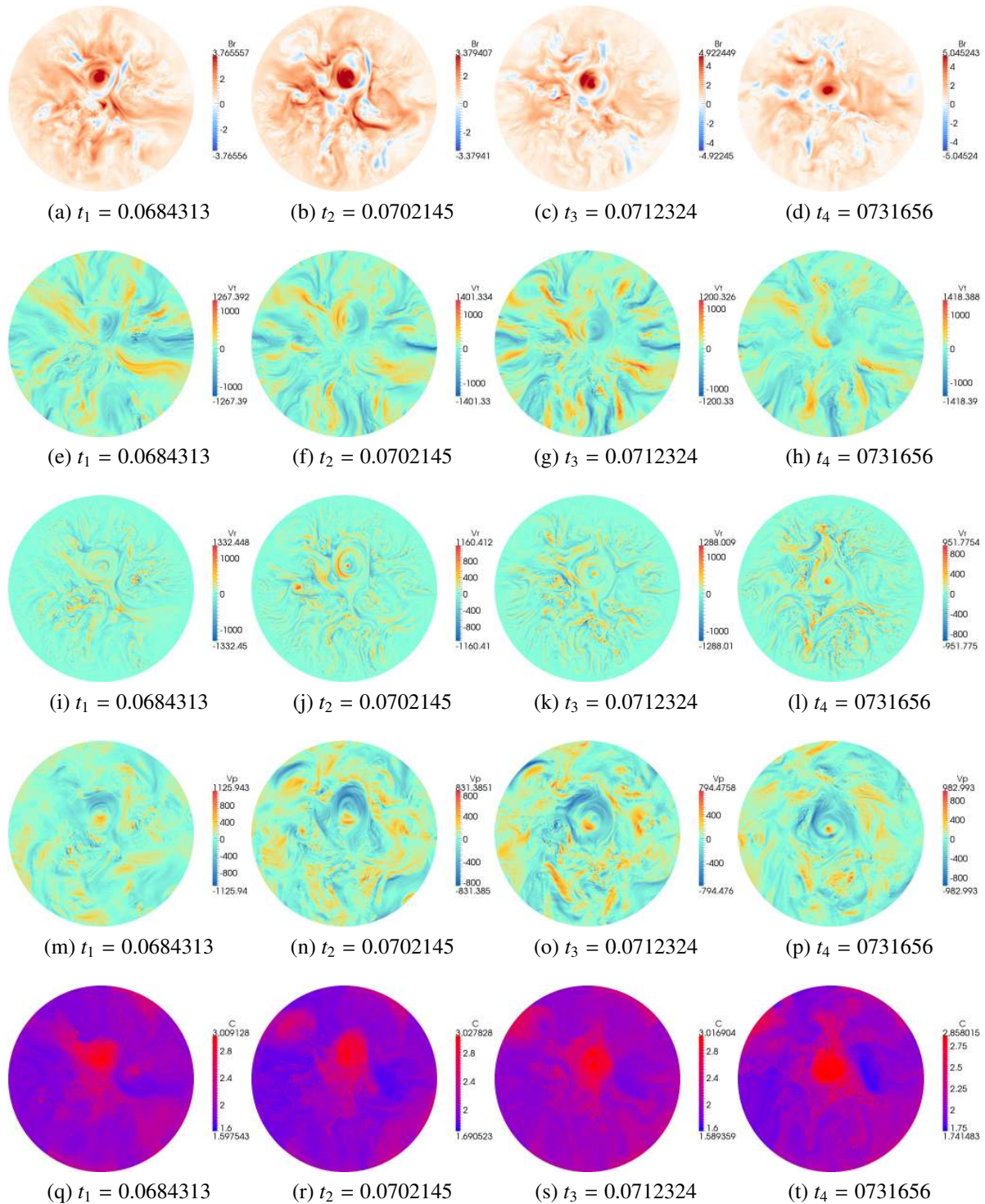
Figure E.16: *Fields in the plane $z = r_i + 0.5$, Case 4. The fields "C" and "V" denote temperature T and velocity* **u**; *subscripts "$_p$" and "$_t$" denote φ and θ components respectively.*

(a) $t_1 = 0.0684313$ (b) $t_2 = 0.0702145$ (c) $t_3 = 0.0712324$ (d) $t_4 = 0731656$

(e) $t_1 = 0.0684313$ (f) $t_2 = 0.0702145$ (g) $t_3 = 0.0712324$ (h) $t_4 = 0731656$

(i) $t_1 = 0.0684313$ (j) $t_2 = 0.0702145$ (k) $t_3 = 0.0712324$ (l) $t_4 = 0731656$

(m) $t_1 = 0.0684313$ (n) $t_2 = 0.0702145$ (o) $t_3 = 0.0712324$ (p) $t_4 = 0731656$

(q) $t_1 = 0.0684313$ (r) $t_2 = 0.0702145$ (s) $t_3 = 0.0712324$ (t) $t_4 = 0731656$
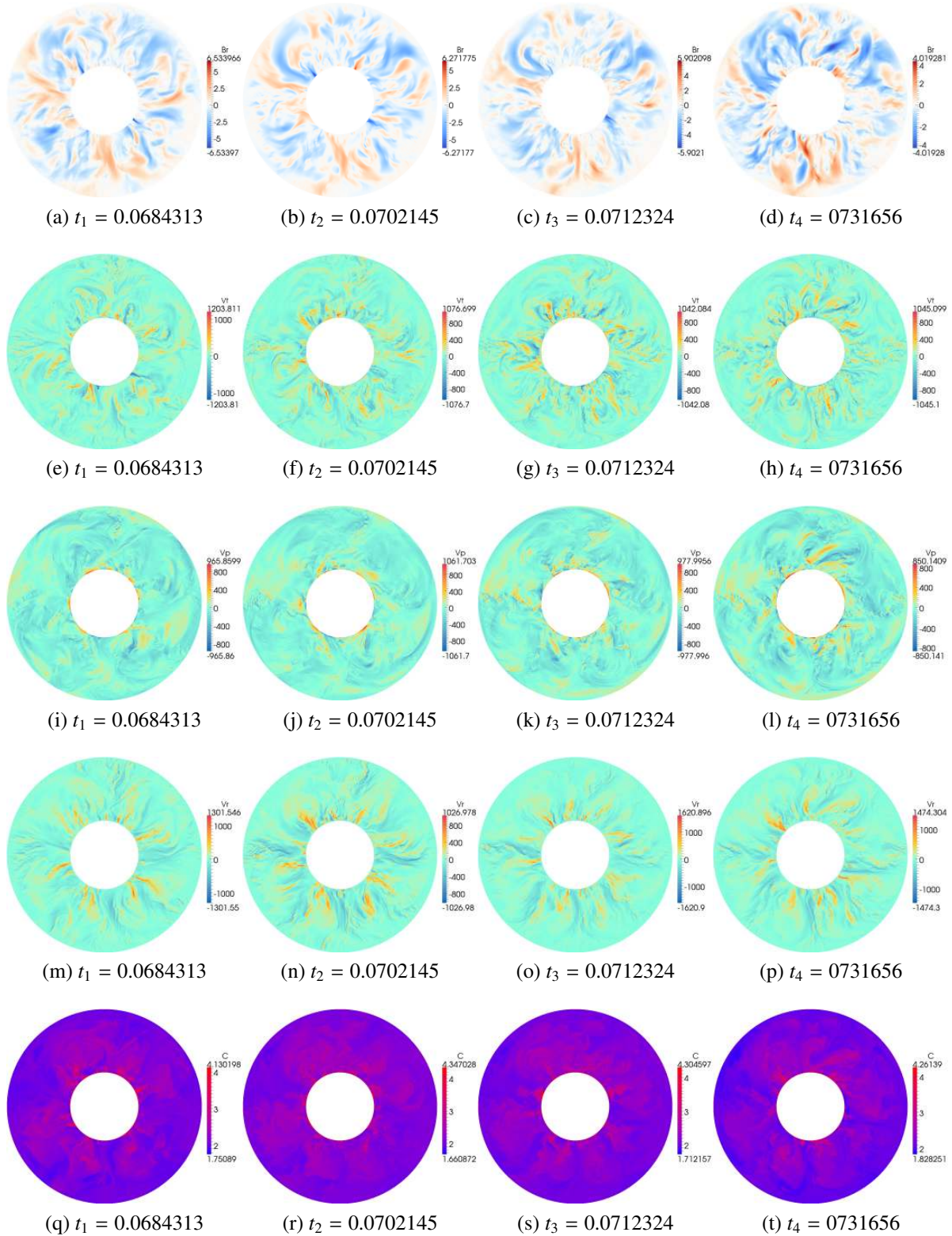
Figure E.17: *Fields in the plane z=0.0, Case 4. The fields "C" and "V" denote temperature T and velocity $\mathbf{u}$; subscripts "$_p$" and "$_t$" denote φ and θ components respectively.*

E.2.6 Case 6

(a) $t_6 = 0.326925$ (b) $t_7 = 0.330822$ (c) $t_8 = 0.333401$ (d) $t_9 = 0.340429$

(e) $t_6 = 0.326925$ (f) $t_7 = 0.330822$ (g) $t_8 = 0.333401$ (h) $t_9 = 0.340429$

(i) $t_6 = 0.326925$ (j) $t_7 = 0.330822$ (k) $t_8 = 0.333401$ (l) $t_9 = 0.340429$

(m) $t_6 = 0.326925$ (n) $t_7 = 0.330822$ (o) $t_8 = 0.333401$ (p) $t_9 = 0.340429$
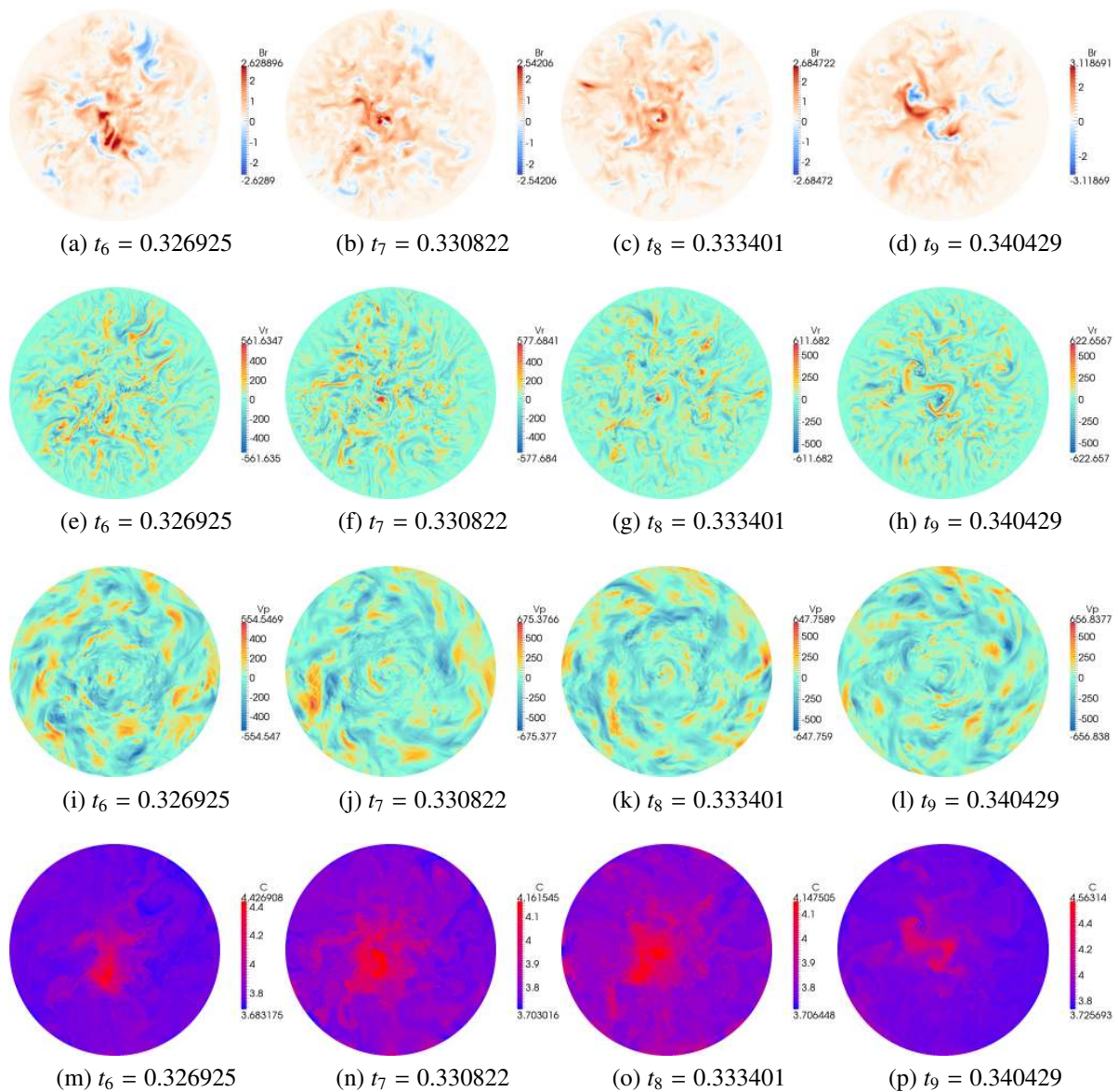
Figure E.18: *Fields in the plane $z = r_i + 0.5$, Case 6. The fields "C" and "V" denote temperature T and velocity $\mathbf{u}$; subscripts "$_p$" and "$_t$" denote φ and θ components respectively.*

(a) $t_6 = 0.326925$ (b) $t_7 = 0.330822$ (c) $t_8 = 0.333401$ (d) $t_9 = 0.340429$

(e) $t_6 = 0.326925$ (f) $t_7 = 0.330822$ (g) $t_8 = 0.333401$ (h) $t_9 = 0.340429$

(i) $t_6 = 0.326925$ (j) $t_7 = 0.330822$ (k) $t_8 = 0.333401$ (l) $t_9 = 0.340429$

(m) $t_6 = 0.326925$ (n) $t_7 = 0.330822$ (o) $t_8 = 0.333401$ (p) $t_9 = 0.340429$
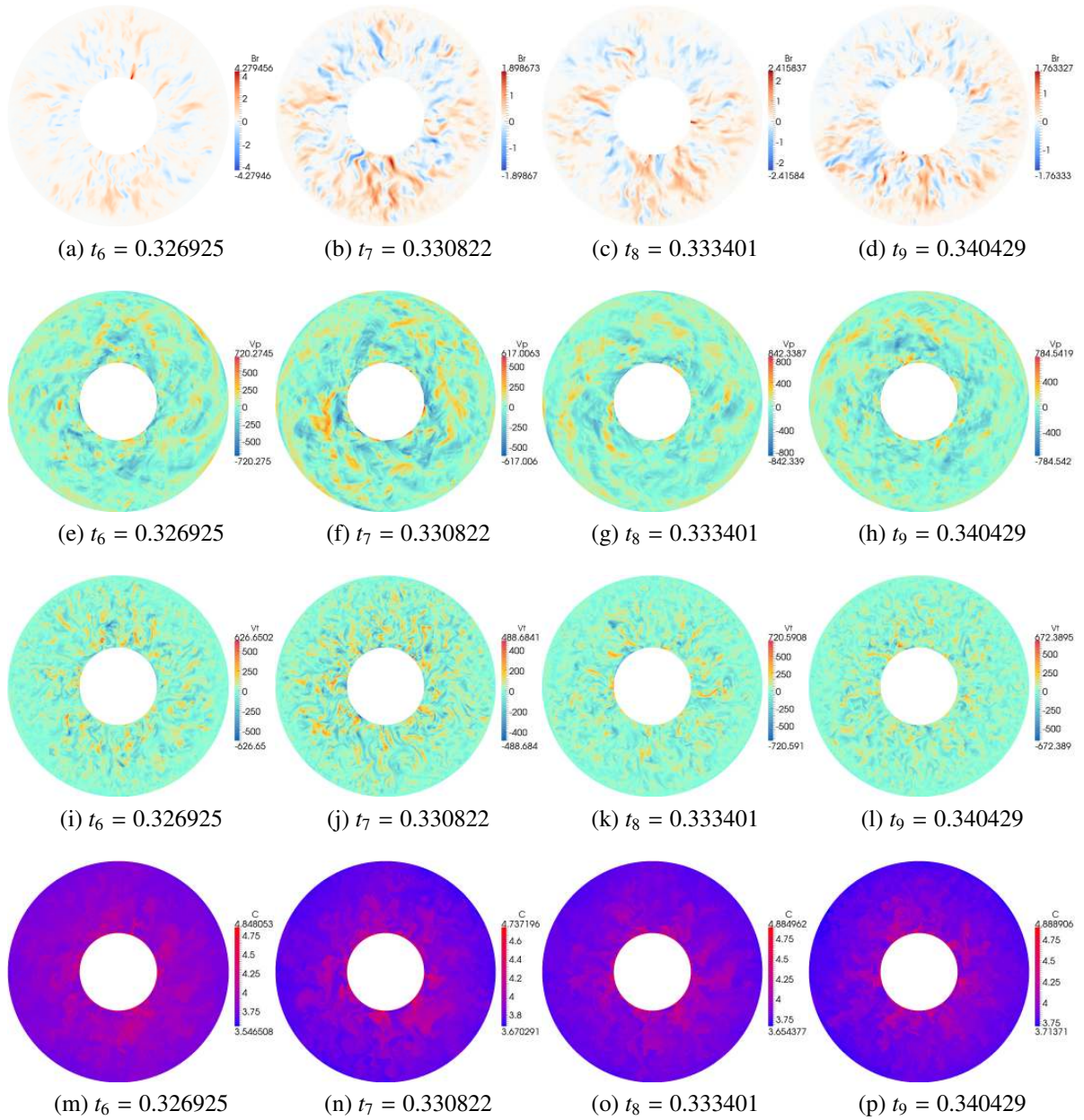
Figure E.19: *Fields in the plane z=0.0, Case 6. The fields "C" and "V" denote temperature T and velocity* $\mathbf{u}$*; subscripts "$_p$" and "$_t$" denote φ and θ components respectively.*

Bibliography

Abramowitz, M. and Stegun, I. A. *Handbook of Mathematical Functions*. Dover Publications, Inc., 1970.

Acheson, D.J. *Elementary fluid dynamics*. Oxford University Press, New York, 1990.

Alfvén, H. Existence of electromagnetic-hydrodynamic waves. *Nature*, 150, 405–406, 1942.

Anufriev, A.P., Jones, C.A., and Soward, A.M. The Boussinesq and anelastic liquid approximations for convection in the Earth's core. *Physics of the Earth and Planetary Interiors*, 152(3), 163 – 190, 2005.

Arai, M. and Suidzu, T. Porous ceramic coating for transpiration cooling of gas turbine blade. *Journal of Thermal Spray Technology*, pages 1–9, 2013.

Arsenin, V. *Mathematical methods and special functions (Metodi Matematicheskoi fiziki i specialnie funkcii)*. Nauka, Moscow, second edition, 1984.

Aubert, J. Steady zonal flows in spherical shell dynamos. *Journal of Fluid Mechanics*, 542, 53–67, October 2005.

Aubert, J., Amit, H., and Hulot, G. Detecting thermal boundary control in surface flows from numerical dynamos. *Physics of the Earth and Planetary Interiors*, 160(2), 143 – 156, 2007.

Aubert, J., Aurnou, J., and Wicht, J. The magnetic structure of convection-driven numerical dynamos. *Geophysical Journal International*, 172(3), 945–956, 2008.

Aubert, J., Labrosse, S., and Poitou, C. Modelling the palaeo-evolution of the geodynamo. *Geophysical Journal International*, (179), 1414–1428, 2009.

Aurnou, J. Planetary core dynamics and convective heat transfer scaling. *Geophysical & Astrophysical Fluid Dynamics*, 101(5-6), 327–345, 2007.

Backus, G. A class of self-sustaining dissipative spherical dynamos. *Annals of Physics*, 4(4), 372 – 447, 1958.

Backus, G. Gross Thermodynamics of Heat Engines in Deep Interior of Earth. *Proceedings of the National Academy of Sciences of the USA*, 72, 1555–1558, 1975.

Backus, G. Poloidal and Toroidal Fields in Geomagnetic Field Modeling. *Reviews of Geophysics*, 24(1), 75–109, February 1986.

Bloxham, J. The expulsion of magnetic flux from the Earth's core. *Geophysical Journal of the Royal Astronomical Society*, 87(2), 669–678, 1986.

Boyd, J.P. *Chebyshev and Fourier Spectral Methods*. Dover Publications, Inc., 31 East 2nd Street Mineola, New York 11501, second edition, 2000.

Braginsky, S.I. Structure of the F layer and reasons for convection in the Earth's core. *Doklady Akademii Nauk SSSR*, 149, 8–10, 1963.

Braginsky, S.I. Magnetic waves in the Earth's core. 7, 851–859, 1967.

Braginsky, S.I. Dynamics of the stably stratified ocean at the top of the core. *Physics of the Earth and Planetary Interiors*, 111(1-2), 21–34, 1999.

Braginsky, S.I. and Roberts, P.H. Equations governing convection in Earth's core and the geodynamo. *Geophysical & Astrophysical Fluid Dynamics*, 79, 1–97, August 1995.

Brown, B.P., Miesch, M.S., Browning, M.K., Brun, A.S., and Toomre, J. Magnetic cycles in a convective dynamo simulation of a young solar-type star. *The Astrophysical Journal*, 731 (1), 69, 2011.

Brush, S.G. Discovery of the Earth's core. *American Journal of Physics*, 48(9), 705–724, 1980.

Bullard, E.C. and Gellman, H. Homogeneous dynamos and terrestrial magnetism. *Philosophical Transactions of the Royal Society of London. Series A, Mathematical and Physical Sciences*, 247, 213–278, November 1954.

Canuto, C.G., Hussaini, Y., Quarteroni, A., and Zang, T.A. *Spectral Methods: Fundamentals in Single Domains*. Scientific Computation. Springer, 2010.

Chandrasekhar, S. *Hydrodynamic and hydromagnetic stability*. Clarendon Press, 1961.

Christensen, U.R. and Aubert, J. Scaling properties of convection-driven dynamos in rotating spherical shells and application to planetary magnetic fields. *Geophysical Journal International*, 166(1), 97–114, 2006.

Christensen, U.R., Aubert, J., Cardin, P., Dormy, E., Gibbons, S., Glatzmaier, G.A., Grote, E., Honkura, Y., Jones, C., Kone, M., Matsushima, M., Sakuraba, A., Takahashi, F., Tilgner, A., Wicht, J., and Zhang, K. A numerical dynamo benchmark. *Phys. Earth Planet. Interiors*, (128), 25–34, 2001.

Christensen, U.R., Olson, P., and Glatzmaier, G.A. A dynamo model interpretation of geomagnetic field structures. *Geophysical Research Letters*, 25(10), 1565–1568, 1998.

Christensen, U.R. and Wicht, J. Numerical Dynamo Simulations. In Schubert, G., editor, *Treatise on Geophysics*, pages 245 – 282. Elsevier, Amsterdam, 2007.

Cowling, T.G. The magnetic field of sunspots. *Monthly Notices of the Royal Astronomical Society*, 94, 39–48, November 1933.

Cowling, T.G. *Magnetohydrodynamics*. Adam Hilger, 1975.

Cowling, T.G. Astronomer by accident. *Annual review of astronomy and astrophysics*, 23, 1–18, 1985.

Daube, O. Resolution of the 2D Navier-Stokes equations in velocity-vorticity form by means of an influence matrix technique. *Journal of computational Physics*, 103(2), 402–414, 1992.

Dolginov, A.Z. and Urpin, V.A. The inductive generation of the magnetic field in binary systems. *Astronomy & Astrophysics*, 79, 60–69, O 1979.

Dumberry, M. and Finlay, C.C. Eastward and westward drift of the Earth's magnetic field for the last three millennia. *Earth and Planetary Science Letters*, 254(1–2), 146 – 157, 2007.

Dziewonski, A.M. and Anderson, D.L. Preliminary reference Earth model. *Physics of the Earth and Planetary Interiors*, 25(4), 297 – 356, 1981.

Einstein, A. Die ursache der mäanderbildung der flußläufe und des sogenannten baerschen gesetzes. *Naturwissenschaften*, 14, 223–224, 1926. 10.1007/BF01510300.

Finlay, C.C. *Hydromagnetic waves in Earth's core and their influence on geomagnetic secular variation*. PhD thesis, The University of Leeds, School of Earth and Environment, May 2005.

Finlay, C.C. and Jackson, A. Equatorially dominated magnetic field change at the surface of Earth's core. *Science*, 300(5628), 2084–2086, 2003.

Finlay, C.C., Jackson, A., Gillet, N., and Olsen, N. Core surface magnetic field evolution 2000–2010. *Geophysical Journal International*, 189(2), 761–781, 2012.

Gans, R.F. Viscosity of the Earth's core. *Journal of Geophysical Research*, 77(2), 360–366, 1972.

Gauss, C.F. Allgemeine theorie des erdmagnetismus. *Resultate aus den Beobachtungen des magnetischen Vereins im Jahre 1838*, 1839.

Gibbons, S. LEOPACK (Leeds, Exeter, Oslo PACKage) user's guide. November 2001.

Gibson, R.D. and Roberts, P.H. *The Bullard-Gellman dynamo*. S.K. Runcorn, ed., Wiley-Interscience, New York (1969), 1967. The Application of Modern Physics to the Earth and Planetary Interiors.

Glatzmaier, G.A. Geodynamo simulations-how realistic are they? *Annual Review of Earth and Planetary Sciences*, 30(1), 237–257, 2002.

Glatzmaier, G.A. and Roberts. A three-dimensional convective dynamo solution with rotating and finitely conducting inner core and mantle. *Physics of the Earth and Planetary Interiors*, 91(1 - 3), 63 – 75, 1995.

Grote, E., Busse, F. H., and Tilgner, A. Effects of hyperdiffusivities on dynamo simulations. *Geophysical Research Letters*, 27(13), 2001–2004, 2000.

Gubbins, D. *Encyclopedia of Geomagnetism and Paleomagnetism*. Nature Publishing Group, 2007.

Gubbins, D., Willis, A.P., and Sreenivasan, B. Correlation of earth's magnetic field with lower mantle thermal and seismic structure. *Physics of the Earth and Planetary Interiors*, 162(3 - 4), 256 – 260, 2007.

Gutenberg, B. Über die Konstitution des Erdinnern, erschlossen aus Erdbeben-beobachtungen. *Physikalische Zeitschrift*, 14, 1217–1218, 1913.

Harder, H. and Hansen, U. A finite-volume solution method for thermal convection and dynamo problems in spherical shells. *Geophysical Journal International*, (161), 522–532, 2005.

Herzenberg, A. Geomagnetic dynamos. *Philosophical Transactions of the Royal Society of London. Series A, Mathematical and Physical Sciences*, 250(986), 543–583, 1958.

Hollerbach, R. A spectral solution of the magneto-convection equations in spherical geometry. *International Journal for numerical methods in fluids*, (32), 773–797, 2000.

Hollerbach, R. Volume 31 of *Geodyn. Ser.*, chapter The range of timescales on which the geodynamo operates, pages 181–192. AGU, Washington, DC, 2003.

Holme, R. Treatise of geophysics. Core Dynamics, 2007.

Hori, K., Wicht, J., and Christensen, U.R. The effect of thermal boundary conditions on dynamos driven by internal heating. *Physics of the Earth and Planetary Interiors*, 182(1), 85–97, 2010.

Hori, K., Wicht, J., and Christensen, U.R. The influence of thermo-compositional boundary conditions on convection and dynamos in a rotating spherical shell. *Physics of the Earth and Planetary Interiors*, 196, 32–48, 2012.

Jackson, A. Intense equatorial flux spots on the surface of Earth's core. *Nature*, (424), 760–763, 2003.

Jackson, A., Jonkers, A.R.T., and Walker, M.R. Four centuries of geomagnetic secular variation from historical records. *Philosophical Transactions of the Royal Society of London. Series A, Mathematical, Physical and Engineering Sciences*, 358(1768), 957–990, 2000.

Jackson, A., Sheyko, A., Marti, P., Tilgner, A., Cébron, D., Vantieghem, S., Simitev, R., Busse, F., Zhan, X., Schubert, G., et al. A spherical shell numerical dynamo benchmark with pseudo-vacuum magnetic boundary conditions. *Geophysical Journal International*, 196(2), 712–723, 2014.

Jacobs, J.A. *Geomagnetism*, Volume 2. Academic press, Cambridge, 1987.

Jeffreys, H. The viscosity of the Earth. *Philosophical Magazine*, 2, 833–844, 1926.

Jones, C.A., Mussa, A.I., and Worland, S.J. Magnetoconvection in a rapidly rotating sphere: the weak-field case. *Proceedings of the Royal society London A*, 459(2031), 737–797, March 2003.

Jones, C.A., Soward, A.M., and Mussa, A.I. The onset of thermal convection in a rapidly rotating sphere. *Cambridge University Press*, 405, 157–179, 2000.

Kolmogorov, A.N. The local structure of turbulence in incompressible viscous fluid for very large Reynolds numbers. In *Dokl. Akad. Nauk SSSR*, Volume 30, pages 299–303, 1941.

Kraichnan, R.H. Turbulent thermal convection at arbitrary prandtl number. *Physics of Fluids (1958-1988)*, 5(11), 1374–1389, 1962.

Kuang, W. and Bloxham, J. Numerical Modeling of Magnetohydrodynamic Convection in a Rapidly Rotating Spherical Shell: Weak and Strong Field Dynamo Action. *Journal of computational Physics*, 153, 51–81, 1999.

Lallemand, S. and Funicello, F. *Subduction zone geodynamics*. Springer, 2009.

Larmor, J. How could a rotating body such as the sun become a magnet? *Report of the British Association for the Advancement of Science.*, pages 159–160, 1919.

Lehmann, I. P'. *Publications du Bureau Central Séismologique International, Série A, Travaux Scientifiques*, 14, 87–115., 1936.

Lehnert, B. Magnetohydrodynamic Waves Under the Action of the Coriolis Force. *Astrophysical Journal*, 119, 647, May 1954.

Livermore, P.W., Ierley, G., and Jackson, A. The evolution of a magnetic field subject to taylor's constraint using a projection operator. *Geophysical Journal International*, 187(2), 690–704, 2011.

Lundquist, S. Experimental investigations of magneto-hydrodynamic waves. *Physical Review Letters*, 76, 1805–1809, Dec 1949.

Marti, P. *Convection and boundary driven flows in a sphere*. PhD thesis, Eidgenössische Technische Hochschule ETH Zürich, 2012.

Marti, P. and Willis, A. P. *A Spherical Dynamo Code*, 1.2.1 edition, January 2009.

Miyagoshi, T., Kageyama, A., and Sato, T. Formation of sheet plumes, current coils, and helical magnetic fields in a spherical magnetohydrodynamic dynamo. *Physics of Plasmas (1994-present)*, 18(7), –, 2011.

Moffatt, K. The amplification of a weak applied magnetic field by turbulence in fluids of moderate conductivity. *Journal of Fluid Mechanics*, 11, 625–635, 11 1961.

Morize, C., Moisy, F., and Rabaud, M. Decaying grid-generated turbulence in a rotating tank. *Physics of Fluids*, 17(9), 095105, 2005.

Oldham, R.D. The constitution of the interior of the Earth, as revealed by Earthquakes. *Quarterly Journal of the Geological Society 1906*, 62, 456–475, 1906.

Olson, P. and Christensen, U.R. The time-averaged magnetic field in numerical dynamos with non-uniform boundary heat flow. *Geophysical Journal International*, 151(3), 809–823, 2002.

Pastukhov, V.P. Adiabatic separation of motions and reduced mhd equations. *Plasma Physics Reports*, 26(6), 529–538, 2000.

Pozzo, M., Davies, C., Gubbins, D., and Alfe, D. Thermal and electrical conductivity of iron at earth's core conditions. *Nature*, 485(7398), 355–358, 2012.

Press, W.H. *Numerical recipes 3rd edition: The art of scientific computing*. Cambridge university press, 2007.

Riley, K.F., Hobson, M.P, and Bence, S.J. *Mathematical methods for physics and engineering*. University Press, Cambridge, second edition, 2002.

Roberts, P.H., Jones, C.A., and Calderwood, A.R. *Energy fluxes and ohmic dissipation in the Earth's core.*, Volume Earth's Core and Lower Mantle. London: Taylor & Francis, 2003. In Jones, C A., Soward, A.M., and Zhang, K. (eds.).

Sakuraba, A. and Roberts, P.H. Generation of a strong magnetic field using uniform heat flux at the surface of the core. *Nature*, 2(165), November 2009.

Soderlund, K., King, E., and Aurnou, J. The influence of magnetic fields in planetary dynamo models. *Earth and Planetary Science Letters*, 333-334(0), 9 – 20, 2012.

Stelzer, Z. and Jackson, A. Extracting scaling laws from numerical dynamo models. *Geophysical Journal International*, 2013.

Takahashi, F. and Shimizu, H. A detailed analysis of a dynamo mechanism in a rapidly rotating spherical shell. *Journal of Fluid Mechanics*, 701, 228–250, 2012.

Takeuchi, H. and Shimazu, Y. On a self-exciting process in magneto-hydrodynamics. *Journal of Geophysical Research*, 58(4), 497–518, 1953.

Tobias, S.M. and Cattaneo, F. Limited role of spectra in dynamo theory: Coherent versus random dynamos. *Physical Review Letters*, 101, 125003, Sep 2008.

Trefethen, L.N. and Bau III, D. *Numerical linear algebra*, Volume 50. Siam, 1997.

Treumann, R.A. and Baumjohann, W. *Advanced Space Plasma Physics*. College Press, 1997.

Turing, A.M. A.M. Turing's ACE Report of 1946 and Other Papers. edited by B.E. Carpenter and R.W. Doran (MIT, Los Angeles, CA, 1986), 1946.

Walker, M.R., Barenghi, C.F., and Jones, C.A. A note on dynamo action at asymptotically small Ekman number. *Geophysical & Astrophysical Fluid Dynamics*, 88(1-4), 261–275, 1998.

Wicht, J. and Christensen, U.R. Torsional oscillations in dynamo simulations. *Geophysical Journal International*, 181(3), 1367–1380, 2010.

Willis, A. P., Sreenivasan, B., and Gubbins, D. Thermal core-mantle interaction: Exploring regimes for 'locked' dynamo action. *Physics of the Earth and Planetary Interiors*, (165), 83–92, 2007.

Zhang, K. On equatorially trapped boundary inertial waves. *Journal of Fluid Mechanics*, 248, 203–217, 1993.

Zhang, K. and Jones, C.A. The effect of hyperviscosity on geodynamo models. *Geophysical Research Letters*, 24(22), 2869–2872, 1997.

Zhou, Ye. A phenomenological treatment of rotating turbulence. *Physics of Fluids*, 7(8), 2092–2094, 1995.

List of Tables

List of Figures

Index

Curriculum vitæ

Personal data:

Name:	Andrey Alexandrovich Sheyko
Address:	via Ceresio 8a, 6900 Massagno, Ticino, Switzerland
E-Mail:	andrey.sheyko@gmail.com
Skype:	andrey.sheyko
Marital status:	married, one child
Date of birth:	06/12/1984
Place of birth:	Volgograd, USSR
Citizenship:	Russian

Education:

08/2008 - 06/2014	Ph.D. candidate. Institute of Geophysics, ETH.
12/2006 - 05/2007	Master's diploma work: "Wireless Telemetry, electromagnetic field around cased well". Schlumberger research centre (Clamart, France).
08/2006 - 11/2006	Courses: Arctic water resources, Ocean Polar Climate, Arctic Offshore Engineering. UNIS (University centre In Svalbard, Norway).
09/2005 - 09/2007	Master's course: "Physics of geospheres interaction and Earth's ecology". MIPT (Moscow Institute of Physics and Technology), Russian Federation.
09/2004 - 09/2005	Laboratory studies for the Bachelor's degree: "Investigation of optical properties of dense plasma". Institute of Problems of Chemistry Physics in Chernogolovka.
09/2001 - 09/2005	Bachelor's degree in Applied Mathematics and Physics. MIPT (Moscow Institute of Physics and Technology), Russian Federation.
1999-2001	Taganrog Municipal Lyceum of General Education affiliated with TSURE (Taganrog State University of Radioengineering), Russian Federation.
1991-1999	Secondary School, Belogorsk, Amur region, Russian Federation.

Work and Research Experience:

04/2013 - Present	Scientific Computing Support Specialist.
	Swiss National Supercomputing Centre (CSCS).
10/2008 - 12/2012	Research Assistant.
	Institute of Geophysics, ETH, Zürich.
09/2007 - 03/2008	Research Assistant.
	CIPR Centre for Integrated Petroleum Research, Bergen, Norway.
09/2005 - 05/2007	Internship.
	Schlumberger Research and Development, Moscow, Russia & Clamart, France.
09/2004 - 09/2005	Research Assistant.
	Institute of Problems of Chemical Physics, Chernogolovka, Russia.
1999 - 2001	Web-Designer.
	Infotecs Taganrog Telecom, Russia.
1997 - 1999	Graphics-Designer.
	VideoService, local TV-broadcaster, Amur region, Russia.